
The sub-mJy radio population in the Extended Chandra Deep Field South

Margherita Bonzini



München 2014

The sub-mJy radio population in the Extended Chandra Deep Field South

Margherita Bonzini

Dissertation
an der Fakultät für Physik
der Ludwig-Maximilians-Universität
München

vorgelegt von
Margherita Bonzini
aus Mailand, Italien

München, den 2 Juni 2014

Erstgutachter: Prof. Dr. Joseph Mohr

Zweitgutachter: PD Dr. Klaus Dolag

Tag der mündlichen Prüfung: 17 Juli 2014

Ad M.D.G.

Contents

Zusammenfassung	xv
Abstract	xvii
1 Introduction	1
1.1 Extragalactic radio sources	1
1.1.1 Historical introduction	1
1.1.2 Radio source number counts	3
1.2 The faint radio sky	5
1.2.1 Astrophysical continuum radio emission mechanisms	5
1.2.2 Active galactic nuclei	6
1.2.3 Star forming galaxies	16
1.3 AGN-host galaxy connection	22
1.4 The content of this Thesis	27
2 Radio observations and source catalog	31
2.1 Introduction	32
2.2 Improved Imaging	34
2.2.1 Background	34
2.2.2 General Procedure	35
2.2.3 Summary of Final Data and Images	37
2.3 Source Catalog	41
2.3.1 Source Detection	41
2.3.2 Source Morphology	42
2.3.3 Multiple Component Sources	47
2.3.4 Source Flux Density	48
2.3.5 Final Catalog	49
2.4 Summary and Discussion	52
2.A Multiple-Component Source Images	58
3 Optical and infrared counterpart identification.	63
3.1 Introduction	63
3.2 Data	64

3.2.1	The radio catalog	64
3.2.2	Auxiliary data	64
3.3	Counterpart identification method	68
3.3.1	Likelihood ratio technique	68
3.3.2	Identification results	70
3.3.3	Multiple component radio systems	74
3.3.4	Revisited associations	76
3.3.5	Spurious associations and cross-correlation method comparison . . .	76
3.3.6	Comparison with previous work	78
3.4	Redshift associations	79
3.4.1	New VIMOS spectra and redshifts	79
3.4.2	Spectroscopic redshifts	82
3.4.3	Photometric redshifts	82
3.4.4	Redshift distribution	86
3.5	X-ray counterparts	89
3.5.1	Average X-ray properties of radio-only detected sources	89
3.6	Catalog description	90
3.7	Discussion and Conclusions	92
3.A	New VIMOS/VLT spectra.	93
3.B	Notes on individual sources.	96
4	Radio source populations in the E-CDFS	99
4.1	Introduction	99
4.2	Sample and data	100
4.2.1	Radio catalog, optical-IR counterparts and redshifts	100
4.2.2	Mid infrared data	101
4.2.3	X-ray data	101
4.3	AGN or SFG?	102
4.3.1	Classification criteria	102
4.3.2	Our classification scheme	105
4.3.3	Sources without redshift	105
4.3.4	Unidentified sources	108
4.3.5	Further checks	108
4.3.6	Results	111
4.4	The sub-mJy population	115
4.5	Host galaxy properties	115
4.5.1	Morphology	115
4.5.2	Stellar masses	117
4.5.3	Rest Frame colours	119
4.5.4	The 4000 Å break	122
4.6	Discussion	124
4.6.1	Selection caveats	124
4.6.2	Host galaxies properties vs. radio loudness	126

4.6.3	Radio emission in RQ AGN	127
4.7	Summary and conclusions	128
5	Star formation and black hole activity in the faint radio sky	131
5.1	Introduction	131
5.2	Sample description	133
5.2.1	Radio data	133
5.2.2	Radio source populations	133
5.2.3	<i>Herschel</i> data	134
5.3	FIR luminosity of radio sources	134
5.4	Radio-FIR correlation	135
5.5	Star formation rate estimate	138
5.6	Radio emission in RQ AGN	138
5.6.1	AGN contribution in the FIR	139
5.6.2	Stacking of <i>Herschel</i> undetected sources	141
5.7	SFR versus stellar mass	143
5.8	Specific Star Formation Rate	145
5.8.1	SF in RL AGNs	146
5.8.2	SF in RQ AGNs and SFGs	147
5.8.3	AGN content as a function of sSFR	150
5.9	Discussion	152
5.9.1	Comparison with a FIR selected sample	152
5.9.2	What changes using a different SFR tracer?	155
5.9.3	$L_X - L_{\text{FIR}}$ relation	156
5.10	Summary	157
5.A	Choice of the model parameter	159
5.A.1	SFGs mass function	159
5.A.2	Main sequence and its redshift evolution	160
5.A.3	Comparison with VLA observations	160
5.B	Stellar masses and SFRs catalog of VLA sources	161
6	Conclusions	163
	Acknowledgments	181
	Curriculum Vitae	182

List of Figures

1.1	Optical image of 3C 273 with contours showing the radio jet.	2
1.2	Radio number counts at 1.4 GHz.	4
1.3	Synchrotron spectral energy distribution.	5
1.4	Radio and FIR emission in M82.	7
1.5	AGN continuum spectrum	8
1.6	Unified model of AGNs.	12
1.7	X-ray spectra of AGNs with increasing absorption.	13
1.8	Lacy et al. (2004) IRAC color space.	15
1.9	Stern et al. (2005) IRAC color space.	15
1.10	Spectra evolution of a single stellar population galaxy.	17
1.11	Optical-to-FIR SED of a typical forming galaxy.	18
1.12	Evolution of the SFG main-sequence.	21
1.13	Cosmic history of black hole and stellar mass growth.	23
1.14	Bimodality of galaxy optical colors.	24
1.15	<i>Chandra</i> X-ray image of the Perseus cluster core.	25
1.16	Example of detection of kpc scale AGN driven outflows.	26
2.1	Mosaic radio image.	38
2.2	Fractional area covered at a given sensitivity.	40
2.3	Ratio of integrated to peak flux densities.	44
2.4	Bandwidth smearing.	46
2.5	Number of radio sources as a function of SNR.	55
2.6	Images of multi-component sources.	58
3.1	Flux density distribution.	65
3.2	Multi-wavelength coverages overplotted on the VLA image.	68
3.3	Background source distributions.	69
3.4	Examples of IRAC sources not present in the SIMPLE catalog.	72
3.5	Multi-wavelengths cutouts at the position of the radio sources.	75
3.6	Cutouts of radio sources with complex radio morphology.	77
3.7	Cumulative distribution radio sources-counterparts separation.	80
3.8	Redshift distribution.	83
3.9	Radio power as a function of redshift.	84

3.10	Normalized redshift distribution.	85
3.11	New VIMOS/VLT spectra of the radio sources.	94
4.1	X-ray luminosity as a function of redshift.	103
4.2	q_{24obs} values as a function of redshift.	106
4.3	IRAC colour-colour plot.	107
4.4	R versus q_{24obs}	110
4.5	Radio power distributions.	114
4.6	Relative fraction of the various classes of radio sources.	116
4.7	Sèrsic index distributions.	118
4.8	Two examples of 2-component SED fit results.	120
4.9	Stellar mass distributions.	121
4.10	Rest-frame U-B colours.	123
4.11	Strength of the 4000 Å break.	125
5.1	Examples of the optical-to-FIR SED fitting.	135
5.2	Radio power versus FIR luminosity for SFGs detected by <i>Herschel</i>	137
5.3	Comparison of the SFR derived from FIR and radio luminosity.	140
5.4	SFR from the full photometry and UV-to-optical data ratio.	142
5.5	SFR versus stellar mass for different redshift bins.	144
5.6	Fraction of starburst, MS galaxies, and passive galaxies versus redshift.	146
5.7	Fraction of starburst, MS galaxies, and passive galaxies versus stellar mass.	146
5.8	Stellar mass versus radio power for RL AGN.	147
5.9	Relative fraction of sources classes as a faction of $\Delta \log(sSFR)_{MS}$	151
5.10	SFR comparison for the mock catalog.	153
5.11	SFR versus stellar mass for the VLA and PACS sample	154
5.12	MS and starburst fractions vs. radio flux density.	155
5.13	Fraction of SB, MS, and passive derived using SFR_r vs. stellar mass.	156
5.14	$L_X - L_{IR}$ and $P_r - L_{IR}$ relations.	157

List of Tables

2.1	Pointing Coordinates	35
2.2	Flux Density Comparisons	50
2.3	Main Catalog of Radio Sources	53
2.4	Individual Components of Multiple-Component Radio Sources	54
3.1	List of auxiliary catalogs.	67
3.2	Counterparts and spurious sources.	71
3.3	Radio information and identification process results.	73
3.4	List of the spectroscopic catalogs.	81
3.5	Characteristics and redshifts of the radio source counterparts.	88
3.6	Redshift distribution of the counterparts.	89
3.7	Net counts and HR for radio sources without X-ray detection.	90
4.1	Classification of radio sources.	112
5.1	Results of the stacking analysis.	143
5.2	Star formation properties of the VLA sources.	162

Zusammenfassung

Tiefe Beobachtungen im Radiobereich ermöglichen einen Blick auf aktive schwarze Löcher („black holes“, BH) und auch Gebiete aktiver Sternentstehung („star formation“, SF), ohne dass die Beobachtungen durch den Staub in Galaxien beeinflusst werden. Daher sind Radiobeobachtungen ideal, um deren Entwicklung und eine mögliche gegenseitige Beeinflussung von BH und SF Aktivität über kosmische Zeiten hinweg zu untersuchen. Radioastronomie gewinnt darum für die Erforschung von Galaxienentwicklung zunehmend an Bedeutung. Dies ist auch bedingt durch die zahlreichen neuen Radioanlagen, die im Bau oder in Planung sind. Um das Potential dieser neuen Instrumente zu maximieren, ist es essentiell Vorhersagen darüber zu machen, was wir beobachten werden und zu erfahren, wie wir die Radiodaten am besten mit Multiwellenlängendaten ergänzen.

Das ist die Motivation meiner Doktorarbeit, in der ich eine Auswahl von 900 Radioquellen untersucht habe, die in einer der tiefsten jemals durchgeführten Radiodurchmusterungen detektiert wurden. Die Beobachtungen wurden bei 1.4 GHz mit dem Very Large Array auf dem „Extended Chandra Deep Field South“ durchgeführt. Ich habe eine Multiwellenlängenmethode entwickelt, um die optischen und infraroten Pendanten dieser Radioquellen zu identifizieren und sie als radiolaute („radio loud“, RL) aktive galaktische Kerne („active galactic nuclei“, AGNs), radioleise („radio quiet“, RQ) AGNs und Galaxien mit aktiver Sternentstehung („star forming galaxies“, SFGs) zu klassifizieren. Als erste war es mir möglich, die jeweiligen Anteile dieser verschiedenen Klassen an Quellen bis zu einer Flussdichte von nur $\sim 30 \mu\text{Jy}$ zu bestimmen.

Ich charakterisierte die Galaxieneigenschaften (Sternmasse, optische Farben, Morphologie) der Radioquellen; RQ AGN Galaxien und SFGs sind ähnlich bezüglich der Scheibenmorphologie und der blauen Farben, während RL AGN Galaxien massiver, röter und meist elliptisch sind. Dies legt nahe, dass RQ und RL Aktivität auf zwei verschiedenen Entwicklungsstufen der BH – Galaxien Koevolution stattfindet. Die RQ Phase findet früher statt, wenn die Galaxie noch gasreich ist und aktiv Sterne bildet, während BHs erst als Radioquelle aktiv werden, wenn die Galaxie bereits den Großteil ihrer Sternpopulation gebildet hat, der Gasvorrat gesunken ist und die SF erheblich zurückgegangen ist.

Ich quantifizierte die Sternentstehungsrate („star formation rate“, SFR) der Radioquellen durch zwei unabhängige Indikatoren, die Radio- und die Ferninfrarotleuchtkraft. Ich habe Belege gefunden, dass der Hauptanteil der Radioemission von RQ AGNs durch die SF Aktivität der Galaxie entsteht. Dieses Ergebnis eröffnet die bemerkenswerte Möglichkeit, den Radiobereich des Spektrums zu benutzen um die SFR auch in Galaxien mit hellen,

RQ AGNs abzuschätzen, bei denen die optische bis mittlere Infrarot Emission vom AGN dominiert sein kann. Ich habe gezeigt, dass tiefe Radiodurchmusterungen benutzt werden können um die kosmische Sternentstehungsgeschichte zu erforschen; Ich habe den Anteil des sogenannten „Starburst“-Modus an der gesamten SFR-Dichte abgeschätzt und das Vorkommen von AGNs in Galaxien mit verschiedenem Grad an SF quantifiziert.

Abstract

Deep radio observations provide a dust unbiased view of both black hole (BH) and star formation (SF) activity and therefore represent a powerful tool to investigate their evolution and their possible mutual influence across cosmic time. Radio astronomy is therefore becoming increasingly important for galaxy evolution studies thanks also to the many new radio facilities under construction or being planned. To maximise the potentiality of these new instruments it is crucial to make predictions on what they will observe and to see how best to complement the radio data with multi-wavelength information.

These are the motivations of my Thesis in which I studied a sample of 900 sources detected in one of the deepest radio surveys ever made. The observations have been performed at 1.4 GHz with the Very Large Array on the Extended Chandra Deep Field South. I developed a multi-wavelength method to identify the optical-infrared counterparts of the radio sources and to classify them as radio-loud active galactic nuclei (RL AGNs), radio-quiet (RQ) AGNs, and star forming galaxies (SFGs). I was able for the first time to quantify the relative contribution of these different classes of sources down to a radio flux density limit of $\sim 30 \mu\text{Jy}$.

I characterized the host galaxy properties (stellar masses, optical colors, and morphology) of the radio sources; RQ AGN hosts and SFGs have similar properties with disk morphology and blue colors while radio-loud AGN hosts are more massive, redder and mostly ellipticals. This suggests that the RQ and RL activity occurs at two different evolutionary stages of the BH-host galaxy co-evolution. The RQ phase occurs at earlier times when the galaxy is still gas rich and actively forming stars while the radio activity of the BH appears when the galaxy has already formed the bulk of its stellar population, the gas supply is lower, and the SF is considerably reduced.

I quantified the star formation rate (SFR) of the radio sources using two independent tracers, the radio and far-infrared luminosities. I found evidence that the main contribution to the radio emission of RQ AGNs is the SF activity in their host galaxy. This result demonstrates the remarkable possibility of using the radio band to estimate the SFR even in the hosts of bright RQ AGNs where the optical-to-mid-infrared emission can be dominated by the AGN. I have shown that deep radio surveys can be used to study the cosmic star formation history; I estimated the contribution of the so-called "starburst" mode to the total SFR density and quantified the AGN occurrence in galaxies with different levels of SF.

Chapter 1

Introduction

Understanding the role of active galactic nuclei (AGNs) in shaping the properties of their host galaxies is one of the crucial issues in galaxies formation and evolution studies. Many different approaches are possible to tackle this problem; some works concentrate on a limited number of objects investigated in great details, while others have a more statistical approach studying large samples, like the one considered in this Thesis. A key ingredient for both methods is a multi-wavelength analysis as different spectral windows reveal different physical processes and are therefore crucial for a comprehensive view of the problem. For this reason, in this introduction I will present the multi-wavelength properties of AGNs and active galaxies and the evidences for their coeval growth across cosmic time.

Moreover, since the sample studied in this Thesis has been selected from one of the deepest radio survey up to date, I will first summarize the history of extragalactic radio astronomy. We are at the beginning of a "golden era" for radio astronomy as many new radio facilities have been planned or are currently under construction. Therefore, the multi-wavelength analysis presented in this Thesis represents an important reference showing the issues and the potentiality of the upcoming radio surveys, in synergy with panchromatic studies, in studying the evolution of active galaxies and black holes.

1.1 Extragalactic radio sources

1.1.1 Historical introduction

The beginning of radio astronomy corresponds to the Karl Jansky's serendipitous discovery of a strong radio signal from the center of the Milky Way, back in the early 30s', while he was studying the causes of disturbances to radio telephone communications. However, it was only after the end of the Second World War that radio detectors were used and built specifically for studying the cosmic radio emission. After our galactic center, the first resolved radio source was Cygnus A in 1946 (Hey, 1946) but its association with a distant galaxy was recognized only some years later (Baade & Minkowski, 1954). Indeed, the major challenge for radio astronomers at that epoch was to identify the optical counterparts

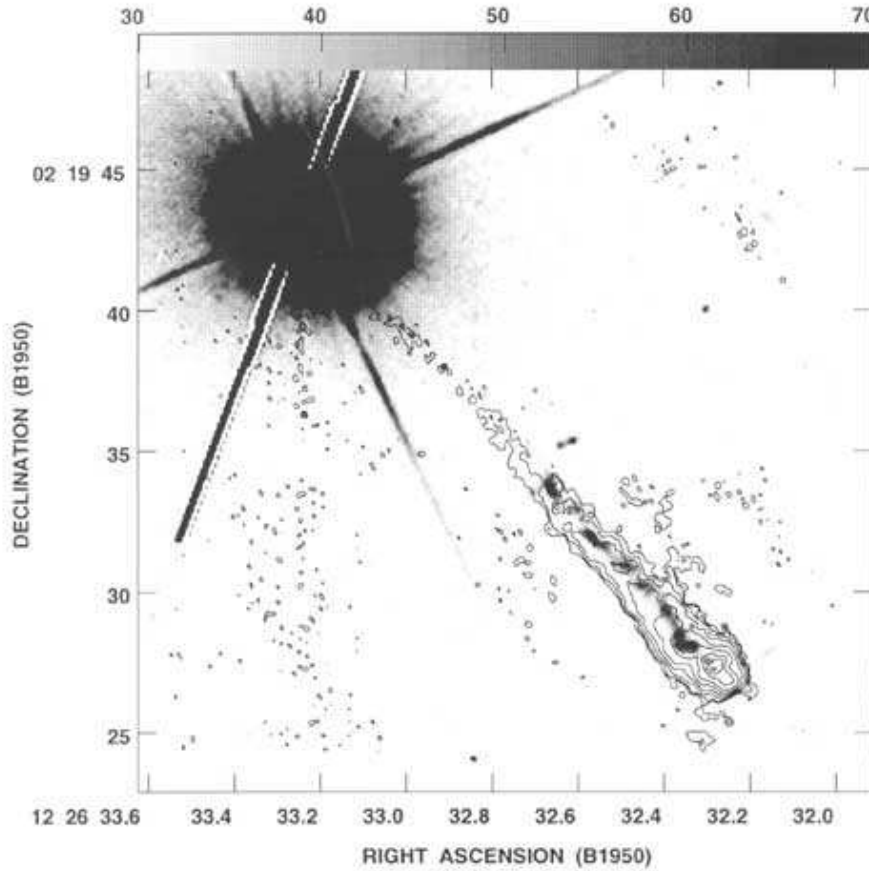


Figure 1.1: Optical image of 3C 273 with contours showing the radio jet.

of the radio sources in order to understand their nature. The first work suggesting an extragalactic origin of the radio emission is Bolton et al. (1949) where two bright radio sources were identified with external galaxies. However, progress was slow because of the poor source position accuracy and only in the mid '50s, the association of high latitude radio sources with "radio galaxies" was widely accepted.

Starting in the 60s', with the increased use of interferometric telescopes, large samples of radio galaxies were matched with optical observations and used for cosmological studies. In particular, radio astronomers realized they could use faint radio sources to discover the highest redshift objects. The radio source 3C 295 at $z=0.46$ (Minkowski, 1960) remained for ten years the most distant galaxy known and only forty years later the record of the highest redshift source was obtained in surveys other than at radio wavelengths (e.g. Stern, 2000).

The year 1963 represents an important cornerstone for radio astronomy; the optical counterpart of a bright radio source, 3C 273 (Fig. 1.1), was identified with a 13 magnitude object at a redshift of 0.16 (Schmidt, 1963; Hazard et al., 1963). Its corresponding optical luminosity was some hundred times brighter than any radio galaxies previously

identified. Also the spectrum of 3C 273 was peculiar showing a broad profile of the Balmer series lines and a "ultraviolet excess" when compared with normal stars. Hence, it was soon realized that the source of this unusual emission must be a new astrophysical object (Hoyle & Fowler, 1963) later identified with an active galactic nucleus (AGN; Lynden-Bell, 1969). After 3C 273, many other "quasi-stellar objects" (QSOs) or "quasars" were discovered both as radio counterparts or thanks to their ultraviolet (UV) excess (Sandage et al., 1965). Because of their huge luminosity they could be detected up to high redshift and became crucial for cosmological studies. One example was the role of early radio surveys in the debate on the Steady State versus evolving Universe, as I will explain in the following section.

1.1.2 Radio source number counts

One of the easiest cosmological tests is the measurement of the source counts, i.e. the cumulative distribution of the number of sources (N) brighter than a given flux density limit (S). Indeed, in a static and uniformly filled (Euclidean) Universe, the number of sources out to a distance R would be $N \propto R^3$ and the flux density would scale as $S \propto R^{-2}$. This implies that $N \propto S^{-3/2}$ and in differential form $dN/dS \propto S^{-5/2}$.

Early radio surveys (e.g. the Cambridge 2C survey; Shakeshaft et al., 1955) measured instead a steeper slope of the source counts; this implied an evolution, in number or luminosity, of the sources and therefore it provided evidence against the non-evolving, Steady State cosmological models (Ryle & Scheuer, 1955).

These first observations were sensitive only to the most luminous radio sources ($\gtrsim 1 \text{ Jy}^1$) and it was only with the development of new radio facilities, the best example of which is the Very Large Array (VLA), that radio surveys reached unprecedented sensitivity down to the sub-mJy level (Windhorst et al., 1984; Fomalont et al., 1984; Condon, 1984). At such depth, the shape of the source counts does not depend only on the cosmology, but it is the result of the sum of the contributions from the different radio populations, each of which can have an independent evolution (Wall, 1994).

To illustrate that, a recent compilation of several radio surveys at 1.4 GHz down to the sub-mJy level is shown in Fig. 1.2; the differential counts are normalized to the "Euclidean" form, i.e. multiplied by $S^{2/5}$. Reading the plot from right to left, the rise above 1 Jy is due to the strong evolution of powerful radio sources as discussed above. The presence of a peak is a combination of the evolution reaching a peak at $z \approx 3$ and the geometry of the Universe (Wall, 1994). Below 1 mJy a flattening in the number counts has been observed (Windhorst et al., 1984; Fomalont et al., 1984; Condon, 1984) and was interpreted as the signature of the rise of another radio population: star forming galaxies (SFGs). However, determining the relative contribution of radio AGNs and SFGs in the sub-mJy regime remained an open issue for more than twenty years and it was one of the key goals of this Thesis. Deep radio observations as well as a very good understanding

¹The Jansky (Jy) is the flux density unit used in radio astronomy corresponding to $10^{-26} \text{ W m}^{-2} \text{ Hz}^{-1}$ in SI or $10^{-23} \text{ erg s}^{-1} \text{ cm}^{-2} \text{ Hz}^{-1}$ in cgs.

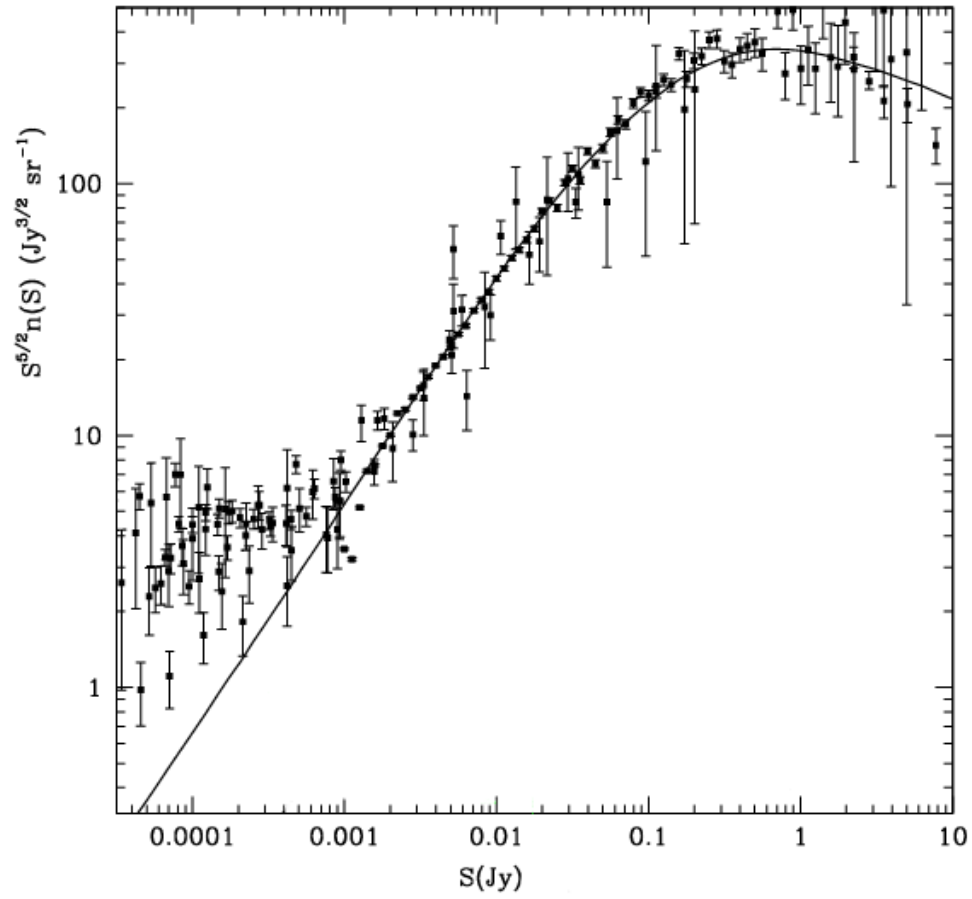


Figure 1.2: Euclidean normalized number counts of radio sources at 1.4 GHz combining different radio surveys (adapted from de Zotti et al., 2010).

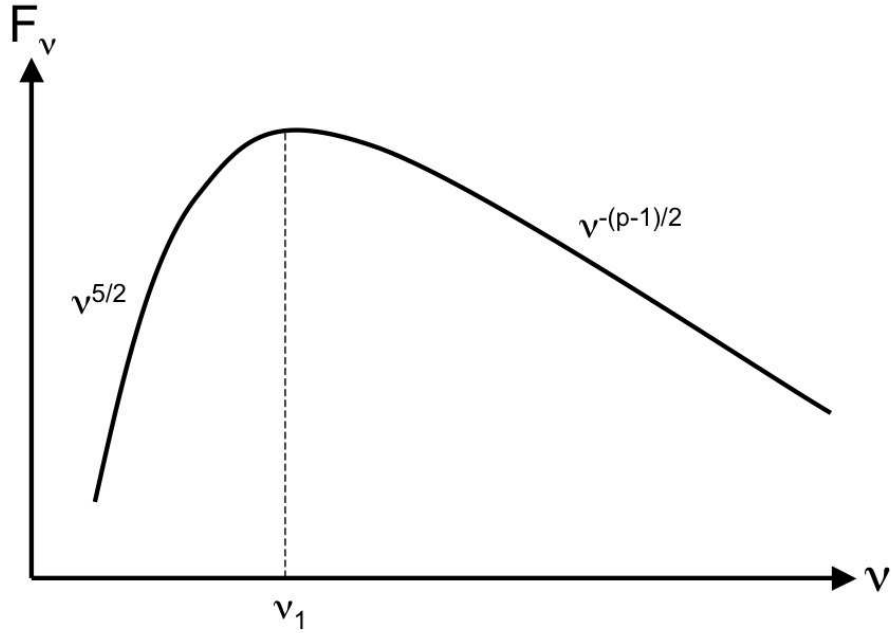


Figure 1.3: Synchrotron SED: at low frequency self-absorption is important and the spectral index is $\alpha = 5/2$, after the turnover at ν_1 the spectrum decline as $\nu^{-(p-1)/2}$, being in the optically thin regime.

of the multi-wavelength properties of both SFGs and AGNs are required to tackle this problem.

Therefore, in the next section I will first briefly describe the radio emission mechanisms that contribute to the continuum radio emission in the different astrophysical sources. I will then summarize the observational characteristics of active radio sources across the electromagnetic spectrum, and illustrate the main physical models proposed to explain the observations.

1.2 The faint radio sky

1.2.1 Astrophysical continuum radio emission mechanisms

The main mechanism of radio continuum emission in both AGNs and SFGs is the synchrotron emission. Synchrotron radiation is produced when relativistic particles (usually electrons) are accelerated in a magnetic field. In SFGs cosmic-ray electrons are accelerated in supernova (SN) explosions of massive ($M > 8 M_\odot$) stars, while in AGNs the electrons are accelerated in relativistic jets powered by the accretion onto a supermassive black hole.

The resulting spectrum of a population of electrons depends on their energy distribution $N(E)$. The typical energy distribution of the cosmic-rays electrons is a power-law of the

form:

$$dN(E) = CE^{-p}dE \quad (1.1)$$

where p is the spectral index. In a constant magnetic field, that produces a synchrotron spectrum $F(\nu)$ that is also a power-law:

$$F(\nu) \propto \nu^{-\frac{p-1}{2}}. \quad (1.2)$$

The observed flux density $S(\nu)$ of astrophysical system emitting synchrotron radiation in the optically thin regime is therefore $S(\nu) \propto \nu^{-\alpha}$, with $\alpha = (p - 1)/2$ (see right side of Fig. 1.3). In the wavelength range 1–100 μm , the median value of α observed in SFGs and AGNs is ≈ 0.7 .

At low frequencies the emission becomes optically thick and synchrotron self-absorption causes a turnover in the spectral energy distribution (SED). In the optically thick regime, the spectrum starts decreasing with decreasing frequency as $S(\nu) \propto \nu^{2/5}$ (see left side of Fig. 1.3). The typical frequency of the turnover in astronomical radio sources ranges from 0.1–10 GHz. At the opposite side, at high frequencies, a spectral steepening has been observed in some AGNs. The reason is that the highest-energy electrons radiate away their energy via synchrotron radiation most rapidly ($\propto E^2$), thus depleting the high-energy end of the emitted spectrum.

In SFGs, thermal Bremsstrahlung (or free-free) radiation also contributes about 10% of the total radio emission (see Condon, 1992, for a review). The Bremsstrahlung emission is due to the energy loss of a free charge accelerated in the potential of protons or ions. It arises from HII regions ionized by massive ($M > 15 M_{\odot}$) stars and as it falls down less rapidly ($\propto \nu^{-0.1}$) than the synchrotron emission, it becomes dominant at mm-wavelengths (see Fig. 1.4).

For a more detailed description of the astrophysical radiation mechanisms see Shu (1991).

1.2.2 Active galactic nuclei

Active Galactic Nuclei (AGNs) are a class of objects that, from the observational point of view, can be defined as apparently stellar sources with non-thermal spectra and high bolometric luminosity ($\gtrsim 10^{42} \text{ erg s}^{-1}$) that, in some cases, can exceed that of the host galaxy. The source of energy is the accretion of material onto a supermassive black hole (SMBH) located in the central region of the host galaxy. An AGN emits radiation at all wavelengths, from radio to X/ γ -rays. Thanks to their brightness, they can be detected up to cosmological distances and, for this reason, they offer the opportunity of studying the Universe up to ten billions years ago and of tracing their evolution across most of the Hubble time.

AGNs display a variety of properties, which explains the historical classification in several classes often without recognizing the common physical origin. Many of the observed differences were then explained as the result of their different orientation with respect to the observer, leading to the so called AGNs Unification Scheme (Antonucci, 1993;

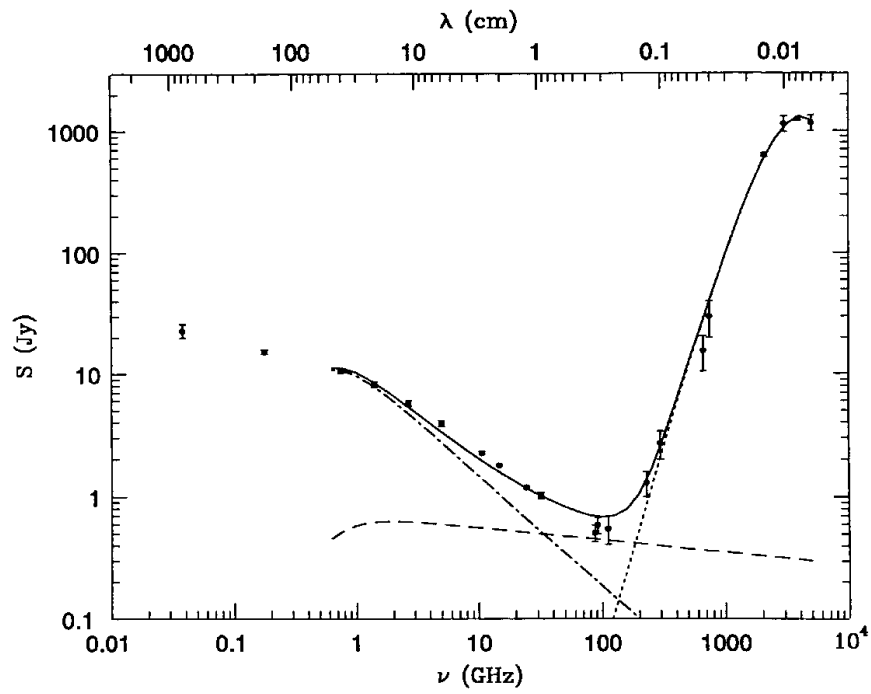


Figure 1.4: The observed radio-to-far-infrared SED of the star forming galaxy M82 (symbols) modelled as the sum (solid line) of synchrotron (dot-dashed line), free-free (dashed line), and dust (dotted line) emissions.

Urry & Padovani, 1995). More recently, as AGN studies have been extended to higher redshift and to a wide range of luminosities, it has been suggested that some properties might also depend on their evolutionary stage and on the rate of fuelling on their central engine. The extent to which these various factors play a role is currently a topic of active research.

In the following I will first present the main features of the typical spectral energy distribution (SED) of an AGN and later discuss the different structural components responsible for the wide range of phenomena observed.

AGN spectral energy distribution

The AGN emission spans from γ -rays to the radio, with almost equal power per decade of frequency. Closer inspection reveals a number of features as dips and bumps in their SED; the most notable ones, ordered by decreasing frequency (ν), are the following (see Fig. 1.5):

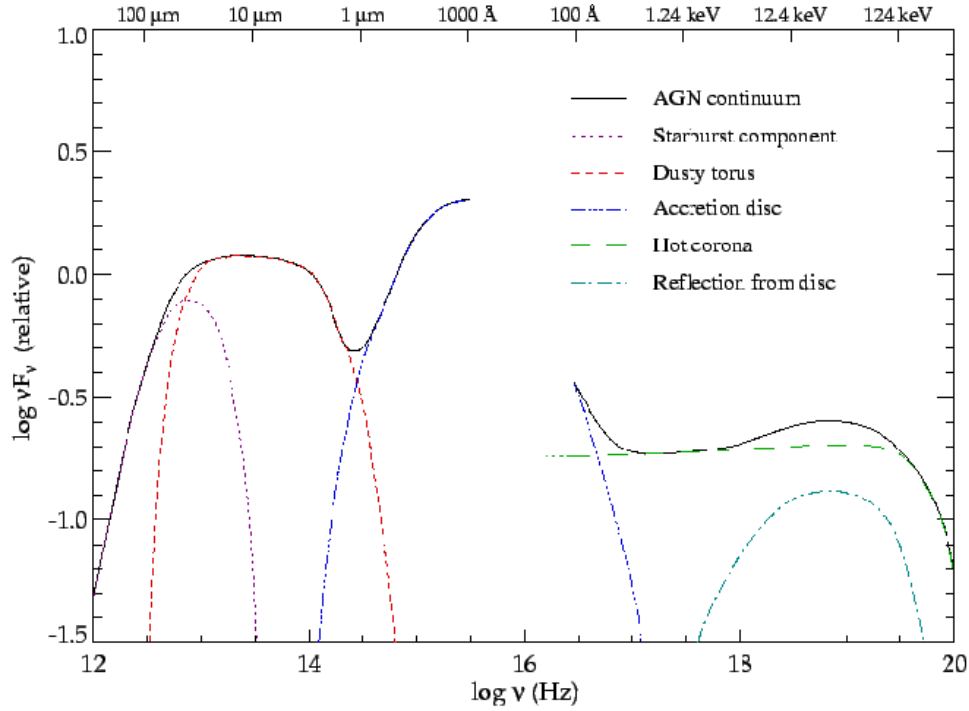


Figure 1.5: Schematic representation of an AGN continuum spectrum including a possible source for each emission component. Image obtained by J. Manners on the basis of the mean spectrum of a sample of quasars from Elvis et al. (1994).

- The X-rays continuum above ~ 2 keV can be modelled to first order with a power law of the form $F_\nu \propto \nu^\alpha$, with $\alpha \sim -0.7$. Here, F_ν is the source flux density (measured

in $\text{erg cm}^{-2} \text{ sec}^{-1} \text{ Hz}^{-1}$) and α is the spectral index. An excess of emission, relative to an extrapolation from the previous power law, between $\sim 0.2\text{-}1 \text{ keV}$ is observed in some AGNs. It is referred to as “soft X-rays excess” whose origin is still matter of debate: either thermal emission, as expected by gas heated by shocks induced by AGN outflows or episodes of intense star formation, or emission from gas photoionized by the AGN primary emission. At about 200 keV an exponential energy cut-off is often present (Perola et al., 2002). Harder spectra (i.e. with larger α) are observed in case of absorption due to gas along the line of sight. The X-ray spectrum shows heavy elements emission lines at low-ionization stage. The most prominent is the iron feature at 6.4keV .

- The so called “Big Blue Bump” dominates the SED from $\sim 1000 \text{ \AA}$ to at least 4000 \AA . Whether this feature extends further into the extreme UV is unclear because our Galaxy becomes opaque at wavelengths between $\sim 100 \text{ \AA}$ and 912 \AA due to absorption by neutral hydrogen. Beyond the peak, the spectrum declines in the optical towards the IR as a power law with spectral index $\alpha \sim 1/3$. AGNs can present rich atomic emission and absorption lines spectra. Based on the differences in the optical-UV regime AGNs can be divided into two categories, type 1 and type 2 AGNs. In type 1 AGNs, the UV bump is clearly visible and some emission lines have a broad component. In Type 2 galaxies, the spectrum appears redder and the host galaxy stellar light dominates these wavelengths. Moreover, the emission lines in type 2 AGNs lack the broad component.
- The “near-infrared inflection” appears as a dip between $1 \text{ }\mu\text{m}$ and $1.5 \text{ }\mu\text{m}$ and is almost the only continuum feature with a well defined wavelength (Neugebauer et al., 1987).
- The “infrared bump” is a broad feature between the $1 \text{ }\mu\text{m}$ inflection and $\sim 100 \text{ }\mu\text{m}$, whose emission is generally comparable in strength to the Big Blue Bump.
- The “submillimeter break” marks a sharp drop in emission at $\lambda \gtrsim 100 \text{ }\mu\text{m}$. The exact location of this feature and the size of the drop vary within the AGN population.
- A small fraction of AGNs ($<10\%$) have also strong radio emission in many cases with extended double-lobes morphology.

AGN structural components

The large amount of energy necessary to reach the extreme bolometric luminosity (L_{bol}) observed in the brightest AGNs ($L_{bol} \sim 10^{46} \text{ erg s}^{-1}$) and the wide frequency range covered by the emission require an extremely efficient mechanism of energy production. Moreover, the short time-scale variability observed in optical and especially in the X-rays bands (e.g. Turner, 1988) suggests that energy is generated in a very compact region.

Among the models proposed, the most commonly accepted one identifies the central engine of the nuclear activity with the gravitational accretion of matter onto a SMBH ($M_{\text{BH}} > 10^6 M_{\odot}$).

In the optically thick case, accretion takes place in a geometrically thin disc of plasma which extends from the last stable orbit around the black hole outwards. The plasma rotates around the black hole following approximately circular orbits (Shakura & Sunyaev, 1973) and dissipative processes redistribute the angular momentum within the disc causing the disc material to move to progressively narrower orbits until it is accreted on the central compact object. The accretion disc has a radial temperature profile of the form $T \propto R^{-3/4}$ (Shakura & Sunyaev, 1973; Lynden-Bell & Pringle, 1974) and the UV-optical emission in AGNs can be in first approximation be interpreted as thermal disc emission with a power-law shape: $F_{\lambda} \propto \lambda^{-1/3}$. More complex models suggest that the UV-optical emission arise from reprocessing X-rays in the disc (Begelman, 1994).

In the inner regions, a corona of hot optically thin plasma above the disc can scatter photons from the accretion disc through inverse-Compton scattering up to X-ray energies, thus potentially explaining the emission in the X-ray band (Maraschi et al., 1991).

In some AGNs relativistic jets originate close to the BH and extend up to tens of kpc, and, in some cases, up to Mpc scales. Jets can have different energetics; the weaker ones decelerate closer to the central SMBH, often still inside the host galaxy, while the most powerful jets propagate into the interstellar and intergalactic medium before originating large scale radio lobes. The physical origin of the radio jets and the reason why they are so powerful in some AGN and absent in others is one of the fundamental problems of high-energy extragalactic astrophysics.

Most of the AGNs also show high ionization lines in their spectra, which reveal the presence of gas, probably photo-ionized by the radiation coming from the accretion disc. This gas is supposed to be arranged in optically thick clouds that surround the central black hole. The clouds motion is governed by the gravitational potential of the SMBH. The direction of this motion is randomly oriented, causing a Gaussian broadening of the emission lines. The line width is proportional to the mean velocity of the gas clouds. Based on the width of the observed emission lines, two distinct regions can be identified around the AGN core:

- The Broad Line Region (BLR); it is composed of clouds which are close to the accretion disc (~ 1 parsec). The ionized gas has relatively high orbital velocity and thus is associated with the broad emission lines component observed in Type 1 AGNs. The BLR is characterized by high temperatures, $T \sim 10^4 K$, and electron column densities, $N_e \sim 10^{9-12} \text{cm}^{-3}$. Since the gas is prevalently Hydrogen this density is equivalent to the number density of atoms. In such a condition no forbidden line can be observed since the frequent collisions cause their de-excitation.
- The Narrow Line Region (NLR); it is made of clouds situated at larger distances from the nucleus (10-1000 parsec). Here the clouds have smaller velocities providing the narrow lines component in the spectra observed in both type 1 and type 2 AGNs.

Typical values for temperatures and densities are 10^3 K and 10^{3-4} cm $^{-3}$, respectively. Narrow permitted lines and forbidden lines are supposed to be emitted in this NLR.

To explain the strong emission in the IR (infrared bump), many models propose the existence of large amounts of dust that, heated up by the accretion disc, thermally re-emits the received energy at these wavelengths. The exact distribution and characteristics of this dust are still unclear. Antonucci (1993); Urry & Padovani (1995) proposed that this obscuring material could be present in all AGN types and that is anisotropically distributed around the SMBH. This anisotropic dust structure is usually referred to as dusty or molecular torus. When the accretion disc and the BLR are seen directly the object is classified as type 1 AGN. Only when the line of sight from the core to the observer intercepts the torus, the nucleus is obscured and the AGN is classified as type 2. As the dust is optically thick the emission from the accretion disc and the hot corona will be absorbed producing a suppression of both the big blue bump and the X-rays emission in these sources. The lack of broad lines in obscured sources suggests that the dust surrounds also the BLR. This model was referred to as “unification scheme” because it was the first attempt to explain the different AGN classes as manifestation of different aspects of the same phenomenon. A schematic visualization of the model is represented in Fig. 1.6.

A separate category of AGNs that is worthy to mention are the so-called “low-excitation” radio AGNs (see Heckman & Best, 2014, for a review). In these sources, the accretion onto the SMBH occurs at a low rate and it is radiatively inefficient. It has been proposed that the optically thick accretion disk described above is absent or truncated in the inner regions of these AGNs. The accretion take place in a geometrically thick advection-dominated accretion flow (e.g., Narayan & Yi, 1994, 1995; Narayan & Quataert, 2005; Ho, 2008) and the bulk of the energetic output is released from relativistic radio jets. The radiative emission is low but can partly ionize the NLR and weak, low-ionization lines are sometimes observed in the optical spectra.

AGN selection methods

As described in the previous sections AGNs emit across the whole electromagnetic spectrum with almost constant energy density. However, AGN samples selected in different spectral windows can be very different and with little overlap between each other. The main reasons for that are: (i) the possible presence of dust, in the torus or in the host galaxy, along the line of sight that obscure part of the AGN emission, especially at UV-optical and soft X-ray frequencies. Therefore, AGN samples selected from these spectral windows tend to be biased towards type 1 objects. (ii) The intrinsic differences in AGN properties, like the presence of radio jets. (iii) The contamination from stellar light that, especially in low luminosity AGNs, can hide the presence of the active BH. Therefore, for a complete AGNs census a multi-wavelength approach is needed.

Here, we summarize the most commonly used methods for selecting AGNs, from the longer to the shortest wavelength, underlying the strengths and limitations of each.

- X-ray:

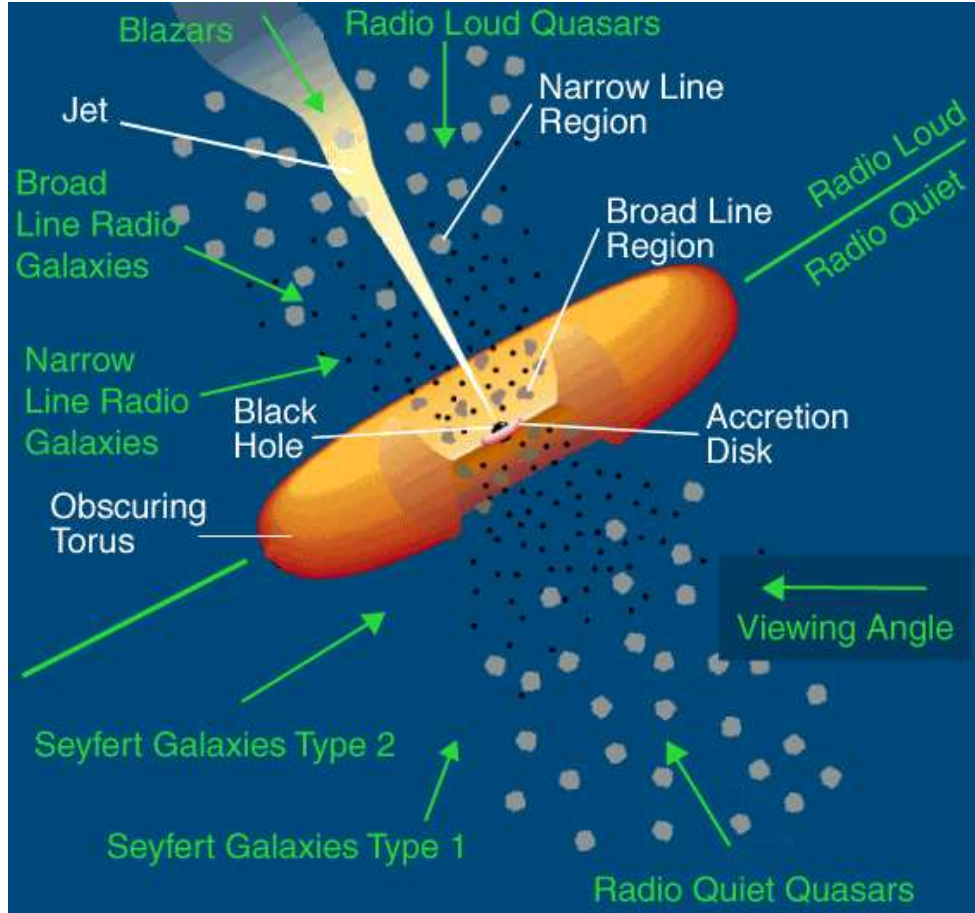


Figure 1.6: Schematic representation of the main elements of an AGN according to the unification scheme (adopted from (Urry & Padovani, 1995)).

The most complete and less biased way of identifying AGNs is the hard X-ray selection. AGNs are the only astrophysical sources that can reach very high X-ray luminosity. Hence, usually a cut in unabsorbed X-ray luminosity at 10^{42} erg s $^{-1}$ is considered as a threshold dividing AGNs and SFGs (e.g., Szokoly et al., 2004). Even in the current deepest X-ray observations (4 Ms *Chandra* exposure Xue et al., 2011) only 35% of the detected sources are non-AGNs.

However, when optically thick dust is present along the line of sight, the soft (0.5-2 keV) X-ray emission is progressively suppressed for increasing obscuration and the X-ray spectrum become "harder" (see Fig. 1.7). Some sources, the so-called "Compton thick" (CT) AGNs, are so obscured that they cannot be detected neither in the hard (2-10 keV) X-ray band (e.g., Comastri & Fiore, 2004; Brandt & Hasinger, 2005) and higher energy surveys would be necessary.

The major problem of selecting AGNs in the X-ray is that to reach the sensitivity

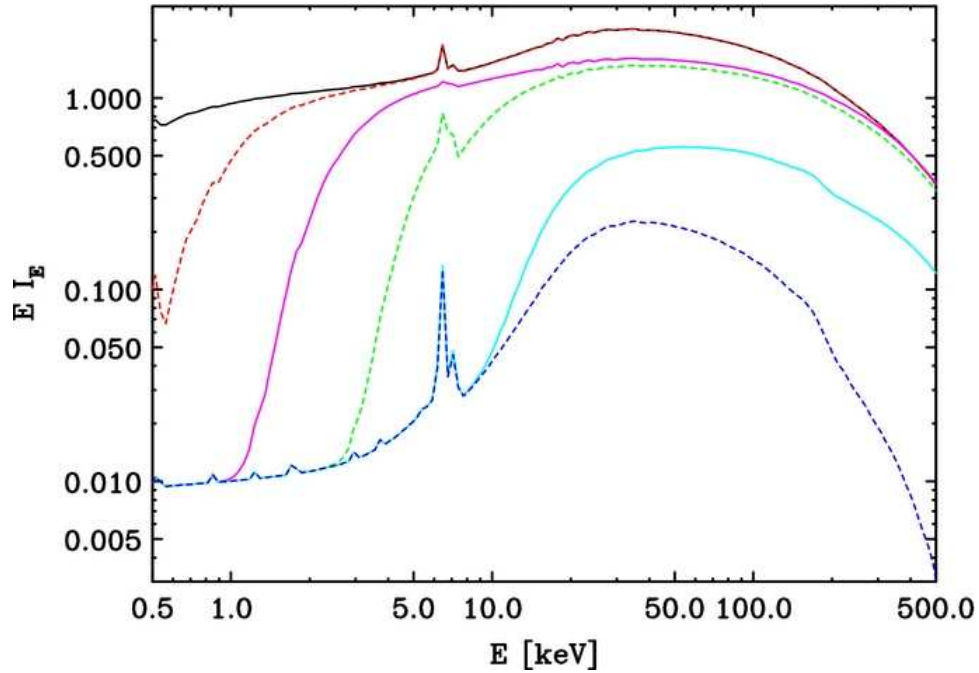


Figure 1.7: X-ray spectra of AGNs with increasing absorption; different colors correspond, from top to bottom, to a logarithm of the column density of 20.5, 21.5, 22.5, 23.5, 24.5, 25.5 cm^{-2} , respectively (from Ueda et al., 2014).

necessary to detect moderately luminosity AGNs at high redshift ($z \approx 2$), very long observing time is needed. Therefore, deep X-ray observations are only available in pencil beam observation on small area of the sky.

- Optical:

As mentioned in section 1.1.1, one of the first methods used to identify bright quasars was based on their optical colors (Sandage & Luyten, 1969). Indeed, AGNs are usually bluer compared to normal galaxies and a combination of multicolor optical data can be used to select large samples of AGNs candidate from optical surveys like the Sloan Digital Sky Survey (SDSS Fan, 1999; Richards et al., 2001). This selection method is biased towards type 1 sources and it is strongly dependent on the AGN luminosity relative to its host galaxy. Moreover, the contamination from stars can be high and therefore spectroscopic follow ups are often needed.

The gas in the BLR and NLR, photo-ionized by the accretion disc radiation, emits strong emission lines that can be used to identify AGNs. The presence of broad lines in the optical spectra is a clear AGN signature since only in the proximity of the BH the gas clouds can have such high velocities. However, in type 2 AGNs the view to the BLR is blocked by the dusty torus and only narrow lines are visible in the spectra. As also young stars can photo-ionize the surrounding gas, the detection

of narrow emission lines is not sufficient to conclude on the presence of an AGN. However, SFGs and AGNs have different relative line strengths and can therefore be distinguished. Many diagnostic methods based on line ratios, such as the Baldwin, Phillips & Terlevich (BPT) diagram (Baldwin et al., 1981), have been proposed in the literature (e.g., Kauffmann et al., 2003; Smolčić et al., 2006; Best & Heckman, 2012). However, the spectral coverage of the optical spectra makes the BPT selection possible only for local sources ($z \lesssim 0.5$). Moreover, in case of low luminosity type 2 AGNs these methods become highly incomplete as the host galaxy emission dominates at optical wavelength.

- Mid-infrared:

The MIR bands can be used to select AGNs because the radiation emitted by the accretion disk is absorbed by the surrounding dust and thermally re-emitted at longer wavelength. The peak emission is around 20-30 μm that is at higher frequency compared to the emission from star heated dust, at few hundreds μm , as the AGN radiation is so intense that heats the dust grains up to their sublimation temperature. As a consequence, the AGN spectrum in the 2-20 μm rest frame wavelength range has a power-law behaviour.

Instruments particularly powerful in identifying AGNs thanks to their MIR spectral shape are the Infrared Array Camera (IRAC; Fazio et al., 2004) and the Multi-band Imaging Photometer for *Spitzer* (MIPS; Rieke et al., 2004) both on board of the *Spitzer* space telescope launched in 2003. IRAC observes in four bands at 3.6, 4.5, 5.8, and 8.0 μm and MIPS at 24, 70 and 160 μm , thus probing the full AGN heated dust emission regimes. Selection methods that employ color cuts in two representation of IRAC color-color space have been proposed by Lacy et al. (2004) and Stern et al. (2005) and are widely used in the literature (see Fig. 1.8 and 1.9).

Other diagnostics are based on the MIR to optical flux ratios and have been shown to be powerful tool for identifying CT AGNs that, as explained above, are elusive to X-ray selections (Martínez-Sansigre et al., 2005; Yan et al., 2007; Daddi et al., 2007b; Fiore et al., 2008; Polletta et al., 2008; Pope et al., 2008; Fiore et al., 2009; Luo et al., 2011).

The major problem of these traditional MIR diagnostics is the contamination from non-AGN sources (Hatziminaoglou et al., 2005; Donley et al., 2008), mainly high redshift SFGs (see Fig. 1.8 and 1.9). Therefore, more strict criteria to select AGNs using the IRAC color space have been defined and provide relatively clean AGN samples (e.g., Donley et al., 2012, and reference therein). However, this new method has a completeness that is a strong function of the AGN luminosity going from $\sim 75\%$ for AGN with X-ray luminosity $> 10^{44} \text{ erg s}^{-1}$ to $< 20\%$ as the AGN luminosity decrease (Donley et al., 2012).

- Radio:

As already discussed in section 1.1.2, the bright radio sky is dominated by jet emission

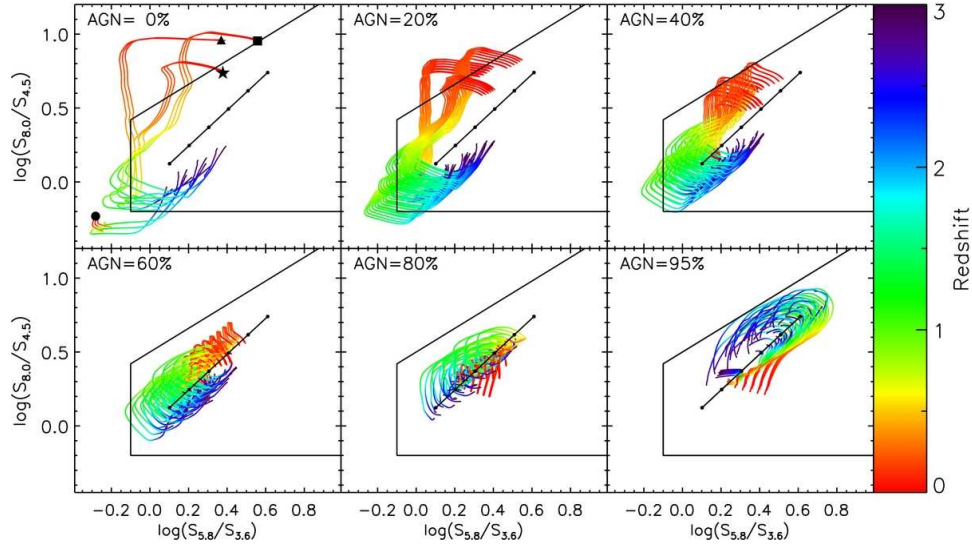


Figure 1.8: Evolutionary tracks of sources with different fraction of AGN contribution in the Lacy et al. (2004) color space (from Donley et al., 2012).

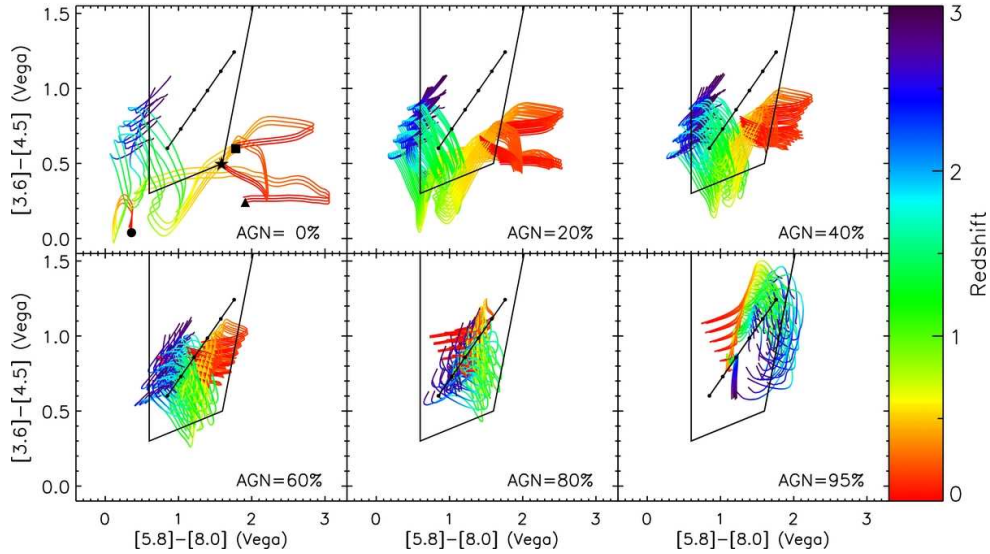


Figure 1.9: Evolutionary tracks of sources with different fraction of AGN contribution in the Stern et al. (2005) color space (from Donley et al., 2012).

from AGNs. Therefore, large radio surveys can provide numerous samples of RL AGNs. However, RL AGNs are only a tiny fraction ($< 10\%$) of the AGN population and therefore the bright radio sky offers a highly biased prospective. On the other hand, some AGNs (low-excitation sources) do not show any other signature of activity in other bands rather than the radio (e.g., Evans et al., 2006; Hardcastle et al., 2007a)

and hence a radio identification is the only way to select them. Del Moro et al. (2013) have interestingly pointed out that the selection of "radio excess" sources, that is sources with a smaller far-infrared-to-radio ratio compared to normal galaxies, can be a powerful way to find the most obscured CT objects that elude also X-ray surveys (see above), as the radio band is almost unaffected by dust extinction. At low flux densities (< 1 mJy), a radio selected sample becomes strongly contaminated by SFGs and identifying AGNs using only the radio information becomes more challenging (e.g., Padovani et al., 2009; Bonzini et al., 2013). However, it is only in the sub-mJy regime that the bulk of the AGN population, the radio quiet AGNs, become an important fraction of the radio source population. I refer to Chapter 4 for a detailed discussion on the classification of faint radio sources.

In summary, optical surveys are used to select large samples of AGNs as deep optical observation are less challenging compared to other wavelengths. However, they are highly biased towards dust unobscured sources and therefore the most efficient and cleanest method to identify AGNs remains the hard X-ray band selection. Nevertheless, MIR and radio observation are necessary to complement the AGN census with heavily obscured sources. In addition, low excitation radio-loud AGNs can often be only identified via the detection of their radio jets as the emission from both the accretion disk and the corona can be extremely low or absent.

1.2.3 Star forming galaxies

As described in Section 1.1.2, deep radio surveys below ~ 1 mJy detect not only radio AGN but also SFGs.

A SFG is a galaxy with recent or ongoing formation of new stellar populations from the collapse of dense gas clouds. Since the most massive stars ($M > 8M_{\odot}$) of a stellar population are short lived, with typical lifetime of 3×10^7 years, they progressively disappear as the galaxy ages if they are not continuously replaced by new generations of stars. Therefore, the observation of massive stars is a direct evidence of recent episodes of star formation activity in the galaxy.

These young massive stars leave several imprints in the overall SED of a galaxy; as they are hotter (10,000–30,000 K) compared to low-mass stars, they emit the bulk of their radiation in the optical-UV. Consequently, SFGs appear bluer compared to "passive" galaxies which are dominated by an older stellar population (see Fig.1.10). Moreover, the strong radiation from hot stars ionizes the surrounding gas forming HII regions and generating strong recombination lines (mainly $H\alpha, H\beta$) and forbidden lines ([OII] and [OIII]) often observed in the optical spectra.

However, as SFGs are usually rich in gas and dust, the materials from which stars form, both the UV radiation and the line flux can be obscured to the observer. In case of strong dust extinction, the continuum appear redder with rest-frame optical colors similar to those of passive galaxies. The dust is also responsible for another important feature of the SED of typical SFGs, that is a prominent peak of emission between 80 and 200 μm

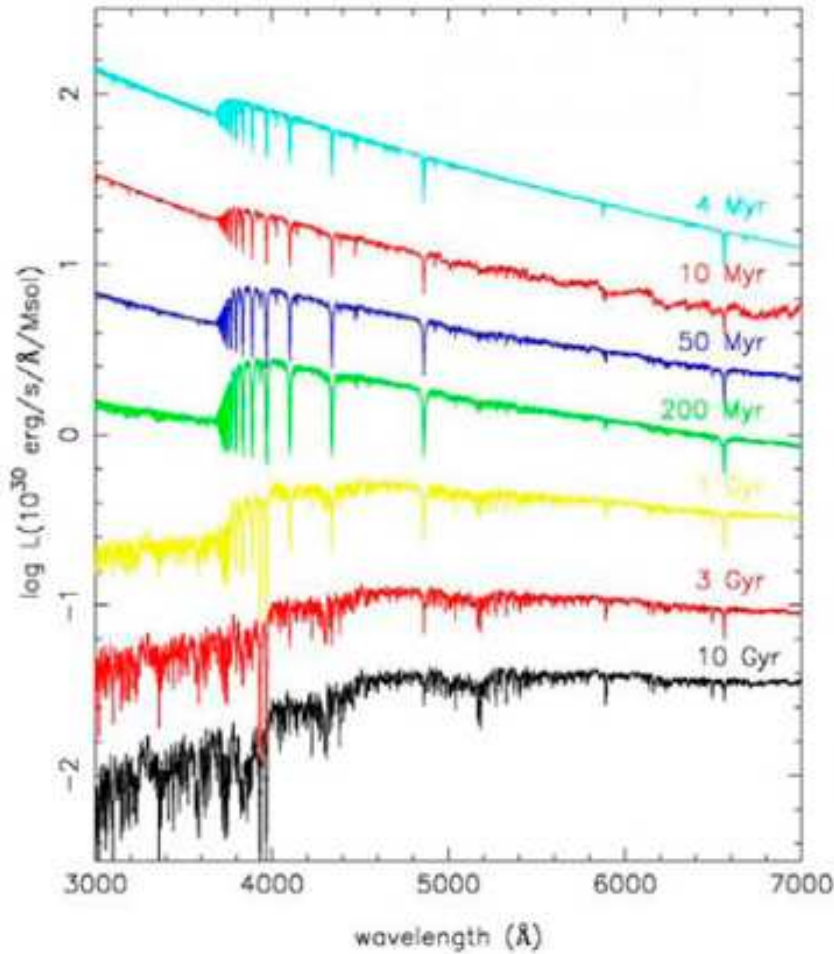


Figure 1.10: Model of spectral evolution of a single stellar population galaxy with solar composition (Bruzual & Charlot, 2003). Ages from top to bottom are 4 Myr, 10 Myr, 50 Myr, 200 Myr, 1 Gyr, 3 Gyr, and 10 Gyr. As the galaxy gets older, the optical spectrum become progressively redder.

(see Fig. 1.11). It is due to the reprocessed UV star light that is absorbed by the dust and re-radiated at longer wavelength, in the FIR.

Other typical characteristics of the SFG SED are: (i) the presence of emission features associated with the polycyclic aromatic hydrocarbons (PAHs), produced in star forming regions and observable at $\lambda = 3.3, 6.2, 7.7, 8.6, 11.3$ and $12.7 \mu\text{m}$ in the MIR rest frame (1.11). (ii) A power law shape, without significant intrinsic absorption, in the X-ray bands (0.5–10 keV; e.g., Norman et al., 2004). This X-ray emission is mainly due to the combined emission of young SN remnants, hot plasma associated with star forming regions, and the accretion in low and high mass X-ray binaries (LXRB and HXRB) (e.g., Fabbiano, 1989; Grimm et al., 2003; Fabbiano, 2006).

Finally, as already described in Section 1.2.1, the radio continuum of SFGs is dominated

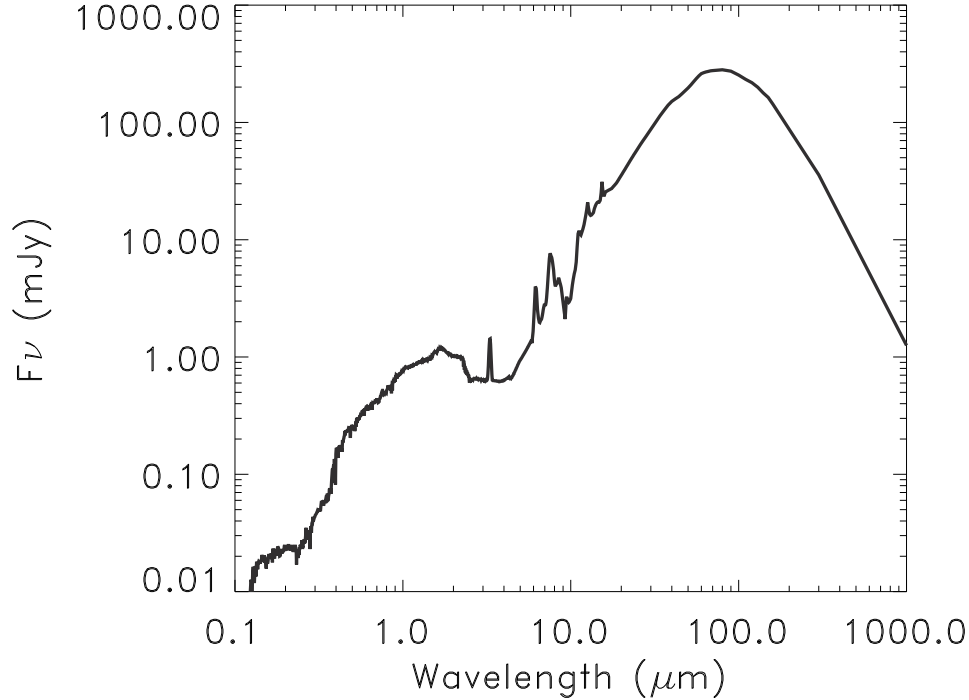


Figure 1.11: Optical-to-FIR SED of the star forming galaxy M82; the optical continuum is reddened by dust attenuation and the NIR (around $1\ \mu\text{m}$) is dominated by the emission from more evolved stars. In the MIR ($\sim 3\text{--}12\ \mu\text{m}$), prominent PAH features are present and, at longer wavelength, the peak of the dust emission is observed around $100\ \mu\text{m}$ (SED from Polletta et al., 2007, library).

by the synchrotron radiation ($\sim 90\%$) associated with SN remnants and by the free-free emission ($\sim 10\%$) of gas photo-ionized by massive stars (see Fig. 1.4).

From the morphological point of view, SFGs have typically disk-like morphology, with rotationally supported stellar kinematic. At higher redshift ($z > 1$), the SFG disks are often characterized by a clumpy structure as, being richer in gas than in the local Universe, gravitational instability naturally leads to large turbulence and giant star-forming clumps (Genzel et al., 2011, and reference therein).

Star formation rate indicators

The star formation rate (SFR) is the rate at which stars are being formed in a galaxy. The typical SFR of local SFGs is a few solar masses per year, but extreme systems with thousands of solar masses per year are also observed, especially at high redshift (see next section). Measuring the SFR of galaxies across cosmic time is important to study how and

when galaxies build up their stellar mass (see also Section 1.3). Most of the methods used by astronomers to measure the SFR are aimed estimating the young stars abundance in a galaxy. Assuming an initial mass function (IMF), that is the mass distribution of the stars formed from a gas cloud, it is then possible to convert it to the total SFR of the galaxy (Kennicutt, 1983). As described in the previous section, young stars leave direct or indirect signatures at almost all wavelengths and therefore, in principle, any spectral window could be used as SFR indicator. However, converting the information derived from one band to the intrinsic SFR is all but trivial and it is further complicated by some systematics such as the contamination from AGNs or the uncertainties on the IMF (e.g., Calzetti, 2008; Kennicutt & Evans, 2012; Lutz, 2014, for reviews.).

Here, I briefly summarize the SFR indicators most commonly used in the literature, highlighting strengths and possible weaknesses of each of them.

- Ultraviolet continuum emission: only hot, short-lived, young stars emit a significant fraction of their radiation in the UV. Hence, the UV luminosity is in principle a good tracer of recent star formation (e.g., Wuyts et al., 2011b). However, dust attenuation also peaks in the UV and causes both extinction and spectral reddening and it is therefore necessary to correct for these effects. In addition, a correlation between dust attenuation and SFR has been observed, implying that the most active galaxies requires the largest corrections (Wang & Heckman, 1996; Heckman et al., 1998; Calzetti, 2001; Hopkins et al., 2001; Sullivan et al., 2001; Buat et al., 2002; Calzetti et al., 2007; Buat et al., 2010).

Another strong source of uncertainty in UV-based SFR measurements is the possible contamination from AGNs radiation as the accretion disk emission also peaks at these wavelengths.

- Optical lines: the strength of recombination lines produced in HII regions, and in particular of the $H\alpha$ that is usually the strongest, is a measure of the ionizing radiation from young stars. Optical spectroscopy has been therefore widely used to estimate the SFR and the conversion factor between line fluxes and SFR have been carefully calibrated (e.g., Kennicutt, 1998a; Rosa-González et al., 2002; Kennicutt & Evans, 2012). However, the major limitation of these methods is that line emission must be corrected for dust attenuation and, in the case of forbidden lines, for variations in excitation and metallicity (e.g., Moustakas et al., 2006). In addition, these diagnostics are usually limited to low redshifts ($z \lesssim 0.5$) unless using near-infrared spectroscopy (Roseboom et al., 2012, 2013)
- Infrared thermal emission: this method is somehow complementary to the previous ones as it is based on the measurements of the UV light absorbed by the dust and re-emitted in the FIR. The total FIR luminosity, defined as the integrated luminosity between 8 and $1000\mu\text{m}$, is therefore a calorimetric measurement of the SFR (e.g., Kennicutt, 1998a). Infrared telescopes like *IRAS*, *Spitzer*, and in particular *Herchel*, have been used to measure the peak of the dust emission in large samples of

galaxies, both at low and high redshift, allowing a good calibration of this method (e.g., Domínguez Sánchez et al., 2012; Rodighiero et al., 2011; Nordon et al., 2013). However, a fraction of UV light might escape the dust without being absorbed and hence the FIR must be added to the uncorrected UV emission to obtain the total SFR.

Nevertheless, recent work based on *Herschel* observations has shown that the FIR luminosity provides a good estimate of the SFR especially for the high redshift Universe where, due to the larger fraction of dust in SFG, the fraction of escaping UV photons is often negligible (e.g., Lutz, 2014, and reference therein).

The two major sources of contamination come from the contribution to the total FIR luminosity from dust heated by the AGN or by more evolved stars (e.g., Netzer et al., 2007; Hatziminaoglou et al., 2010; Mullaney et al., 2012; Mor & Netzer, 2012). Another possible problem associated with this method is the relatively poor angular resolution of single-dish, space-based telescopes that leads to rapid source confusion when used for deep surveys.

- Radio continuum emission: The synchrotron emission associated with SN remnants is also linked to the young stars (Helou et al., 1985; Condon, 1992). Even if not completely understood from the theoretical point of view, a very tight empirical correlation between the radio and FIR luminosity, known as radio–FIR correlation (RFC), has been observed (Kennicutt, 1998b) and hence the use of the radio luminosity as SFR indicator has been well calibrated (e.g., Yun et al., 2001; Bell, 2003). The advantages of the radio band are that it is almost unaffected by dust extinction compared to UV-optical bands and that its higher angular resolution compared to current FIR images reduces the source confusion. One possible problem is the contamination from the AGN emission, as for almost all the other methods. I addressed this issue in my Thesis and I refer to Chapter 5 for a more detailed discussion.
- Hard X-ray emission: The hard (2–10 keV) X-ray band is also almost unaffected by dust extinction and the emission in this band in SFGs comes mainly from high mass X-ray binaries, which couples to young stellar population (e.g., Norman et al., 2004). Therefore, it can be used as SFR tracers even if the scatter is larger compared to other SFRs indicators like the FIR or the radio (e.g., Ranalli et al., 2003; Daddi et al., 2007b; Vattakunnel et al., 2012, and Chapter 5). Since AGNs are strong emitters in the hard X-ray band, this method can be applied only to galaxies with inactive black holes.

Main sequence and starburst galaxies

In the large majority of local SFGs, the SFR correlates tightly with the stellar mass of the galaxy, over more than two decades in stellar mass and with only 0.3 dex dispersion (e.g., Salim et al., 2007; Noeske et al., 2007). These galaxies are therefore characterized by the same specific SFR (sSFR), that is the SFR divided by the stellar mass, and form

the so-called "main-sequence" (MS) of star forming galaxies. Also at higher redshift, the correlation holds with almost the same slope as in the local Universe but the normalization of the MS is about a factor of 7 higher at redshift ~ 1 and a factor of 20 higher at $z \sim 2$ (e.g., Daddi et al., 2007a; Elbaz et al., 2007; Pannella et al., 2009; Rodighiero et al., 2011; Wuyts et al., 2011a; Peng et al., 2010). This implies that the typical sSFR has rapidly declined with cosmic time causing the dramatic drop in the overall star formation rate density (SFRD) of the Universe (e.g., Lilly et al., 1996; Madau et al., 1998; Le Floch et al., 2005; Magnelli et al., 2009). One of the biggest astrophysical open issues is to understand what is responsible for such fast decline. The simplest approach is to assume that the level of SF is regulated by the amount of cold gas available in the galaxy, which implies that the decrease of the normalization of the main sequence corresponds to the overall decrease of cold gas in galaxies (e.g., Bouché et al., 2010; Lilly et al., 2013). For the cause of the decrease in gas content the main mechanisms proposed in the literature are stellar-driven winds, AGN mechanical or radiative feedback (see next section for more details), or a combination of the two.

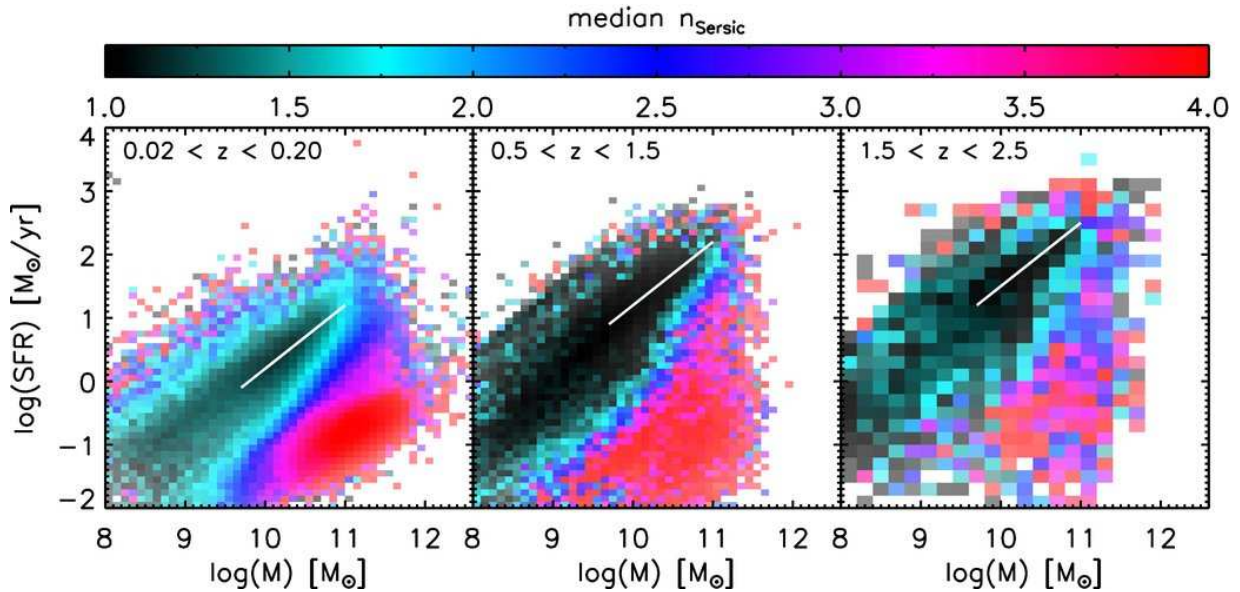


Figure 1.12: SFR versus stellar mass for a large sample of galaxies divided in three redshift bins. The color code represents the Sérsic index (Sérsic, 1963), a parameter that describes the intensity profile of a galaxy, which is generally lower for disk-like galaxies and larger in elliptical galaxies. In all panels, the MS of SFGs, characterized by disk morphology, is clearly visible and well approximated by a constant slope that increases with lookback time (white line). Below the MS, a population of passive, mostly elliptical galaxies is observed at all epochs. (from Wuyts et al., 2011a).

A minority of SFGs are characterized by very high sSFR compared to the MS galaxies and are often referred to as "starburst" galaxies. They were originally identified through their extreme IR or mm luminosity (e.g., Sanders & Mirabel, 1996) and are hence some-

times referred to as luminous IR galaxies (LIRG; $L_{IR} \approx 10^{10} - 10^{11} L_{\odot}$), ultra-luminous IR galaxies (ULIRG; $L_{IR} > 10^{11} L_{\odot}$) or, at higher redshift, as sub-millimetre galaxies (SMG) (e.g., Tacconi et al., 2008). These galaxies are often associated with disturbed morphology, signature of the occurrence of a recent major merger (Sanders et al., 1988; Elbaz et al., 2007; Tacconi et al., 2008; Daddi et al., 2007a, 2010b; Engel et al., 2010).

These observations suggest the existence of two different modes of star formation: in MS galaxies star formation occurs on long time-scales ($\sim 1 - 2$ Gyr) and is usually extended over the whole galaxy disk. In starbursts instead the consumption of gas is much faster ($\sim 0.01 - 0.1$ Gyr), possibly triggered by episodic violent events like major mergers and star formation is concentrated in dense regions (Daddi et al., 2010a; Genzel et al., 2010).

What is the contribution of the starburst mode to the total SFRD is another open question. Recent work based on *Herschel* observation has shown that starburst galaxies represent only $\sim 2\%$ of the star forming galaxy population at $1.5 < z < 2.5$ and contribute to less than 10% to the total SFRD (Rodighiero et al., 2011). Gruppioni et al. (2013) estimated a starburst contribution about two times larger but this result was based on shallower observations. In the same work, the evolution of the relative contribution of MS and starburst to the SFRD is found in qualitative agreement with that expected from the models of Sargent et al. (2012) and Béthermin et al. (2012). These models predict a fast rising of the starburst contribution up to $z \sim 1$ followed by a flattening at higher redshift. However, stronger observational constraints are still needed.

In this Thesis, I demonstrated how deep radio surveys can represent a powerful tool to study the evolution of the SFRD, as will be detailed in Chapter 5.

1.3 AGN-host galaxy connection

As already mentioned above, one fundamental question in modern astrophysics is whether AGN activity may play a role in shaping the properties of its host galaxy. From the energetic point of view, an AGN has a binding energy that largely exceeds the one of its host galaxy. If only a few per cent of the AGN energy output could efficiently couple to the surrounding material, then the whole galaxy could be blown away (Silk & Rees, 1998).

There are many observational evidences of a coeval growth of the SMBH and their hosts. The most famous is the tight correlation observed in the local Universe between the mass of the BH and the mass of its host galaxy bulge (see Kormendy & Ho, 2013, for a review), thus suggesting some mechanisms of AGN feedback that self-regulate the BH growth or influence the conversion of gas in stars, for example quenching or triggering the SF.

AGN feedback is also invoked to solve problems in galaxy formation simulations (e.g. Springel et al., 2005). For example, the mass function (MF) of galaxies, i.e. the total number of sources with stellar mass in a certain mass bin as a function of mass, predicted by cosmological simulation shows an excess of galaxies at the high mass end compared to the observed distribution (e.g., Ilbert et al., 2010, 2013). In the feedback scenario, the AGN may inject momentum and radiation in the inter-stellar medium (ISM) preventing

the cold gas to further collapse and form stars thus reconciling theoretical predictions and observations.

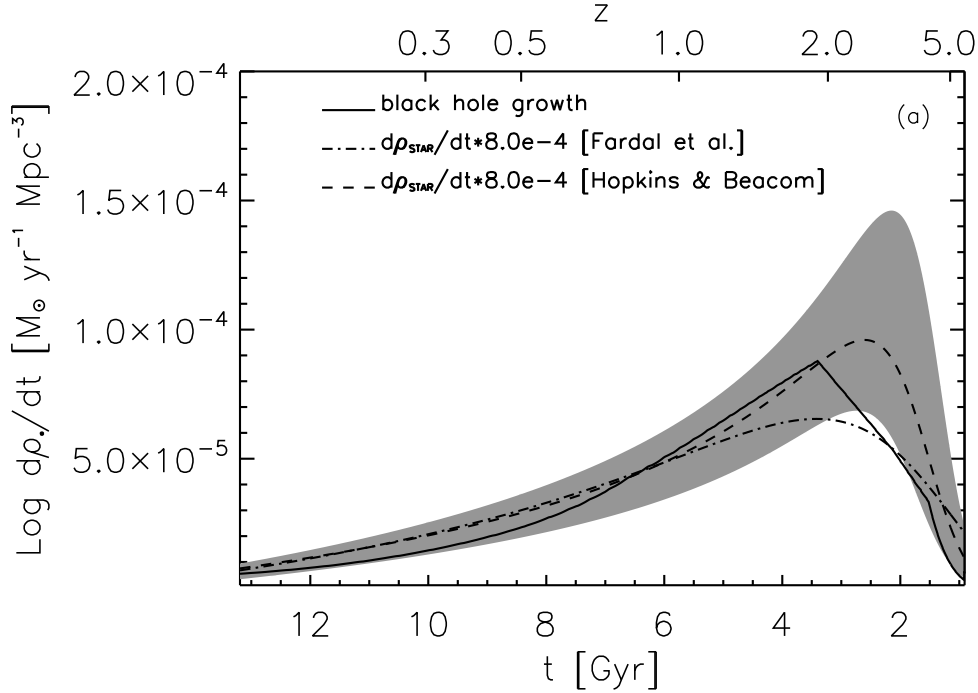


Figure 1.13: The cosmic history of black hole growth and stellar mass growth. The average black hole accretion rate is compared to the SFR as a function of redshift, where the latter is given by Hopkins & Beacom (2006) and Fardal et al. (2007), scaled by the factor 0.8×10^{-3} . The shaded grey area shows the 3σ uncertainty region from Hopkins & Beacom (2006). Figure from Shankar et al. (2009)

The cosmic histories of SFG and AGN also show many similarities; both the AGN and SF activity peaked at $z \sim 2$ and then progressively decline (see Fig. 1.13 and previous section). In addition, the evolution of both seems to follow the so-called "downsizing" meaning that the most massive galaxies and most luminous QSOs formed first while smaller systems and less luminous AGN are more common at lower redshift (Ueda et al., 2003; Hasinger et al., 2005; Barger et al., 2005).

Furthermore, AGN feedback has been proposed to explain the observed strong bimodality in the galaxy population optical colors (Strateva et al., 2001; Hogg et al., 2002; Baldry et al., 2004; Peng et al., 2010; Schawinski et al., 2014). Indeed, when optical colors are plotted against stellar masses as shown in Fig. 1.14, galaxies divide in a so-called "red sequence" with passive and relatively more massive galaxies and a "blue cloud" populated by smaller galaxies with younger stellar population. The much lower number density of galaxies in the region in between, the "green valley", implies the existence of a mechanism that rapidly quenches the SF in blue clouds galaxies and bring them into the red sequence.

AGN feedback seemed a good candidate given the large fraction of AGNs detected in the "green valley" (e.g., Nandra et al., 2007; Schawinski et al., 2007).

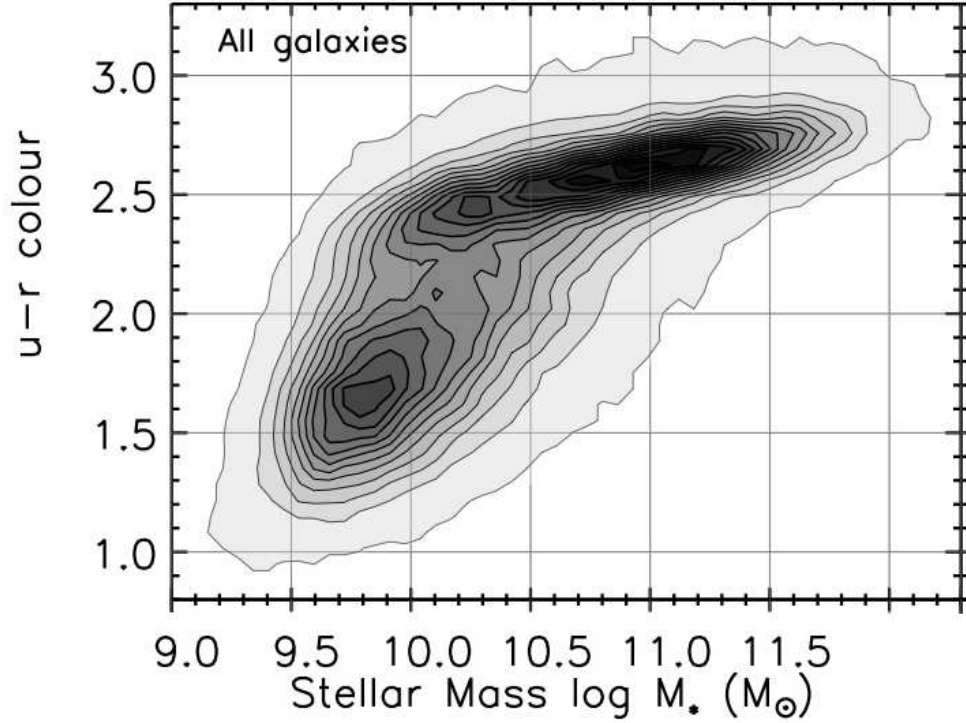


Figure 1.14: Optical U–R color vs. stellar mass for SDSS galaxies. A strong bimodality is observed with red massive galaxies forming the so-called "red sequence" in the upper part of the plot and less massive, bluer galaxies in the "blue cloud" on the bottom left.

Finally, another observational evidence supporting the idea of a connection between the AGN and SF activity is the correlation of the AGN fraction with the IR luminosity, and consequently with the SFR, of its host. While AGNs are a small fraction of the overall galaxy population at $L_{IR} < 10^{11}$, they are more than 50% in ULIRG (e.g., Kartaltepe et al., 2010) suggesting that the AGN activity is linked to the strongest starburst events. A possible scenario explaining these observations has been proposed by Di Matteo et al. (2005) and (Hopkins et al., 2008). Both the AGN and the intense SF are triggered by a gas rich major merger that provides fuel both to form new stars and to feed the black hole. In this phase, due to the large amount of dust present in the system, the AGN is often heavily obscured. The strong radiation from the AGN will then clean the surroundings quenching on one hand the star formation and on the other hand removing the obscuration of the AGN itself.

So far, I described only indirect evidences of possible AGN feedback but more direct observations of the influence of the AGN on the surroundings has been detected. They are usually divided in two categories according to the source of energy that could be either

mechanical, often referred to as "radio" mode, or radiative and in this case it is called "quasar" mode feedback.

Radio mode feedback

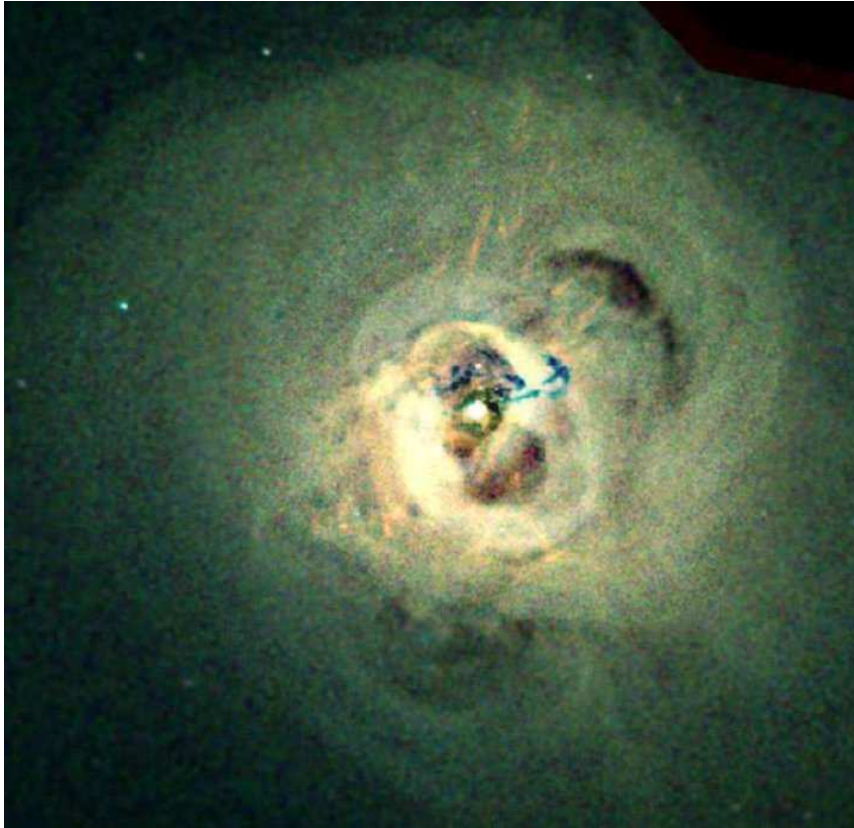


Figure 1.15: *Chandra* X-ray image of the Perseus cluster core.

In the radio mode the source of feedback are radio jets. They can provide mechanical energy, which shocks onto the surrounding material, removing or heating it and hence preventing its collapse. Radio mode feedback has been observed on the scale of galaxy clusters where the radio jets from the central elliptical galaxy inflate cavities into the X-ray emitting hot gas halo that fills the potential well of the cluster (see Fabian, 2012, for a review and Fig.1.15).

However, it is less clear if radio jets can efficiently deposit their energy on kpc scales and hence impact the SF activity of the galaxy. IFU spectroscopy has revealed that the jets of powerful ($> 10^{26} \text{ W Hz}^{-1}$ at 1.4 GHz) RL AGNs can drive massive outflows of ionized and cold gas in the proximity of the AGN ($< 10 \text{ kpc}$) (Nesvadba et al., 2006, 2007, 2008, 2010). However, as jets are collimated, it is still a matter of debate if they can have an impact on large scales especially in the direction perpendicular to the jet propagation direction.

Recently, simulations of radio jets propagating in a structured, multi-phase ISM predict that the radio jet can deposit significant amounts of energy on kpc scales and therefore can be responsible for the SF suppression in the galaxy (Wagner & Bicknell, 2011).

Quasar mode feedback

The source of energy in the so-called quasar mode feedback is the AGN radiation. Several models predict the presence of fast winds launched from the accretion disk of the AGN that generate shocks against the surrounding gas (King, 2003; Menci et al., 2008; Zubovas & King, 2012). The shocks drive outflows which could propagate out to large (kpc) distances and may clear galaxies of most interstellar gas, preventing star formation (Zubovas & King, 2012), or over-compress the dense gas and trigger a starburst (Zubovas et al., 2013), depending on the characteristics of the surrounding material.

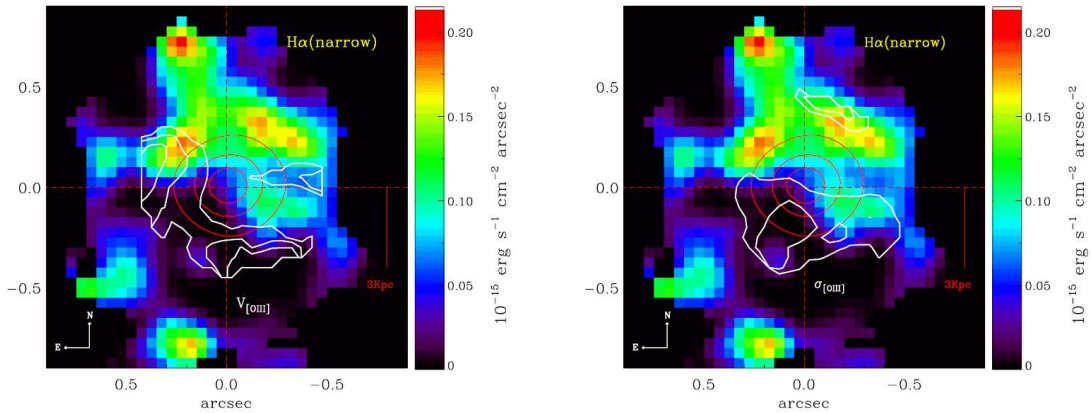


Figure 1.16: Example of detection of kpc scale AGN driven outflows. The VLT-SINFONI map shows the narrow component of $H\alpha$ with contours tracing the $[OIII]$ velocity shift (left panel) and velocity dispersion (right panel) in the luminous quasar 2QZJ002830.4-281706 at $z = 2.4$. Star formation, traced by $H\alpha$, is heavily suppressed in the region where the strongest outflow is traced by $[OIII]$ (from Cano-Díaz et al., 2012)

Several observations have confirmed that outflows are ubiquitous in AGN hosts. However, as also star formation processes can drive outflows, via stellar winds of SN explosions, it is often difficult to disentangle these phenomena from AGN-driven winds. X-ray and UV absorption line studies revealed outflows with velocities of thousands km/s or even higher in the proximity of high-accreting AGNs (e.g., Crenshaw et al., 1999; Chartas et al., 2002; Tombesi et al., 2010). It is unlikely that stellar processes can accelerate the gas up to these very high velocities and it is believed that AGN activity is required to drive these outflows. However, these winds are confined on pc scales and therefore it is not obvious the impact they may have on the overall SF of the host galaxy. More recently, AGN-driven outflows have been observed on scale of several kpc (see Fig. 1.16) via high-resolution IR and mm spectroscopic studies (Alexander et al., 2010; Feruglio et al., 2010; Sturm et al., 2011;

Rupke & Veilleux, 2011; Cano-Díaz et al., 2012; Harrison et al., 2012; Cicone et al., 2014; Förster Schreiber et al., 2014; Harrison et al., 2014) Hence, there is accumulating evidence that radiatively-driven winds powered by AGNs can have an impact on the global SF in their host. What is still poorly understood is the link between AGN properties, e.g. its accretion rate or radio luminosity, and the characteristics of the outflows.

1.4 The content of this Thesis

In the following, I briefly summarize the content of the next Chapters, highlighting the original results of this Thesis.

- **Chapter 2** This Chapter presents the radio survey and the sample used in this Thesis. The Very Large Array (VLA) observations of the Extended *Chandra* Deep Field South (E-CDFS) are described, and particular attention is dedicated to the compilation of the 5σ rms source catalog. It includes 883 sources down to a flux density limit of $32.5 \mu\text{Jy}$ and therefore represents one of the deepest radio samples up to date. I significantly contributed to the identification of the extended and multi-component sources. It required an analysis of the sources morphology and the search for their multi-wavelength counterpart. The compilation of the source catalog, the rejection of spurious sources, and an accurate computation of the source flux densities are essential to investigate the populations that contribute to the radio sky.
- **Chapter 3** A multi-wavelength approach is crucial when dealing with deep radio images as most of the sources are unresolved and little information can be extracted by a single frequency catalog. Therefore, at the beginning of Chapter 3, I describe the wealth of multi-wavelength data available in the E-CDFS, from the X-ray to the MIR. The main topic of this Chapter is the identification of the optical-to-MIR counterparts of the radio sources. I adopted a likelihood ratio technique in order to minimize the number of spurious matches. As a result, I found a counterpart for 94% of the radio sources. Interestingly, 26% of them are not detected in the optical and 21% are only detected in the MIR. These sources are particularly important as they might represent a population of high redshift, heavily obscured sources that are easily missed by optical or X-ray surveys. Being the radio band almost unaffected by dust obscuration, it provides a more complete census of the dust obscured Universe.

Once identified the counterpart of the radio sources, it is then extremely important to associate a redshift to each object. Indeed, only knowing the distance of the radio source it is possible to derive its intrinsic properties like the radio power. Therefore, I collected and combined spectroscopic and photometric redshift information from the literature, together with newly acquired spectra. That allowed me to reach a redshift completeness of 81% for the identified source, with 35% of spectroscopic redshifts. Finally, in this Chapter I also describe the X-ray properties of the radio sources and the stacking analysis performed for the X-ray undetected sources. I found that

objects with counterpart only in the MIR tend to have hard X-ray spectra supporting the hypothesis that they are heavily obscured objects.

- **Chapter 4** The method developed to disentangle the different classes of sources that populate the radio sky is described in this Chapter. In more details, I classify sources as SFGs, RQ AGNs and RL AGNs combining radio, MIR and X-ray data. A series of other methods commonly used to identify AGNs (e.g., optical spectra and colors, X-ray variability, etc.) are considered and used to validate my approach. The VLA sample splits in $\sim 60\%$ of SFGs and 40% of AGNs further divided in about half of RQ and half of RL AGNs. The relative contribution of the different classes to the total radio population is investigated as a function of radio flux density. As expected, while at high flux densities the RL AGNs constitute the large majority, SFGs become the dominant population below 0.1 mJy. For the first time, I also carefully quantify the contribution of RQ AGNs to the total of the AGNs finding that it is increasingly important going to fainter flux densities becoming the majority below 0.1 mJy.

I also derived the physical properties of the radio sources in terms of morphology, stellar masses and optical colors. I found that SFGs and RQ AGNs have similar galaxy properties being preferentially characterized by lower masses and bluer colors compared to RL AGNs. They have late type morphology while the RL AGNs are more likely to be hosted by elliptical galaxies. This suggests that RQ and RL AGNs represent two different stages of an evolutionary scenario where the RQ phase occurs at earlier times when the host galaxy is gas rich and is still actively forming stars while the onset of the RL activity happens later in an already quenched galaxy.

- **Chapter 5** The Chapter focuses on the study of the star formation activity in the host galaxies of the radio selected sources. In the first part, I estimated the SFR from their FIR luminosity, constrained using *Herschel* photometry. This is then compared with the SFR as traced by the radio power. I found very good agreement, with 0.2 dex of dispersion, between the two independent SFR tracers across four orders of magnitude in luminosity for both SFGs and, more interestingly, for RQ AGNs. With this result I confirmed the hypothesis that the major contribution to the radio power in RQ AGNs comes from the SF activity in their host galaxies rather than from the accretion onto the BH. This is not the case for RL AGNs that indeed scatter off the correlation due to the strong contribution from radio jets to the radio luminosity.

In the second part of the Chapter, I estimated the occurrence of starburst galaxies and its evolution across cosmic time both in my radio flux density limited sample and, using an empirical model, for the underlying stellar mass selected population. In the latter, starburst galaxies represent a tiny fraction of the total SFGs population ($< 10\%$) but their importance increases with redshift. Moreover, I found that while the majority of the RQ AGNs live in main sequence galaxies, their relative fraction increases in the starburst sources. This is consistent with the scenario of a common triggering mechanism of both the burst of the SF and the BH activity, by an episodic event like a major merger.

-
- **Chapter 6** In this last Chapter I summarize the main results and propose further developments of this Thesis.

Chapter 2

The VLA 1.4 GHz Survey of the Extended Chandra Deep Field South: Second Data Release

*Published as Miller, N. A.; **Bonzini, M.**; Fomalont, E. B.; Kellermann, K. I.; Mainieri, V.; Padovani, P.; Rosati, P.; Tozzi, P.; Vattakunnel, S., 2013, *Astrophysical Journal Supplement Series*, 205, 13*

Abstract

Deep radio observations at 1.4 GHz for the Extended Chandra Deep Field South were performed in June through September of 2007 and presented in a first data release (Miller et al. 2008). The survey was made using six separate pointings of the Very Large Array (VLA) with over 40 hours of observation per pointing. In the current paper, we improve on the data reduction to produce a second data release (DR2) mosaic image. This DR2 image covers an area of about a third of a square degree and reaches a best rms sensitivity of $6\ \mu\text{Jy}$ and has a typical sensitivity of $7.4\ \mu\text{Jy}$ per $2''.8$ by $1''.6$ beam. We also present a more comprehensive catalog, including sources down to peak flux densities of five or more times the local rms noise along with information on source sizes and relevant pointing data. We discuss in some detail the consideration of whether sources are resolved under the complication of a radio image created as a mosaic of separate pointings each suffering some degree of bandwidth smearing, and the accurate evaluation of the flux densities of such sources. Finally, the radio morphologies and optical/near-IR counterpart identifications (Bonzini et al., 2012) are used to identify 17 likely multiple-component sources and arrive at a catalog of 883 radio sources, which is roughly double the number of sources contained in the first data release.

2.1 Introduction

The *Chandra* Deep Field South (CDF-S) continues to be one of the most important deep fields for multiwavelength investigation of the cosmological evolution of galaxies. Originally devoted 1 Msec of *Chandra* integration (Giacconi et al., 2002), subsequent observations have pushed ever deeper in X-ray flux by increasing the net exposure first to 2 Msec (Luo et al., 2008) and recently to 4 Msec (Xue et al., 2011). This makes the CDF-S the most sensitive X-ray view of the universe, reaching sources with full-band (0.5 - 8.0 keV) fluxes down to $\approx 3.2 \times 10^{-17}$ erg s $^{-1}$ cm $^{-2}$. The area covered by relatively deep X-ray observations has also increased over the initial survey, with an additional one Msec divided among four *Chandra* pointings to produce the Extended CDF-S (E-CDF-S; Lehmer et al., 2005). Likewise, *XMM-Newton* has observed the field in increments over the past nine years and has now accumulated over 3 Msec of integration in a region that covers much of the E-CDF-S. These data will provide quality X-ray spectra of detected sources (e.g., Comastri et al., 2011).

In addition to X-ray coverage, *Hubble* and *Spitzer* have produced deep near-ultraviolet through infrared data for the field. The deepest images ever obtained with *Hubble* are located in the CDF-S, with the *Hubble* Ultra Deep Field using the Advanced Camera for Surveys (ACS) to obtain deep *F435W* ($\sim B$), *F606W* ($\sim V$), *F775W* ($\sim i$), and *F850LP* ($\sim z$) images (Beckwith et al., 2006) and more recently the Wide Field Camera 3 (WFC3) instrument exploring the near-IR *F105W* (Y), *F125W* ($\sim J$), and *F160W* ($\sim H$) with a 192-orbit “Treasury” program (PI G. Illingworth). The Great Observatories Origins Deep Survey (GOODS; Giavalisco et al., 2004) targets the CDF-S as one of its two fields, using both *Hubble* and *Spitzer* images to study galaxy evolution across cosmic time. Analogous to the widening of the CDF-S to the E-CDF-S in X-ray surveys, programs have expanded the covered area using *Hubble* (Galaxy Evolution from Morphologies and SEDs, GEMS; Rix et al., 2004) and *Spitzer* (the *Spitzer* IRAC/MUSYC Public Legacy Survey, SIMPLE, at near-IR wavelengths and the Far-Infrared Deep Extragalactic Legacy survey, FIDEL, in mid-IR; Damen et al., 2011; Magnelli et al., 2011). Most recently, the “Cosmic Assembly Near-IR Deep Extragalactic Legacy Survey” (CANDELS) is capitalizing on *Hubble*’s WFC3 camera to provide deep near-IR imaging of several fields including the CDF-S (Grogin et al., 2011; Koekemoer et al., 2011). In terms of allocated orbits, CANDELS is the largest project in the history of *Hubble* and its three near-IR filters will identify and characterize galaxies over the approximate redshift range $1.5 \leq z \leq 8$. *Spitzer* observations continue with warm mission *Spitzer* activity (e.g., the “*Spitzer* Extragalactic Representative Volume Survey,” or SERVS¹; Mauduit et al., 2012). Finally, *Herschel* has pushed the deep IR data into the far-IR portion of the spectrum with the GOODS-*Herschel* program (Elbaz et al., 2011) and the *Herschel* Multitiered Extragalactic Survey (“HerMES;” Oliver et al., 2012).

Ground-based observatories have also supplied much ancillary data at optical and near-IR wavelengths. These programs include *J H K_s* imaging (Retzlaff et al., 2010) with the

¹See also the *Spitzer* Extended Deep Survey, SEDS (<http://www.cfa.harvard.edu/SEDS/index.html>).

Infrared Spectrometer And Array Camera (ISAAC) of the European Southern Observatory's Very Large Telescope (VLT) and $U B V R I$ imaging from the Garching-Bonn Deep Survey (Hildebrandt et al., 2006) using the Wide Field Imager (WFI) at the 2.2m La Silla telescope. The E-CDF-S is also one of four fields covered by the Multiwavelength Survey by Yale-Chile (MUSYC; Gawiser et al., 2006), with this program using the Cerro Tololo Inter-American Observatory (CTIO) 4 m telescope and the MOSAIC II and ISPI instruments to obtain deep coverage of the E-CDF-S region at $U B V R I z' J H K_s$. The MUSYC project has also acquired medium-band imaging in 18 filters using the Subaru Telescope and used these along with the broad-band and *Spitzer* IRAC photometry to produce accurate photometric redshifts for tens of thousands of galaxies (Cardamone et al., 2010). In addition to photometric redshifts, there are a host of spectroscopic programs providing critical spectroscopic redshifts and source classifications. These have often been associated with the GOODS program and capitalized on the VLT with the FORS2 and VIMOS instruments (Vanzella et al., 2008; Balestra et al., 2010, and associated papers). Many other spectroscopic campaigns have also targeted the field, including specific targeting of radio-selected sources (e.g., Mao et al., 2012) and recent efforts to expand the area from the well-sampled GOODS region (essentially the CDF-S) to the full $30' \times 30'$ E-CDF-S (e.g., Cooper et al., 2012, using the Inamori-Magellan Areal Camera and Spectrograph, IMACS, on the Magellan-Baade telescope).

The field has also received extensive attention at radio wavelengths. Norris et al. (2006) used the Australia Telescope Compact Array (ATCA) at 1.4 GHz to observe a large (3.7 deg^2) area, with the E-CDF-S region reaching down to an rms sensitivity of $\sim 15 \mu\text{Jy}$ per $17'' \times 7''$ beam. Kellermann et al. (2008, hereafter K08) used the National Radio Astronomy Observatory (NRAO) Very Large Array (VLA) to obtain deeper and higher resolution 1.4 GHz data ($8.5 \mu\text{Jy}$ rms noise per $3''.5 \times 3''.5$ beam) in a field centered on the CDF-S. These latter data were exploited in a sequence of papers on optical counterparts (Mainieri et al., 2008), radio-X-ray properties (Tozzi et al., 2009), and source populations and evolution (Padovani et al., 2009, 2011a). In addition to 1.4 GHz, VLA observations at 5 GHz are presented in K08 with an rms sensitivity of $8.5 \mu\text{Jy}$ rms for a $3.5'' \times 3.5''$ beam and Huynh et al. (2012) present an ATCA 5.5 GHz survey of the E-CDF-S with a $\sim 12 \mu\text{Jy}$ rms per $4.9'' \times 2.0''$ beam. At longer wavelengths, Ivison et al. (2010a) included Giant Metre-Wave Radio Telescope data at 610 MHz ($\sim 40 \mu\text{Jy}$ rms noise for a $6.5'' \times 5.4''$ beam) in their investigation of evolution in the FIR-radio correlation.

In June through September 2007, we observed the E-CDF-S with the National Radio Astronomy Observatory (NRAO)² Very Large Array (VLA) under program code AM889. The observations were performed at a frequency of 1.4 GHz and consisted of over 250 hours of time (about 690 ksec time on source) spread across six separate pointings. The survey description, strategy, and initial image and catalog were presented in Miller et al. (2008). The rapid turnaround time between data collection and publication was motivated by the strong community interest in the field, which has been justified by the number of studies

²The National Radio Astronomy Observatory is a facility of the National Science Foundation operated under cooperative agreement by Associated Universities, Inc.

which have relied upon the data to set or confirm the astrometry for observations made at other wavelengths (e.g., Truch et al., 2009; Weiß et al., 2009; Scott et al., 2010; Xue et al., 2011), identify counterparts to sub-millimeter surveys (Coppin et al., 2009; Dye et al., 2009; Biggs et al., 2011; Yun et al., 2012), extend the far-infrared/radio correlation out to cosmological redshifts (Ivison et al., 2010a; Bourne et al., 2011; Mao et al., 2011), and identify and study star-forming galaxies and active galactic nuclei (Moncelsi et al., 2011; Vattakunnel et al., 2012; Fiore et al., 2012; Danielson et al., 2012). Naturally, this rapid release of the calibrated radio images necessitated some minor compromises. In regards to the imaging of the data, these amounted to postponing some time- and computational-intensive techniques that produce slight improvements to the depth and cosmetics of the resulting images. Similarly, the initial catalog was conservative in only going to a 7σ point-source detection limit and providing little detail about source morphology. In the current paper, we present the second data release (DR2) associated with this program. It incorporates these finer imaging techniques yielding a typical reduction in the rms noise of about $0.5 \mu\text{Jy}$ across the full E-CDF-S area, and this improvement plus moving to a 5σ detection threshold produces a deeper and more comprehensive but still highly-reliable source catalog.

We describe the details associated with the improvements to the imaging in Section 2.2. In Section 2.3 we discuss the detection and characterization of sources applied in the construction of a source catalog, and briefly discuss the catalog and future directions in Section 2.4.

2.2 Improved Imaging

2.2.1 Background

To fix our terminology for the ensuing discussion, we provide a brief summary of the observations. In order to cover the full E-CDF-S area at near-uniform sensitivity, we pointed the VLA at six separate coordinate locations arranged in a hexagonal grid around the adopted center of the CDF-S, (J2000) $03^h32^m28.0^s -27^\circ48'30.00''$. We refer to these as “pointings” and often reference them with a numerical designation from 1 to 6 starting due east of the center coordinate and proceeding clockwise; Table 2.1 includes the numerical designations and coordinate centers. Our observations were spread over many days on account of the low declination of the field and typically amounted to five hours of time per calendar date. Thus, the full program consists of about fifty of these “tracks.” We opted to observe a single pointing on any given calendar date, meaning that each pointing was observed on at least eight separate dates. While this was done largely for efficiency and convenience, it also allows for a deep investigation of possible radio transient populations (Frail et al., in preparation). We refer those interested in the survey strategy and design to Miller et al. (2008, hereafter M08).

Table 2.1. Pointing Coordinates

Pointing ID	RA(J2000)	Dec(J2000)	RMS ^a
ECDFS 1 ^b	03:33:22.25	-27:48:30.0	10.5 μ Jy
ECDFS 2	03:32:55.12	-27:38:03.0	9.4 μ Jy
ECDFS 3	03:32:00.88	-27:38:03.0	9.7 μ Jy
ECDFS 4	03:31:33.75	-27:48:30.0	9.5 μ Jy
ECDFS 5	03:32:00.88	-27:58:57.0	10.0 μ Jy
ECDFS 6	03:32:55.12	-27:58:57.0	9.3 μ Jy

^aRMS sensitivity for final image associated with all data for that pointing, prior to correction for primary beam.

^bOne observation intended for this position was erroneously offset to 03:33:22.25 -27:47:30.0. This offset observation is not included in the pointing 1 data imaged to produce the indicated RMS sensitivity.

2.2.2 General Procedure

At the time of the observations the VLA was undergoing improvements paving the way toward full “Expanded” VLA (Perley et al., 2011) operations, a now complete process that includes the official renaming as the Karl G. Jansky Very Large Array. In general, these modifications to the array had little effect, and the procedures for calibrating and imaging the data followed the standard prescriptions for deep, multi-channel continuum VLA observations at 1.4 GHz using NRAO’s Astronomical Image Processing System (AIPS). The most notable exception was the retirement of the original VLA control computers on 2007 June 27, which led to slight errors in how the (u, v, w) coordinates were written at various times during the range of dates covering our observations. For the first data release, we relied upon the AIPS task UVFIX to recalculate the (u, v, w) data based on the antenna positions which are included among the data tables associated with each observation. Several of the observations were also afflicted by a glitch which reversed the channel indexing for brief periods of time, and we fixed this error using a sequence of existing AIPS procedures. Finally, in a few instances the most-recently retrofitted EVLA antenna had incorrect system temperature values which produced spuriously large weights that we had to manually adjust down to more representative values.

Each of these problems has now been corrected in the NRAO Data Archive, and in this second pass at data calibration and imaging we essentially started “from scratch.” We re-obtained the raw (u, v, w) data from the Archive, and followed the same general procedure

of data editing, calibration, and imaging as was described in M08. One minor improvement was the inclusion of a very small amount of extra data relative to that previous reduction. As VLA antennas are retrofit to become EVLA antennas, they are placed on a “master pad” for testing. There were some times during the course of our observations when such antennas were included in the array and we were able to calibrate such data and include it in our current imaging. Although we mainly started from scratch and paralleled the previous reduction procedure, we did have one significant saving: the presence of first data release deep images associated with each pointing. These were used to self-calibrate the (u, v, w) data after the initial data edits and amplitude and phase calibration.

The basic sequence of initial steps is identical to that presented in M08. For each observing track, we inspected and edited the calibrator (u, v, w) data (3C48 and J0340-213). These data were then used to establish the bandpass calibration (using 3C48), flux density scale (from 3C48, with J0340-213 bootstrapped to 3C48), and phase calibration (using J0340-213) for the target data. After application of the calibrations, the (u, v, w) data for the target were inspected and edited to remove obvious errors. The resulting (u, v, w) data were then self-calibrated on phase using the deep individual pointing images created for the first data release. We proceeded to then image the data, subtract the determined clean components, edit the resulting source-removed (u, v, w) file to flag obvious interference and data errors, and then return the clean components. Once all the data associated with an individual pointing were thus calibrated and edited, we combined them into single, deep (u, v, w) data set associated with that pointing.

These combined single-pointing datasets were then imaged and subjected to further self-calibration and editing. First, we applied a strong taper to the (u, v, w) data and generated a wide-field, low resolution map. Over this image we laid the grid of 127 facets arranged in a “flys-eye” pattern that would be used in our imaging, with these smaller facets allowing for correction of image distortions caused by sky curvature. Each of these facets was 512×512 $0''.5$ pixels, and the flys-eye thus covered about $52'$ in diameter – not quite out to the first null of the VLA primary beam at 1.4 GHz. We were thus able to search the wide-field image for additional faint sources outside of our principal imaged area, including a small number within the primary beam and a larger number within the sidelobes. While these same basic steps were performed previously on individual tracks of data, repeating them on the deeper combined datasets warranted an increase in the radial coverage of individual facets (previously 91 were used) and revealed additional faint sources outside the flys-eye coverage. We identified about 30 such additional small fields to image for each pointing. Finally, we searched within the main 127-facet coverage for particularly bright sources (those with flux densities uncorrected for primary beam response of a few mJy and higher). This identified between seven and 10 additional small facets for imaging, and thus in total each pointing was imaged as the combination of between about 160 and 175 facets.

Successive rounds of imaging and self-calibration were then performed, with each newer set of images used as the source model for self-calibration in both amplitude and phase. Our final steps of self-calibration on the full data for each pointing used the AIPS task PEELR, which “peels” off individual bright sources to improve the overall calibration. These

sources are returned to the data once all corrections are made. Between one and four bright sources per field were subjected to PEELR, with these sources typically having an apparent flux density (uncorrected for primary beam attenuation) of about 7.5 mJy and greater.

The final imaging was done in segments of the full (u, v, w) data. This provides a fine correction to several effects, each of which relates to the shape of the primary beam and how it can differ slightly for different portions of the data. These minor differences cause the response to sources to vary over the course of an observing track. First, the VLA observed in a pair of frequency bands (intermediate frequencies, or IFs) that bracket 1.4 GHz. These separate IFs imply slightly different resolutions. Second, the feeds for the right and left circular polarization are not coincident and thus have slightly different pointing centers. Third, the power pattern of the VLA primary beam is not perfectly circular and over the course of observations as the hour angles of sources change their responses vary. We consequently separated the data into 12 segments, consisting of three ranges in hour angle and separately for each IF and polarization. As before, we imaged each segment of the data and performed a round of self-calibration on that segment before producing the final image for that segment. The images corresponding to the 12 segments for each pointing were then combined using variance weighting based on their individual rms sensitivities. Relative to the first data release, the final images for the six pointings had net improvements in sensitivity ranging from about $0.1\mu\text{Jy}$ to $0.7\mu\text{Jy}$. Table 2.1 includes the achieved rms sensitivity per pointing.

2.2.3 Summary of Final Data and Images

The images corresponding to the six individual pointings were then combined to form the final mosaic image. The mosaic step corrects for the power pattern of the primary beam, and data out to the radial distance where the power pattern is 33% of that at the pointing center were included (i.e., just under $20'$ in radius). This choice of radial cutoff is somewhat arbitrary but was motivated by the consideration that data this distant from a pointing center are de-weighted by about an order of magnitude in creation of the mosaic image. It is also consistent with that used in other radio surveys (e.g., Huynh et al., 2005; Schinnerer et al., 2010). The contribution at each point in the output mosaic is weighted by the inverse of the power pattern squared at that point. We also included a single track of data from early in the observing campaign where we had inadvertently shifted the pointing center by $1'$. The area covered by the final mosaic is $\sim 34' \times \sim 34'$ (0.324 square degrees), being 4096×4096 $0''.5$ square pixels. This is the main image associated with this second data release and is shown in Figure 2.1. It will be used in subsequent characterization and compilation of a source catalog. We note that the actual coverage of the individual pointings extends well beyond the boundaries of this mosaic image but experiences the drop-off in sensitivity associated with the power pattern of the VLA primary beam. Users interested in sources that fall within the coverage of such pointings but outside the final mosaic image are directed to the individual pointing images and a larger mosaic image that incorporates all of the data.

The sensitivity and coverage thereof was evaluated via the construction of an rms

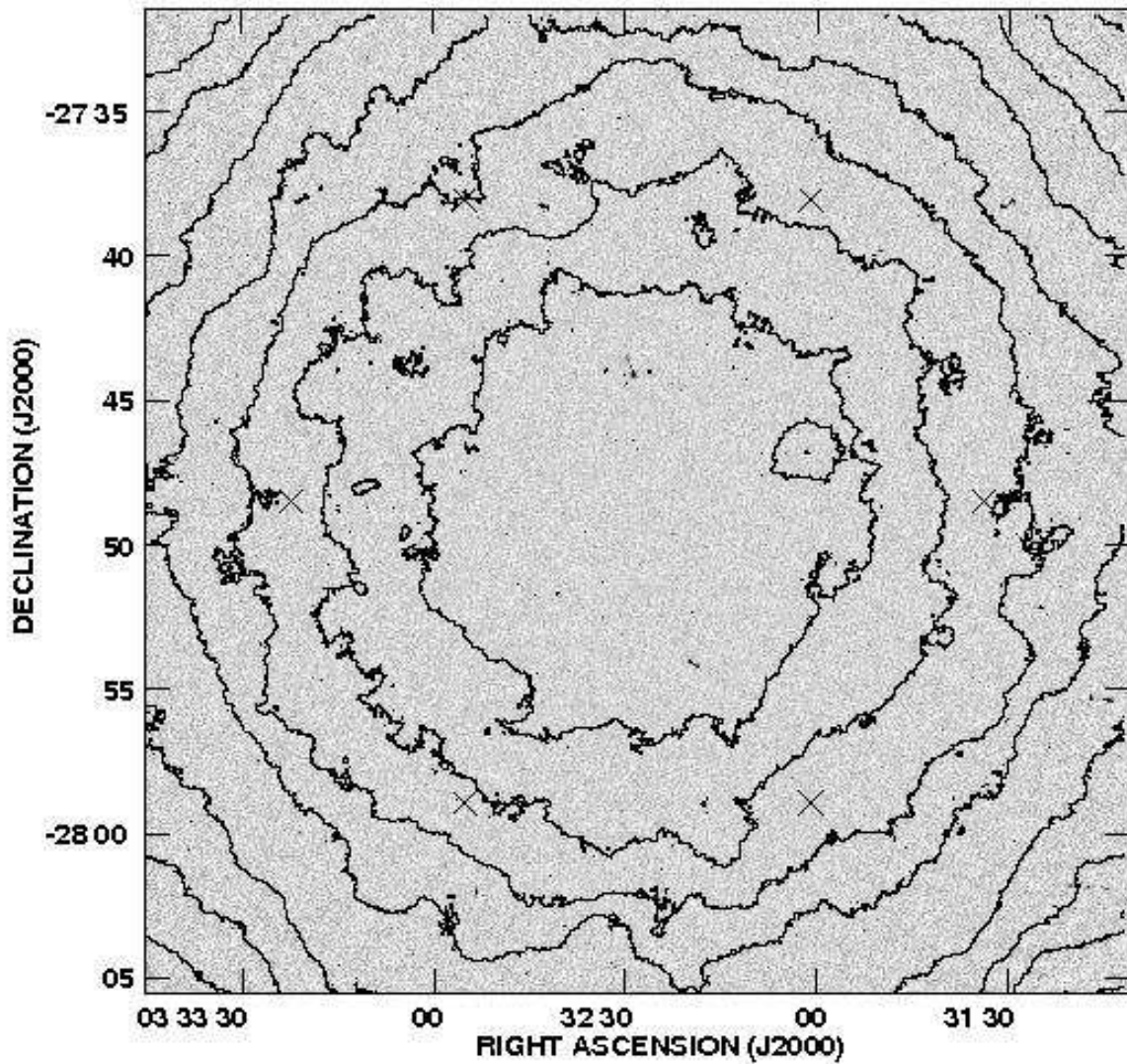


Figure 2.1: Greyscale depiction of the DR2 mosaic image, with overlaid contours of constant RMS noise. From the center, these contours represent 6.5 μJy , 7.0 μJy , 7.5 μJy , 8.0 μJy , 9 μJy , 10 μJy , 11 μJy , and 12 μJy per beam. The six pointing centers for the observations (Table 2.1) are indicated by crosses.

sensitivity map. To construct this map, we took the final mosaic image and removed all sources with peak flux densities greater than $150 \mu\text{Jy}$, chosen as approximately 20σ point source detections. The rms noise at each pixel in the mosaic map was then determined from this bright-source-removed map, based on the value calculated within a $135''$ -diameter circle centered on that pixel. This “background mesh” size is considerably larger than some other radio surveys which suggest that sizes on the order of just ten beam widths across are sufficient (Schinnerer et al., 2010; Huynh et al., 2012, e.g.,). We found that, given the resolution of our survey and the existence of extended sources that approached the size of these smaller background mesh apertures, their usage produced inaccurate small-scale variations in rms sensitivity maps. The larger size that we used was also consistent with what was used in the first data release, although in that release the background mesh was square but of the same equivalent area. The evaluation of the rms noise in constructing the rms sensitivity map was iterative, with points differing by more than three times the calculated rms noise removed prior to re-calculation until convergence was achieved. The final sensitivity map, hereafter called the RMS map, is relatively smooth as seen by the overlaid contours of constant rms included in Figure 2.1.

Figure 2.2 depicts the area covered at a given sensitivity or better based on this RMS map. The most sensitive regions of the mosaic image have an rms noise of $6 \mu\text{Jy}$ per beam, and half of the full mosaic image has an rms noise of $7.4 \mu\text{Jy}$ per beam or better. This represents an improvement of about $0.5 \mu\text{Jy}$ over the first data release mosaic image. The regions at the center of the mosaic where all six individual pointings can contribute are the most sensitive, and these correspond to the CDF-S coverage. The CDF-S 4 Msec X-ray data correspond to 54 separate *Chandra* images collected using ACIS-I and thus each having a field size of about $16'.9$ by $16'.9$. The exposure-weighted center of these data is (J2000) $03^h32^m28.06^s -27^\circ48'26.4''$ (Xue et al., 2011), and for the range of roll angles and slight shifts in aim point of the separate exposures it is reasonable to assume approximately uniform coverage out to about $7'$ in radius from this central point. Within this restricted area of the deepest X-ray coverage (0.043 square degrees, or 13% of the mosaic image) the radio mosaic image has a typical rms noise of $6.3 \mu\text{Jy}$ and is never worse than $6.7 \mu\text{Jy}$. This is depicted with the dotted line in Figure 2.2. We also define a subset of the full mosaic over which there are enough ancillary multiwavelength data to provide counterpart identification and spectroscopic redshifts or reasonable photometric redshifts (Padovani et al., in preparation; this region amounts to 0.282 square degrees or 87% of the mosaic image). The rms sensitivity as a function of area for this restricted region is depicted by the dashed line in Figure 2.2, and is used in correcting the source counts for investigation of contributions by source type.

Our data release consists of the six (u, v, w) data sets, nine images, and one catalog. The (u, v, w) data are the final combined and edited collections for each of the six pointings, and allow interested users to perform imaging with their own choices of weighting parameters. The nine images correspond to the final mosaic image and its associated RMS map, the final images corresponding to each of the six individual pointings (each with an rms near $10 \mu\text{Jy}$ at the field center), and a large mosaic map made from these six individual pointing images and representing the full imaging coverage (i.e., out past the coverage of the main

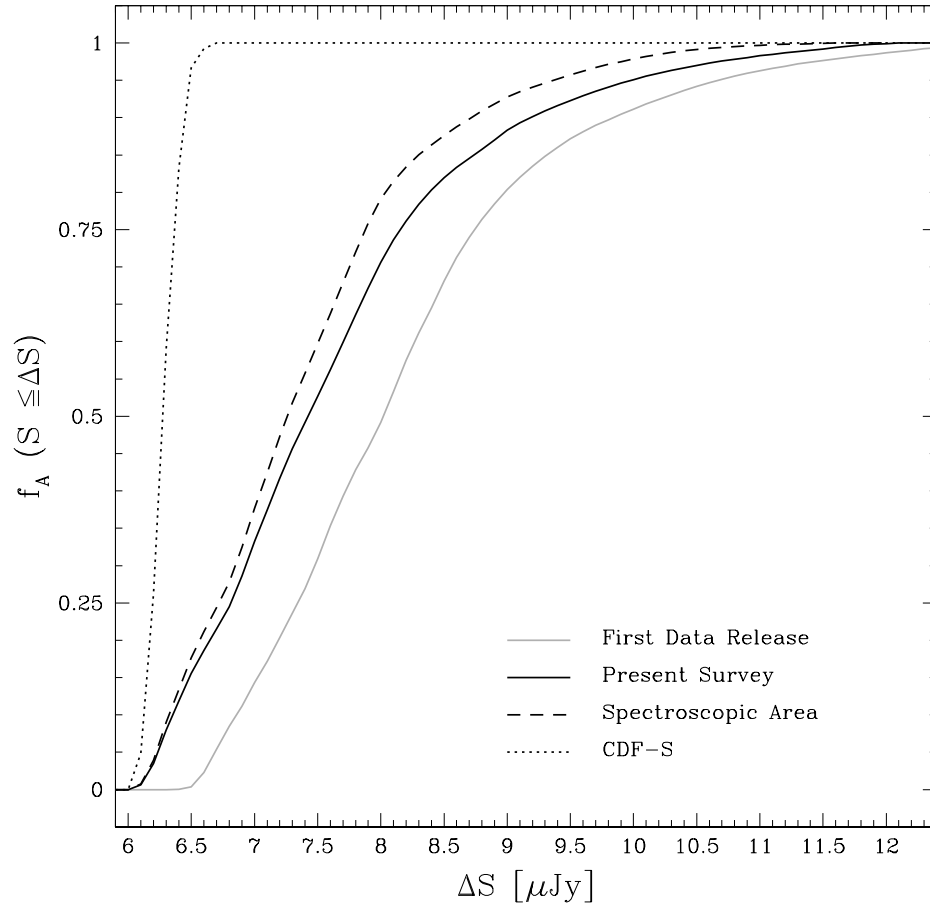


Figure 2.2: Fractional area covered at a given sensitivity or better, for the released mosaic image of 34'.1 by 34'.1. The image described in this paper is shown in black, while the results presented in the first data release are shown in grey. The improvement is about $0.5\mu\text{Jy}$ across the entire area. Also shown are the fractional areas covered at a given sensitivity or better for two smaller regions within the mosaic image, corresponding to a large region with multiwavelength data for quality photometric redshifts (dashed line) and a small central region corresponding to the deepest uniform coverage within the CDF-S 4 Msec data (dotted line).

final mosaic image). The catalog is based entirely on the final mosaic map, and will be discussed now in greater detail.

2.3 Source Catalog

2.3.1 Source Detection

The basis for the detection of sources was a signal-to-noise ratio (SNR) map, constructed by dividing the final mosaic image by its corresponding RMS map. The AIPS task SAD was used to pick out all sources in this SNR map with peaks above 3, and thus three times the local noise. We note that the effect of using an RMS map generated with a larger background mesh size is to slightly increase the number of sources above the detection threshold by smoothing over small-scale variation produced by the presence of bright sources and the more rapid fall-off in sensitivity at the edges of the mosaic. SAD fits Gaussians to the sources above the 3σ threshold and subtracts them from the SNR map to produce a residual image which may then be inspected to find sources that were either missed or poorly fit. These include sources with extended radio morphologies as well as blends of multiple and possibly independent radio sources. The residual image was inspected by eye with the help of overlaid contours to reveal such missed or poorly fit sources (indicated by large positive or negative values) and these were manually added to the list for subsequent analysis.

We then proceeded to evaluate all sources with peaks above 4σ identified in the SNR image by either SAD or our manual inspection. Our initial choice of 3σ was based on prior knowledge that sometimes single faint sources might be incorrectly split into a pair of fainter sources, and we used the SAD list to recover these objects as multiple $< 4\sigma$ objects at nearly identical position. In this round of source cataloging, we used the AIPS task JMFIT to fit Gaussians to the sources on the final mosaic image in order to evaluate source peak and integrated flux densities. JMFIT was provided with a guess for the peak flux density and its position (based on manual inspection of the image), but no corrections for primary beam attenuation or bandwidth smearing were applied. A correction for the former was explicitly applied in construction of the mosaic image, while the latter is complicated by the lack of a single pointing center for the image. The output parameters of JMFIT included the source coordinates, major and minor axis size and position angle, and the peak and integrated flux density. We used the RMS map to determine the local noise at the coordinates of the fitted source, and accepted those sources with peak flux density greater than five times their local noise value for inclusion in the final catalog. For those sources poorly fit by Gaussians in the initial investigation using the SNR map, we directed JMFIT to fit multiple components where applicable and performed aperture photometry on the more extended sources using the TVSTAT task.

For some work correlating the radio catalog with other wavelengths, it might seem of value to release the initial automated catalog that extended to down 3σ . However, we deem the danger of misinterpretation of such low-significance sources outweighs the

possible utility of such a catalog. In addition to some issues already discussed (i.e., false decomposition of single faint sources), we note here that if the mosaic image were truly described by Gaussian noise there would be over 1,100 noise peaks greater than 3σ across its large area. This number becomes reasonable at 4σ , where about 26 noise peaks would be expected. Using the traditional 5σ detection threshold the number of anticipated false sources has dropped to less than one across the full area of the final mosaic. The true noise distribution is not perfectly Gaussian as a result of the presence of real sources and their sidelobes, so these numbers may be considered lower limits to the estimate of the number of false sources at these thresholds. Finally, we note that the availability of the actual mosaic image allows users to directly assess possible low-significance radio sources at their positions of interest.

2.3.2 Source Morphology

Source morphology is an important aspect of source catalogs, often providing a coarse way to discriminate between emission mechanisms at appropriate resolutions. Radio emission associated with star formation is generally extended across galaxy disks, and thus resolved at arcsecond scales even for sources at high redshifts (Muxlow et al., 2005). Evaluation of the true flux density of a source is also often dependent on source morphology, with compact sources at lower signal-to-noise ratio better described by their peak flux density than by their integrated flux density (e.g., see Owen & Morrison, 2008).

Unfortunately, the careful consideration of source morphology is complicated by the mosaic nature of the final image. Every location in the output mosaic is the combination of the contributions of up to six separate pointings, and thus up to six separate corrections each dependent on differing values of angle and radial distance. If these corrections do not alter the apparent morphology of a source but only its apparent flux density, they are easily applied. This is the case for primary beam attenuation, and the simplification that the power pattern is radially symmetric is applied and accounted in the creation of the mosaic map. However, other effects such as bandwidth smearing are not so easily handled. A given location in the output mosaic is the combination of up to six separate images each of which suffers some degree of smearing in the radial direction relative to its relevant pointing center, and while corrections for this effect may be made on sources extracted from single-pointing data they are not so easily achieved when multiple pointings are combined. Bandwidth smearing does not change the integrated flux density in the limit of a noiseless image, and in M08 we confirmed that for the E-CDF-S radio survey the standard Gaussian fitting for source integrated flux densities provided consistent results with aperture photometry. However, the combination of up to six separate bandwidth smearing corrections does affect source morphology and the determination of whether a source is resolved.

In light of this complication, we performed multiple tests of source morphology that are encapsulated in the source catalog. The simplest of these is the direct fit to the mosaic image, which produces a major axis, minor axis, and position angle of the Gaussian which best fits the source in the mosaic image. In addition to ignoring effects such as bandwidth

smearing, these results are also still the convolution of the primary beam and the intrinsic morphology of the source. As such, they are not tremendously useful except in the very general sense of providing a quick handle on which sources are clearly resolved (i.e., those with axial sizes well above the $2''.8$ by $1''.6$ beam size). Similarly, sources in the mosaic image which were poorly fit were identified in the residual maps produced as the difference between the mosaic image and the best Gaussian fits to sources. The presence of large residuals is strongly suggestive of an extended source, and the integrated flux density for these sources was evaluated using manually-sized aperture photometry with the task TVSTAT.

For single pointing data we can incorporate the effect of bandwidth smearing into the source fitting. The distances between each source and the six separate pointing centers was determined, and when such distances were less than the 33% power point of the primary beam these pointings were noted. This provides a listing of the pointings which directly contributed to the mosaic image at the location of each source. We then determined the rms sensitivity of each contributing pointing at the coordinates of each source in order to determine which individual pointing provided the best signal-to-noise for source measurement. This is usually the pointing nearest to the source, but slight differences in achieved depth per pointing did occasionally mean a more distant pointing provided a marginally lower rms sensitivity. We then evaluated the Gaussian fit to each source using just this “best” single pointing, incorporating the effects of both primary beam attenuation and bandwidth smearing. The parameters of these fits, deconvolved to remove the primary beam geometry, are included in the source catalog. The major and minor axis parameters are provided as $\pm 1\sigma$ ranges, so that sources with fitted axes differing from zero may be identified and thus provide an evaluation that a source is resolved (i.e., the minimum size for its major axis is greater than zero). This represents the first of our two tests on whether a source is resolved.

A second technique to evaluate whether a source is resolved involves comparison of the fitted integrated and peak flux densities. A comparison of the ratio of integrated to peak flux density as a function of signal-to-noise ratio (defined as the peak flux density divided by the local rms sensitivity) is an empirical estimate of the errors in source fitting, and can be used to identify resolved sources as those for which the integrated flux density is clearly in excess of the peak flux density after accounting for the fitting errors (e.g., Huynh et al., 2005). Although this method does not provide direct indicators of source sizes and morphologies, it is quite helpful in the determination of the better estimate of a source’s true flux density. In Figure 2.3 we plot the ratio of the integrated to peak flux densities as a function of signal-to-noise based on the Gaussian fits to sources in the mosaic image. Situations where the integrated flux density is less than the peak flux density are clearly the result of errors inherent to source fitting, and we can determine a function which bounds these cases. Under the assumption that it is equally likely that such errors can result in fits for which the integrated flux density is greater than the peak flux density, we can mirror this function above the line where the peak flux density equals the integrated flux density and thus define an envelope which contains sources that are consistent with being unresolved. Sources for which the ratio of integrated to peak flux density is greater

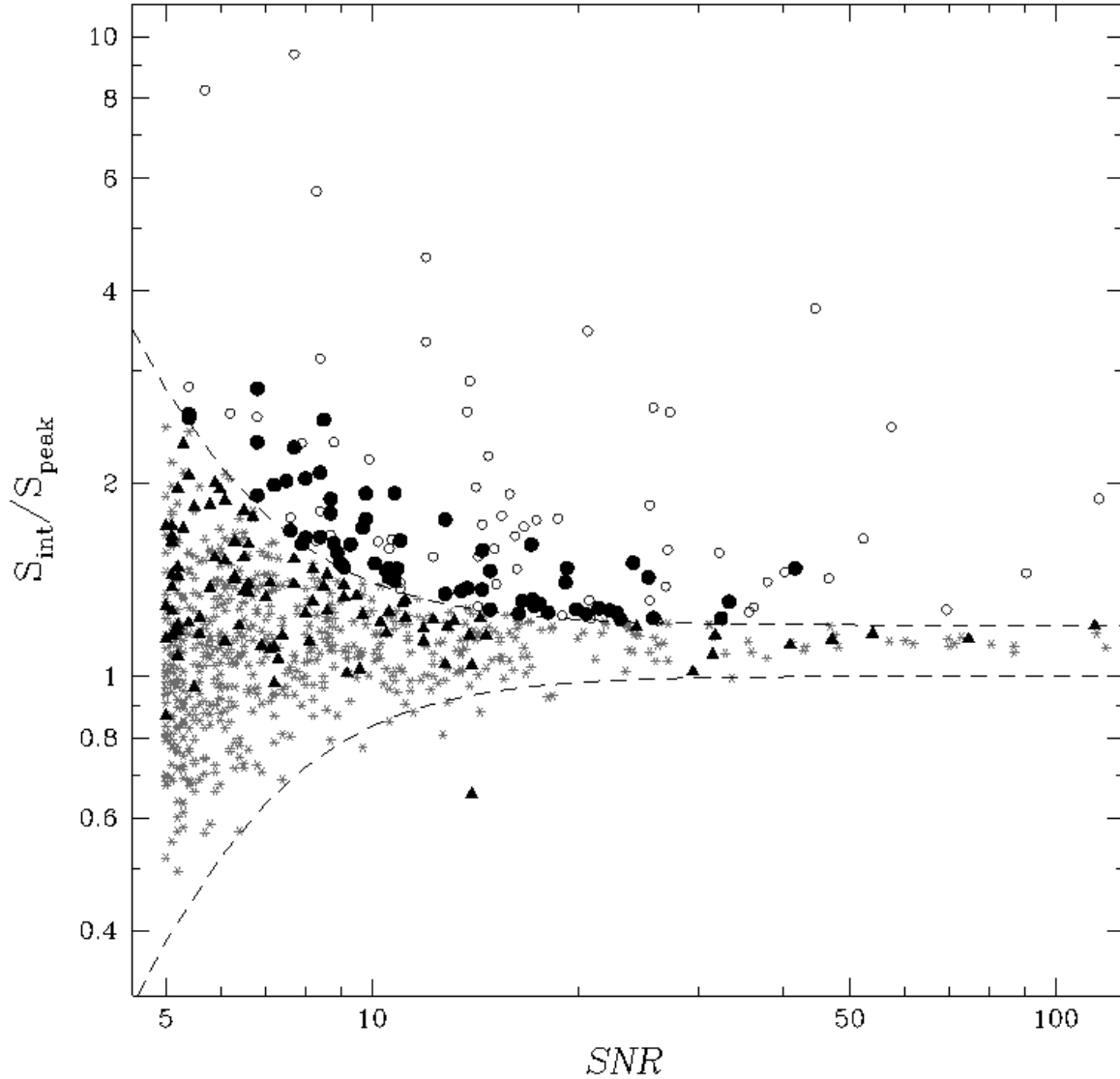


Figure 2.3: Analysis of whether sources are resolved, based on SNR and the ratio of integrated to peak flux densities from the mosaic image. The dashed lines show the envelope within which sources are assumed to be unresolved, with sources above the upper dashed line being resolved according to this approach. Grey asterisks are sources which are unresolved by both this method and investigation of their fitted axes in single-pointing data (including corrections for primary beam response and bandwidth smearing), and open circles are objects for which each method indicates a resolved source. Sources whose classification differs between the two methods are shown by filled black points, with filled circles being resolved according to this method but not by the Gaussian fit to their individual pointing data and filled triangles being the opposite.

than this envelope are those that are likely to be resolved.

We follow the functional form presented in Huynh et al. (2005) to fit the lower envelope of the distribution in Figure 2.3 as

$$\frac{S_i}{S_p} = \frac{1}{1 + (200/SNR^3)} \quad (2.1)$$

where S_i and S_p represent the integrated and peak flux densities and SNR is the signal-to-noise ratio, defined as the peak flux density divided by the local rms sensitivity. We determined the constant, 200, by finding its value such that 95% of all sources with $S_i/S_p < 1$ are bound by the function.

It is clear from Figure 2.3 that the distribution of the ratio of peak to integrated flux density is not centered on unity. This is the aforementioned effect of combining separate pointings each with their own degrees of bandwidth smearing and the creation of the mosaic image not explicitly accounting for this bandwidth smearing. The resulting source will appear to have a core representing the region for which each pointing contributes to the flux density and a much fainter irregular extended halo consisting of the bandwidth-smearred flux densities of the separate pointings. The net effect is that sources with high signal-to-noise will always have an integrated flux density greater than their peak flux density, although due to the mosaic nature of the map such sources are not unambiguously resolved.

We can model the expected size of this effect using reasonable assumptions. The spatial distribution of VLA antennas and our weighting of the resulting (u, v, w) data imply that our (u, v, w) coverage is approximately a circularly-symmetric Gaussian, and the individual 3.125 MHz channels after bandpass calibration can be assumed to have nearly square response. Under these simplifications, the reduction in measured amplitude of a point source caused by bandwidth smearing relative to its true amplitude is:

$$\frac{I}{I_0} = \frac{\sqrt{\pi}}{\gamma\beta} \operatorname{erf} \frac{\gamma\beta}{2} \quad (2.2)$$

(Bridle et al., 1994), where I_0 is the amplitude of the point source in the absence of bandwidth smearing, $\gamma \equiv 2\sqrt{\ln 2}$, and $\beta = \frac{\Delta\nu}{\nu} \frac{\theta}{\theta_{FWHM}}$. This latter term is the fractional bandwidth of the observations (in our case, 3.125 MHz divided by 1.4 GHz) times the distance from the pointing center expressed in number of beams (the separation θ divided by the FWHM of the beam, θ_{FWHM}). For simplicity in our estimation of the effect of bandwidth smearing we “circularize” the beam and assume it is symmetric with a FWHM of 2". We can then apply Equation 2.2 to determine the reduction in peak response associated with each pointing that contributes to the mosaic image at the position of each source, and weight these per-pointing responses in the same manner that was used to generate the mosaic image. This yields the reduction in peak response caused by bandwidth smearing, and since in the absence of noise the net flux density is conserved, the inverse of the left-hand side of Equation 2.2 is the ratio of the integrated flux density to the peak flux density: the ratio examined in Figure 2.3.

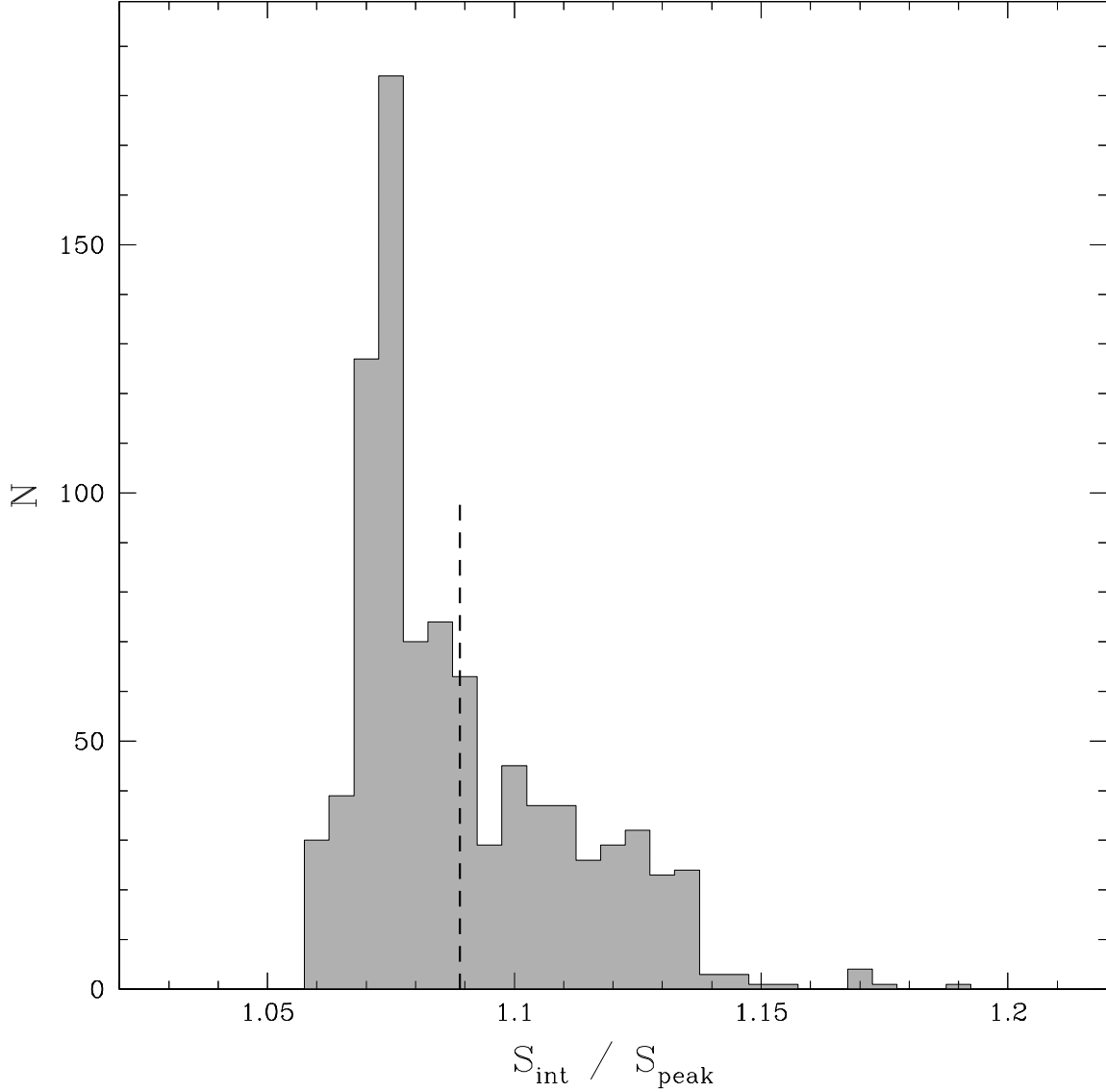


Figure 2.4: Histogram of modeled bandwidth smearing at the positions of sources in the mosaic image. Bandwidth smearing reduces the peak flux density of sources but conserves the total flux density, so the ratio S_i/S_p is greater than 1. The dashed vertical line marks the average, $S_i/S_p = 1.089$. By design of the survey, most sources lie reasonably close to a pointing center and thus the histogram peaks at a value of $S_i/S_p \sim 1.07$. Near the center of the pointing ring the sensitivity is best because all six pointings contribute to the mosaic image, but the distance to each pointing is relatively large so bandwidth smearing is greater. This causes the large tail to values of $S_i/S_p \lesssim 1.14$. The small number of sources with higher S_i/S_p fall at the corners of the mosaic image.

We plot a histogram of the modeled effect of bandwidth smearing in Figure 2.4, which is based on the positions of actual sources in our mosaic image. The results are consistent with the offset seen in Figure 2.3, with the mean ratio of S_i to S_p being 1.09 with a dispersion of 0.02. For perspective, the range in values is understood by considering limiting cases. The least possible bandwidth smearing occurs for a source coincident with a single pointing center, for which the mosaic map is dominated by data associated with that pointing but also includes contributions from its two adjacent pointings. In this case, the ratio of S_i to S_p is 1.06. At the other extreme, a source directly in the center of the mosaic image is equidistant from all six pointings and thus suffers modest bandwidth smearing from each. For such a source, the ratio of S_i to S_p is 1.14. It can be seen in Figure 2.4 that these values do indeed bracket the majority of sources and the peak in the histogram around $S_i/S_p \approx 1.07$ indicates that, by design, most sources fall reasonably close to a single pointing center. The small number of sources at $S_i/S_p > 1.14$ correspond to the corners of the mosaic image.

Returning to Figure 2.3 and the evaluation of whether a source is resolved, instead of simply mirroring Equation 2.1 about $S_i/S_p = 1$ we include an offset to account for bandwidth smearing. Based on the spread of values for S_i/S_p from bandwidth smearing shown in Figure 2.4 and its consistency with that measured for sources that appear unresolved based on the Gaussian source fitting to their single best pointing, we set the upper envelope for evaluating whether a source is resolved at

$$\frac{S_i}{S_p} = 1.2 + (200/SNR^3) \quad (2.3)$$

Sources for which S_i/S_p is above this signal-to-noise based threshold are thus considered to be resolved using this approach. This is indicated by a flag in the source catalog, and additional justification for the 20% offset in the upper envelope is provided in Section 2.3.4 when we compare our flux densities with those of single-pointing data.

The points in Figure 2.3 are coded to reflect whether individual sources appear to be resolved under each of the two techniques. Grey asterisks represent all sources for which both fitted axes have minimum values of zero and the ratio of peak to integrated flux density lies below the curve described by Equation 2.3; these points were associated with unresolved sources in each technique. Similarly, open circles represent those sources that appear to be resolved when evaluated using both techniques. The filled black symbols represent the less conclusive cases, with filled triangles signifying sources that appear resolved in their best single-pointing data yet do not lie above the fitted relationship of Equation 2.3 and filled circles signifying sources that appear unresolved in their single-pointing data yet lie above the fitted relationship thus suggesting that they are resolved.

2.3.3 Multiple Component Sources

Powerful radio galaxies are often resolved into multiple components, with the classic example being FR II sources typically composed of a pair of bright, extended radio lobes

surrounding the progenitor galaxy which sometimes is also coincident with a distinct radio core (Fanaroff & Riley, 1974). The sensitivity and resolution of the survey can also “break up” the contiguous radio emission associated with a single progenitor galaxy into multiple apparently separate components. Possible associations are generally made by the experienced radio astronomers who collect, reduce, and analyze the radio data and are thus inherently subjective, although usually accurate. In M08, we relied upon the listing of identified multiple component sources from K08 and added new possible components that the slightly higher resolution of our survey provided.

In the present work, we take advantage of the outstanding available multiwavelength coverage to assess multiple component sources. Bonzini et al. (2012) use a likelihood ratio technique to identify counterparts for the radio sources associated with this survey, relying on deep optical, near- and mid-infrared data. This is highly effective at assessing possible multiple component sources, as sometimes radio sources thought to be components associated with a nearby but spatially-separate galaxy are shown to have much stronger associations with a unique, fainter coincident galaxy. Similarly, the outstanding depth of the optical and IR data make radio sources without a coincident counterpart very rare. This means that close positional coincidence of a radio source with an optical or IR counterpart is almost certainly an association with a single galaxy rather than a component associated to a neighboring galaxy. Our radio catalog is thus guided by the counterpart identification. If a single galaxy has multiple associated radio components, we list their combined properties as a single entry in the main catalog and provide a flag indicating that the source consists of multiple components. A subsequent catalog then includes the information on each separate component of the combined source. There are 17 such multiple-component sources, with a total of 49 individual components ascribed to them. We stress that no information is lost by this approach; every distinct peak in the radio emission of the final image is included in one of the two catalogs, and users interested in the total radio emission associated with a given galaxy will find such information in the first catalog. Images of the 17 multiple-component sources are provided in the Appendix.

2.3.4 Source Flux Density

Of greater practical importance to most users is the question of what flux density should be used for each source? As previously discussed, this is related to the issue of source morphology even if such detail is not needed by the user. In M08 we confirmed the general consistency of our flux density scale with prior radio observations of this region, particularly the deep single-pointing data of K08. We also confirmed that the flux densities based on Gaussian fitting were consistent with simple aperture photometry, indicating that although considerations such as bandwidth smearing do affect the apparent morphology of sources the standard approach of using Gaussian fits to evaluate flux densities was still appropriate. We rely on the same basic approach here to specify which flux density measurement, peak or integrated, should be adopted in order to most accurately reflect the true flux density of a source. This was accomplished by calculating the mean and dispersion of the ratio of flux density from our catalog with that of K08, using various prescriptions to choose

between peak and integrated flux density measurements. In general, these prescriptions paralleled the discussion of source morphology and the two evaluations thereof, one based on whether the fitted deconvolved axial sizes were consistent with zero and one based on the ratio of integrated to peak flux density and the parametrized envelope bounding unresolved sources. These will henceforth be referred to as “Fitted Axis” and “Envelope,” respectively. For resolved sources we used the integrated flux density measurement while for unresolved sources we used the peak flux density measurement. We also explored the use of a threshold in SNR , using integrated flux densities for sources above the threshold and peak flux densities for those below. Combinations of these various prescriptions were also examined and Table 2.2 summarizes the findings.

The flux densities associated with the Fitted Axis method are slightly lower than those reported in K08 ($< S/S_{K08} >= 0.985$), while the Envelope method yields slightly higher flux densities ($< S/S_{K08} >= 1.020$). After performing a single round of 3σ clipping to remove outliers (for example, sources with intrinsic variability over the ~ 6 years between the K08 observations and this survey), the dispersions associated with the two methods are similar at 0.218 and 0.225, respectively. At this point we note that adding the 20% offset to the upper curve in the Envelope method and using this to evaluate whether sources are resolved and hence whether to adopt their integrated flux density measurements has a large effect. Simply mirroring the envelope determined for $S_i/S_p < 1$ without including the offset produces flux densities that are about 7% higher than those in K08. This is just a consequence of the convergence to $S_i/S_p \approx 1.1$ for brighter unresolved sources (see Figures 2.3 and 2.4). Since the two methods have opposing effects relative to the K08 flux density scale, we investigated logical combinations of “OR” (if either method indicated a source was resolved, its integrated flux density was adopted) and “AND” (a source was assumed to be resolved only if both methods agreed that it was). Neither of these produced an improvement on simply adopting one of the two methods, although the dispersion with the “AND” combination after clipping outliers was the lowest we found.

These findings led us to identify a “Hybrid” solution. The “Hybrid” method applies a cut of $SNR = 20$, with all sources detected at greater than this threshold being represented by their integrated flux density measurement. For sources with lower SNR , the peak flux density measurement is adopted unless both the Fitted Axis and Envelope methods indicate the source is resolved in which case its integrated flux density is used. This prescription yields flux densities nearly identical to those of the K08 survey, $< S/S_{K08} >= 1.005$ and $< S/S_{K08} >= 0.997$ before and after clipping. The dispersion in the ratio of the flux densities after the clipping is also very low. We recommend this Hybrid solution for the selection of peak or integrated flux density, and indicate its selection in the final source table.

2.3.5 Final Catalog

The final source catalog is presented in Tables 2.3 and 2.4 and encapsulates all of the above discussion. Table 2.3 is the main catalog of radio sources, wherein the 17 sources thought to consist of multiple components associated with a single host object are listed

Table 2.2. Flux Density Comparisons

Method	Full Sample		Clipped Sample		
	Mean	Disp	Mean	Disp	N_{clip}
Fitted Axis	0.985	0.248	0.978	0.218	6
Envelope	1.085	0.290	1.071	0.256	6
Envelope+20	1.020	0.276	0.994	0.225	10
Both-OR	1.041	0.278	1.013	0.227	11
Both-AND	0.964	0.241	0.960	0.213	5
SNR	0.938	0.421	0.938	0.421	0
Hybrid	1.005	0.258	0.997	0.220	6

Note. — Columns: (1) Method used to select between peak and integrated flux density measurement. For each method, sources considered to be resolved are described by their integrated flux density while unresolved sources are described by their peak flux density. In “Fitted Axis,” sources for which the fitted minimum of the major axis is greater than zero are considered resolved; in “Envelope,” sources with integrated to peak flux density ratios above the envelope described by the reflection of Equation 2.1 above integrated equals peak flux density are considered resolved; in “Envelope+20,” sources with integrated to peak flux density ratios above the envelope described by Equation 2.3 (i.e., the reflected envelope of Equation 2.1 offset upward by 20%) are considered resolved; in “Both-OR” and “Both-AND” the two methods are combined with logical operators, so that a source is considered resolved if either method indicates that it is (“OR”) or only if both methods indicate that it is (“AND”); in “SNR” sources with $SNR > 10$ have their integrated flux densities adopted, while sources below this threshold use peak flux densities; and in “Hybrid” a mix of the methods is adopted, such that for sources with $SNR > 20$ the integrated flux density is used while for sources below this threshold the peak flux density is used unless both methods indicate a resolved source, in which case the integrated flux density is used. Numbers in Columns (2) through (5) refer to the statistics based on the ratio of flux density from the current catalog to that of the K08 catalog, with (2) and (3) being the mean and dispersion based on all common objects and (4) and (5) being the mean and dispersion after clipping of sources that differ from the mean by more than 3σ . Column (6) indicates the number of outlier objects removed by this single iteration of clipping.

with a single aggregate integrated flux density. Gaussian fits to the individual components associated with these sources are listed in full detail in Table 2.4. The data columns for each table are identical, and are summarized as follows:

(1) - (6) *Source position* (J2000). In most cases, the listed position is that of the center of the Gaussian that best fits the data. The typical position errors for strong, unresolved sources observed with the VLA at 1.4 GHz are $0''.1$, and position errors attributed to the Gaussian fitting in the presence of noise are on the order of the beam size divided by twice the signal-to-noise ratio (Condon, 1997). Thus, the position error in Right Ascension for a 5σ -point source would be $\sqrt{0.1^2 + \{1.6/(2 \times 5)\}^2} \approx 0''.2$ while the position error in declination for the same source would be $\sqrt{0.1^2 + \{2.8/(2 \times 5)\}^2} \approx 0''.3$. For some resolved sources, the radio emission is poorly fit by a Gaussian and the source is evaluated using an irregularly-shaped aperture that covers the apparent emission (AIPS task TVSTAT). These sources are flagged (column 29) and their positions are usually just the location of the maximum emission within the aperture.

(7) *Signal-to-noise ratio*. This is defined as the fitted peak flux density divided by the local rms noise (i.e., column 8 divided by column 9).

(8) *Peak flux density* in units of μJy per beam.

(9) *Local rms noise* in units of μJy per beam. This is evaluated using the RMS map and thus represents the local noise within a $135''$ -diameter circle around the source position.

(10) - (11) *Integrated flux density* and associated error, in units of μJy . As with the prior columns, these values represent the Gaussian fit to the source unless otherwise noted. For the extended sources poorly fit by a Gaussian, the total flux density within the irregularly-shaped aperture is indicated and its error is just the square root of the number of beams covering the aperture times the local rms noise.

(12) - (14) *Source size and position angle from mosaic image*, in units of arcsec and degrees. These represent the fitted source size including convolution with the $2''.8$ by $1''.6$ beam, with the position angle measured in degrees east from north (e.g., the beam has $PA = 0$). In addition, these parameters include the differing contributions of bandwidth smearing from each of the pointings contributing to the mosaic image at the position of the source. Note that these columns are only present in the online version of the tables.

(15) *Best pointing*. The index number of the individual pointing which has the lowest rms noise at the position of the source. The pointings are numbered 1 through 6 starting due east of the center of the mosaic and progressing clockwise (see Table 2.1).

(16) *rms noise in best pointing* in units of μJy per beam.

(17) - (21) *Source size and position angle from best pointing*, in units of arcsec and degrees. The sizes are presented as $\pm 1\sigma$ range for the major axis (columns 17 and 18) and minor axis (columns 19 and 20), while the position angle (column 21) is just the nominal value. Since these values are based on Gaussian fitting to the source in the single pointing with the lowest rms, they have accounted for bandwidth smearing and have been deconvolved to remove the synthesized beam.

(22) *Extended flag*. If the source was found to be extended using the “envelope” method (see Section 2.3.2), this column is set to 1. Sources that were unresolved under this test

have a value of 0 in this column.

(23) *Flux density choice flag*. The recommended flux density measurement to use for the source (see Section 2.3.4). If the value in this column is “P” the flux density is better represented by the peak flux density (column 8) whereas if it is “I” the integrated flux density (column 10) is recommended.

(24) *Pointings contributing to mosaic image*. This is a listing of the pointings that contribute to the mosaic image at the position of the source. Thus, if the source position falls within the 33% power point of the primary beam (about 20') associated with an individual pointing that pointing is noted here. This information allows users to inspect the images associated with the individual pointings to further assess source morphology and characteristics. This column is only available in the online version of the tables.

(25) - (28) *Source information from Kellermann et al. (2008)*. For sources that were identified in K08, the associated identification number (column 25), flux density and error (columns 26 and 27) in units of μJy , and deconvolved source size (column 28, including upper limits) are provided. These columns are only available in the online version of the tables.

(29) *Notes*. Flags indicating details such as extended source morphologies and other source fitting details. Multiple-component sources are indicated here (Table 2.3) and cross referenced to their individual fitted components (Table 2.4), with figures provided in the Appendix.

2.4 Summary and Discussion

Table 2.3 provides a listing of 883 distinct radio sources, 17 of which are single entries for multiple-component sources where the total radio emission appears to be associated with a single host galaxy. The details on the individual separate components for these 17 sources form the basis for the second table, which contains a total of 49 separate components for these sources. To summarize, the final mosaic image consists of 915 separate peaks in radio emission (883 in Table 2.3 minus the 17 multiple component sources, plus the 49 individual components of these sources listed in Table 2.4). For comparison, the early data release catalog of M08 consisted of 495 unique components. Figure 2.5 reveals the primary reason for this greatly increased number, as the *SNR* limit for inclusion has decreased from 7 to 5 for this catalog relative to the first data release. In addition, the *SNR* for any given source will usually be increased in the present catalog on account of the improved imaging, which typically amounts to an rms noise that is $0.5 \mu\text{Jy}$ lower than that of the first data release at any point in the mosaic image.

In addition to the catalogs, this second data release consists of 9 images and 6 calibrated (u, v, w) datasets. There are individual images and calibrated (u, v, w) files for each of the six pointing centers (refer to Table 2.1), along with the main mosaic image that uses all six pointings and its associated RMS image. The final released image is a larger area mosaic that incorporates all data out to the 33% power point of the VLA primary beam. While there is no catalog associated with the additional area provided by this larger mosaic, it is

Table 2.3. Main Catalog of Radio Sources

RA (J2000)			Dec (J2000)		SNR	S_p [μ Jy bm $^{-1}$]	RMS [μ Jy bm $^{-1}$]	S_i [μ Jy]	$e_{\bullet}S_i$ [μ Jy]	Best Ptg	RMS $_{best}$ [μ Jy bm $^{-1}$]	Maj $_{best}$ [$''$]	Min $_{best}$ [$''$]	PA $_{best}$ [$^{\circ}$]	Ext?	Choice	Notes			
(1)	(2)	(3)	(4)	(5)	(6)	(7)	(8)	(9)	(10)	(11)	(15)	(16)	(17)	(18)	(19)	(20)	(21)	(22)	(23)	(29)
3	31	10.69	-28	03	22.8	18.7	207.5	10.6	365.2	26.9	5	14.6	1.4	2.3	0.0	0.7	169	1	I	...
3	31	10.81	-27	55	52.8	13.8	123.1	8.8	156.6	18.0	4	11.8	0.0	2.0	0.0	1.4	120	0	P	...
3	31	10.83	-27	55	57.8	5.3	47.3	8.9	32.7	12.1	4	11.9	0.0	3.1	0.0	0.0	2	0	P	...
3	31	10.93	-27	49	55.5	5.1	40.8	8.0	35.3	12.6	4	10.2	0.0	2.6	0.0	2.7	168	0	P	...
3	31	10.95	-27	58	10.4	12.7	121.2	9.5	136.9	17.9	4	12.9	0.0	1.3	0.0	1.5	21	0	P	...
3	31	11.48	-27	52	59.0	12.8	105.9	8.0	185.8	20.5	4	10.9	0.0	2.7	0.0	1.9	165	1	P	...
3	31	11.63	-27	55	06.3	5.4	47.1	8.7	69.0	20.1	4	11.4	0.0	4.7	0.0	1.6	49	0	P	...
3	31	11.69	-27	31	44.2	211.2	2555.0	12.1	3232.0	65.4	3	15.2	0.2	0.5	0.0	0.0	29	1	I	a
3	31	11.84	-27	58	18.0	8.1	77.2	9.4	92.5	18.4	4	12.7	0.0	2.9	0.0	1.3	162	0	P	...
3	31	11.89	-27	59	52.3	6.8	65.8	9.5	90.3	20.5	5	13.7	0.0	2.7	0.0	0.6	22	0	P	...

Note. — Only ten rows of data are displayed here to demonstrate the format, and columns (12) - (14) and (24) - (28) are omitted in this print version. The full table is available in the electronic version of the journal. See text for description of columns.

Table 2.4. Individual Components of Multiple-Component Radio Sources

	RA (J2000)			Dec (J2000)		SNR	S_p [$\mu\text{Jy bm}^{-1}$]	RMS [$\mu\text{Jy bm}^{-1}$]	S_i [μJy]	$e\angle S_i$ [μJy]	Best Ptg	RMS_{best} [$\mu\text{Jy bm}^{-1}$]	Maj_{best} [$''$]		Min_{best} [$''$]		PA_{best} [$^\circ$]	Ext?	Choice	Notes
(1)	(2)	(3)	(4)	(5)	(6)	(7)	(8)	(9)	(10)	(11)	(15)	(16)	(17)	(18)	(19)	(20)	(21)	(22)	(23)	(29)
3	31	13.99	-27	55	19.9	144.4	1242.0	8.6	7180.0	57.3	4	11.3	7.1	7.2	2.0	2.1	81	1	P	1
3	31	15.06	-27	55	18.9	120.9	1040.0	8.6	1206.0	16.5	4	11.2	0.0	0.6	0.0	0.7	42	1	P	1
3	31	17.05	-27	55	15.	103.6	870.0	8.4	3650.0	43.0	4	11.0	4.6	4.7	3.0	3.1	157	1	P	1
3	31	14.69	-28	01	51.7	8.7	90.1	10.4	1367.0	168.5	5	13.6	16.0	20.9	1.2	2.8	77	1	P	2
3	31	17.35	-28	01	47.4	26.5	270.2	10.2	358.8	21.0	5	12.9	0.0	1.6	0.0	1.0	48	1	P	2
3	31	20.16	-28	01	46.2	9.9	98.5	9.9	856.7	95.5	5	12.4	5.1	6.7	3.1	4.6	100	1	P	2
3	31	24.83	-27	52	08.9	1043.0	8032.0	7.7	24670.0	30.5	4	10.2	4.0	4.1	1.7	1.7	64	1	P	3
3	31	25.01	-27	52	07.7	960.5	7396.0	7.7	15380.0	22.3	4	10.2	2.1	2.2	2.0	2.0	179	1	P	3

Note. — Only eight rows of data are displayed here to demonstrate the format, and columns (12) - (14) and (24) - (28) are omitted in this print version. The full table is available in the electronic version of the journal. See text for description of columns.

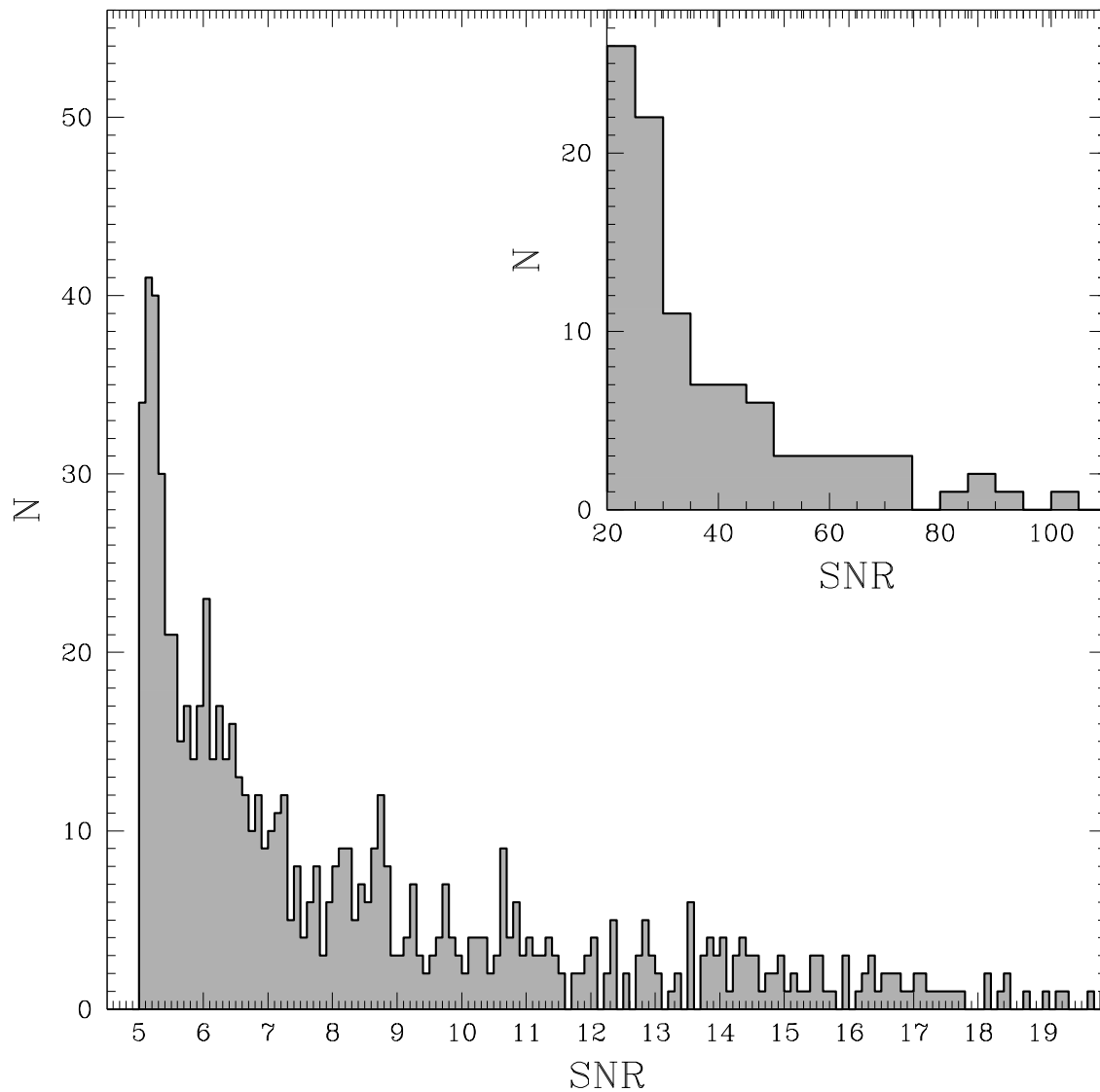


Figure 2.5: Histogram of number of radio sources as a function of signal-to-noise ratio, created using all detected peaks in the mosaic image (i.e., inclusive of individual components of multiple-component sources). The main histogram uses a bin size of 0.1, and the inset for higher signal-to-noise ratios uses a bin size of 5. There are an additional 47 sources with $SNR > 100$.

useful for identification and measurement of sources found in other wide-area surveys.

The depth of the survey makes the surface density of radio sources competitive with that determined in X-rays. For the full mosaic image (0.324 square degree) and its associated 5σ catalog presented in Table 2.3, there are over 2,700 sources per square degree. This is over 30 times the source density associated to the Faint Images of the Radio Sky at Twenty centimeters survey (FIRST; White et al., 1997). Because the sensitivity is fairly uniform across the mosaic image this figure increases only slightly towards the image center. For the portion of the mosaic image with good multiwavelength coverage to provide photometric redshifts (refer to Section 2.2.3 and Figure 2.2) the source density approaches 2,800 sources per square degree, and for the region of deep and uniform coverage from the CDF-S 4 Msec observations (i.e., the $7'$ radius about the exposure-weighted center point) it is nearly 3,100 sources per square degree. In the central $5'$ around the center of the mosaic (i.e., the center of the pointing ring) where the rms sensitivity ranges from $6 \mu\text{Jy}$ per beam to $6.6 \mu\text{Jy}$ per beam, the density is over 3,500 sources per square degree. For comparison, the X-ray source density within the inner $3'$ of the 4 Msec CDF-S is roughly 16,700 sources per square degree (Xue et al., 2011) but over the full CDF-S coverage it is only about twice the surface density of radio sources although the observing time for the radio observations was about a factor of six less than for the X-ray observations.

Similarly, simple positional matching of X-ray and radio catalogs provides some illuminating numbers. Considering just the region of deep and uniform coverage from the CDF-S 4 Msec observations, 16.8% (80/475) of the Xue et al. (2011) X-ray sources have matches in the radio catalog using a simple positional match of $2''$. The detection fraction within this same area only rises slightly as the *Chandra* integration time declines, being 18.2% (50/274) for the CDF-S 2 Msec catalog of Luo et al. (2008), 19.0% (38/200) for the CDF-S 1 Msec catalog of Giacconi et al. (2002), and 21.8% (19/87) for the shallower E-CDF-S catalog of Lehmer et al. (2005). Looking at this from the other direction, the increasing integrations with *Chandra* are gradually producing larger detection fractions of the radio sources. While only 14.5% of the radio sources within this region are detected in the E-CDF-S observations (19/131), 29.0% (38/131) are detected in the 1 Msec data, 38.2% (50/131) are detected in the 2 Msec data, and 61.1% (80/131) are detected in the full 4 Msec data. At this rate of increase, should the CDF-S be expanded to 10 Msec (e.g., Lehmer et al., 2012) we can expect X-ray detections for over 90% of the radio sources from within this central area.

Emphasis on the E-CDF-S continues with additional radio surveys either in process or planned. The rebirth of the VLA as the Karl G. Jansky Very Large Array, with new receivers and electronics as well as a wide-bandwidth, many channel correlator, will greatly advance this objective. The RMS sensitivity of a radio image is inversely proportional to the square root of the bandwidth, meaning the new correlator produces a dramatic improvement in the depth that VLA images can achieve in reasonable duration programs. Consequently, future deep fields will routinely achieve RMS sensitivities of $\sim 1 \mu\text{Jy}$ at frequencies near 1.4 GHz (e.g., Condon et al., 2012). This will translate to thousands of detected radio sources in the E-CDF-S, and the wide bandwidth will also provide spectral indices for brighter sources where signal-to-noise is high. One of the tradeoffs in survey

imaging is the size of the primary beam (and hence field of view), which is inversely proportional to the frequency of observation. This means that doubling the frequency of observation requires four times as many pointings to cover the same area, and the attendant increase in program duration has greatly limited the number of wide-field surveys performed at frequencies above 1.4 GHz. The vast improvement in sensitivity arising from increased bandwidth will counteract this problem, and deep surveys at higher observing frequencies will also be achievable in reasonable observing times. These will provide spectral measurements for a large fraction of the sources.

2.A Multiple-Component Source Images

Figures for each of the 17 multiple-component sources described in Section 2.3.3 and listed in Table 2.4 are presented here. Unless otherwise noted, each image is $1'$ by $1'$ with the greyscale ranging from $-35 \mu\text{Jy beam}^{-1}$ to $105 \mu\text{Jy beam}^{-1}$. Contours are depicted at 5, 8, 13, 21, ... , and 987 times the local RMS noise. Information regarding distinct sources may be found in Bonzini et al. (2012).

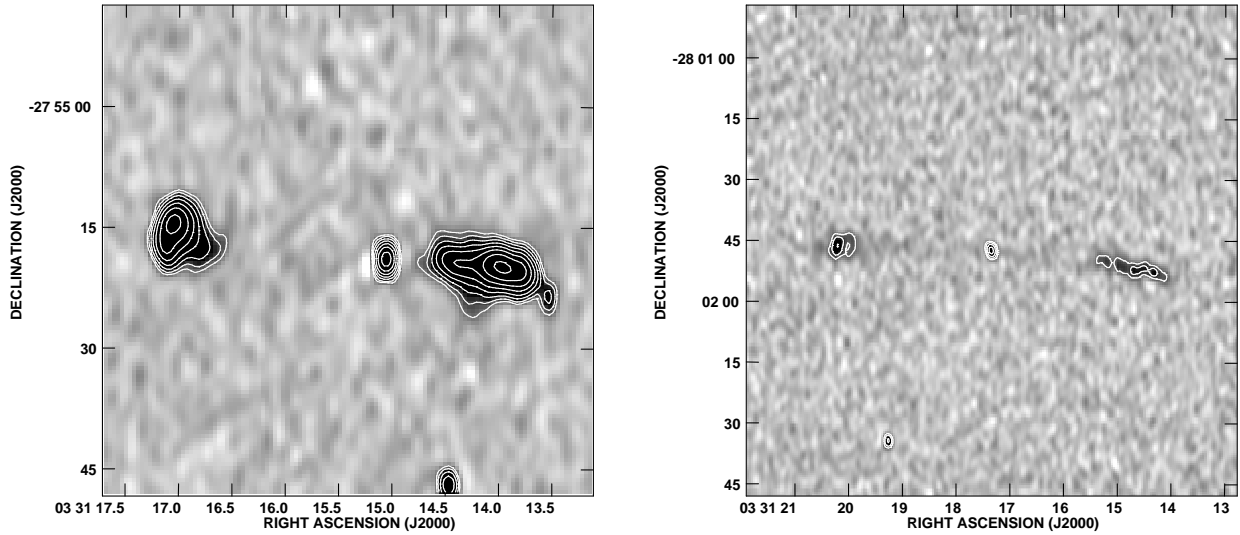


Figure 2.6: *Left:* Multiple-component source at 033115.0-275519, consisting of three components (core, east and west lobes). Note that the point source just to the edge of the western lobe (033113.53-275524.3) is a separate source associated with a counterpart in Bonzini et al. (2012). *Right:* Multiple-component source at 033117.3-280147, consisting of three components (core, east and west lobes). The size of this image is $2'$ by $2'$.

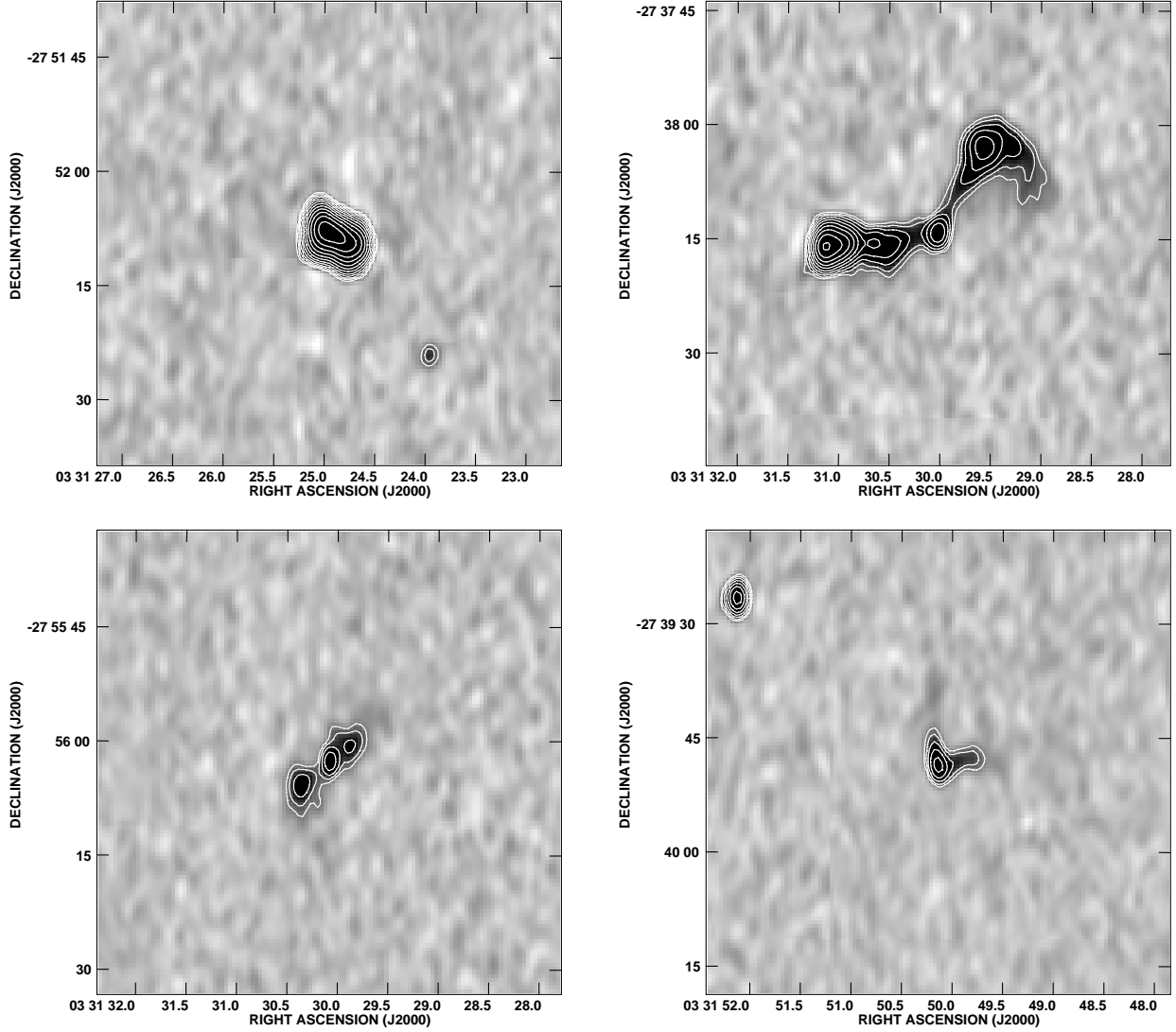


Figure 2.6: (*Continued*). *Top left*: Multiple-component source at 033124.9-275208, consisting of two blended components. *Top right*: Multiple-component source at 033130.0-273814, consisting of four components. These correspond to the core, the extended lobe to the northwest, and a pair of blended components comprising the eastern lobe. *Bottom left*: Multiple-component source at 033130.1-275603, consisting of three components (core, northwest and southeast lobes). *Bottom right*: Multiple-component source at 033150.1-273948, consisting of three components. The source has been deblended into a main component and an extension to the north, along with a third component extending to the west. The bright source at the northeast corner of the image is unrelated.

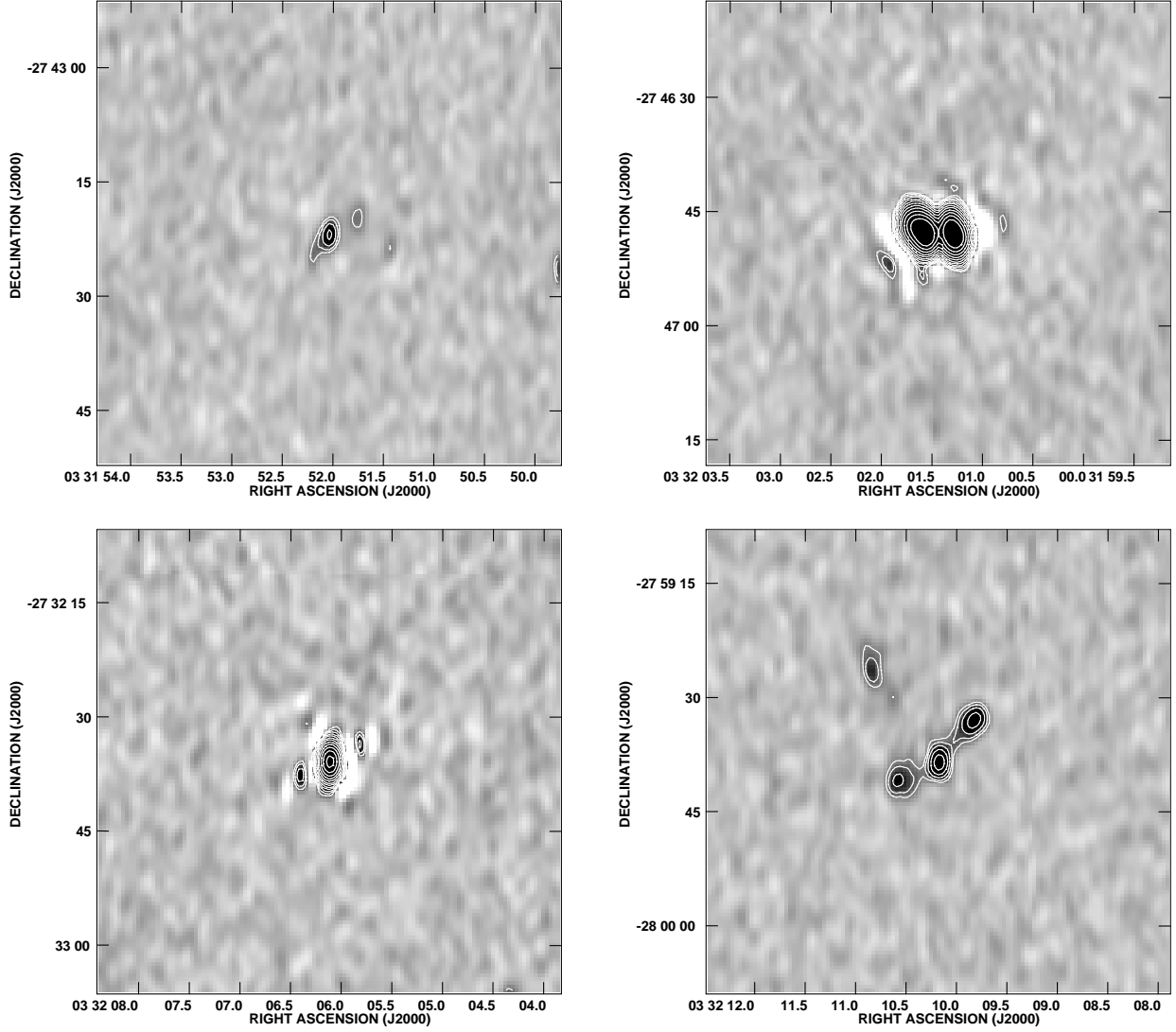


Figure 2.6: (*Continued*). *Top left*: Multiple-component source at 033152.0-274322, consisting of three components. The core has been deblended into a main core and an extension to the southeast, with the third component being the faint emission to the northwest. *Top right*: Multiple-component source at 033201.4-274648, consisting of a compact double with overlapping lobes to the east and west. *Bottom left*: Multiple-component source at 033206.1-273236. This is almost certainly a single bright (> 11 mJy) source with side lobes. The decreased dynamic range of the image is caused by this bright source lying near the northern edge of the mosaic image. *Bottom right*: Multiple-component source at 033210.2-275938, consisting of three components (core plus northwest and southeast lobes).

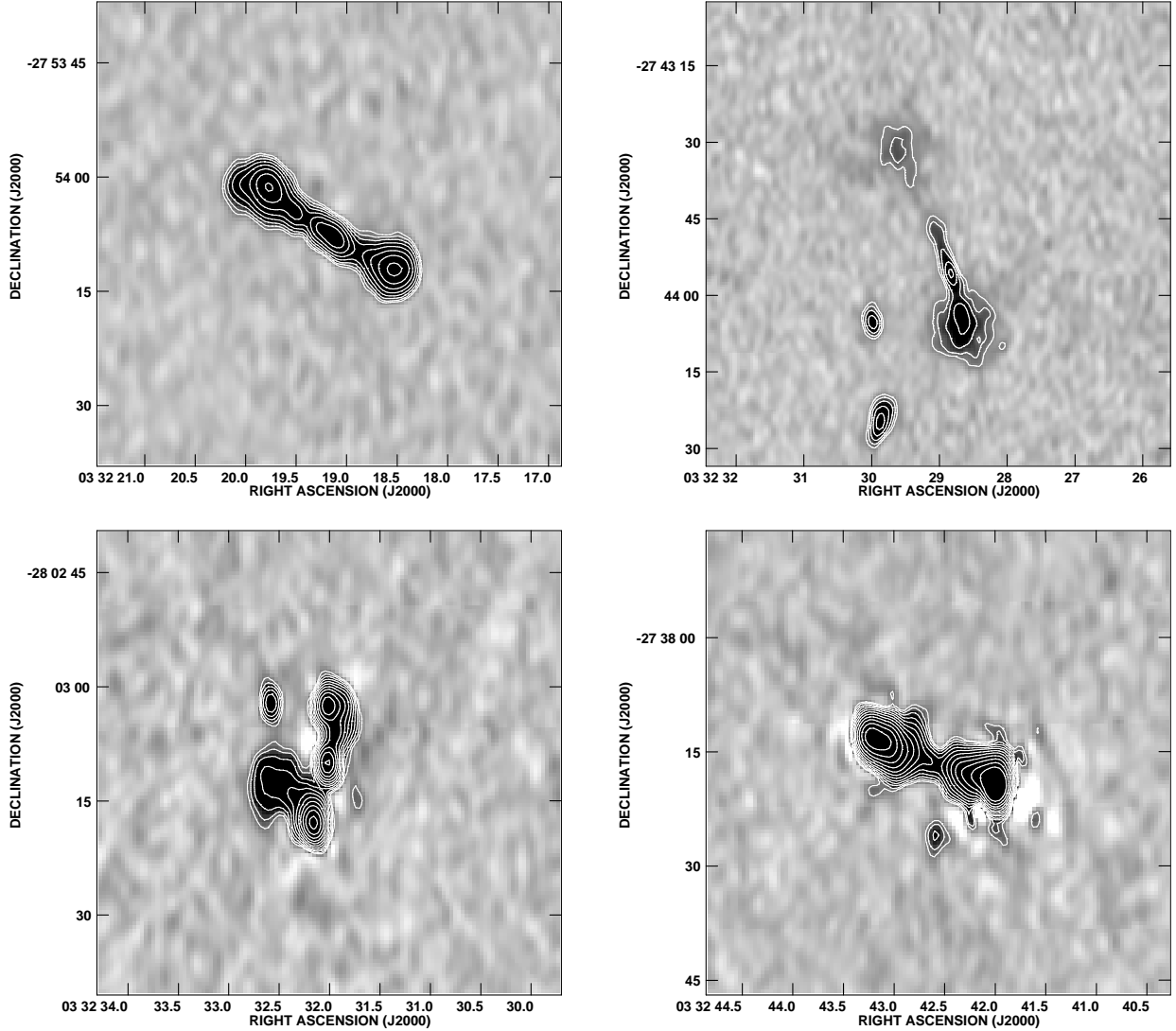


Figure 2.6: (*Continued*). *Top left*: Multiple-component source at 033219.2-275407, consisting of three components (core plus northeast and southwest lobes). *Top right*: Multiple-component source at 033228.8-274356, consisting of four components. This image is $1''.5$ by $1''.5$, and consists of a core, a component associated with the northern jet, the diffuse northern lobe, and the brighter southern lobe. Note that the pair of bright sources to the east and south are individual sources with counterpart identifications (Bonzini et al., 2012) and not components of this source. *Bottom left*: Multiple-component source at 033232.0-280310, consisting of four components. These are the core, the lobe to the north, and the lobe to the south deblended from its diffuse emission extending toward the east. The bright source just to the northeast is associated with a unique counterpart (Bonzini et al., 2012) and is thus unrelated to the multiple-component source. *Bottom right*: Multiple-component source at 033242.6-273816. This is the brightest radio source in the field and it consists of a pair of bright radio lobes. The apparent low-level structures at the edges of the source are imaging artifacts. The point source just to the south is associated with a separate galaxy, and is thus unassociated with this complex.

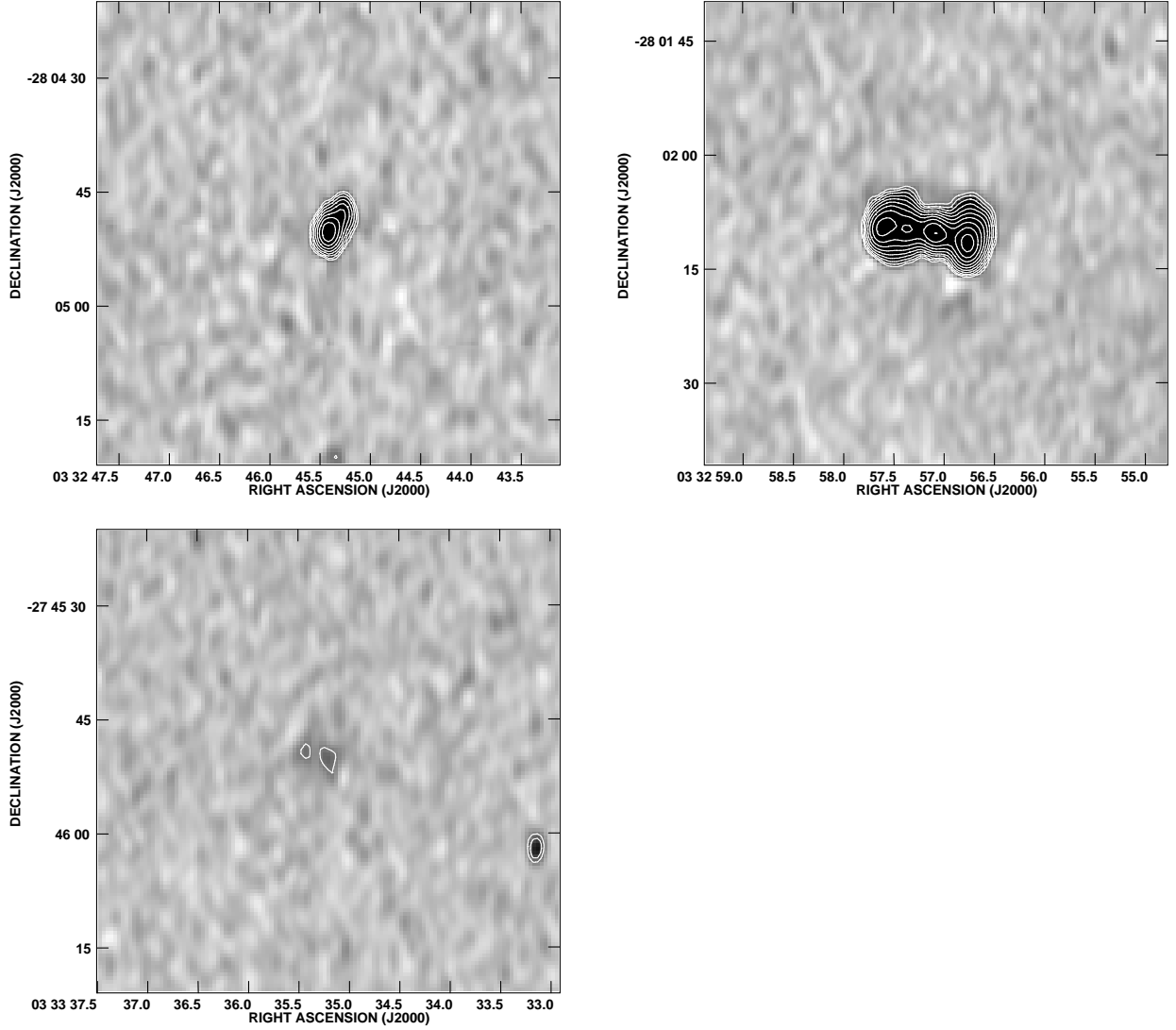


Figure 2.6: (*Continued*). *Top left*: Multiple-component source at 033245.4-280450, which has been deblended into a pair of components (core and extension to the northwest). *Top right*: Multiple-component source at 033257.1-280210, consisting of four components. These are a core, a western lobe, and the deblending of the eastern lobe into a pair of components. *Bottom*: Multiple-component source at 033335.2-274549, which has been deblended into a pair of faint components. These are both associated with disk emission in a spiral galaxy (Bonzini et al., 2012).

Chapter 3

Optical and infrared counterpart identification.

3.1 Introduction

*Published as **Bonzini, M.**; Mainieri, V.; Padovani, P.; Kellermann, K. I.; Miller, N.; Rosati, P.; Tozzi, P.; Vattakunnel, S.; Balestra, I.; Brandt, W. N.; Luo, B.; Xue, Y. Q., 2012, *Astrophysical Journal Supplement Series*, 203, 15*

Deep radio observations provide a powerful opportunity to investigate the high redshift Universe. Moreover, since radio observations are almost unaffected by dust extinction, they allow us to observe objects, which are heavily obscured in other bands. While bright radio sources are mostly powerful radio galaxies and radio-loud (RL) active galactic nuclei (AGN), at lower flux densities we observe an increasing fraction of star-forming galaxies (SFG) and radio-quiet (RQ) AGN (e.g., Padovani et al., 2009, and references therein).

Source classification of deep radio surveys is not easy and requires multi-frequency data. This approach was adopted in a series of papers, which studied a radio selected sample of 266 objects in the Chandra Deep Field South (CDFS; Kellermann et al., 2008; Mainieri et al., 2008; Tozzi et al., 2009; Padovani et al., 2009, 2011a). Combining the information from different wavelengths, these authors were able first to classify the sources as SFG, RQ AGN and RL AGN and then to study the properties and the evolution of the different classes separately. The promising results of this work have encouraged us to apply it to a new radio catalog (Miller et al., 2013) that reaches a lower flux density limit and has a more uniform coverage of the Extended-CDFS (E-CDFS). As a consequence, we have three times more objects, with most of the new sources in the sub-mJy regime (at 1.4 GHz).

This paper focuses on the identification of the optical and IR counterparts of the radio sources. Our main goal is to assign a redshift to the radio sources and to associate them with the correct photometry. This information will be then used in future papers to classify the sources and study their evolutionary properties. As mentioned above, a faint radio selected sample includes sources of widely different nature: SFG with a blue stellar

population together with radio galaxies commonly hosted in redder objects, and obscured AGN together with bright unobscured quasars. For this reason, it is important to consider a large wavelength range, from the ultraviolet to the mid-infrared (MIR). Faint radio sources often correspond to faint optical counterparts. Therefore, deep optical observations are needed. This has an impact on the methodology that should be adopted in the identification process.

The structure of the paper is as follows: in Section 3.2 we present the datasets, while in Section 3.3 we describe the likelihood ratio method we used to identify the counterparts of our sources and the results of the identification process, including an estimate of the spurious association fraction and a comparison with the cross-correlation method. Section 3.4 discusses the redshift distribution (spectroscopic and photometric) of our sample. In Section 3.5 we deal with the X-ray counterparts of the radio sources, while the description of the released catalog is given in Section 3.6. In Section 3.7 we discuss our results and report our conclusions. Finally, in Appendix 3.A we present new redshifts and spectra for the optical counterparts of 13 Very Large Array (VLA) sources and in Appendix 3.B we report on some peculiar sources. In this paper we use magnitudes in the AB system, if not otherwise stated, and we assume a cosmology with $H_0 = 70 \text{ km s}^{-1} \text{ Mpc}^{-1}$, $\Omega_M = 0.3$ and $\Omega_\Lambda = 0.7$.

3.2 Data

3.2.1 The radio catalog

The E-CDFS was observed at 1.4 GHz with the VLA between 2007 June and September (Miller et al., 2008). The mosaic image covers an area of about 34×34 arcmin with near-uniform sensitivity. The typical rms is $7.4 \mu\text{Jy}$ for a $2.8'' \times 1.6''$ beam. The second data release (Miller et al., 2013) provides a new source catalog with a 5σ point-source detection limit, for a total of 883 sources. We assigned a progressive identification number (RID) to the sources ordered by increasing right ascension. The flux density distribution of the sample is shown in Fig. 3.1, where we use the peak flux density or the integrated flux density according to the specifications of Miller et al. (2013). The median value of the distribution is $58.5 \mu\text{Jy}$ and the median signal to noise ratio (S/N) is 7.6. We note that $\sim 90\%$ of the sample has flux density below 1 mJy, a regime where RQ AGN and SFG become the dominant populations (e.g., Padovani et al. 2009, 2011a). A classification of the radio sources will be presented in Bonzini et al. (2013).

3.2.2 Auxiliary data

The E-CDFS is one of the most studied patches of the sky and has been observed in many wavebands. As we will discuss in the following sections, this wealth of data is crucial to select the correct counterpart of a radio source. Here we describe the large amount of optical and IR data used in this work. We considered a total of ten catalogs. The complete list is

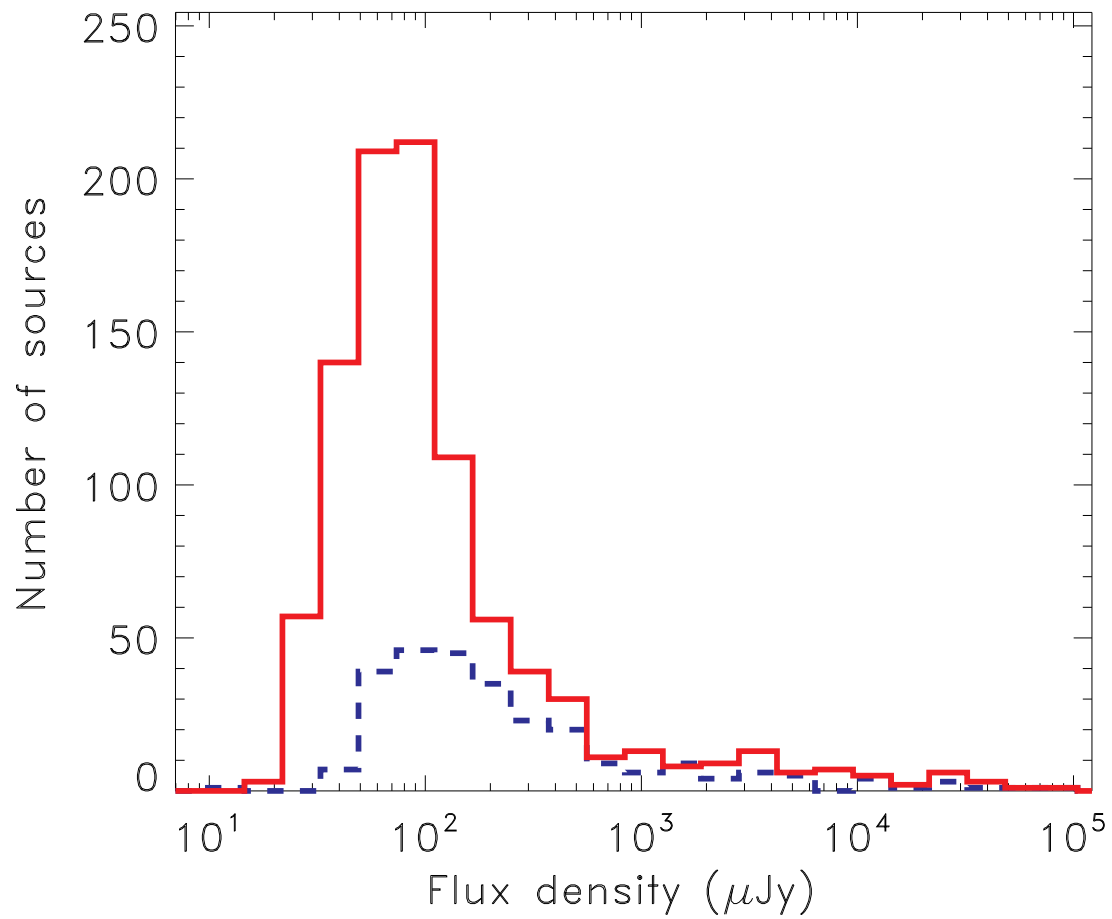


Figure 3.1: Flux density distribution of the 5σ E-CDFS radio catalog (solid line) compared to the sample described in Kellermann et al. (2008) (dashed line). The 5σ sample is about three times larger and the majority of the sources have sub-mJy flux densities.

reported in Table 3.1 together with some basic information: the instrument used (column 2), the effective wavelength (column 3), the typical point spread function (PSF) (column 4), the 5σ AB magnitude limit (column 5), and the total area covered (column 6). The latter is also shown in Fig. 3.2, where the footprint of each mosaic image is plotted over the VLA image. For details on the different data sets, we refer to the papers listed in column 7. We divide the auxiliary catalogs in three groups according to their selection band: optical, near-infrared (NIR) and mid-infrared (MIR). The first group includes U-VIMOS, v-GEMS, R-WFI, and z-GOODS. We note that the Wide Field Imager (WFI) observations are the only optical images covering the whole VLA area. Therefore, even if they are shallower than the others and with a lower spatial resolution, they were crucial in the identification process. The U-VIMOS catalog has been produced by us using the SExtractor software (Bertin & Arnouts, 1996) from the original images. In the NIR, we used the H-GNS, H-SOFI, Ks-MUSYC and Ks-ISAAC catalogs. The H-GNS data, consisting of 30 pointed observations, cover a very small area of the E-CDFS but have a better resolution compared to the ground-based observations. At longer wavelengths, the E-CDFS was mapped with the *Spitzer Space Telescope* as part of the SIMPLE and FIDEL surveys. These data are particularly useful to identify high redshift sources (see Sec. 3.4.4 for details).

Table 3.1: Auxiliary catalogs used for the identification of the radio sources counterparts. A description of the columns is given in Section 3.2.2.

	(1) Catalog ^a	(2) Instrument	(3) λ_{eff}^b (μm)	(4) PSF FWHM (arcsec)	(5) AB mag (5σ limit)	(6) Area (arcmin ²)	(7) References
Optical	U-VIMOS	VIMOS/ESO VLT	0.390	0.2	28.0	~ 800	Nonino et al. (2009)
	v-GEMS	ACS/ <i>HST</i>	0.578	0.1	28.5	~ 800	Rix et al. (2004)
							Caldwell et al. (2008)
	R-WFI	WFI/ESO 2.2m	0.654	0.8	25.5	> 1100	Giavalisco et al. (2004)
	z-GOODS	ACS/ <i>HST</i>	0.912	0.1	28.2	~ 160	Dickinson et al. (2003) Giavalisco et al. (2004)
NIR	H-GNS	NICMOS/ <i>HST</i>	1.607	0.2	26.5	~ 43	Conselice et al. (2011)
	H-SOFI	SOFI/ESO NTT	1.636	0.55	22.0	~ 800	Olsen et al. (2006)
	Ks-ISAAC	ISAAC/ESO VLT	2.745	0.4	24.7	~ 131	Retzlaff et al. (2010)
	Ks-MUSYC	ISPI/CTIO 4m	3.323	0.3	22.3	~ 900	Taylor et al. (2009)
MIR	IRAC-SIMPLE	IRAC/ <i>Spitzer</i>	3.507-4.436 ^c	1.7	23.8-23.6	> 1100	Damen et al. (2011)
	24um-FIDEL	MIPS/ <i>Spitzer</i>	23.209	6	20.2	> 1100	Dickinson & FIDEL Team (2007)

^a Name used in the text to refer to a specific catalog.

^b Filter effective wavelength.

^c The catalog is obtained from a combined image of $3.6\mu\text{m}$ and $4.5\mu\text{m}$ IRAC bands.

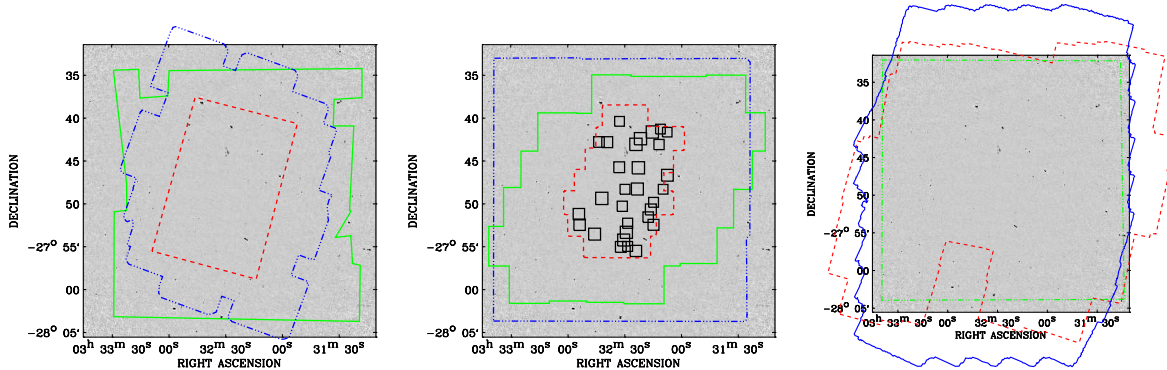


Figure 3.2: Multi-wavelength coverages overplotted on the VLA image. *Left:* Optical catalogs (from outside): v-GEMS (solid line), U-VIMOS (dot-dashed line), and z-GOODS (dashed line). The R-WFI catalog coverage exceeds the VLA image and therefore is not plotted. *Middle:* NIR catalogs (from outside): Ks-MUSYC (dot-dashed line), H-SOFI (solid line), Ks-ISAAC (dashed line) and H-GNS (small squares). *Right:* MIR catalogs: IRAC-SIMPLE (dashed line) and 24um-FIDEL (solid line). The dot-dashed line encloses the area with photometric redshift catalogs coverage (see Section 3.4).

3.3 Counterpart identification method

3.3.1 Likelihood ratio technique

The first step in the identification process consisted of registering each auxiliary catalog to the astrometric frame of the radio image, correcting for the median offsets between the radio and the auxiliary catalogs. An average number of 400 sources was used to perform this registration and the typical median offset is $0.2''$. As already mentioned, a simple cross-correlation method, where the counterpart is selected as the closest object to the radio source given a threshold matching radius, can lead to a large number of spurious association when dealing with deep optical images. Therefore, we adopted a likelihood ratio technique (e.g., Sutherland & Saunders, 1992; Ciliegi et al., 2003). This method allows us to take into account not only the position of the counterpart, but also the background source magnitude distribution and the presence of multiple possible counterparts for the same radio source. Here we briefly describe this technique following the formalism described in Ciliegi et al. (2003). It consists of three main steps:

- (a) Compute the surface density of background sources $n(m)$ as a function of magnitude m .
 - (b) Evaluate the likelihood ratio (LR) for each possible counterpart.
 - (c) Compute the reliability (rel) of each association.
- (a) The magnitude distribution of background sources is obtained by counting all the sources within a $30''$ radius around each radio object and dividing them in magnitude

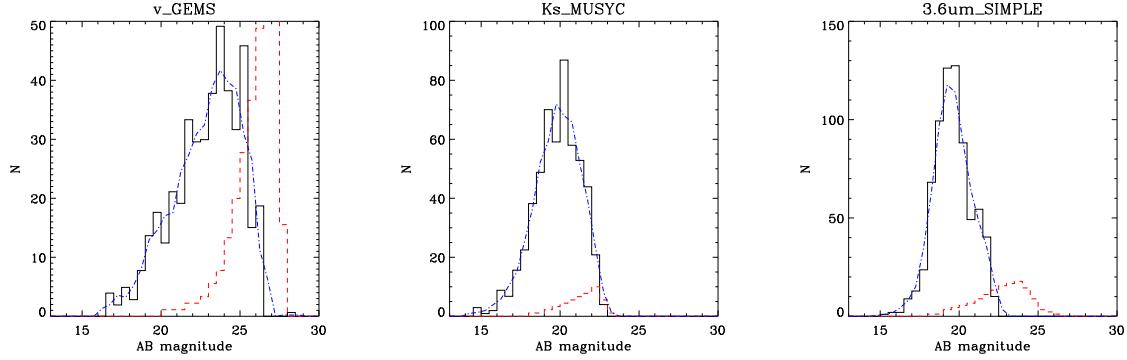


Figure 3.3: Background source distribution, $n(m)$, multiplied for the searching area $(\pi \times (2'')^2 \times N_{radio\ sources})$ (dashed line) and the background subtracted distribution of counterparts, $real(m)$, (solid line) for the v-GEMS catalog (on the left), the Ks-MUSYC catalog (in the middle) and the IRAC-SIMPLE catalog (on the right). The dotted dashed line is obtained by smoothing the $real(m)$ distribution and it is used to compute $q(m)$.

bins ($\Delta m = 0.5$). The size of the searching radius is set to contain, on average, just one radio source and a substantial number (>100) of background sources for the deep optical catalogs. The surface density of background objects $n(m)$ is then computed dividing the obtained distribution by the total searching area $(\pi \times (30'')^2 \times N_{radio\ sources})$.

(b) The likelihood ratio for a counterpart candidate is defined as the ratio between the probability that the source is the correct identification and the corresponding probability for an unrelated background source. Therefore we compute LR as:

$$LR = \frac{q(m)f(r)}{n(m)} \quad (3.1)$$

where $f(r)$ is the probability distribution function of the positional errors and $q(m)$ is the expected distribution of the counterparts as a function of m . As for $f(r)$ we adopt a two-dimensional Gaussian distribution of the form:

$$f(r) = \frac{1}{2\pi\sigma} \exp\left(\frac{-r^2}{2\sigma^2}\right) \quad (3.2)$$

where σ is the average between $\sigma_x = \sqrt{er_{aux}^2 + er_\alpha^2}$ and $\sigma_y = \sqrt{er_{aux}^2 + er_\delta^2}$. er_α and er_δ are the radio positional errors given by the beam size (1.6×2.8 arcsec) divided by two times the S/N ratio of the considered source. To account for further uncertainties on the VLA position, we added in quadrature $0.1''$ to the radio positional error (Miller et al., 2013). The average positional error er_{aux} for the optical catalog is $0.1''$ and $0.3''$ for the others, with the exception of H-GNS ($er_{aux} = 0.2''$) and $24\mu\text{m}$ -FIDEL ($er_{aux} = 0.6''$) (see references given in Table 3.1). To derive an estimate for $q(m)$, we first counted all the objects in the auxiliary catalog within a radius of $2''$ around each radio source. Then, we subtracted the distribution of background objects computed on the same area ($n(m) \times \pi \times (2'')^2 \times N_{radio\ sources}$). The latter is shown in Fig. 3.3 (dashed line), from left to right, for an optical, NIR and MIR

catalog, respectively. The background subtracted distribution, $real(m)$, is plotted in the same figure as a solid line. Finally, we normalized the distribution function as:

$$q(m) = \frac{real(m)}{\sum_i real(m)_i} \times Q \quad (3.3)$$

where the sum runs over the total number of objects in the $real(m)$ and Q represents the probability that the real counterpart is above the catalog detection limit. As already verified by Ciliegi et al. (2003) and Mainieri et al. (2008), the number of identifications and the associated reliabilities have a mild dependence on Q . Therefore, we adopted a fixed value $Q = 0.8$ for all the auxiliary catalogs as it corresponds to the average expected fraction of identifications. Finally, combining $q(m)$, $f(r)$ and $n(m)$ according to eq. 3.1, we computed the LR for each source in the auxiliary catalogs.

(c) The LR does not contain information about the possible presence of many counterpart candidates in the surrounding of a specific radio source. It is therefore useful to define the reliability of each association as (Sutherland & Saunders, 1992):

$$rel_j = \frac{(LR)_j}{\sum_i (LR)_i + (1 - Q)} \quad (3.4)$$

where the sum is over all the candidate counterparts for the same radio source.

3.3.2 Identification results

Following the method described in the previous section, we built a list of possible counterparts for each auxiliary catalog. Initially, we set a very low likelihood threshold (10^{-6}) to be sure not to lose any counterpart. After a careful analysis, we decided to consider as reliable only counterparts with reliability greater than 0.6. This threshold ensures that the expected number of spurious associations is below 5% for each auxiliary catalog (see Section 3.3.5), and at the same time maximizes the number of identified sources. The identification rate for each auxiliary catalog is reported in column (3) of Table 3.2. The number of identified sources is weighted by the number of radio sources inside the area covered by each survey reported in column (2). We note that the number of identifications increases with wavelength, from $\sim 65\%$ in the optical catalogs up to 87% in the MIR. That means that most of the radio sources have a counterpart candidate in more than one auxiliary catalog, and that there is a fraction of sources that are not detected in the optical but only in the IR. In more detail, there are 652 radio sources (74%) that have a counterpart in at least one of the four optical catalogs, 76 (9%) that have no counterpart in any of the optical catalogs, but that are identified in at least one of the NIR catalogs, and 111 (12%) that have a counterpart only in the MIR. We will refer to these three groups as optical, NIR and MIR selected counterparts, respectively. We anticipate that they have different redshift distributions, with NIR and MIR selected sources having on average higher redshift (see Section 3.4.4). High redshift objects, thanks to their positive K-correction, are more easily observed in the IR than in the optical and this explains the higher identification rate observed in the MIR catalogs.

Table 3.2: Counterparts identified in each catalog and spurious association estimate for both the likelihood and cross-correlation methods. In column 2 we report the number of radio sources inside the area of the survey (see Fig. 3.2).

		LR method			cross-correlation	
(1)	(2)	(3)	(4)	(5)	(6)	(7)
Catalog	Radio sources	% counterparts (#)	90% inside ^a (arcsec)	% spurious	% counterparts (#)	% spurious
Optical	U-VIMOS	64% (347)	0.7	5%	64% (346)	12%
	v-GEMS	67% (432)	0.7	5%	67% (435)	11%
	R-WFI	68% (600)	0.7	3%	67% (587)	6%
	z-GOODS	65% (107)	0.5	4%	58% (95)	6%
NIR	H-GNS	70% (24)	0.5	<1%	62% (21)	6%
	H-SOFI	69% (363)	0.7	2%	65% (339)	1%
	Ks-ISAAC	81% (109)	0.7	4%	76% (102)	3%
	Ks-MUSYC	77% (556)	0.7	3%	71% (515)	1%
MIR	IRAC-SIMPLE	87% (746)	0.7	3%	79% (674)	3%
	24um-FIDEL	85% (745)	1.1	4%	79% (692)	2%

^a Radius within 90% of the counterparts are included.

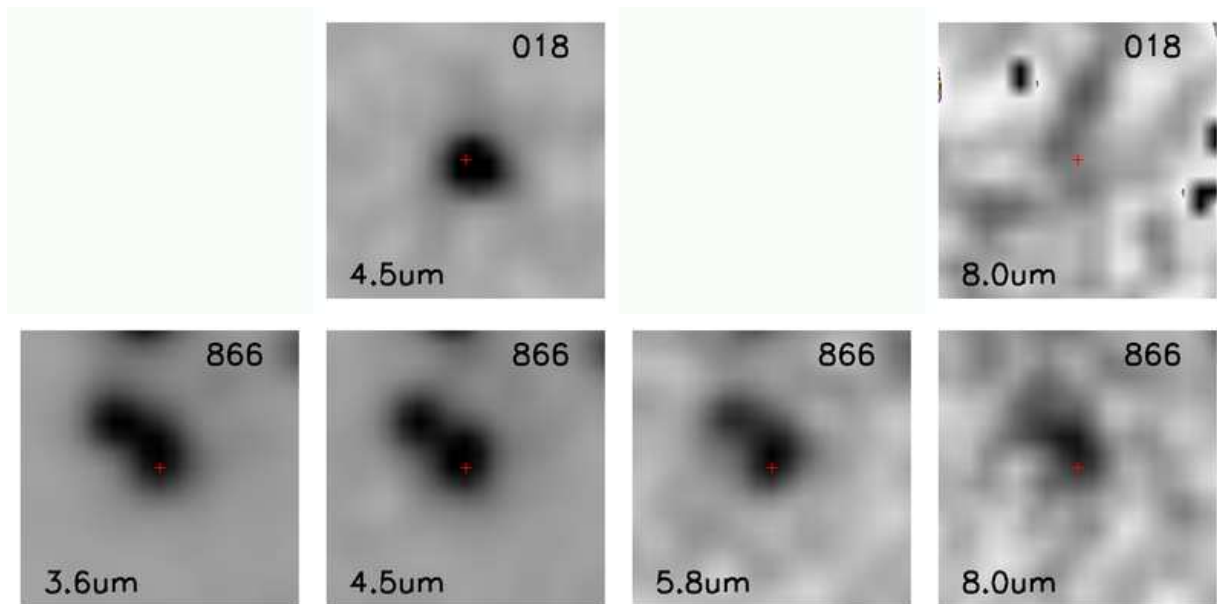


Figure 3.4: *Spitzer*/IRAC images of objects RID 018 (top) and 866 (bottom). They represent examples of IRAC sources not present in the SIMPLE catalog whose position has been manually extracted (see Section 3.3.4 for details): RID 018 has been observed only in two of the four channels, and RID 866 is blended by a nearby source. The position of the radio source is marked by a cross. Each image is 10 arcsec on a side.

Table 3.3: Radio information and identification process results. A description of the table content is given in Section 3.6. (This Table is available in its entirety in a machine-readable form in the online journal. A portion is shown here for guidance regarding its form and content.)

(1) RID	(2) RA radio (J2000)	(3) Dec radio (J2000)	(4) Sr (μ Jy)	(5) S/N	(6) RA counterpart (J2000)	(7) Dec counterpart (J200)	(8) Reliability	(9) Distance (arcsec)	(10) Counterpart catalog
360	3:32:13.09	-27:43:50.9	1380.0 \pm 26.6	115.8	—	—	—	—	unidentified
361	3:32:13.24	-27:40:43.7	58.9 \pm 6.4	9.0	03:32:13.24	-27:40:43.39	0.97	0.2	R-WFI
362	3:32:13.25	-27:42:41.3	86.4 \pm 6.4	13.5	03:32:13.25	-27:42:40.86	1.00	0.2	z-GOODS
363	3:32:13.36	-27:39:35.2	48.5 \pm 6.9	7.0	03:32:13.32	-27:39:35.03	1.00	0.2	24 μ m-FIDEL
364	3:32:13.41	-27:33:04.9	48.4 \pm 7.8	6.2	03:32:13.39	-27:33:04.93	0.97	0.3	R-WFI
365	3:32:13.50	-27:49:53.1	44.0 \pm 6.4	6.9	03:32:13.48	-27:49:52.82	1.00	0.1	z-GOODS
366	3:32:13.61	-27:34:04.3	102.6 \pm 18.5	8.3	03:32:13.58	-27:34:04.37	1.00	0.4	R-WFI
367	3:32:13.65	-28:01:01.2	35.7 \pm 6.9	5.1	03:32:13.62	-28:01:01.06	1.00	0.3	v-GEMS
368	3:32:13.85	-27:56:00.3	44.5 \pm 6.4	6.9	03:32:13.85	-27:55:59.95	1.00	0.2	24 μ m-FIDEL
369	3:32:14.17	-27:49:10.6	95.4 \pm 6.4	14.9	03:32:14.14	-27:49:10.09	0.98	0.4	U-VIMOS
370	3:32:14.46	-27:45:40.8	34.9 \pm 6.2	5.6	03:32:14.43	-27:45:40.72	1.00	0.3	z-GOODS
371	3:32:14.60	-27:43:05.8	32.1 \pm 6.4	5.0	03:32:14.60	-27:43:06.10	9.00	0.3	manual
372	3:32:14.69	-28:02:20.2	44.9 \pm 7.1	6.0	03:32:14.65	-28:02:19.97	1.00	0.4	v-GEMS
373	3:32:14.85	-27:56:40.9	109.7 \pm 6.5	16.9	03:32:14.83	-27:56:40.49	1.00	0.2	v-GEMS
374	3:32:15.17	-28:05:22.7	50.8 \pm 7.9	6.3	03:32:15.14	-28:05:22.24	1.00	0.3	R-WFI
375	3:32:15.34	-27:50:37.6	43.1 \pm 6.4	6.7	03:32:15.32	-27:50:37.25	1.00	0.1	H-GNS

In Table 3.3, we report the complete list of the counterparts of the radio sources (see Section 3.6). The counterpart position is taken from an optical catalog, when available, since these observations have the highest spatial resolution. In particular, we chose the catalog in which the counterpart has the highest reliability. According to this criterion, we selected 104 counterparts from U-VIMOS, 150 from v-GEMS, 301 from R-WFI, and 96 from z-GOODS. If there was no optical counterpart above the reliability threshold, we used the coordinates of the most reliable counterpart found in the NIR catalogs. This happened for 4 sources from H-GNS, 24 from H-SOFI, 4 from Ks-ISAAC, and 47 from Ks-MUSYC. For the remaining counterparts, we used the position from the IRAC-SIMPLE catalog (25 sources) and from the 24 μ m-FIDEL one (74 sources). Finally, there are 10 radio sources (RID: 18, 19, 36, 371, 430, 457, 463, 698, 795, and 866) whose counterpart is clearly visible in the IRAC images but is not listed in the SIMPLE catalog (or in any other catalog). The reason is that, since the SIMPLE catalog is extracted from the combined 3.6 and 4.5 μ m images, either the source was observed only in the first or the second IRAC channel and therefore not included in the catalog, or it was not deblended from a nearby object (see Fig. 3.4). In these cases we have extracted the position of the counterpart from the IRAC image.

As a further check, we extracted 10 \times 10 arcsec cutouts centered at the radio source position of the images in the various bands, to visually inspect the counterpart associations. Examples are presented in Fig. 3.5 where the position of the radio source and of its counterpart are marked by a cross and a square, respectively. In the left panels, radio contours are plotted over a 20 \times 20 arcsec R band image, after the latter has been registered on the astrometric frame of the radio image. This larger size is chosen for a better view of the radio contours. In most cases the selected counterpart is clearly visible in one or more cutouts. In 12 cases, we found a more convincing counterpart and therefore we revisited the association; these cases are discussed in more details in Section 3.3.4.

A total of 44 sources are unidentified: most of them are either very faint radio sources or lie at the edge of the field, where the multi-wavelength coverage is less rich. They are blank fields in all the available images (see, e.g., RID 360 in Fig. 3.5). We expect only few of them to be spurious radio detections since the radio catalog is based on a mosaic image and therefore each object was observed by more than one pointing (Miller et al., 2013). If an object were spurious and due to instrumental effects (e.g., a sidelobe of a nearby bright source) it would not be the same in each pointing. Similarly, if it were just a chance noise spike you would expect to see it in only one pointing. Therefore we perform source fits in the individual pointings for the unidentified radio sources with low S/N and we believe that the radio detections are real, with one or two possible exceptions.

In summary, we found a reliable counterpart for 839 out of 883 radio sources (95%).

3.3.3 Multiple component radio systems

A multi-wavelength approach is crucial to identifying multiple-component systems. Indeed, the analysis of the radio morphology alone cannot distinguish between pairs of radio sources which are close in projection, or physically connected radio components of the same source.

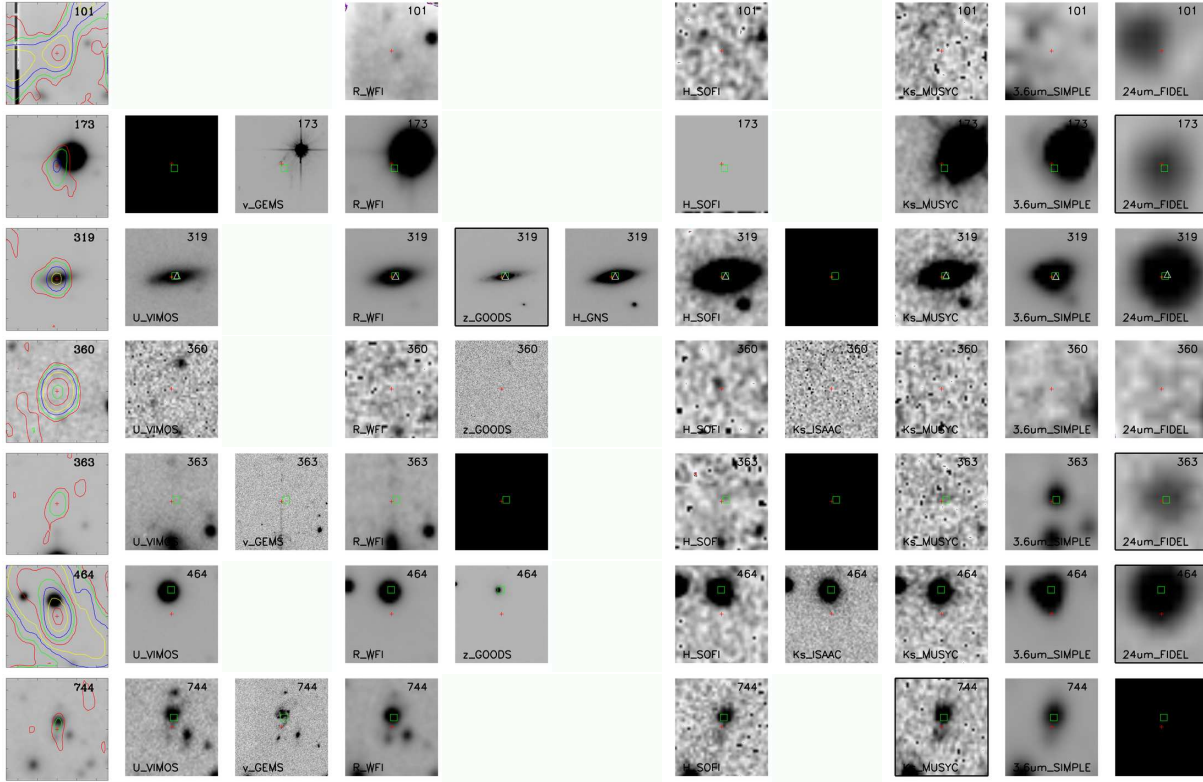


Figure 3.5: *Left panels:* radio contours plotted over a 20×20 arcsec R band image. The RID is shown on the top right of each image. *Other panels:* cutouts of the images in the various bands centered at the position of the radio source (marked by a cross). Each image is 10 arcsec on a side. The corresponding catalog is indicated on the bottom left. The square indicates the position of the selected counterpart. The image from which the counterpart is selected has a black border.

In our sample there are 24 systems, whose radio morphology can be interpreted as multi-component radio sources. Their radio contours are plotted over the R image in Fig. 3.6.

We perform the likelihood ratio analysis described in Section 3.3.1 to look for a possible counterpart of each single radio component. For seven such systems (panels (d), (i), (n), (o), (p), (s), (u) in Fig. 3.6), we find highly reliable counterparts for each component. Therefore, we claim that they represent distinct sources. The other 17 are confirmed to be multiple-component systems. They have extended radio emission, in most of the cases characterized by a core (not always visible in the radio) and radio lobes. The radio lobes have usually comparable radio power and are not associated with any optical or IR counterpart. There are some cases where we cannot exclude a possible contribution to the radio flux density from a superimposed unrelated object like in sources with RID 38, 73, 209, 283, and 647. The complete list of these system with the properties of each radio component is given in Miller et al. (2013). In Appendix 3.B we discuss some peculiar sources.

3.3.4 Revisited associations

In section 3.3.1, we described our method to select the optical and IR counterpart for the radio sources using a likelihood ratio technique. Visually inspecting the results of the identification process, we confirm the association obtained following this procedure in 99% of the cases. In this section, we describe the reasons why we revisited the counterpart association for some peculiar sources. In these cases, the most likely counterpart has a reliability under our threshold and was therefore rejected. The two main reasons for this are: (i) the radio source is in a crowded field and therefore all the possible counterparts have low reliability (RID 70, 407, 417, 458, 561, and 797). We based our choice of the counterpart on the radio morphology and on the overall object properties in the various bands (as an example, see the notes on RID 407 in Appendix 3.B). (ii) The radio source is extended, hence the exact position of the radio emission is not well determined or does not correspond to the optical/IR peak emission (RID 407, 420, 521, 804, 828, and 830). As a consequence, there is an offset between the position of the radio source and the counterpart that has therefore a low reliability.

3.3.5 Estimation of spurious associations and comparison with the cross-correlation method

For each auxiliary catalog, we estimate the rate of spurious associations by randomly shifting the position of the radio sources and computing again the reliability for all the possible counterparts. We apply only shifts between 5 and 15 arcsec in order not to exceed the field coverage. We then compute the likelihood ratio value for each one of the shifted sources using equation 3.1, where $q(m)$ and $n(m)$ are the probability distributions derived for the original catalog (see Section 3.3.1). The same reliability threshold of 0.6 is adopted. The average fraction of false association over 50 different shifts is reported in Table 3.2 for

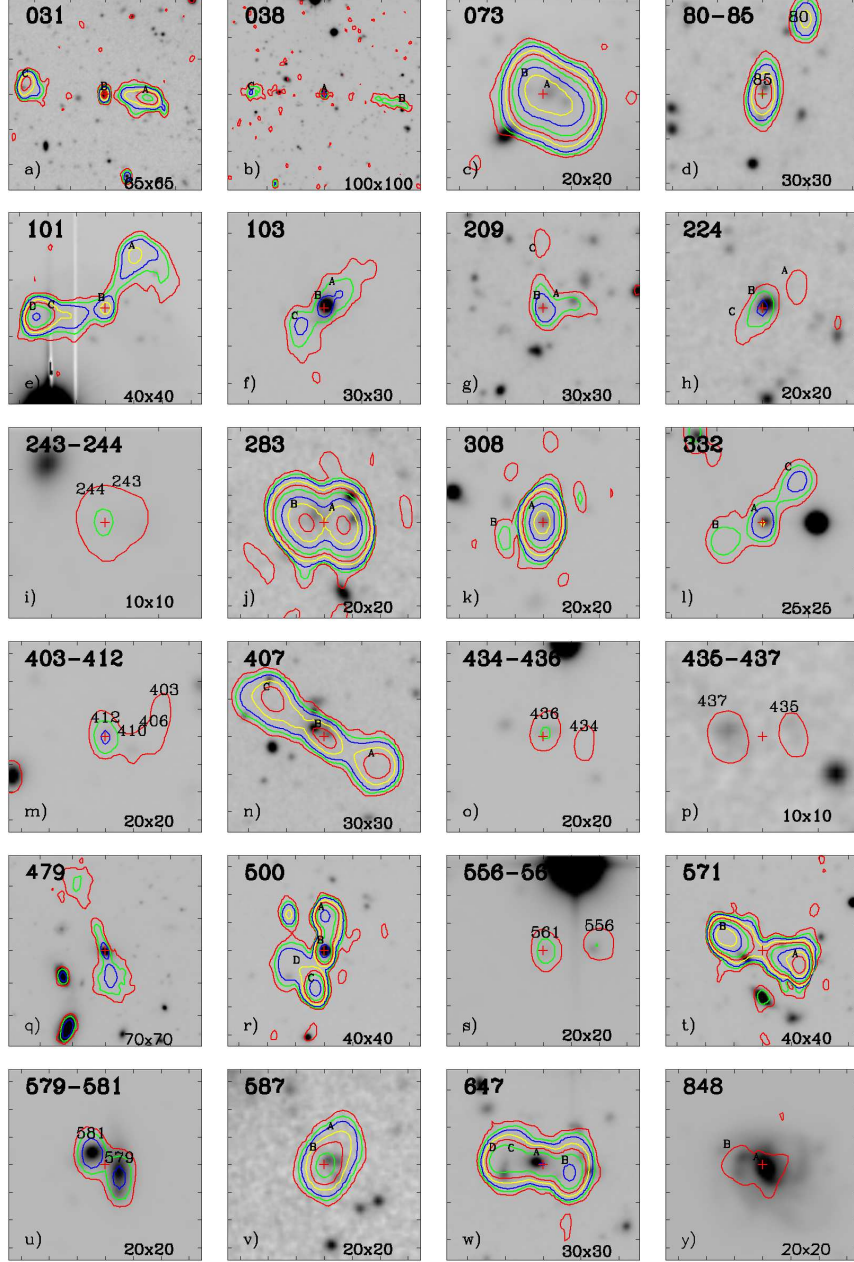


Figure 3.6: Cutouts of radio sources with complex radio morphology. The majority of them (17/24) are confirmed as multiple-component system, while for the remaining we find reliable counterparts for each radio component (see Section 3.3.3 for details). Radio contours are plotted over the R band WFI image. The scale of the cutout is given in arcsec on the bottom right and the RID on the top left.

each auxiliary catalog. We find spurious fractions from 3% up to 5% for the deep optical catalogs. In the case of H-GNS the fraction is very low but it could be underestimated due to the small area covered by this catalog and the consequent small statistics.

We compare these results with the number of spurious associations obtained using a simple cross-correlation method. The matching radius chosen for this test is equal to the radius which includes 90% of the counterparts identified with the likelihood-ratio method. These radii are listed in column (4) of Table 3.2. We find that the two methods identify a similar fraction of sources for the optical catalogs and a somewhat lower one for the IR catalogs. We estimate the fraction of spurious associations similar to what has been done for the likelihood method, namely shifting the radio catalog with respect to the auxiliary one. We used the same set of displacements as in the previous case. As shown in Table 3.2, our likelihood ratio technique is generally less affected by spurious contamination especially when applied to the deep optical catalogs. In particular, in the cases of the U-VIMOS and v-GEMS catalogs the spurious fraction exceeds 10% with the cross-correlation method. If we decrease the searching radius from 0.7 to 0.5 arcsec for all the optical catalogs, the fraction of false counterparts becomes lower (8%, 7%, 3%, for the U-VIMOS, v-GEMS and R-WFI catalogs, respectively), but we also miss a significant fraction of real identification (19%, 23% and 14%, respectively). For NIR and MIR catalogs, the two methods are almost equivalent. We obtain slightly higher fractions of fake associations with the likelihood ratio technique but with the cross-correlation method we miss a larger number of counterparts. This is mainly due to the lower source surface density with respect to the optical catalogs. We note that the shift-and-rematch method tends to overestimate the number of false matches as it ignores the fact that there are a large fraction of the sources that do have counterparts (see Bross et al., 2007; Broos et al., 2011; Xue et al., 2011, for details.). Our estimates should therefore be considered as upper limits. Since this effect is the same both for the likelihood and the cross-correlation method, it does not affect our conclusions. Finally, we assume that the fraction of spurious association in the final catalog is equal to the weighted average of the spurious fraction of each catalog, using the number of counterparts selected from each catalog as weight. We then expect at most 4% spurious counterparts.

3.3.6 Comparison with previous work

The brighter sources of the present catalog were already included in the radio catalog described in Kellermann et al. (2008). We have compared the counterparts found in Mainieri et al. (2008) (M08, hereafter) with those selected in this work for the sources in common. We find that in 90% of the cases the same counterpart is selected. For the remaining 10%, we select a different counterpart compared to M08. In most cases the counterparts were identified in the optical band by M08 while we find a more convincing counterpart in newly acquired MIR observations. For eight out of twelve objects that were unidentified or under the threshold in M08, we now have a reliable counterpart. One example is RID 625 (ID in the Kellermann et al. (2008) catalog KID=202) that was in an empty field in M08 while we identify it at 24 μm . The criteria to identify the best

counterpart candidate of a radio source are slightly different between the two works. In M08 a likelihood ratio threshold of 0.2 was adopted, while we use a cut in reliability to take into account the presence of multiple counterpart candidates of the same radio source. Our reliability threshold of 0.6 is a bit more conservative (it correspond to a LR threshold of ~ 0.3) and it is aimed at reducing the number of spurious identifications. Another difference between the two works is that in M08 the best counterpart was chosen according to an a priori ranking of the auxiliary catalogs. The priority was set according to the depth of the optical/NIR survey and to the wavelength. Given the larger number of auxiliary catalogs used in this work we use a different approach: between catalogs in the same wavelength range (optical, NIR and MIR), we select the counterpart with the highest reliability (see Section 3.3.1). This allows us to fully exploit the information given by the probability distributions obtained with the likelihood ratio technique. Moreover, we minimize the number of tentative associations selected in a high priority optical/NIR catalog yet with a reliability just above the threshold. As a consequence, with our new approach 90% of the counterparts have a reliability greater than 0.96, in contrast to 0.83 obtained in M08 (see Fig. 4 in M08). Moreover, we observe a significant decrease in the average separation between the radio source and its counterpart compared to M08. In this work, we find 90% of the counterparts within 0.7 arcsec around the radio position, which is about half of the radius found in M08 (see Fig. 3.7). This is partially due to the change in resolution of the two radio surveys (from $3.5'' \times 3.5''$ in Kellermann et al. (2008) to $2.8'' \times 1.6''$ in this work).

In summary, using the new MIR imaging in the E-CDFS area, we reach the same fraction of identification (95%) as in M08, although we adopt a higher reliability threshold and a larger fraction of the radio sources is in the outer part of the field, where the multi-wavelength coverage is poorer. There is only one source previously identified that we now consider unidentified: RID 101 (see details in Appendix 3.B).

3.4 Redshift associations

3.4.1 New VIMOS spectra and redshifts

We acquired new optical spectra with the Visible Multi-Object Spectrograph (VIMOS; Le Fèvre et al., 2004) at Very Large Telescope (VLT). We carried out one pointing in the central region of the VLA survey using the low-resolution (LR) blue grism ($R=180$, dispersion= $5.7 \text{ \AA pixel}^{-1}$) that covers the wavelength range 3700-6700 \AA . The total exposure time of five hours was set to identify faint optical counterparts to a limiting point-source magnitude of $R \approx 25$. The mask was designed with the VIMOS Mask Preparation Software (VMMPS; Bottini et al., 2005) that optimizes the slit assignments based on our input catalog. We observed a total of 32 VLA sources. The data were reduced using the VIMOS Interactive Pipeline and Graphical Interface (VIPGI; Scodreggio et al., 2005), and the redshifts were estimated using the EZ¹ software that cross-correlates each spectrum

¹<http://cosmos.iasf-milano.inaf.it/pandora/EZ.html>

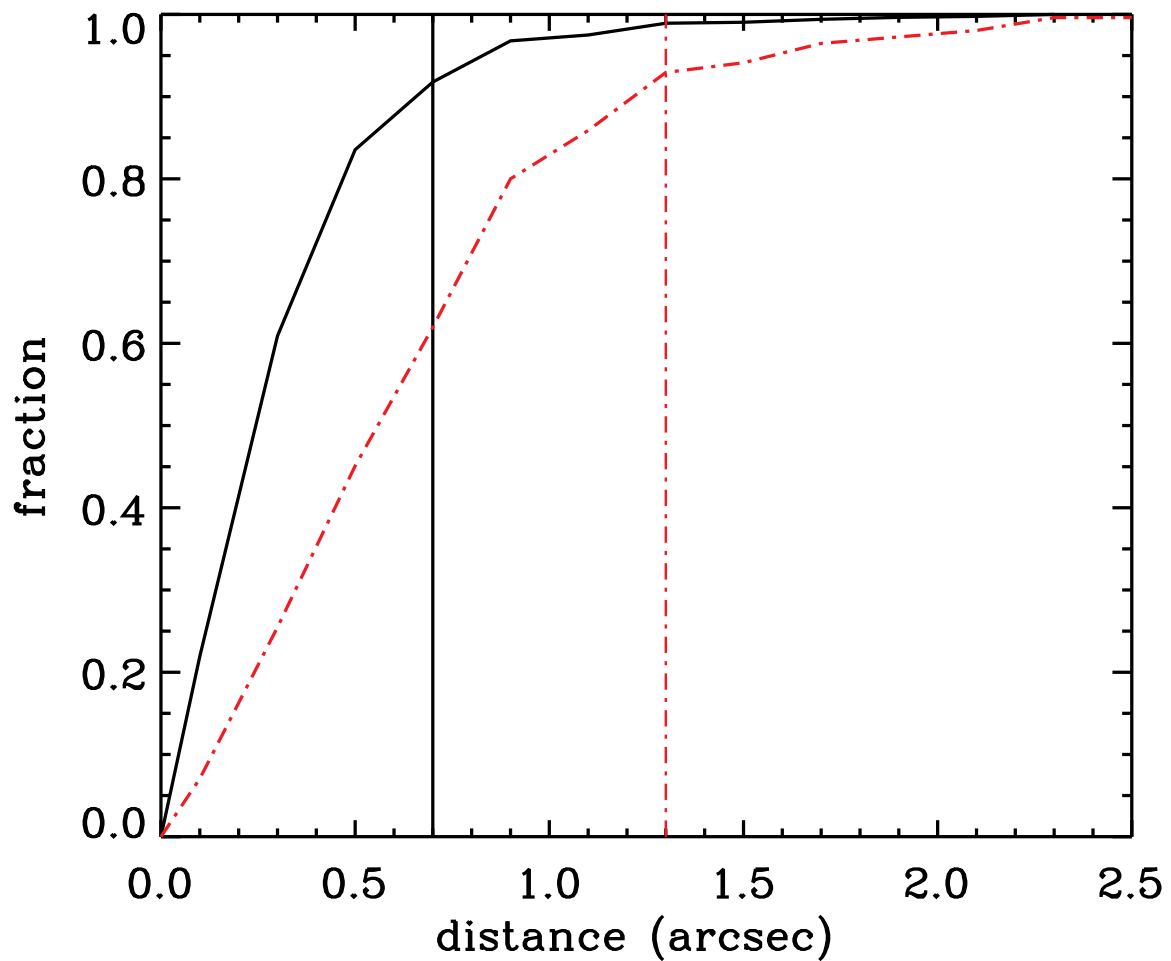


Figure 3.7: Cumulative distribution of the separation between a radio source and its counterpart for the radio catalog presented in this work (solid line) and in Mainieri et al. (2008) (dot-dashed line). The vertical lines mark the separation within 90% of the counterparts are located.

Table 3.4: List of the spectroscopic catalogs considered in this work. The instrument used to obtain the spectra is reported in column (2) and details on the observation and data reduction can be found in the references given in the first column. The label in column (3) are used in the final catalog to identify the source for the spectroscopic redshift. The last column reports the number of spectroscopic redshift adopted from each catalog in this work.

(1)	(2)	(3)	(4)
Reference	Instrument	Label	Number of z-spec adopted
This work	VIMOS	P81	13
Szokoly et al. (2004)	FORS1/FORS2	S04	38
Vanzella et al. (2008)	FORS2	FORS	20
Silverman et al. (2010)	VIMOS	VJB	37
Silverman et al. (2010)	VIMOS	P80	3
Silverman et al. (2010)	Keck	K07	32
Silverman et al. (2010)	Keck	K08	18
Treister et al. (2009)	VIMOS	T09	20
Balestra et al. (2010)	VIMOS-LR	VLR	24
Balestra et al. (2010)	VIMOS-MR	VMR	23
Le Fèvre et al. (2004)	VIMOS	VVDS	19
Ravikumar et al. (2007)	VIMOS	R07	12
Szokoly et al. (2004)	FORS1/FORS2	S04F	1
J. Kurk et al., 2012 (Submitted)	FORS2	GMASS	4
Norris et al. (2006)	2dF	N06	10

with a template spectrum, and via visual inspection to validate the result. We derived a spectroscopic redshift for 13 VLA sources for which previously we had only a photometric redshift estimate. The spectra of these 13 radio sources are shown in Appendix 3.A.

3.4.2 Spectroscopic redshifts

Many spectroscopic campaigns have been conducted in the E-CDFS. A complete reference list for those used in this work can be found in Table 3.4. We combine the publicly available redshifts with our own newly acquired spectra (see Sec. 3.4.1). We assign a quality flag (QF) to each redshift by mapping the ones in the original catalogs to a uniform scale. We use QF=3 to indicate a secure redshift, QF=2 for reasonable redshift, and QF=1 for tentative redshift or for single line detection. The coordinates of the counterparts, identified as described in Sec. 3.3.1, are cross-correlated with the sources reported in the spectroscopic catalogs within 0.2 arcsec. Such a small radius is chosen to minimize the confusion with nearby sources. We find a spectroscopic redshift for 274 sources. If a source has a match in more than one spectroscopic catalog, we verify the consistency between the corresponding redshifts. For 22 sources, multiple spectroscopic redshifts differ by more than 0.1. In all but three of these cases, the QF of the spectroscopic measurements allows us to select the highest quality z . For sources RID= 83, 569, and 706, where the QF in the various spectroscopic catalogs are equivalent, we visually checked the spectra to select the more reliable redshift value. The spectroscopic redshift associated with each radio source is reported in the column 7 of Table 3.5, with the QF, and the reference in columns 8 and 9, respectively. In summary, 33% of the radio sources with counterpart have a spectroscopic redshift, 74% of which are secure redshift (QF=3), 18% have QF=2 and 8% have a tentative redshift measurement (QF=1).

3.4.3 Photometric redshifts

In order to increase the redshift completeness of our sample, we also use photometric redshift estimates. We use the photometric redshift catalog compiled by Luo et al. (2010) and Rafferty et al. (2011). These redshifts are based on a large number of photometric bands: the COMBO-17 optical catalog (Wolf et al., 2004, 2008), the GOODS-S MUSIC catalog (Grazian et al., 2006), the MUSYC BVR-detected catalog (Gawiser et al., 2006), the deep GOODS-S VIMOS U-band catalog (Nonino et al., 2009), the GALEX Data Release 4², the MUSYC near-infrared catalogue (Taylor et al., 2009), and the SIMPLE mid-infrared one (Damen et al., 2011). Starting from this photometric data set, the publicly available Zurich Extragalactic Bayesian Redshift Analyzer (ZEBRA; Feldmann et al., 2006) code was used to derive photometric redshifts via a maximum likelihood technique. The set of templates used includes: 259 galaxy templates constructed from PEGASE stellar population synthesis models, a set of hybrid (galaxy+AGN) templates and ten empirical AGN templates from Polletta et al. (2007). We refer the reader to Luo et al. (2010) and Rafferty et al.

²<http://galex.stsci.edu/GR4/>

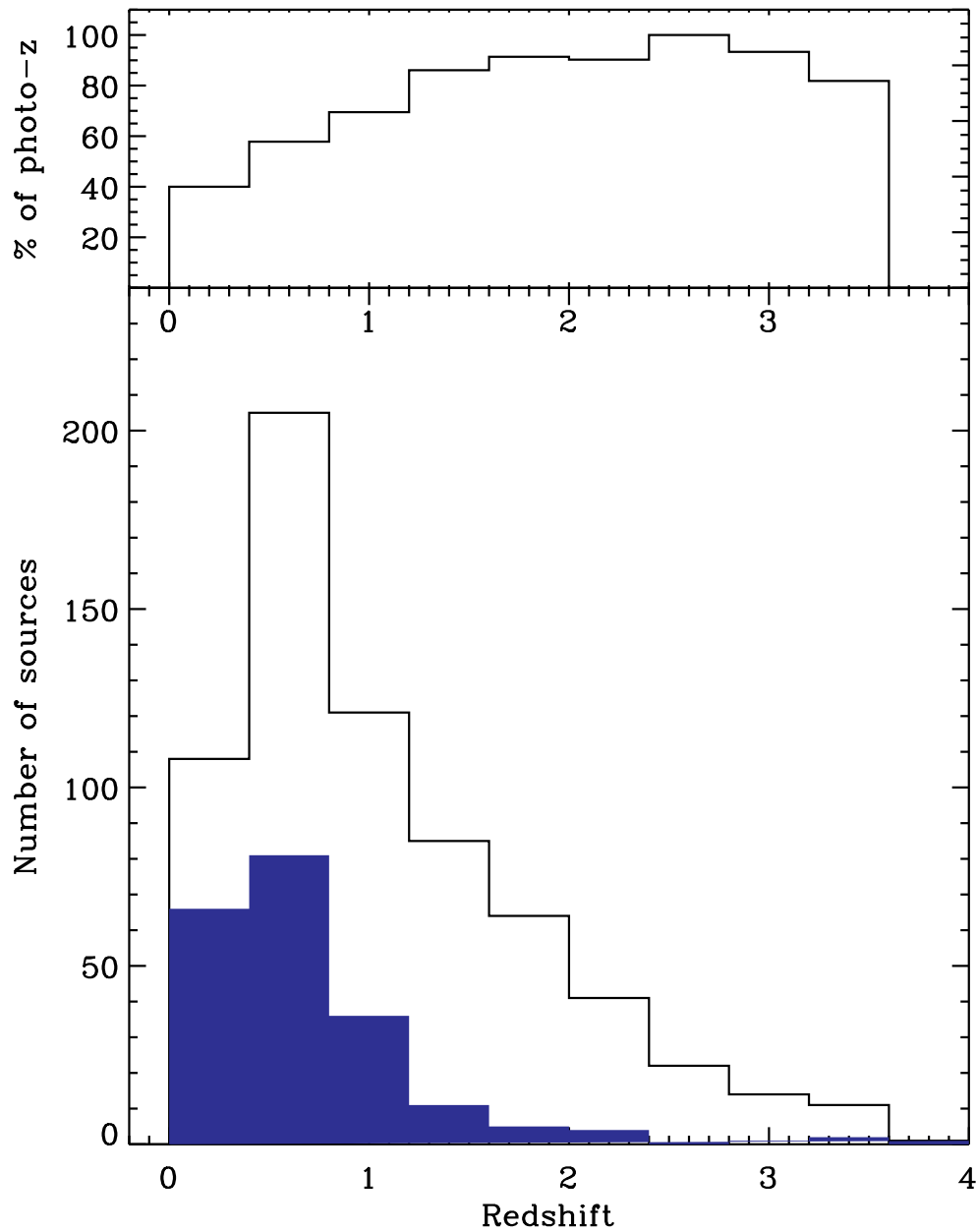


Figure 3.8: *Top panel:* fraction of photometric redshifts as a function of redshift. *Bottom panel:* total (empty) and spectroscopic (filled) redshift distributions. The plot is cut at $z = 4$ for a better view of the range where both photo- z and spec- z are available.

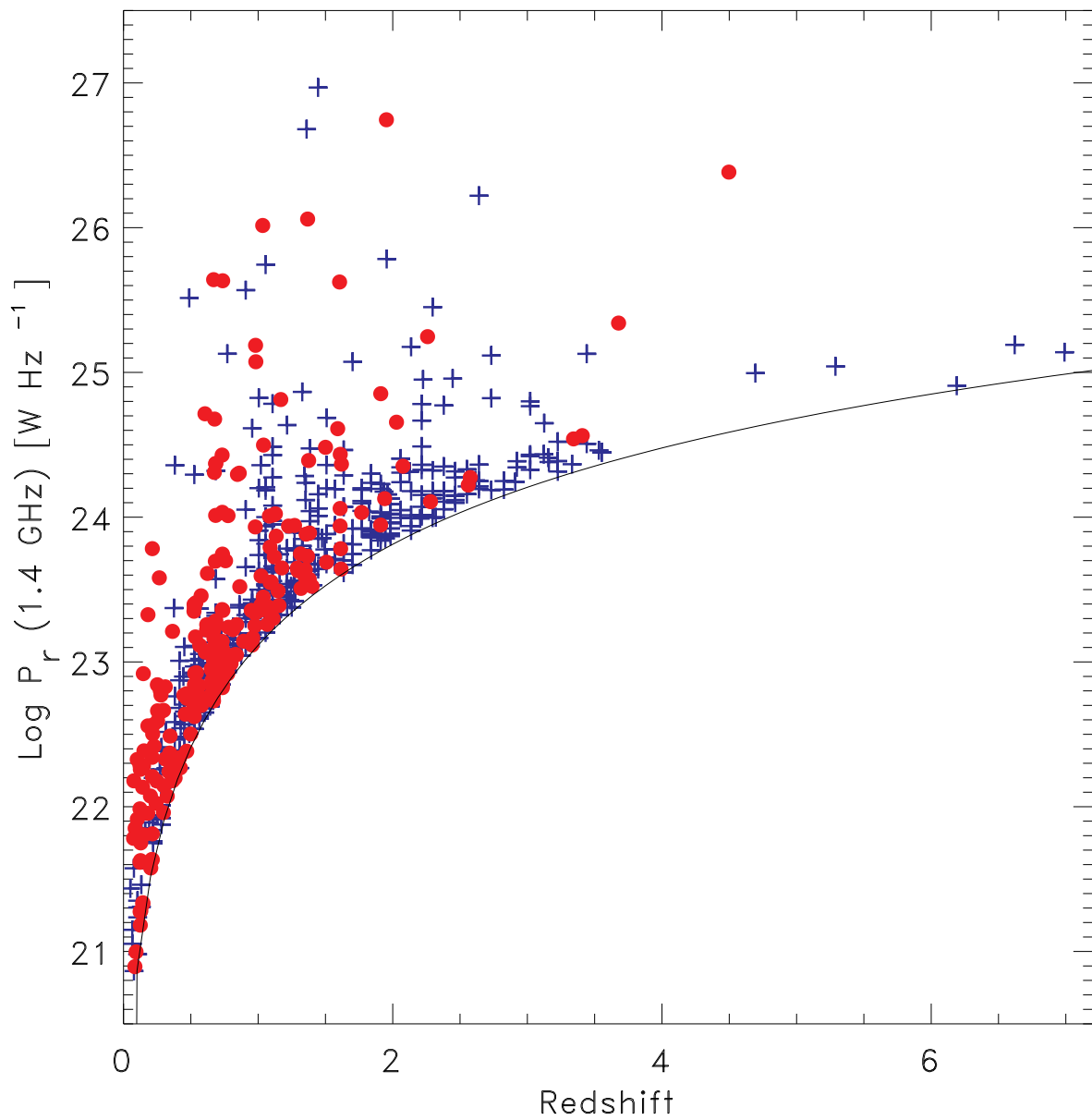


Figure 3.9: Radio power as a function of redshift. Circles indicate spectroscopic redshifts while crosses indicate photometric redshifts. The solid line shows the radio flux density limit of the VLA survey.

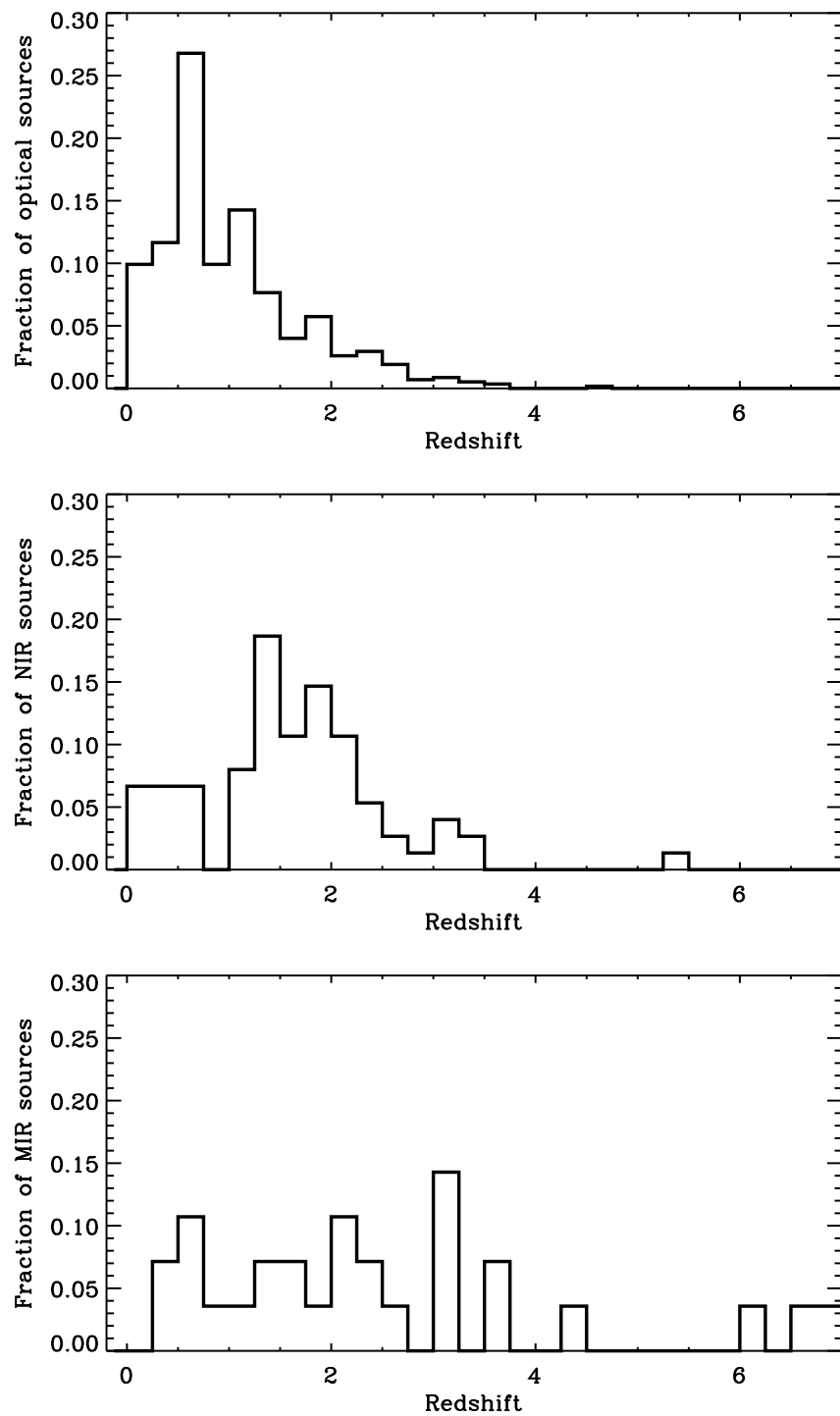


Figure 3.10: Normalized redshift distribution for the radio sources with an optical counterpart (top), with a NIR counterpart (middle) and with a MIR counterpart (bottom). The mean redshift is increasing from 1 for optical identified sources to 2.5 for the MIR ones (see Section 3.4.4).

(2011) for a more detailed description of the procedure adopted to estimate photometric redshifts. We cross-correlate the photometric redshift catalog with the radio source counterparts, selected as described in 3.3.2. Given the high background surface density distribution of the photometric catalog, we adopt a matching radius of 0.2 arcsec. This way we minimize the risk of associating to the radio counterpart the redshift of a nearby source. We find 623 matches out of the 839 identified radio sources. The mean separation between the radio counterparts and the corresponding photometric redshift coordinates is 0.03 arcsec. For the remaining 216 objects we consider three other compilations of photometric redshifts: the MUSYC-E-CDFS catalog (Cardamone et al., 2010), the GOODS-MUSIC catalog (Santini et al., 2009), and the K-selected MUSYC catalog (Taylor et al., 2009). The latter is based on a NIR selected catalog, and therefore is particularly useful to assign a redshift to radio sources with no counterpart in the optical. We find 13, 4, and 35 additional redshifts, respectively. In Summary, we associate a photometric redshift to 673 (80%) out of the 839 identified radio sources.

For the sub-sample with available secure spectroscopic redshift (QF=3), we compute the normalized median absolute scatter,

$$\sigma_{NMAD} = 1.48 \times median \left(\frac{|\Delta z - median(\Delta z)|}{1 + z_{spec}} \right), \quad (3.5)$$

where $\Delta z = z_{phot} - z_{spec}$, which is an estimate of the quality of the photometric redshift which is less sensitive to outliers than the standard deviation (Brammer et al., 2008). We find $\sigma_{NMAD} = 0.01$ that is comparable, and even slightly better, to what found for the same indicator in the photometric redshift catalogs considered (Santini et al., 2009; Taylor et al., 2009; Cardamone et al., 2010; Rafferty et al., 2011). Therefore, we conclude that the accuracy of the photometric redshifts for our radio selected sample is comparable to what estimated for the overall population in the photometric catalogs. We note that this indicator assumes that the spectroscopic sub-sample is representative of the full sample. This assumption is likely not entirely true and consequently it gives an overestimation of the accuracy of the photo-z for the whole sample. Luo et al. (2010) estimated that the uncertainties on the photometric redshifts for the full sample are a factor of six higher. We also note that the photometric redshift errors given in column 6 of Table 3.5 from the Rafferty et al. (2011) catalog are known to be underestimated (see Luo et al. (2010)). A more realistic estimate is given by the σ_{NMAD} parameter, which is around 6% as discussed above.

3.4.4 Redshift distribution

In the case where both spectroscopic and photometric redshifts are available, we use the spectroscopic one if QF ≥ 2 and the photometric redshift otherwise. For spectroscopic redshifts with QF=1 we find $\sigma_{NMAD} = 0.28$, which we interpret as an indication of the poor quality of these spectroscopic redshifts. Combining spectroscopic and photometric information, we assign a redshift to 678 objects, 81% of the radio sources with counterpart (252 spectroscopic redshifts and 426 photometric redshifts). This fraction underestimates

the redshift completeness of our sample since in the outermost part of the field there are no redshift measurements available. Therefore, we restrict our redshift distribution analysis to the sources in the area covered by the photometric redshift catalogs³. This region is plotted with a dot-dashed line in the right panel of Fig. 3.2. The number of radio sources included is 779, and 87% of them have a redshift. The total redshift distribution is plotted in Fig. 3.8, where the filled histogram represents the distribution of sources with spectroscopic redshifts. The top panel shows the fraction of photometric redshifts. We note that photometric redshift measurements become increasingly important at higher redshifts where optical spectroscopic observations become more challenging. The mean redshift for the whole sample is 1.1 and the median is 0.9. Fig. 3.9 shows the radio power as a function of redshift for sources with either spectroscopic (circle) or photometric (cross) redshift. The solid line represents the flux density limit of the survey. If we divide the radio sources based on their identification band, we observe an increase in the mean (median) redshift from 1.0 (0.8) for the optical identified sources to 2.5 (2.1) for the MIR ones (see Table 3.6 and Fig. 3.10). The statistical significance of the different redshift distributions is examined with the Kolmogorov-Smirnov (K-S) test. The difference between the optical and NIR distributions and that between the optical and MIR distributions are confirmed with a significance level $\gg 99\%$. For the NIR and MIR redshift distributions the K-S test gives a significance of 99%. Both spectroscopic and photometric redshift estimates become more challenging moving to high redshift objects and this is the reason why the fraction of sources with a redshift estimate drops from 88% for the optical identified sources to 25% for the MIR ones (see Table 3.6).

³Only three sources outside this region have a spectroscopic redshift.

Table 3.5: Main characteristics and redshift information of the radio source counterparts. A description of the table content is given in Section 3.6. (This table is available in its entirety in a machine-readable form in the online journal. A portion is shown here for guidance regarding its form and content.)

(1) RID	(2) R mag (AB)	(3) Ks mag (AB)	(4) 3.6 μ m mag (AB)	(5) best-z	(6) photo-z	(7) spec-z	(8) QF	(9) reference	(10) $S_{0.5-2\text{keV}}$ (erg cm $^{-2}$ s $^{-1}$)	(11) $S_{2-10\text{keV}}$ (erg cm $^{-2}$ s $^{-1}$)	(13) XID
360	—	—	—	—	—	—	—	—	—	—	—
361	25.92 \pm 0.22	22.02 \pm 0.18	21.02 \pm 0.02	1.39	1.39 $^{+0.02}_{-0.18}$	—	—	—	—	—	—
362	20.40 \pm 0.00	18.47 \pm 0.01	18.46 \pm 0.00	0.61	0.60 $^{+0.00}_{-0.00}$	0.607	3	VMR	(1.58 \pm 0.04) $\times 10^{-15}$	(1.06 \pm 0.02) $\times 10^{-14}$	193
363	—	—	21.33 \pm 0.30	—	—	—	—	—	—	—	—
364	25.57 \pm 0.14	—	22.50 \pm 0.07	3.02	3.02 $^{+0.06}_{-0.14}$	—	—	—	(1.74 \pm 0.23) $\times 10^{-15}$	(8.00 \pm 1.05) $\times 10^{-15}$	1330
365	22.78 \pm 0.02	19.60 \pm 0.03	19.29 \pm 0.00	0.73	0.73 $^{+0.00}_{-0.01}$	0.731	3	FORS	—	—	—
366	22.91 \pm 0.02	19.98 \pm 0.04	19.73 \pm 0.00	0.64	0.64 $^{+0.02}_{-0.02}$	—	—	—	—	—	—
367	21.17 \pm 0.00	19.16 \pm 0.02	19.16 \pm 0.00	0.60	0.60 $^{+0.02}_{-0.03}$	—	—	—	—	—	—
368	—	—	21.60 \pm 0.07	—	—	—	—	—	(2.51 \pm 0.77) $\times 10^{-16}$	(1.59 \pm 0.49) $\times 10^{-15}$	197
369	24.44 \pm 0.06	—	21.40 \pm 0.02	2.08	2.06 $^{+0.02}_{-0.02}$	2.076	3	VJB	(4.89 \pm 0.71) $\times 10^{-17}$	(1.51 \pm 0.22) $\times 10^{-16}$	202
370	21.30 \pm 0.01	19.14 \pm 0.02	19.48 \pm 0.00	0.30	0.28 $^{+0.00}_{-0.00}$	0.296	3	VMR	—	—	—
371	—	—	24.08 \pm 0.29	6.19	6.19 $^{+0.81}_{-5.03}$	—	—	—	—	—	—
372	19.87 \pm 0.00	18.36 \pm 0.01	18.89 \pm 0.00	0.35	0.35 $^{+0.00}_{-0.03}$	—	—	—	—	—	—
373	20.90 \pm 0.01	17.94 \pm 0.01	17.62 \pm 0.00	0.73	0.73 $^{+0.00}_{-0.01}$	0.733	3	VLR	—	—	—
374	19.04 \pm 0.00	—	17.69 \pm 0.00	—	—	—	—	—	—	—	—
375	—	—	—	1.51	1.51 $^{+0.05}_{-0.07}$	—	—	—	(1.21 \pm 0.13) $\times 10^{-16}$	(4.43 \pm 0.48) $\times 10^{-16}$	217

Table 3.6: Redshift distribution of the counterparts divided according to their wavelength selection. The number in column (1) is the number of radio sources whose counterpart is found in the group of catalogs of the corresponding row.

	(1) Identified sources	(2) With z	(3) Fraction	(4) Mean z	(5) Median z
Optical	652	575	88%	1.0	0.8
NIR	76	75	98%	1.6	1.5
MIR	111	28	25%	2.5	2.1

3.5 X-ray counterparts

Chandra has imaged in the X-ray the area of the E-CDFS as part of two different programs. The first is a 250 ks exposure observation that covers almost the whole field (0.28 deg^2) (Lehmer et al., 2005). The survey reaches sensitivity limits of 1.1×10^{-16} and 6.7×10^{-16} ergs $\text{cm}^{-2} \text{ s}^{-1}$ for the soft (0.5 – 2.0 keV) and hard (2 – 10 keV) bands, respectively. The second set is a much deeper 4 Ms *Chandra* observation covering only the central part of the field ($\approx 0.1 \text{ deg}^2$). The on-axis flux limits are 9.1×10^{-18} for the soft band and 5.5×10^{-17} ergs $\text{cm}^{-2} \text{ s}^{-1}$ for the hard band (Xue et al., 2011). We cross-correlated the radio source catalog with the X-ray ones. Due to the low surface density of X-ray sources a simple positional match is almost equivalent to the likelihood ratio technique. The searching radius was set to three times the sum in quadrature of the errors on the radio and X-ray positions. In case of multiple counterpart candidates, we selected the one closest to the radio source position. We find 129 radio sources with X-ray detection from the 4 Ms *Chandra* catalog, and 99 sources from the 250 ks catalog. Combining the two lists, we have X-ray detection for 25% of our radio sources. Their flux in the soft and hard band are reported in columns 10 and 11 of Table 3.5. We refer the reader to Section 4.2 of Vattakunnel et al. (2012) for a description of the properties of the radio sources with X-ray counterpart. In the following section we focus our attention on the sources for which we obtain only upper limits on their X-ray flux.

3.5.1 Average X-ray properties of radio-only detected sources

The majority (75%) of our radio sources has no X-ray counterpart. Even in the region covered by the 4 Ms *Chandra* observation, the fraction of identified sources is only $\sim 60\%$ (Vattakunnel et al., 2012). For the radio-only sources we perform aperture photometry on the X-ray images at the position of the radio source. The X-ray detected sources are masked and replaced with a Poissonian background based on the value of the measured local background. The photometry is done separately in the soft (0.5–2 keV) and in the hard (2–10 keV) bands. To derive the average properties of these objects, we perform a stacking analysis of the *Chandra* images. In particular, we stack separately sources with counterparts selected from an optical catalog, from a NIR catalog and from a MIR one. The net counts obtained in both hard and soft X-ray bands are reported in Table 3.7.

Table 3.7: Net counts and HR for radio sources without X-ray detection. The number in column (1) is the number of radio sources which have a optical/IR counterpart but not detected in the X-ray.

	(1) Number of sources	(2) 0.5–2 keV cts	(3) 2–10 keV cts	(4) HR
Optical	426	676 ± 68	374 ± 97	-0.3 ± 0.1
NIR	59	78 ± 24	—	—
MIR	86	79 ± 33	227 ± 50	0.4 ± 0.2
$\log P_r < 22.9$	122	231 ± 36	162 ± 51	-0.2 ± 0.2
$22.9 \leq \log P_r < 23.5$	121	194 ± 35	98 ± 50	-0.3 ± 0.2
$\log P_r \geq 23.5$	97	120 ± 31	52 ± 43	-0.4 ± 0.4

The detection for the optical selected sources is highly significant in both bands, while for the MIR ones it is only marginal in the soft band. The NIR selected sources have marginal detection only in the soft band and are not detected in the hard band. For each group, we evaluate the average hardness ratio defined as $HR = (H - S)/(H + S)$, where H and S are the total net counts in the hard and soft band, respectively (column 4 in Table 3.7). In particular we note that MIR selected sources have a hard hardness ratio, $HR = 0.4 \pm 0.2$, supporting the hypothesis that these objects are obscured sources. This HR value corresponds to an effective X-ray photon indices $\Gamma = 0.07^{+0.14}_{-0.13}$.

We also split the sample of X-ray undetected sources in radio power bins to investigate if there are any changes in the average X-ray spectral properties as a function of radio power. We consider only sources with $z < 1.5$, where we have a more uniform distribution in radio power, from 10^{20} to 10^{27} W Hz $^{-1}$. The radio power bins, the net counts, and the HR are reported in Table 3.7. We find a roughly constant value of HR and therefore no significant change in the average X-ray spectral properties as a function of radio power.

3.6 Catalog description

In this section we describe the catalog containing the results of the optical and IR counterpart identification process. The information is divided into two tables. In Table 3.3 we include the radio data from Miller et al. (2013) that were used in this work and the results of the identification process. In Table 3.5 we list the main characteristics of the optical or IR counterpart, the redshift information and the X-ray data. The catalog columns are organized as follows. In Table 3.3:

- (1) Identification number of the radio source (RID).
- (2) and (3) Right ascension and declination of the radio source.
- (4) Radio flux density and 1σ error in μJy .
- (5) Signal to noise ratio.

- (6) and (7) Right ascension and declination of the counterpart.
- (8) Reliability of the association⁴.
- (9) Distance between the radio source and the counterpart in arcsec.
- (10) Catalog from which the counterpart is selected (see Table 3.1).

In Table 3.5:

- (1) Identification number of the radio source (RID).
- (2) R-band AB magnitude of the counterpart from the WFI catalog and associated error.
- (3) K-band AB magnitude of the counterpart from the MUSYC catalog and associated error.
- (4) Flux density at $3.6\mu\text{m}$ of the counterpart from the SIMPLE catalog and associated error.
- (5) Best redshift of the counterpart: spectroscopic if $QF \geq 2$, photometric otherwise.
- (6) Photometric redshift with upper and lower 68% confidence level.
- (7) Spectroscopic redshift.
- (8) Quality flag (QF): 3 for secure redshift, 2 for reasonable redshift and 1 for one line detection or tentative redshift.
- (9) Source of the spectroscopic z (see Table 3.4).
- (10) X-ray soft band flux (0.5-2.0 keV) and associated error.
- (11) X-ray hard band flux (2-10 keV) and associated error.
- (12) X-ray ID (from Xue et al. (2011) if <1000 , from Lehmer et al. (2005) if >1000 [ID-Lehmer+1000])

⁴Sources whose identification has been revisited (see Section 3.3.4) or for which the counterpart position has been extracted from the IRAC image (see Section 3.3.2) have $Rel = 9$.

3.7 Discussion and Conclusions

We have presented the optical and IR counterparts of the radio sources in Miller et al. (2013) catalog. The results are collected in a new catalog⁵ containing the counterpart data and the redshift information. A detailed characterization of the physical properties of these sources will be presented in Bonzini et al. (2013). This work has demonstrated the difficulties in, and the requirements for, the identification of the sub-mJy radio population. The main results of our analyses are as following:

1. *Importance of multi-wavelength observations.* We identify the counterparts for a high fraction (95%) of radio sources. In order to reach such a completeness it is necessary to include not only optical observations, but also near and far infrared data. Optical surveys alone, even in the deepest fields, allow us to identify only $\sim 70\%$ of the radio sources. With just MIR observations the fraction rises to 86%, but it is by only combining the information from all wavelengths that we reach 95% completeness. The multi-wavelength coverage is also important to obtain a high redshift completeness. Indeed, only 31% of our radio sources have spectroscopic information, while the majority have a photometric redshift.
2. *Importance of the counterpart analysis to confirm multiple-component radio sources.* In this work we have found many examples that show the importance of the combination of radio and optical/IR data to correctly identify multiple-component radio system. In many cases, sources whose radio morphology suggested a complex radio structure (e.g., KID 114) have been identified as independent sources. The opposite case is represented by source RID 73. Here, we conclude that the radio emission is associated with a single compact radio-lobe source with a single optical counterpart.
3. *Comparison between likelihood ratio and cross-correlation methods.* In Sec 3.3.5, we compare the likelihood ratio technique with the positional matching method. This work has shown that the latter is hardly applicable to deep optical surveys since it leads to a large fraction of spurious matches ($\sim 10\%$). With our technique instead the rate of spurious matches is lower due to the exploitation of the information given by the probability distribution of background sources in the optical catalogs. We have also shown that to reach the same level of spurious contamination with the cross-correlation method the fraction of identified sources decreases by $\sim 18\%$. At longer wavelengths, i.e. in the NIR and in the MIR, the differences of the two methods are negligible. We find a comparable fraction of expected spurious counterparts and a similar completeness. This is mainly due to the lower background surface density of objects in the auxiliary catalogs. In section 3.3.4 we point out two cases where the likelihood ratio method can fail in identifying the correct optical counterpart, that is the presence of many close sources around the radio object and extended radio emission. We note that with the cross-correlation method these problems are

⁵The catalog is available in ASCII format in the on-line material.

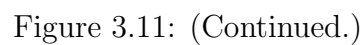
even more severe; in crowded regions it selects the closest source, regardless of its properties. In case of extended radio sources, there could be an offset between the peak of the emission at different wavelengths larger than the searching radius. In this case, the cross-correlation method would not be able to give any counterpart candidate.

4. *Comparison with M08 work.* Compared with the sample studied in M08, our sample is about 3 times larger and most of the new sources have a low radio flux density or lie at the edges of the E-CDFS. That makes their identification more challenging. However, more and deeper catalogs are now available in the E-CDFS and, using these data, we were able to reach the same identification completeness as in M08 for the new sample. We find general agreement between the counterparts found in the two works for the radio sources in common. The main improvement is a more reliable identification in particular of the optically faint radio sources, obtained by adopting a stricter acceptance criteria and giving more importance to the IR selected catalogs (Section 3.3.6).
5. *Importance of MIR observations to find the counterpart of high redshift or heavily obscured radio objects.* Some radio sources (12%) have a reliable counterpart only in the catalogs based on the *Spitzer* data. These sources are particularly interesting since they are the best candidate high- z objects. In Sec. 3.4.4, we describe the redshift distribution of the radio sources divided according to their identification band. Indeed, we find a clear trend for sources identified at longer wavelengths to have higher redshifts, as shown in Fig. 3.10. Moreover, the stacking analysis of the X-ray images of the MIR selected sources, has revealed that they tend, on average, to have hard X-ray spectra ($HR = 0.4$). This supports the idea that they are obscured sources.

3.A New VIMOS/VLT spectra.

Newly acquired VIMOS spectra for the counterparts of 13 VLA sources (see Sec. 3.4.1). We used the low-resolution blue grism ($R=180$), with a total exposure time on source of 5 hours. Each plot of Fig. 3.11 shows the spectra and the position of the main spectral features. We make bold the names of the lines actually used to identify the redshift. The labels report the source RID, the redshift, and the corresponding quality flag (QF).





3.B Notes on individual sources.

- RID 73 (KID 14): there are two possible counterparts for the radio lobes but we believe that they are both associated with the bright central galaxy. One strong indication for this is the strength of the radio flux density, which at 40 mJy is reasonable for a compact double lobed radio galaxy. If separate sources, they would have to both be strong radio AGN very close in projection on the plane of the sky.
- RID 80-85 (KID 18B-18A): they were considered as radio lobes in Kellermann et al. (2008), but they appear to have two different counterparts. Moreover, they have very different flux densities which supports the idea that they are not related to the same source. Finally, there is no good candidate for a single radio core.
- RID 101 (KID 23): double lobed source whose core was tentatively identified in M08 (KID 23) with a faint (R-band magnitude ~ 26) galaxy at $z=0.999$ from the COMBO17 catalog. We think that this association is very unlikely especially because this possible counterpart is not detected at any longer wavelength. From the radio contours we believe that it is a classical radio galaxy. Therefore, we expect for such a galaxy a correlation between the K-band magnitude and the redshift (e.g., Lilly & Longair, 1984). Since we do not detect it in the K-band we think this source may be a high redshift object. This hypothesis is also supported by the presence of a possible counterpart at 24 micron in the FIDEL catalog. Unfortunately no photometric redshift is available.
- RID 209 (KID 48): V-shape radio source at redshift 1.3. Given the radio morphology, we considered the possibility that this is a head-tail radio source due to the interaction with the intracluster medium (ICM) in a high- z galaxy cluster. Any cluster, or large group, with ICM density sufficient to bend the radio jets, would have been clearly detected in the X-ray too. However, we do not observe it in the 4 Ms *Chandra* image. Also the redshift distribution of the sources in the region around RID 209 does not show any hint of clustering. Therefore, we think is unlikely that the V-shape of this radio source is due to the interaction with the ICM. There is instead a possible contamination to the flux density of one of the two radio lobes (A) from a superimposed galaxy.
- RID 283 (KID 73): double-lobe source. There are three optical sources in the region of the radio emission but all have reliability under the threshold (< 0.6) and we believe that none of them are associated with the radio source. The counterpart of the core is identified with an object detected in the Ks-MUSYC catalog.
- RID 308 (KID 80): bright radio source with possibly one or two lobes. However, the quality of the radio image in this region is not good.
- RID 360 (KID 97): powerful single component radio source that was not identified in M08. It has a radio flux density of 1.38 mJy. Although we use deeper catalogs,

still we are not able to identify it in any band. The cutouts of this source are shown in Fig. 3.5 and they are all blank field. The 5σ detection limit for each band is given in Table 3.1. Moreover, this source is in the region covered by the 4Ms *Chandra* observation but it has no X-ray detection. We can therefore put an upper limit on its X-ray flux of 9.1×10^{-18} and 5.5×10^{-17} ergs cm $^{-2}$ s $^{-1}$ for the soft and hard band, respectively.

- RID 403-406-410-412 (KID 114): this group of sources was at first interpreted as a tailed radio source (see radio contours). But since we find a clear counterpart for three of them, we consider these sources as independent. Source 410 is unidentified.
- RID 407 (KID 113): bright and extended double lobed source. Close to the core position there are many optical sources. In particular there is a 21 K-band magnitude galaxy 0.5 arcsec away from the expected core position that was automatically selected by our method. We consider this association spurious since it would imply that this source is far from the K-z relation for radio galaxies (e.g Lilly & Longair, 1984; De Breuck et al., 2002). Therefore, we manually corrected the identification by associating this radio source to a bright elliptical galaxy (K-band mag=18.4) 2 arcsec away from the centroid of the radio image.
- RID 500 (KID 148): this is a complex radio source. We identify a clear core and two radio lobes (KID 148A and 148B). There are two other components, KID 148D and 148E, possibly associated with this source. We found a secure counterpart for 148D and so we listed it as a separated source (RID 504). For the 148E component the only counterpart candidate is a faint galaxy at $\alpha = 03:32:32.59$, $\delta = -28:03:15.4$ with R-mag=23.7, but it is under our reliability threshold and therefore it probably remains unidentified.
- RID 848 (KID 260): the radio source is split into two components both associated with the same spiral galaxy.

Chapter 4

The sub-mJy radio sky in the Extended Chandra Deep Field South: source population

*Published as **Bonzini, M.**; Padovani, P.; Mainieri, V.; Kellermann, K. I.; Miller, N.; Rosati, P.; Tozzi, P.; Vattakunnel, S. , 2013, Monthly Notices of the Royal Astronomical Society, 436, 3759–3771*

Abstract

The sub-mJy radio population is a mixture of active systems, that is star forming galaxies (SFGs) and active galactic nuclei (AGNs). We study a sample of 883 radio sources detected at 1.4 GHz in a deep Very Large Array survey of the Extended Chandra Deep Field South (E-CDFS) that reaches a best rms sensitivity of $6\mu\text{Jy}$. We have used a simple scheme to disentangle SFGs, radio-quiet (RQ), and radio-loud (RL) AGNs based on the combination of radio data with *Chandra* X-ray data and mid-infrared observations from *Spitzer*. We find that at flux densities between about 30 and $100\mu\text{Jy}$ the radio population is dominated by SFGs ($\sim 60\%$) and that RQ AGNs become increasingly important over RL ones below $100\mu\text{Jy}$. We also compare the host galaxy properties of the three classes in terms of morphology, optical colours and stellar masses. Our results show that both SFG and RQ AGN host galaxies have blue colours and late type morphology while RL AGNs tend to be hosted in massive red galaxies with early type morphology. This supports the hypothesis that radio emission in SFGs and RQ AGNs mainly comes from the same physical process: star formation in the host galaxy.

4.1 Introduction

The two main processes that contribute to the extragalactic continuum radio emission at 1.4 GHz are the non-thermal emission associated with relativistic electrons powered by active galactic nuclei (AGNs) and the synchrotron emission from relativistic electrons in

supernova remnants. The latter is therefore a tracer of star formation activity in galaxies. While the bright radio sky is dominated by the emission driven by “radio-loud” AGNs, at fainter flux densities (< 1 mJy) the contribution from star forming galaxies (SFGs) become increasingly important (e.g., Prandoni et al., 2001; Smolčić et al., 2008; Seymour et al., 2008; Padovani et al., 2009). Moreover, recent work has revealed the presence of a third population of sources in the sub-mJy radio sky, the “radio-quiet” AGNs (e.g., Padovani et al., 2009). These sources show the presence of AGN activity in one or more bands of the electromagnetic spectrum (e.g., optical, mid-infrared, X-ray) but the origin of their radio emission has been a matter of debate. It has been proposed that they represent scaled versions of RL AGNs with mini radio jets (e.g., Giroletti & Panessa, 2009) or that their radio emission comes from star formation in the host galaxy (e.g., Padovani et al., 2011b; Kimball et al., 2011). Disentangling the two emission mechanisms is important to investigate the circumstances under which they originate, for example the host galaxy properties, and possibly to study the connection between AGN and star formation activity. Most of the radio sources in surveys as deep as the one discussed in this paper are barely resolved or unresolved. So radio observations alone generally can not be used to distinguish between AGN and star formation driven sources; hence, the need for a multi-wavelength approach. For example, Padovani et al. (2009) showed that the “standard” definitions of radio-loudness, which are based on radio-to-optical flux density ratios, R , and radio powers, are clearly insufficient to identify radio-quiet AGN in faint radio samples. This is because these also include star-forming and radio-galaxies; both of these classes are or can be, respectively, characterized by low R and low radio powers as well. Padovani et al. (2011b) showed instead that a proper classification of faint radio sources requires a combination of radio, IR, and X-ray data. Here, we propose a new simple classification scheme, which is an upgrade of that used by Padovani et al. (2011b). The paper is organized as follows. We present our sample and the data used for the classification of the radio sources in Section 4.2. Our classification scheme is presented in Section 4.3. In Section 4.4 we describe the relative contribution of the different source types to the radio population. The host galaxy properties are analysed in Section 4.5. In Section 4.6 and 4.7 we discuss and summarize our results. Our definitions of AGN, RQ, and RL sources follow those of Padovani et al. (2011b). In this paper we use magnitudes in the AB system, if not otherwise stated, and we assume a cosmology with $H_0 = 70$ km s $^{-1}$ Mpc $^{-1}$, $\Omega_M = 0.3$ and $\Omega_\Lambda = 0.7$.

4.2 Sample and data

4.2.1 Radio catalog, optical-IR counterparts and redshifts

We consider a sample of 883 radio sources detected at 1.4 GHz in a deep VLA survey of the Extended Chandra Deep Field South (E-CDFS) that reaches a best rms sensitivity of $6\mu\text{Jy}$. The average 5σ flux density limit is $37\mu\text{Jy}$ and the spatial resolution is $2.8'' \times 1.6''$. A description of the survey strategy and the data reduction details are given in

Miller et al. (2013). Using the wealth of optical and infrared (IR) data available in the E-CDFS we were able to identify the optical/IR counterpart for 839 (94%) radio sources using a likelihood ratio technique (Bonzini et al., 2012). Combining data from the literature and newly acquired spectra, we assigned a reliable spectroscopic redshift to 274 sources. Including photometric redshift the number of sources with measured redshift increases to 678 and their average redshift is $z \sim 1.1$. The accuracy of the photometric redshift is around 6% (Bonzini et al., 2012). The majority of the objects without a redshift are not detected at optical wavelengths. Their counterparts can be detected only at longer wavelengths, in the near or mid-infrared. Therefore, spectroscopic observations are challenging and photometric estimates, based on a few photometric points, are not robust. In other cases, the lack of photometric redshift information is due to a less rich multi-wavelength coverage, especially in the outskirts of the field.

4.2.2 Mid infrared data

Mid-infrared (MIR) wavelengths can be used to unveil the presence of an AGN (see Section 4.3.1). Therefore, we used deep *Spitzer* IRAC and MIPS data. The IRAC data were obtained as part of the SIMPLE survey (Damen et al., 2011). It covers an area of about 1,600 arcmin² centred on the E-CDFS. The typical 5σ flux density limits are 1.1, 1.3, 6.3, and 7.6 μ Jy at 3.6, 4.5, 5.8, and 8.0 μ m, respectively. We also use MIPS 24 μ m data from the Far-Infrared Deep Extragalactic Legacy Survey (FIDEL) (Dickinson & FIDEL Team, 2007). This survey covers, at 24 μ m, $\sim 90\%$ of the VLA area considered in this paper and the typical flux density limit (5σ) is 30 μ Jy. To associate the correct MIR photometry to our radio sources we cross-correlated the position of their optical/IR counterparts with the SIMPLE and FIDEL catalogues, after correcting for the median offset in right ascension and declination between the two samples. The matching radii are 0.7'' for the SIMPLE catalogue and 1.5'' for the FIDEL catalogue. A total of 91% and 88% of the identified radio sources (839) have a match in the SIMPLE and FIDEL catalogue, respectively. For sources without 24 μ m detection we compute an upper limit to the 24 μ m flux density. Since the exposure time varies across the field the upper limit is extrapolated from the exposure map as: $\text{Flux}_{lim}(1\sigma) = -1.4 + 1369.1(1/t_{exp})$, where t_{exp} is the exposure time in seconds, and the flux density is in μ Jy.

4.2.3 X-ray data

The E-CDFS has been mapped in the X-ray band by *Chandra*. A total of 129 radio sources have a counterpart in the 4 Ms observations of the CDFS presented in Xue et al. (2011) and another 99 in the main E-CDFS catalogue by Lehmer et al. (2005) obtained with shallower (250 ks) observations in each of four pointings. The list of the X-ray counterparts of the radio sources is given in Bonzini et al. (2012). We compute the X-ray luminosity (2-10 keV) to indicate the presence of AGN activity (see Section 4.3.1). Objects without X-ray counterpart, but with redshift (435 sources), have only an upper limit (3σ) on the X-ray luminosity obtained from aperture photometry on the X-ray images at the position of the

radio source (Vattakunnel et al., 2012). A total of 44 radio sources lie in the outermost part of the field and have no X-ray observations available. The X-ray luminosity for our sample as a function of redshift is plotted in Fig. 4.1.

4.3 AGN or SFG?

As discussed in Section 4.1, a proper classification of the faint radio sources requires a wealth of multi-wavelength data. We have identified three diagnostics that can be used to split the population in the different classes of sources. In this section, we first describe these diagnostics and how they are used to classify the sources (Section 4.3.1) and our classification scheme (Section 4.3.2). Then, we present a series of checks that we performed to validate the method or to refine the classification of some peculiar sources (Sections 4.3.3, 4.3.4, and 4.3.5).

4.3.1 Classification criteria

q-values

It is well known that the far-IR and radio emission are tightly and linearly correlated in star-forming systems (e.g., Sargent et al., 2010, and references therein). This is usually expressed through the so-called q parameter, that is the logarithm of the ratio of far-IR to radio flux density, as defined by Helou et al. (1985). Ideally, one would like to derive a bolometric q , but typically insufficient data are available at longer wavelengths to do this reliably. For example, Padovani et al. (2011b) were able to derive only upper limits on q for 50% of the sources. In this paper, we therefore prefer to use q_{24obs} , which is defined as:

$$q_{24obs} = \log_{10}(S_{24\mu m}/S_r), \quad (4.1)$$

where $S_{24\mu m}$ is the observed 24 μm flux density, and S_r is the observed 1.4 GHz flux density. The use of the observed flux densities rather than the rest frame ones minimises the uncertainties due to the modelling. In case of resolved sources, we use integrated radio flux density (see Miller et al., 2013, for details). The distribution of the q_{24obs} values as a function of redshift is plotted in Fig. 4.2. For a given intrinsic spectral energy distribution (SED), this ratio has a redshift dependence. We assume that the IR and radio properties of high redshift SFGs are similar to the local ones (e.g. Sargent et al., 2010). Therefore, to define a locus of SFG, we compute q_{24obs} as a function of z using the SED of M82¹ as representative of the SFGs class from $z = 0$ to the maximum redshift of our sources. For the radio spectra we assume a spectral index α_r ² of 0.7, as expected for a typical SFG (e.g., Ibar et al., 2010). The M82 template is normalized to the local average value of q_{24obs} as obtained in Sargent et al. (2010) ($\langle q_{24obs} \rangle = 1.31^{+0.10}_{-0.05}$ for sources with $0.08 < z < 0.23$). The average spread for local sources is 0.35 dex (Sargent et al., 2010). We define the SFG

¹From the SWIRE library, Polletta et al. (2007)

²We define the spectral index as: $S_\nu \propto \nu^{-\alpha}$

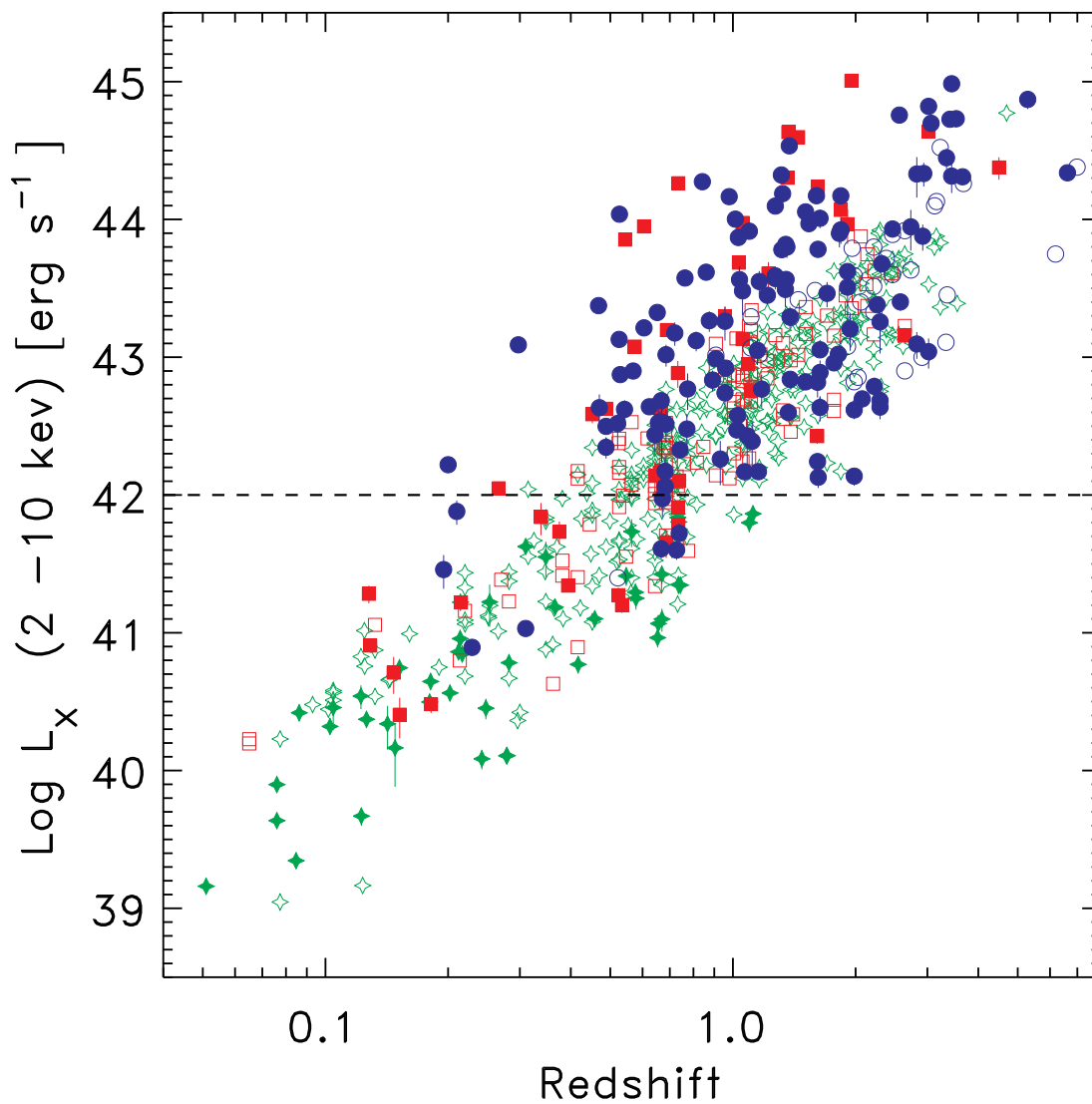


Figure 4.1: X-ray luminosity as a function of redshift for RL AGNs (red squares), RQ AGNs (blue circles), and SFGs (green crosses) (See Section 4.3.2). Filled symbols represent X-ray detections, while open symbols are 3σ upper limits. X-ray detected sources with luminosity above the horizontal line are considered to be AGNs.

locus as the region of $\pm 2\sigma$ centred on the M82 template (see Fig. 4.2). Sources below this locus display a radio excess and therefore do not follow the far-IR – radio correlation and are classified as RL AGNs. Sources without $24\ \mu\text{m}$ detection have only upper limits on the $q_{24\text{obs}}$ value. These sources are classified as RL AGN if their upper limit is smaller than the M82 template at the source redshift -1σ (rather than -2σ).

For a small fraction (16%) of the radio sources $70\ \mu\text{m}$ *Spitzer* photometry from the FIDEL survey is also available (Dickinson & FIDEL Team, 2007). We can therefore check if we obtain the same classification using the longer wavelength data rather than the $24\ \mu\text{m}$ flux density. Following the same procedure described above, we compute the $q_{70\text{obs}}$ value for this sub-sample and define the corresponding SFGs locus. We find an excellent agreement (96% of the cases) which validates our use of the $24\ \mu\text{m}$ data for most of the sources.

X-ray luminosity

Sources with hard band X-ray luminosity above $10^{42}\ \text{erg s}^{-1}$ are considered to be AGN driven (e.g. Szokoly et al., 2004). A total of 162 sources in our sample have X-ray detection above this threshold. When only upper limits are available in the X-ray, we assume that the source is a SFG if there is no indication of black hole driven activity in others bands (e.g. IRAC colours or $q_{24\text{obs}}$). In the central part of the field, where the 4Ms *Chandra* observations are available, the upper limits on the X-ray luminosity are so faint that we miss only the most absorbed AGN. In the outer part of the ECDFS we only have the 250ks *Chandra* observations and therefore it is possible that we are not sensitive even to moderate luminosity ($10^{42}\ \text{erg s}^{-1} < L_x < 10^{44}\ \text{erg s}^{-1}$) AGN. To avoid misclassifying sources as SFGs, sources with upper limits on their flux density 2σ above the local background level and with upper limits on their X-ray luminosity minus 1σ larger than $10^{42}\ \text{erg s}^{-1}$ are classified as AGN. A total of 23 sources satisfy this requirement.

IRAC colour-space

Finally, we use the IRAC colour-colour diagram to help select AGNs. The AGN emission can heat up the surrounding dust that re-emits this energy in the MIR. If the AGN is sufficiently luminous compared to its host galaxy, the emission from the heated dust can produce a power-law thermal continuum across the four IRAC bands. Sources with this spectral shape occupy a specific region in the IRAC colour-colour diagram, the so called "Lacy wedge" (Lacy et al., 2004). However, the "Lacy wedge" is heavily contaminated by high redshift SFGs (Donley et al., 2012). Therefore, to select AGNs we adopt the stricter criteria described in Donley et al. (2012) that are designed to minimize the contamination from both low and high redshift SFG. These criteria require the flux density to monotonically increase in the four IRAC bands and the colours to be such that the source lies in the wedge plotted in Fig. 4.3. The completeness of this AGN selection method is strongly dependent on the AGN luminosity, being high for $L_{2-10\text{keV}} \geq 10^{44}\ \text{erg s}^{-1}$ but relatively low ($< 20\%$) at lower luminosities (Donley et al., 2012). Seyfert 2 galaxies, are also easily missed by this diagram as show by the colour-colour track in Fig. 4.3. This method is also

incomplete for luminous AGN with heavy obscuration and particularly bright host galaxy (Donley et al., 2012). A total of 85 sources in our sample satisfy these criteria. Eight of them were already classified as RL AGN due to their q_{24obs} value and about half of them (44) have also X-ray luminosity above 10^{42} erg s $^{-1}$. But 39 sources are classified as AGN only because of their IRAC colours.

4.3.2 Our classification scheme

- We classify as RL AGNs all sources with q_{24obs} below the SFGs locus (see section 4.3.1 for details).
- Above this threshold, a source is classified as a RQ AGN if it shows clear evidence for an AGN in the X-ray (see Section 4.3.1) or in the MIR bands (see Section 4.3.1).
- Otherwise a SFG classification is adopted.

4.3.3 Sources without redshift

In our sample, there are 161 identified radio sources without redshift. Only the IRAC colour criterion can be used without knowing the redshift as both the classification based on the q_{24obs} value and the X-ray luminosity require this information. However, in the following cases a reliable classification is possible even for sources without redshift: (i) Five sources whose q_{24obs} value (detection or upper limit) is below the SFG locus defined in Section 4.3.1, even assuming a high redshift (namely, $z = 3$), are classified as RL AGNs. Indeed, given the SED shape of SFGs like M82, the threshold value between RL AGNs and RQ AGNs-SFGs decreases with redshift. Therefore, the assumption of high redshift for the sources without z provides a conservative estimate for the number of additional RL AGNs. (ii) When the IRAC flux densities follow the Donley et al. (2012) criteria we classify the source as an AGN. To distinguish between RL and RQ AGNs we use again the q_{24obs} value (detection or upper limit) assuming $z=3$. A total of 26 RQ AGNs without z are identified using their IRAC colours.

(iii) Eleven sources without measured redshift are detected in the X-ray band. They all lie in the region with only 250ks of *Chandra* observations. Even assuming the mean redshift of the sample ($z = 1$) their X-ray luminosity in the total band is greater than 10^{42} erg s $^{-1}$ and therefore we classify them as AGNs. None of them are classified as RL AGN based on their upper limit on the q_{24obs} value. Most of them are in the “Donley” wedge too, but four are “new” RQ AGNs. For all the other 126 identified radio sources without measured redshift we do not have enough evidence to reveal the presence of an AGN (only upper limits on the X-ray luminosity, not in the “Donley wedge”, and not below the SFG locus) and therefore we conservatively consider them as SFGs. Note that a fraction of these could be RQ AGNs.

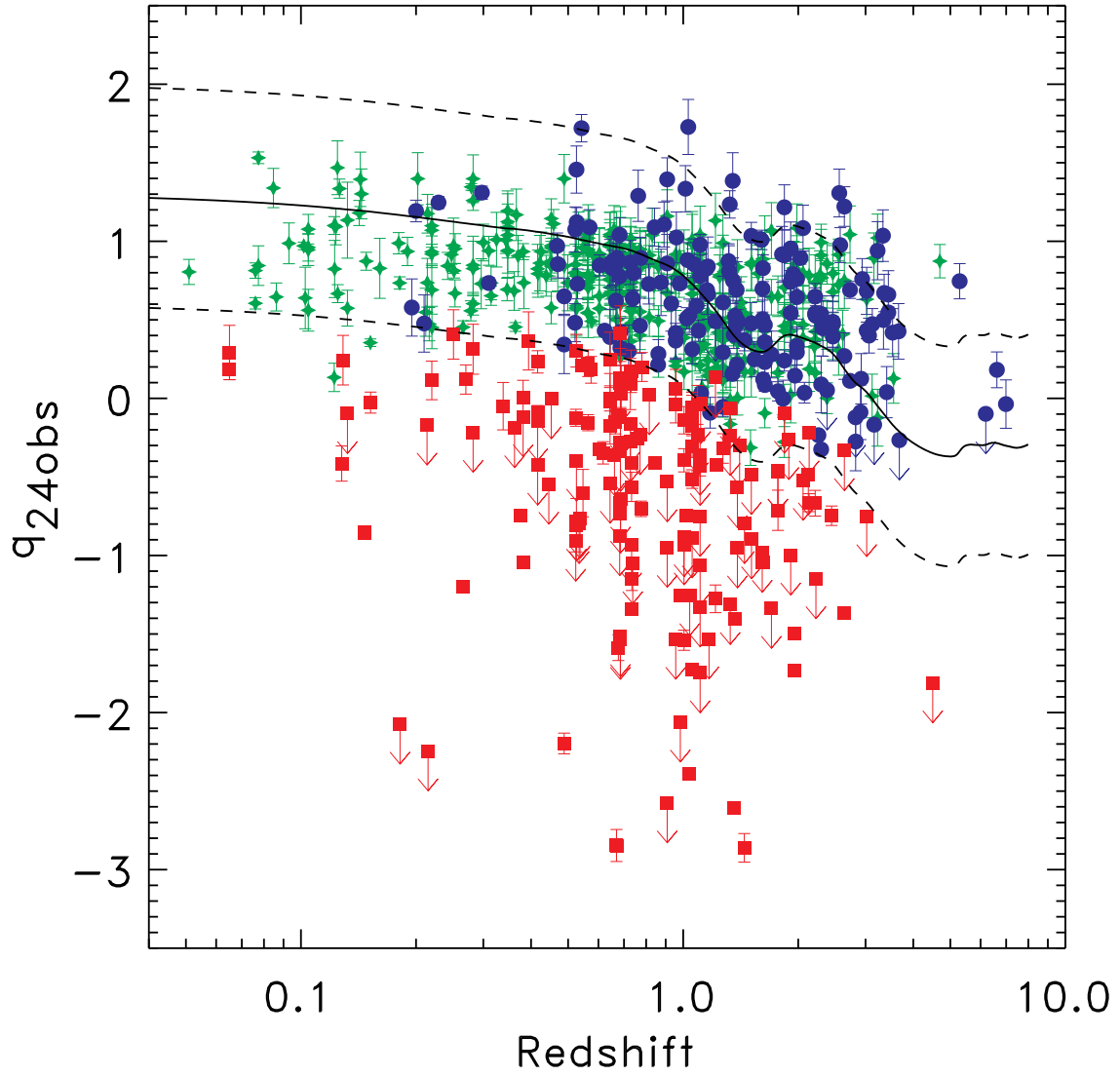


Figure 4.2: q_{24obs} values as a function of redshift for RL AGN (red squares), RQ AGN (blue circles), and SFG (green crosses). Down-pointing arrows represent 3σ upper limits. The solid line show the evolution of q_{24obs} for the M82 template as a function of redshift with $\pm 2\sigma$ dispersion (dashed lines).

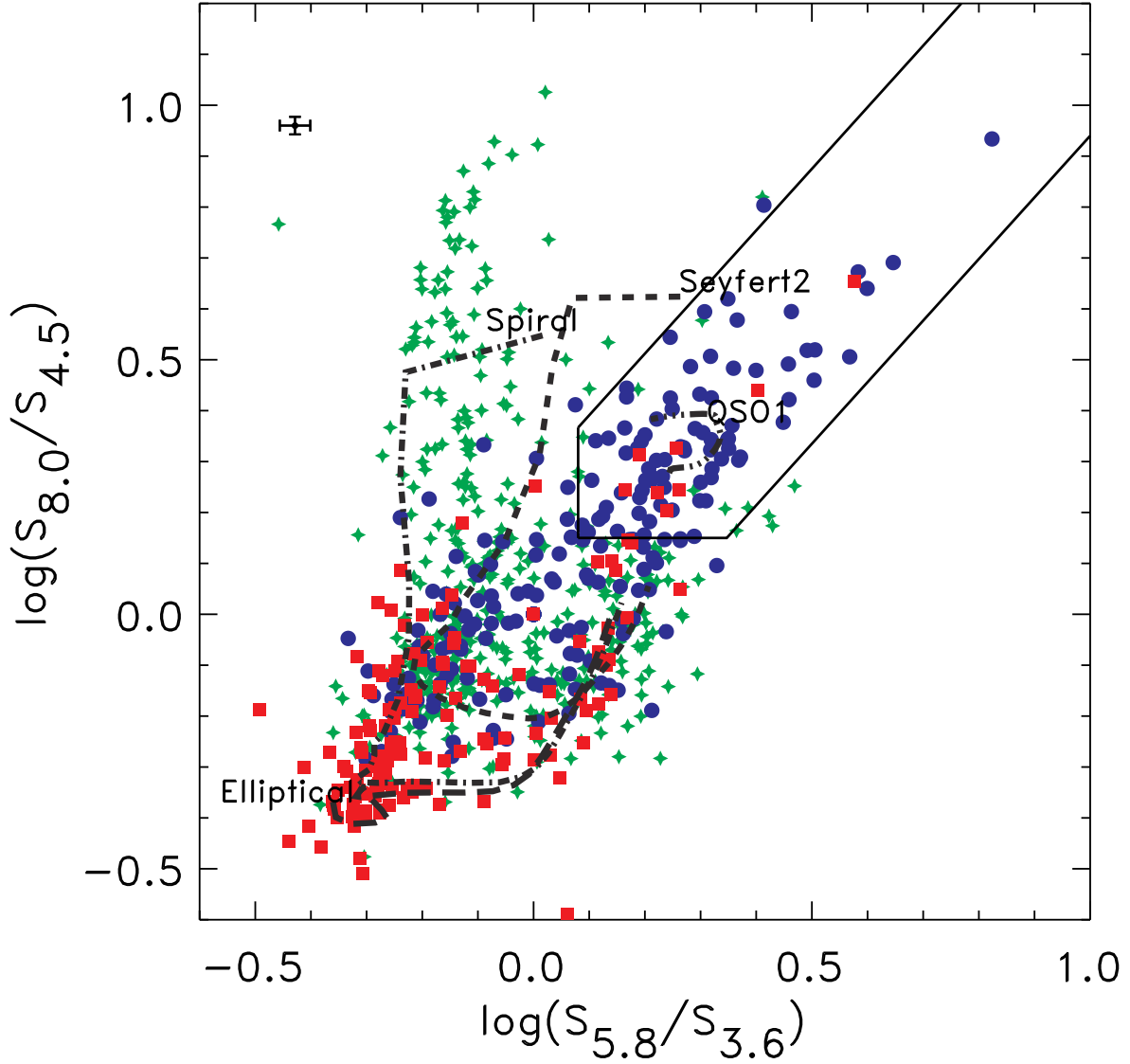


Figure 4.3: IRAC-colours plot for RL AGNs (red squares), RQ AGNs (blue circles), and SFGs (green crosses). The black line encloses the "Donley wedge" (Donley et al., 2012); sources whose AGN emission dominates the MID-IR populate this region. The black cross on the top left shows the typical uncertainties. Colour-colour tracks of a 13 Gyr old elliptical galaxy (long dashed line), a spiral galaxy (dot-dashed line), a Seyfert 2 galaxy (dashed line), and a Type 1 QSO (dot-dot-dashed line) (Polletta et al., 2007) in the redshift range 0.1–3 are also plotted.

4.3.4 Unidentified sources

There are 44 sources without any optical, IR or X-ray counterpart. For these, the only information we have is the radio flux density. All but four of them (RID 1, 78, 853, and 865) have been observed by the FIDEL survey and hence we have an upper limit on their 24 μm flux density. Having no information about the source redshift we assume $z=3$ (see discussion in Section 4.3.3) to find additional RL AGNs. Out of the 40 sources for which we can compute an upper limit on the $q_{24\text{obs}}$, we classify four more objects as RL AGNs.

Note that sources without redshift and unidentified sources are not included in the host galaxy properties analysis presented in Section 4.5 since no reliable morphology, stellar mass, and colours can be derived for these sources. Therefore, the possible overestimation of the number of SFGs discussed above should not effect our results.

4.3.5 Further checks

We have checked our classifications using additional data such as radio observations at other frequencies and optical and X-ray spectra. These checks are summarized below, from longer to shorter wavelength.

- Inverted radio spectra sources:

The E-CDFS has been also observed in the ATLAS 5.5 GHz survey (Huynh et al., 2012). This survey has an almost uniform sensitivity of $\sim 12 \mu\text{Jy}$ rms with a resolution of $4.9 \text{ arcsec} \times 2.0 \text{ arcsec}$. In the central part of the field, deeper VLA observations at 4.8 GHz are available, down to a rms noise of $7 \mu\text{Jy}$ (Kellermann et al., 2008). We combine these sets of data to compute the radio spectral index, α_r , of our sources. We use the VLA measurements in the central part of the field and the ATLAS ones outside this region. A discrepancy between the flux density measured in the VLA and ATCA surveys has been noted by Huynh et al. (2012). The ATLAS flux densities are about 20 per cent greater than the VLA ones and they have been therefore corrected before computing the spectral indexes. We measured the radio spectral index for a total of 215 sources excluding the multiple component sources as the interpretation of their spectral index is complicated by their core-jet structure. An inverted radio spectrum ($\alpha_r < 0$) is the signature of compact core emission typical of radio AGNs (e.g., Kellermann & Pauliny-Toth, 1969). Only one source (RID 640) with a reliable inverted radio spectrum has been initially classified as an SFG. It lies at the bottom of the SFGs locus shown in Fig. 4.2, and has therefore been re-classified as a RL AGN.

- VLBA sources:

Middelberg et al. (2011) have detected 21 VLA-CDFS sources with the Very Long Baseline Array (VLBA) using a resolution of $\sim 0.025''$. With a flux density limit of $\sim 0.5 \text{ mJy}$, very long baseline interferometry (VLBI) detections above $z > 0.1$ are most likely to be due to AGN. Reassuringly, all of the 20 detected VLBA objects

with $z > 0.15$ had been classified as RL AGN by our method. The single object with $z < 0.15$ ($z = 0.08$) has a VLBI detection offset from the centre of the galaxy and quite a low core radio power ($\sim 5 \times 10^{21} \text{ W Hz}^{-1}$) and was therefore classified as an SFG by Middelberg et al. (2011), in agreement with our classification.

- Optical spectra:

The presence of broad lines or high excitation emission lines in optical spectra is another indicator of AGN activity. Therefore, we inspected the spectra of the sources that we classify as SFGs, when available. Out of the 100 spectra that we inspected, none have broad emission lines and only one (RID 618) shows a high excitation emission line (NeV). Therefore, we changed its classification to a RQ AGN. Many diagnostic methods based on line ratios, such as the Baldwin, Phillips & Terlevich (BPT) diagram (Baldwin et al., 1981), have been proposed in the literature (e.g., Kauffmann et al., 2003; Smolčić et al., 2006; Best & Heckman, 2012). The spectral coverage of the optical spectra makes these methods feasible only for local sources ($z < 0.3$). In our sample, only 4% of the sources have the required redshift and a good quality spectrum available. Therefore we do not have the data for a statistically significant comparison with the spectral line ratio diagnostic methods.

- R values:

The ratio between the rest-frame radio-to-optical flux density ratio R can also be used as an indicator of radio loudness (e.g. Kellermann et al., 1989). Following Padovani et al. (2009) we define R as the logarithm of the ratio between the rest frame flux density at 1.4 GHz and in the V band, which means that the “classical” dividing line between radio-loud and radio-quiet AGN is at $R \sim 1.4$. The numerator is computed using the observed radio spectral index, where available, or assuming $\alpha_r = 0.7$ in case of sources with no detection at 6 cm, while the K-correction for the V-band flux density is computed interpolating the observed optical photometry at the rest frame V-band wavelength. The optical photometry for our sources is taken from Cardamone et al. (2010) and Taylor et al. (2009). We obtained an estimate of R for a total of 574 source. The others have no detection in the observed optical and NIR wavelength (K-band) or lack a redshift estimate. The R values are plotted versus q_{24obs} in Fig. 4.4. At $z < 1$, SFGs and RQ AGNs are both characterized by low values of R , with mean of 0.5 and 0.6, respectively. These values increase as the redshift increases. This behaviour is due to our flux density limit: at high redshift we can detect only galaxies with high star formation rate. Such sources are usually dusty and, for a given optical luminosity, have higher infrared emission. Therefore, they can have R values as high as 2 but, at the same time, follow the radio-far-infrared correlation indicating that they radio emission is due to star formation rather than to the presence of a RL AGN. On the other hand, RL AGNs span a wide range of R values at all redshift. Therefore we do not apply a cut in R to separate RQ and RL AGN since these include radio quasars and radio galaxies.

- PAH:

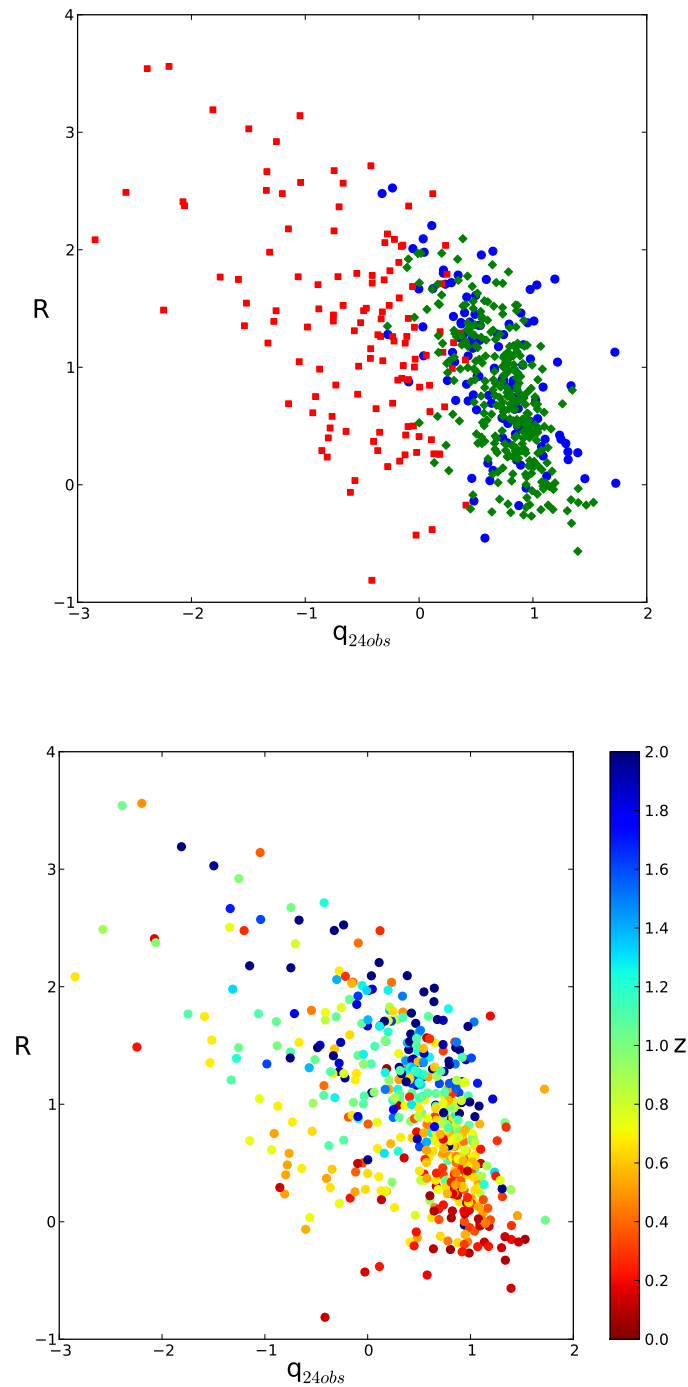


Figure 4.4: R versus q_{24obs} . In the left panel the different symbols correspond to the three classes of sources: RL AGN (red squares), RQ AGN (blue circles), and SFG (green diamonds). In the right panel the colour scale indicates the redshift.

The top left region in the IRAC colour-colour plot in Fig. 4.3, $\text{Log}(S_{8.0}/S_{4.5}) > 0.3$ and $\text{Log}(S_{5.8}/S_{3.6}) < 0$, is populated by sources whose SED is dominated by the Polycyclic Aromatic Hydrocarbons (PAH) features, typical of SFG. In particular, only low redshift SFG have IRAC colours that fall in this region since higher redshift objects tends to move to the bottom part of the plot. Only two (RID 568 and 438) among the ~ 80 sources in this region are classified as RL AGNs according to their $q_{24\text{obs}}$ value. All the others are SFGs according to our classification scheme. For these two objects it is possible that the $24\ \mu\text{m}$ flux density is underestimated. Indeed, the FIDEL catalogue is obtained using aperture photometry, and for local extended sources some of the flux density might be lost. These two sources has been reclassified as SFGs (in Fig. 4.2 they are the only two green points below the SFG locus).

- X-ray spectral analysis and variability:

Tozzi et al. (2009) and Vattakunnel et al. (2012) performed a full X-ray spectral analysis for the X-ray detected radio sources in the E-CDFS. They considered as further diagnostics to discriminate between AGNs and SFGs the intrinsic absorption in the X-ray spectrum and the presence of the iron emission line. Indeed, the detection of a significant intrinsic absorption reveals that the X-ray flux is dominated by nuclear emission (e.g., Alexander et al., 2005; Brightman & Nandra, 2011). We adopt as a threshold a column density of $10^{22}\ \text{cm}^{-2}$. Out of the 87 sources above these threshold, only three (ID 143, 397, and 734) were initially considered SFGs. We changed their classification to RQ AGNs. Another strong indicator of nuclear activity is the presence of a K-shell Fe line at 6.4 keV in the source spectra (e.g., Nandra & Pounds, 1994). Four sources, that were initially classified as SFGs, have a clear detection of the Fe line and were therefore re-classified as RQ AGN. Finally, the time X-ray variability is another signature of the presence of an AGN. A total of 23 sources in our sample have X-ray variability with high confidence level ($> 97\%$) (Paolillo et al., 2004, Paolillo et al. 2013, in prep.). They were all already classified as AGNs according to our criteria.

To summarize, only 11 sources needed to be reclassified, supporting the validity of our classification method described in Section 4.3.2. The majority of them (6/11) are RQ AGNs that were previously classified as SFGs: in such systems only the X-ray spectral analysis has revealed the clear presence of an AGN, while the other indicators were inconclusive.

4.3.6 Results

According to the criteria described in the previous sections, out of the 883 radio sources, we identify 173 (19%) RL AGNs, 208 (24%) RQ AGNs, and 502 (57%) SFGs.

Table 4.1: Classification of radio sources. A full version of the Table is available in the journal on-line material.

(1)	(2)	(3)	(4)	(5)	(6)	(7)	(8)	(9)	(10)	(11)	(12)	(13)
RID	RA	DEC	Class	z	Pr	Lx	$q24_{obs}$	$\log(S_{5.8}/S_{3.6})$	$\log(S_{8.0}/S_{4.5})$	α_r	B Mag	QF
601	03:32:48.18	-27:52:56.60	RQ AGN	0.67	22.79	42.68	0.62	0.53	0.53	—	-22.77	3
602	03:32:48.30	-27:56:26.91	SFG	0.35	22.53	<41.44	0.69	0.61	1.18	0.8	-22.08	2
603	03:32:48.57	-27:49:34.36	SFG	1.12	23.69	41.86	0.07	0.63	0.62	0.4	-22.00	2
604	03:32:49.19	-27:40:50.49	RL AGN	1.22	25.63	43.61	-0.42	2.53	2.76	0.8	-23.79	3
605	03:32:49.22	-28:03:44.64	RQ AGN	0.64	22.89	42.44	0.86	1.09	1.16	—	—	3
606	03:32:49.33	-27:58:45.19	SFG	2.21	24.84	<42.96	0.16	1.25	1.49	0.8	-24.61	1
607	03:32:49.39	-27:36:36.22	SFG	0.64	22.87	<42.28	1.03	0.75	0.92	—	-22.31	1
608	03:32:49.42	-27:42:35.14	RL AGN	0.98	25.36	<42.12	-1.25	0.56	0.78	1.3	-22.33	3
609	03:32:49.92	-27:34:45.69	SFG	0.25	22.59	<41.20	0.95	0.79	4.37	—	-21.16	3
610	03:32:49.95	-27:34:32.74	SFG	0.25	22.86	<41.11	0.81	0.75	3.52	0.8	-22.05	3
611	03:32:50.84	-27:31:41.16	SFG	—	—	—	0.54	1.22	1.36	—	—	1
612	03:32:50.86	-28:03:17.64	SFG	0.10	21.34	<40.57	1.08	0.72	5.23	—	-18.91	3
613	—	—	SFG	—	—	—	<-0.02	—	—	—	—	1
614	03:32:51.59	-27:59:18.46	SFG	0.91	23.15	<42.42	1.16	0.79	0.98	—	-22.85	1
615	03:32:51.65	-27:39:36.79	RL AGN	0.78	23.56	—	0.20	1.07	0.70	1.8	-20.70	3
616	03:32:51.73	-27:49:51.02	SFG	0.74	22.89	<41.80	0.88	0.84	0.87	—	-22.00	3
617	03:32:51.79	-27:59:56.18	SFG	0.53	22.95	<41.96	0.78	0.90	1.15	—	-20.43	3
618	03:32:51.84	-27:44:36.78	RQ AGN	0.52	22.85	<41.40	1.08	1.01	2.02	0.1	-22.29	2
619	03:32:51.83	-27:42:29.49	RQ AGN	1.03	23.44	42.58	0.88	0.68	1.00	—	-23.18	3
620	03:32:52.07	-27:44:25.12	RL AGN	0.53	23.00	41.20	<-0.80	0.48	0.38	-0.1	-22.37	3

In Table 4.1 we report the classification for each radio source together with the information used to identify it. The identification number (column 1) corresponds to that given in Miller et al. (2013) and Bonzini et al. (2012). The position of the optical-IR counterpart is given in column 2 and 3 (Bonzini et al., 2012). The table also includes the source redshift (5), the logarithm of the radio luminosity in W Hz^{-1} (6), the logarithm of the unabsorbed X-ray luminosity in erg s^{-1} (for undetected sources a 3σ upper limit is given) (7), $q_{24\text{obs}}$ (8), the IRAC-colours (9 and 10), the radio spectral index (assumed to be $= 0.7$ when not available) (11), and the rest frame absolute B magnitude (12). We also define a quality flag (QF) which ranges from 3, for secure classification, to 1, for a tentative classification (column 13). Sources for which all the criteria agree (or are not in contradiction) have $\text{QF}=3$ (45% of the sources). We assign a $\text{QF}=2$ to sources with $q_{24\text{obs}}$ value just above the RL AGNs threshold ($q_{24\text{obs},M82} - 2\sigma < q_{24\text{obs}} < q_{24\text{obs},M82} - 1\sigma$). Sources without redshift but with clear signature of AGN activity (e.g., in the Donley wedge or with very low values of $q_{24\text{obs}}$ value) have also $\text{QF}=2$. A total of 18% of the sources have $\text{QF}=2$. The remaining sources have classification with $\text{QF}=1$. Examples of this last category are sources without redshift and without clear signature of AGN activity or without an optical/IR counterpart. Also sources with upper limits on the X-ray luminosity $> 10^{42} \text{ erg s}^{-1}$, not in the Donley wedge, and above the RL AGN threshold have $\text{QF}=1$. These sources are classified as SFGs but, even if we can exclude that they are RL AGNs, there might be a contamination from RQ AGNs. Deeper X-ray observations are needed to discriminate between the two classes of sources.

In Fig. 4.5 we show the radio power distribution for the three classes of sources. The distribution of the RL AGNs is the widest since it includes both low power radio galaxies and the most powerful radio AGNs. This means that with a simple cut in P_r one would exclude a significant fraction of RL sources. We also note that only 44 RL AGN out of a total of 177 have X-ray luminosity greater than $10^{42} \text{ erg s}^{-1}$ (35 sources) or are MID-IR selected AGN (9 sources). All the other are identified as AGN only based on their radio emission through the $q_{24\text{obs}}$ parameter. We expect most of these X-ray undetected AGN to be intrinsically X-ray faint low power radio galaxies (e.g., Padovani, 2011), but there could also be a fraction of heavily obscured sources (e.g., Del Moro et al., 2013). Radio observations are almost unaffected by dust extinction and therefore we can in principle detect even the most obscured systems. The mean radio power for SFGs is $\sim 10^{23} \text{ W Hz}^{-1}$ but there are also galaxies with P_r as high as $10^{24.5} \text{ W Hz}^{-1}$. These sources have all redshift > 2 but $\text{QF} = 1$.

We stress that our classification scheme tends to overestimate the number of SFGs. We consider AGNs only those sources that have strong evidences of the presence of an AGN in one of the wavelength range considered: radio, MIR, and X-ray.

With this new scheme we confirm 80% of the classification for the sample of 193 sources presented in Padovani et al. (2011b). The remaining sources were reclassified because of new redshift measurements, different optical/infrared counterparts, deeper X-ray data, and deeper $24 \mu\text{m}$ data, that allowed us to compute their q -value, whereas previously only an upper limit was available.

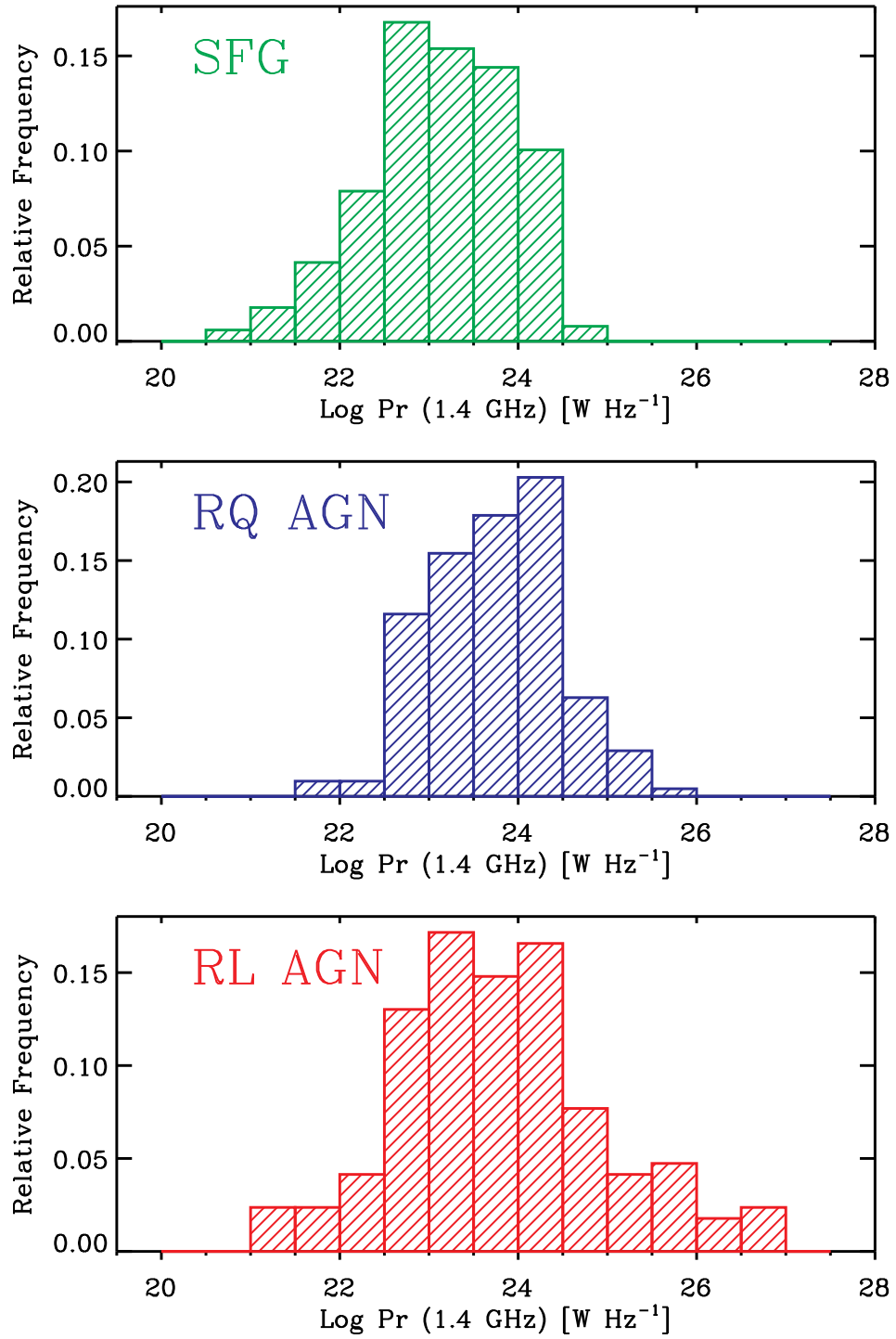


Figure 4.5: Radio power distribution for SFGs (top), RQ AGN (middle), and RL AGN (bottom).

4.4 The sub-mJy population

To investigate the relative contribution of the different source types to the radio population as a function of flux density, we exclude the outermost part of the field, since there we do not have enough ancillary multi-wavelength data to provide reasonable photometric redshift and therefore the classification of the sources is more uncertain. We then consider the sub-sample within an area of 0.282 deg^2 where we have photometric redshift coverage (see Bonzini et al., 2012, for details), which includes 779 radio objects for which we have redshift for 90% of the sources with optical/IR counterpart (compared to the 81% of the whole radio sample). We consider radio sources down to an rms noise of $6.5 \mu\text{Jy}$, or a 5σ flux density limit of $32.5 \mu\text{Jy}$. The sensitivity of our sample is somewhat a function of the position in the field, although a much less strong one than for the CDFS sample of Kellermann et al. (2008). Consequently, the area of the sky covered at any given flux density is flux density dependent (see Miller et al., 2013). To estimate the relative fractions of sources as a function of flux density we therefore weigh each source by the inverse of the fraction of the area corresponding to that value. The results are plotted in Fig. 4.6, which shows that AGNs dominate at large flux densities ($> 1 \text{ mJy}$) but SFGs become the dominant population below $\approx 0.1 \text{ mJy}$. Similarly, radio-loud AGNs are the predominant type of AGNs above 0.1 mJy but they drop fast at lower flux densities.

In more detail, AGNs make up $43 \pm 4\%$ (where the errors are based on binomial statistics: Gehrels, 1986) of sub-millijansky sources and are seen to drop at lower flux densities, going from 100% of the total at $\sim 10 \text{ mJy}$ down to 39% at the survey limit. SFGs, on the other hand, which represent $57 \pm 3\%$ of the sub-millijansky sample, are missing at high flux densities but become the dominant population below $\approx 0.1 \text{ mJy}$, reaching 61% at the survey limit. Radio-quiet AGNs represent $26 \pm 6\%$ (or 60% of all AGNs) of sub-millijansky sources but their fraction appears to increase at lower flux densities, where they make up 73% of all AGN and $\approx 30\%$ of all sources at the survey limit, up from $\approx 6\%$ at $\approx 1 \text{ mJy}$. These results are in good agreement with those of Padovani et al. (2011b).

4.5 Host galaxy properties

4.5.1 Morphology

A fraction of our sample has ACS/HST images available. We use this sub-sample to characterize the morphology of the host galaxy of our sources. We obtain the morphological information from the publicly available ACS-GC catalog (Griffith et al., 2012). The ACS images have been fitted with the GALAPAGOS method (Häußler et al., 2011) that analyses the images through the GALFIT code (Häussler et al., 2007). The GALFIT code models each source with a Sérsic profile (Sérsic, 1963), a parameter that describes the intensity profile of a galaxy, after a convolution with a point-spread function. In particular, we consider the results of the fit performed on the z-band (F850LP) ACS images. At the average redshift of our sample ($z = 1.1$), this filter corresponds to rest-frame B band.

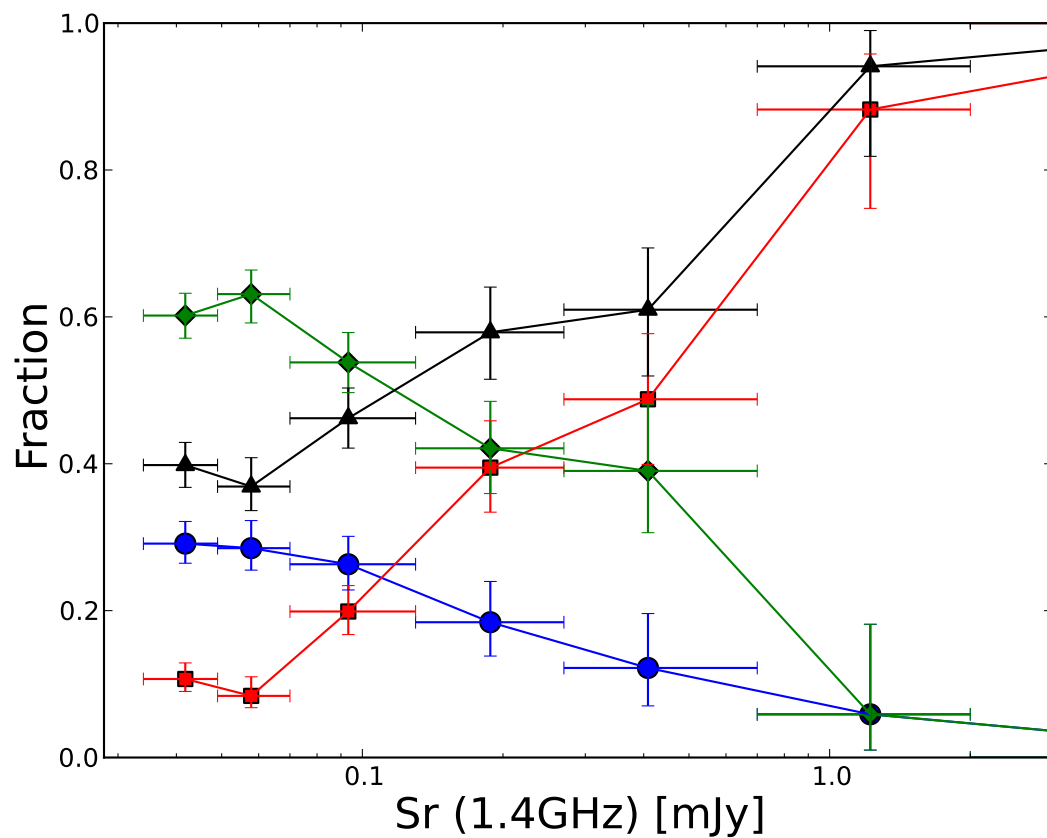


Figure 4.6: Relative fraction of the various classes of radio sources: SFGs (green diamonds), all AGN (black triangles), radio-quiet AGN (blue circles), and radio-loud AGN (red squares). Error bars correspond to 1σ Poisson errors (Gehrels, 1986).

We exclude from our analysis all the sources for which GALFIT gives an unreliable fit (FLAG=1 in the Griffith et al. (2012) catalog). Moreover, sources with z-band magnitude ≥ 24 suffer large uncertainties on the Sèrsic index measurements and are therefore excluded. Finally we remove also low surface brightness galaxies since they are known to produce unreliable results (Griffith et al., 2012).

The total number of objects with good fit results is 362. Of these, 75 are RL AGNs, 60 RQ AGNs and 227 SFGs. The average redshift of this sub-sample is 0.76. For these sources we have an estimate of the Sèrsic index, which is generally lower for late type galaxies, where the disk dominates the intensity profile, and larger in elliptical galaxies.

The Sèrsic index distribution for the three classes is shown in Fig. 4.7. The majority of RQ AGNs and SFGs have Sèrsic indexes < 2 implying that the host galaxies of both classes are preferentially late-type objects. The distribution for the RQ AGNs is broader than the one of SFG, but it is important to note that the results of the GALFIT fit tend to overestimate the Sèrsic index in the presence of bright central point source (Gabor et al., 2009). Therefore, the brightest QSOs among the RQ AGNs can produce a tail at high Sèrsic indexes in the RQ distribution. RL AGNs Sèrsic indexes instead peak around 4, a value typical of galactic bulges and early-type galaxies. Performing a Kolmogorov-Smirnov test (KS-test) we find a significant difference ($> 99.9\%$) between the Sèrsic index distribution of RL AGNs and the other two classes. This result suggests that the host galaxies of RL AGNs are morphologically different from the host galaxies of RQ AGN and SFG: RL AGN are preferentially hosted in elliptical galaxies while RQ AGN and SFG are found in late-type galaxies.

4.5.2 Stellar masses

To estimate the stellar mass of the host galaxies we used an SED fitting technique. We modeled the observed photometry with two components: a galactic and an AGN component as in Bongiorno et al. (2012). For the AGN component we use the Richards et al. (2006) mean QSO SED. We applied an SMC-like dust-reddening law (Prevot et al., 1984) and we consider different amount of dust extinction, $E_{AGN}(B - V)$, from 0 to model unobscured, type I AGN, to 9 for the most obscured, type II sources, in steps of 0.1. For the galactic component we use the stellar population synthesis models of Bruzual & Charlot (2003). Assuming a universal initial mass function from Chabrier (2003), we generate SEDs assuming different star formation histories (SFH): ten exponentially declining SFH ($SFR \propto e^{-Age/\tau}$) with e-folding times (τ) ranging from 0.1 to 30 Gyr, four models with constant SFR (1, 5, 10, 50 $M_{\odot} \text{ yr}^{-1}$) and five models with rising SFH ($\tau = -0.5, -1, -5, -10, -15$). For each SFH, we generate SEDs for different ages from 50 Myr to 9 Gyr. We exclude the models with age larger than the age of the Universe at the source redshift. For the galactic component we assume a Calzetti's reddening law (Calzetti et al., 2000). We consider colour excess $E_{gal}(B - V)$ in the range $0 \leq E_{gal}(B - V) \leq 0.5$ in steps of 0.1. We impose the prior that $E_{gal}(B - V) < 0.15$ if $Age/\tau > 4$ to exclude models with large dust extinction in absence of a significant star formation rate (Fontana et al., 2004; Pozzetti et al., 2007).

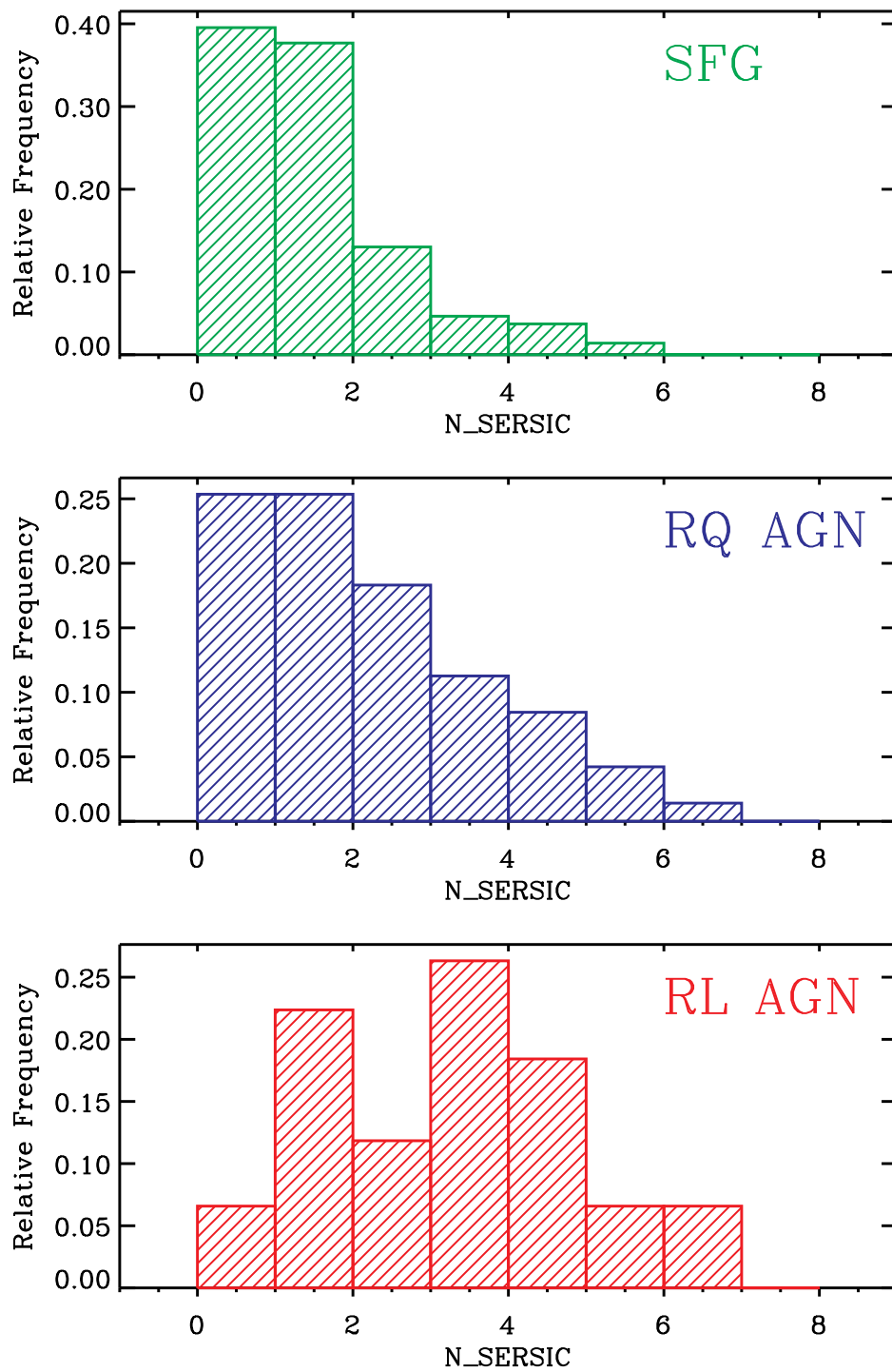


Figure 4.7: Sersic index distribution for SFGs (top), RQ AGN (middle), and RL AGN (bottom).

The observed flux is modelled as the sum of the AGN and galactic component such as:

$$f_{obs} = af_{AGN} + bf_{GAL}, \quad (4.2)$$

where a and b are the normalization constants for the two templates. The best fit template combination and normalization are found using a standard χ^2 minimization. The photometry for our radio sources is taken from the BVR selected Cardamone et al. (2010) catalogue. We matched their catalogue with the position of our counterparts using a searching radius of $0.2''$ and we found 569 matches. For the remaining sources we use the photometry from the K selected Taylor et al. (2009) catalogue. We found 78 additional matches. Finally, for those sources not detected in both the BVR and K selected catalogues, we use the photometry from the Damen et al. (2011) IRAC selected SIMPLE catalogue. We found 145 more sources but only 24 of them have a redshift and can therefore be used in the fitting procedure.

We fitted all sources with known redshift and at least eight photometric points in the wavelength range from the U-band to the $24\mu\text{m}$ for a total of 655 sources (23% RL AGNs, 23% RQ AGNs, 54% SFGs). Two examples of the fitting results are shown in Fig. 4.8.

From the best fit galaxy model we derived the stellar mass of our galaxies. We excluded 24 sources whose flux density in the rest-frame K-band is dominated by the AGN ($f_{AGN} > 2f_{GAL}$), since the stellar mass measurement in these cases is too uncertain. The stellar mass distributions for the three classes are plotted in Fig. 4.9. Our radio selected SFGs have typical stellar masses of $10^{10.5}M_{\odot}$. The RL AGNs have on average higher stellar masses ($10^{11}M_{\odot}$) and a KS-test shows that the stellar mass distribution of RL AGNs is different from the SFGs one at the $>99.9\%$ level. RQ AGN host galaxies have stellar masses slightly higher than SFGs hosts. However, a KS-test shows that the mass distributions of SFGs and RQ AGNs are not significantly different. Moreover, it is important to note that most of our RQ AGNs (76%) are identified as AGN as their total X-ray luminosity is above $10^{42} \text{ erg s}^{-1}$. It has been suggested in recent works (e.g., Aird et al., 2012; Bongiorno et al., 2012) that a threshold in X-ray luminosity introduces a bias towards higher host galaxy stellar masses. The probability of a galaxy hosting an AGN of a given Eddington ratio is independent of stellar mass and the number density of AGNs increases for decreasing Eddington ratio. Therefore in a flux density limited sample, one can detect AGNs of low Eddington ratios only in the most massive galaxies. Considering this bias, we cannot conclude that the host galaxy of RQ AGNs are intrinsically different from the SFGs ones.

We also note that only 20% of our RL AGNs have X-ray luminosity greater than $10^{42} \text{ erg s}^{-1}$ and therefore their high stellar masses cannot be explained by this effect. We then confirm the tendency of RL AGNs to be hosted in the most massive objects (e.g., Dunlop et al., 2003; Best et al., 2005).

4.5.3 Rest Frame colours

From the best-fit galaxy model we derived the rest frame U-B colours. These colours are commonly used to distinguish between evolved stellar population galaxies, that populate

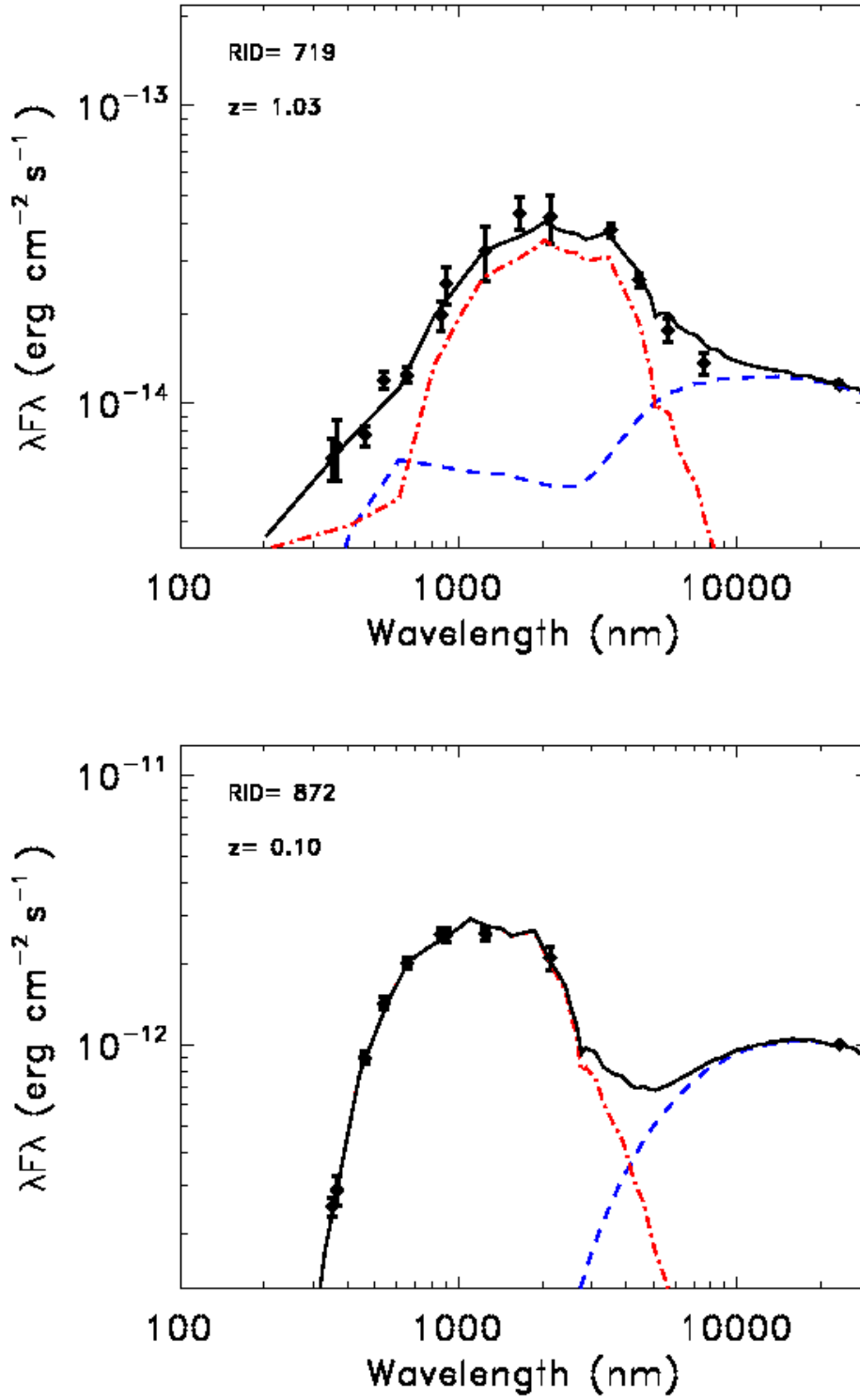


Figure 4.8: Two examples of 2-component SED fit results. The galaxy component is plotted with the dot-dashed red line and the AGN component with the dashed blue line.

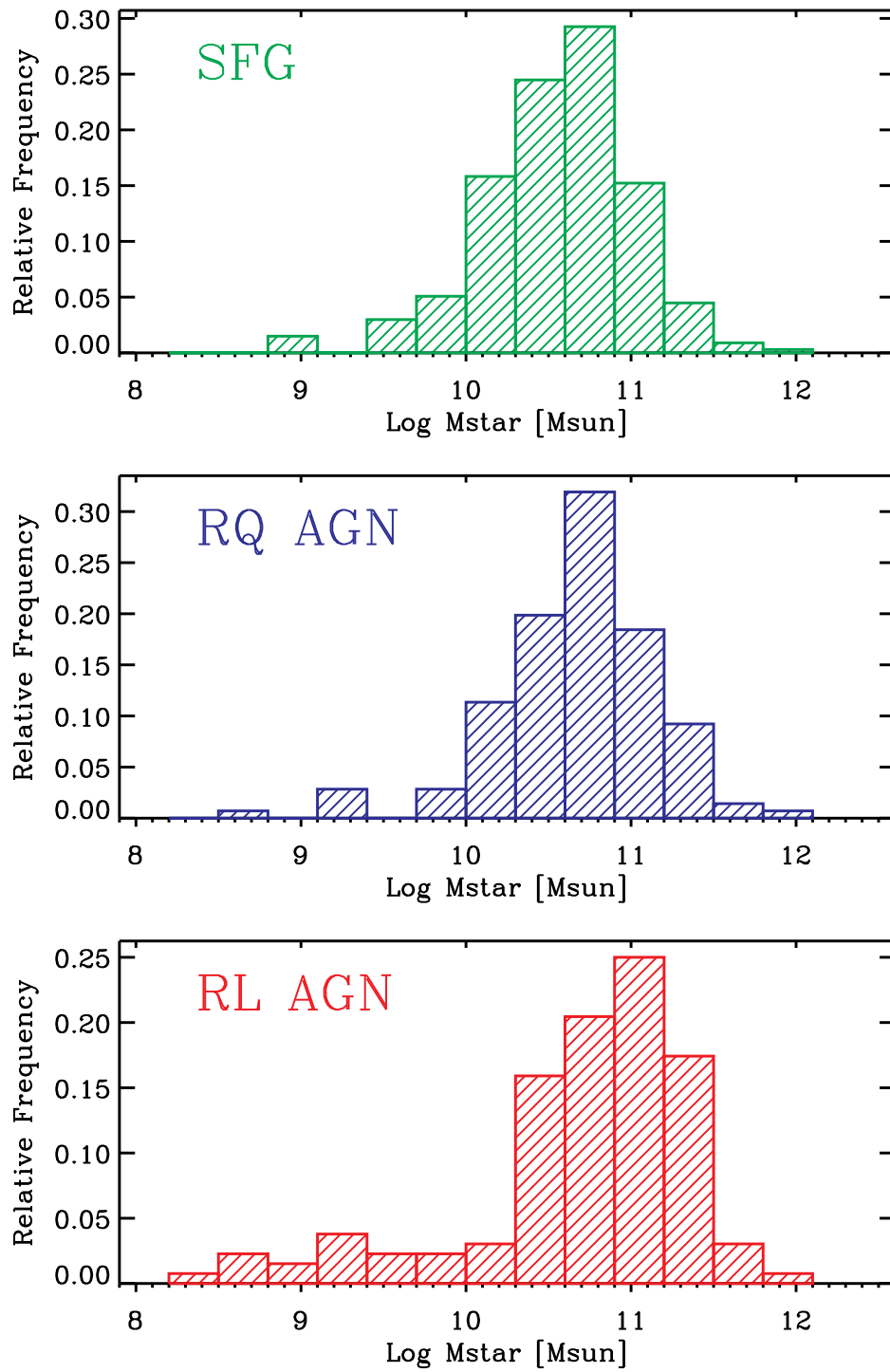


Figure 4.9: Stellar mass distribution for SFGs (top), RQ AGN (middle), and RL AGN (bottom) in units of solar mass.

the so called “red sequence” from young stellar population system usually found in the “blue cloud” (e.g., Bell et al., 2004). In the left panel of Fig. 4.10 we plot the measured rest frame U-B colours as a function of stellar mass. RL AGNs show preferentially red colours confirming previous results (e.g., Dunlop et al., 2003). RQ AGNs and SFGs have instead a wider range of colours occupying both the blue cloud and the red sequence, as well as the region in between, called the “green valley.” But the red colours in these type of systems should probably be interpreted as a signature of dust obscuration rather than as an indication of old stellar population. This can be tested by considering the de-reddened colours. The intrinsic colours are derived from the best-fit galaxy model corrected for dust extinction. The latter are shown in the right panel of Fig. 4.10 as a function of the stellar mass. Comparing the left and right panel, we see more clearly the impact of dust reddening: RL AGNs hosts, intrinsically characterized by old stellar population, are nicely displayed along the red sequence, while SFGs and RQ AGNs have moved towards bluer colours. In particular, it is interesting to note how the two type of radio AGNs have very different host galaxies properties, in agreement with what was found from considering their morphology (see Section 4.5.1).

Rest-frame optical colours as classification method

Smolčić et al. (2008) present a method to separate SFGs from AGNs, based on the rest-frame optical colours. This makes use of the rest frame colour P1 that is a linear combination of the colours obtained from the modified Strömberg filters, as described in Smolčić et al. (2006). In particular, according to Smolčić et al. (2008), a source with $P1 < 0.15$ is classified as SFG while it is an AGN otherwise. This method does not apply to QSO defined as point-like sources in the optical image (Smolčić et al., 2008). Therefore, we concentrate on the sub-sample described in Sec.4.5.1 for which the results of the GALFIT analysis Griffith et al. (2012) are available and with known redshift. After removing the point-like sources we are left with 336 objects. We computed the rest-frame P1 colour for these sources from the best fit of the SED as in Smolčić et al. (2008). We find that this method recovers about 70% of our RL AGNs, but only 25% of our RQ AGNs. As described in Section 4.3.2, our RQ AGNs show clear evidences of AGN activity in the X-ray or in the MIR. The reason why these sources can easily be misclassified by a method based on optical colours is that the host galaxy can dominate the total emission at these wavelength. RQ and RL AGNs have, on average, different host galaxy properties (see Sec. 4.5); therefore using the rest-frame optical colours it is possible to identify the RL AGN hosted in red, old galaxies, while it is hard to find RQ AGNs as they share the same parameter space as SFGs.

4.5.4 The 4000 Å break

The strength of the 4000 Å break (D_{4000}) is a proxy for the mean stellar age of a galaxy. In Best et al. (2005) it has been used to separate starburst galaxies from RL AGNs. We computed the D_{4000} for our sources from the best fit galaxy template obtained as described

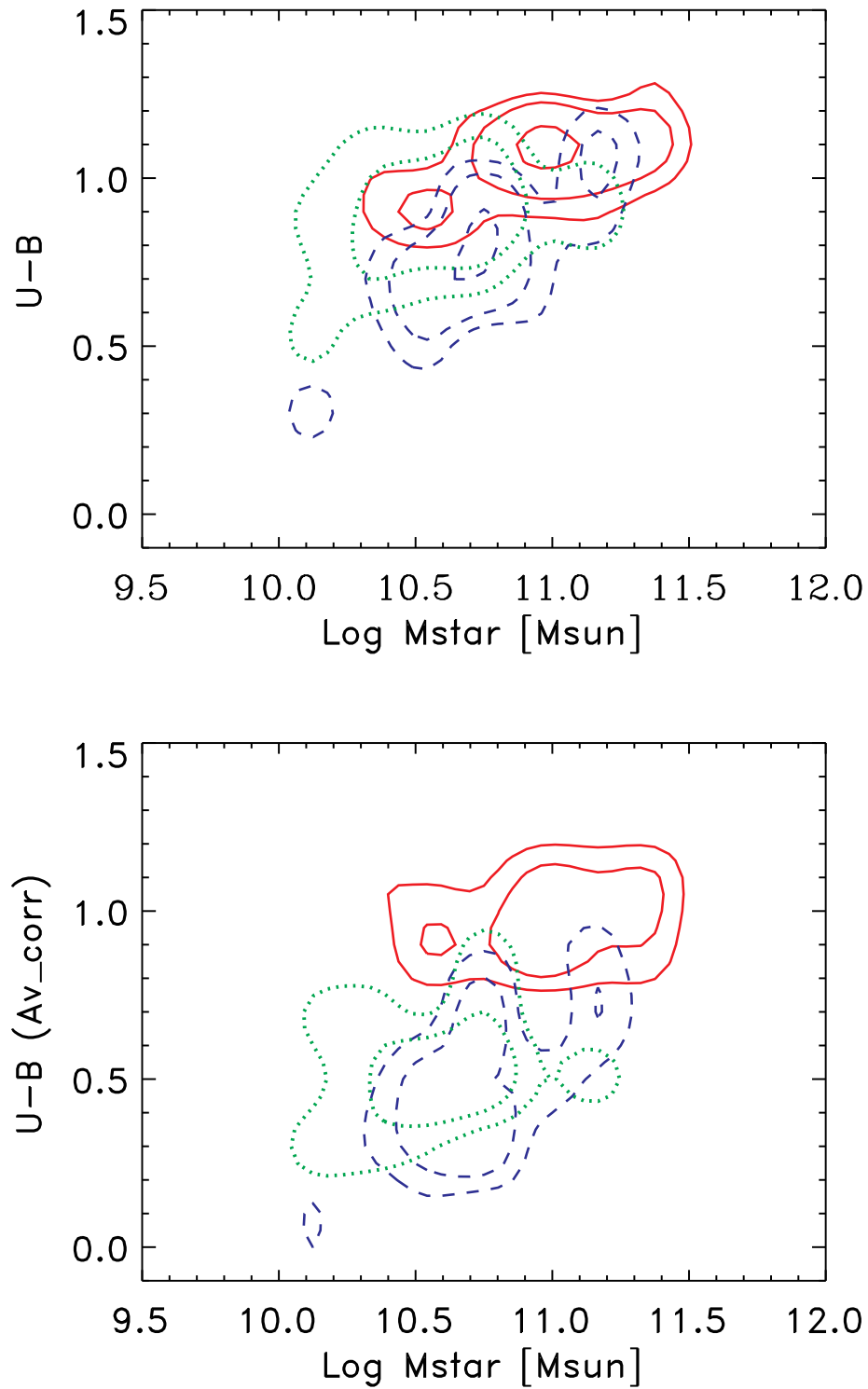


Figure 4.10: Observed rest-frame U-B colours (left panel) and rest-frame U-B colours corrected for dust extinction (right panel) as a function of stellar mass for RL AGNs (red solid contours), RQ AGNs (blue dashed contours), and SFGs (green dotted contours).

in Sec. 4.5.2. Deriving this quantity from the photometry, the uncertainties are large (~ 0.1) as discussed in e.g., Smolčić et al. (2008). In Fig. 4.11, D_{4000} is plotted as a function of the 1.4 GHz luminosity normalized by stellar mass. The dashed line marks the separation between RL AGNs and starburst galaxies as defined in Best et al. (2005). The majority (65%) of our RL AGNs lie above the separation line, in agreement with what expected for classical RL. The RL AGNs below this line are on average less powerful and the host masses are smaller. A total of 86% of our SFGs are below the separation line. Given the large uncertainties on our D_{4000} measurements due to the lack of spectroscopy, we can conclude that our classification method is in good agreement with the one proposed by Best et al. (2005). We confirm that the strength of the 4000 Å break can be successfully used to separate SFGs from RL AGNs, especially for sources with large stellar masses. Note that also in the D_{4000} vs. $L_{1.4\text{GHz}}/M_*$, RQ AGNs share the same parameter space with SFGs. Indeed, 83% of our RQ AGNs are below the starburst–AGN separation line, indicating the presence of a young stellar population in their hosts. One more time we stress the need of a multi-wavelength approach to identify this population of AGNs, whose emission can be overshadowed by the host galaxy one or be heavily absorbed at optical wavelength.

4.6 Discussion

4.6.1 Selection caveats

As already mentioned, the major source of uncertainty in our scheme comes from the possible misclassification of low luminosity RQ AGNs as SFGs where we do not have deep X-ray observations. To get a rough estimate of the magnitude of this effect, we considered only the area covered by the 4 Ms Chandra observations (i.e., the 7' radius around the center). In this region we have a flux density limit for the hard X-ray band of $\sim 3.2 \times 10^{-17} \text{ erg cm}^{-2} \text{ s}^{-1}$ (Xue et al., 2011) and we find 43 RQ AGNs and 63 SFGs. Using the flux density limit of the 250 ks observations ($\sim 5.5 \times 10^{-17} \text{ erg cm}^{-2} \text{ s}^{-1}$; Lehmer et al., 2005) we would not detect 12 RQ AGNs that therefore would have been classified as SFGs having only an upper limit on their X-ray luminosity. From this comparison we can estimate that the contamination to the SFG population from RQ AGN in the outer part of the field is $\sim 16^{+7}_{-5}\%$ ($12/(63+12)$).

A second source of contamination in our selection scheme can come from RL AGNs being classified as RQ AGNs due to strong $24\mu\text{m}$ emission related to AGN heated dust. Indeed a strong contribution to the $24\mu\text{m}$ from the AGN can boost the $q_{24\text{obs}}$ value in the SFGs/RQ AGNs locus at a given radio flux density. At $z \sim 1$, the mean redshift of our sample, the $24\mu\text{m}$ emission correspond to a rest frame $12\mu\text{m}$ emission. To estimate the AGN contribution to the total flux density at this wavelength we use the correlation found by Gandhi et al. (2009) between the hard band (2–10 keV) X-ray luminosity and the MIR luminosity: $\log L_{\text{MIR}} = (-4.37 \pm 3.08) + (1.106 \pm 0.071) \log L_{\text{X}}$, where L_{MIR} is the monochromatic luminosity at $12.3\mu\text{m}$, in units of λL_{λ} expressed in erg s^{-1} . This relation holds for both obscured and unobscured AGNs (Gandhi et al., 2009). We then

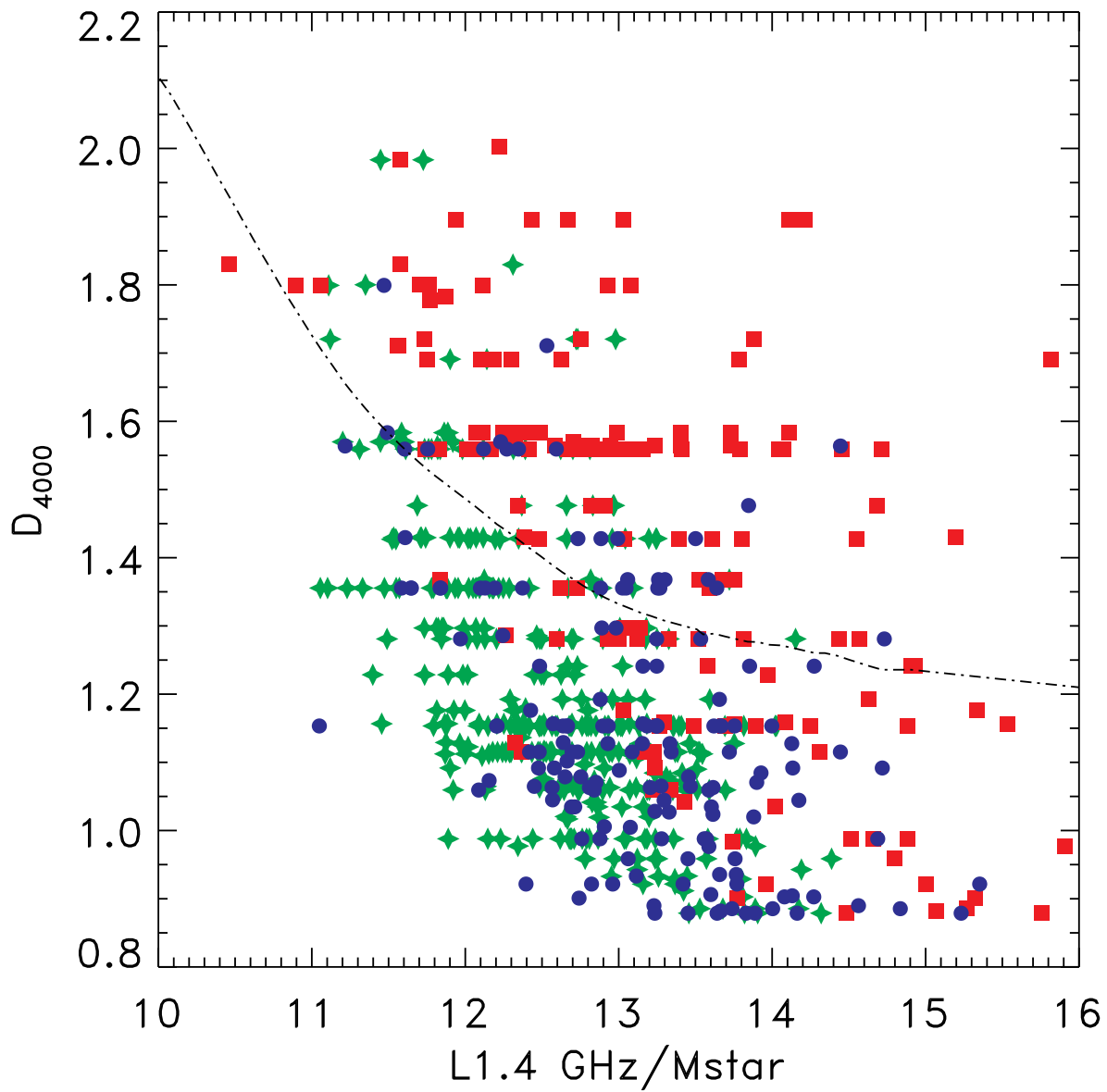


Figure 4.11: Strength of the 4000 Å break as a function of the 1.4 GHz luminosity normalized by stellar mass for RL AGNs (red squares), RQ AGNs (blue circles), and SFGs (green crosses). The dashed line correspond to the separation between RL AGN and SFG as defined in Best et al. (2005).

subtract the corresponding flux density from the measured $24\mu\text{m}$ one and re-computed the $q_{24\text{obs}}$ value, corrected for the AGN emission, for all our RQ AGNs in the redshift range $0.85 < z < 1.15$ (20 objects). We find that only one object would be classified as RL AGN after the correction for the AGN emission of the $q_{24\text{obs}}$ value. Therefore, we can estimate that the contamination of the RL AGN population from RQ AGN is $\approx 5\%$.

4.6.2 Host galaxies properties vs. radio loudness

Focusing our attention on the AGN population, we can study the properties of AGN host galaxies as a function of radio loudness.

While we find that RL AGNs are preferentially hosted in high stellar mass galaxies, we do not observe a similar trend for RQ AGNs (Sect. 4.5.2). Both the morphology and the rest-frame optical colours show a clear separation between the two types of AGNs. RL AGNs are preferentially found in elliptical galaxies (Sèrsic index ~ 4), while RQ AGNs have usually lower Sèrsic indexes typical of late-type galaxies (Section 4.5.1). In Section 4.5.3, we computed the rest-frame optical colours from the results of the two component (AGN+galaxy) SED fitting. We note that since the rest-frame colours are computed from the best-fit galaxy template only, we minimize the contamination from the AGN emission itself (see Bongiorno et al., 2012, for a more detailed discussion). RL AGNs lie along the red sequence (see Fig. 4.10) suggesting that their host galaxies are old stellar population systems. If we look at the measured rest-frame U-B colours, we observe that RQ AGNs have a wider range of colours but the red objects are more likely dusty systems rather than old stellar population objects. This appears more clearly when we consider the dust extinction corrected colours (right panel of Fig. 4.10); the intrinsic rest-frame optical colours of RQ AGN are bluer compared to RL AGNs, implying the presence of young stars in the host galaxies of these AGNs. Also in the IRAC colour-colour diagram (Fig. 4.3), we see that RL AGNs are more concentrated in the bottom left part of the diagram. Here, we expect to find passive systems, with a declining power law behaviour across the four IRAC bands (See elliptical colour-colour track in Fig. 4.3) .

Given these differences in the host galaxy properties, we suggest that the RQ and RL activity occurs at two different evolutionary stages of the BH-host galaxy co-evolution. RQ AGN are in an early phase, when the galaxy is gas rich, is still forming stars, has a young stellar population, and the AGN is efficiently accreting. The radio activity of the AGN occurs instead at later times when the galaxy is gas poor, the accretion on the BH is inefficient, the star formation in the host decreases, and the stars get older and redder.

RL AGN can be further divided in high and low excitation sources (e.g., Laing et al., 1994; Baldi & Capetti, 2008; Hardcastle et al., 2007b). The excitation level of a source is usually quantified using a combination of different line ratios (e.g., Best & Heckman, 2012). Given the high redshift of our sample and the incomplete spectroscopic coverage, the excitation parameter can be computed only for very few (< 10) RL AGNs. For these reasons, a detailed discussion about the excitation level of our RL AGNs goes beyond the scope of this paper. In Best & Heckman (2012), the host galaxy properties of high and low excitation RL AGNs have been compared. Low excitation sources are found to have

on average larger D_{4000} and higher stellar masses compared to high excitation sources. Our sample of RL AGNs spans the whole range of D_{4000} found in the Best & Heckman (2012) sample suggesting that it is a mixture of low and high excitation sources. However, given the large uncertainties of our measurement of the 4000 Å break strength and the intrinsic large scatter in the D_{4000} distribution for both low and high excitation sources, a quantitative estimate is not reliable. More recently, it has been found that it is possible to separate low and high excitation radio-loud sources on the basis of their MIR luminosities (Gürkan et al., 2013). They propose an empirical 22 μm luminosity threshold of $5 \times 10^{43} \text{ erg s}^{-1}$ below which almost all the RL AGN are low excitation sources. We extrapolated the 22 μm luminosity from the sources photometry. We find that about 85% of the RL AGN have MIR luminosity typical of low excitation sources. However, this method has not yet been tested for a faint sample as the one presented in this paper. Therefore, this fraction can only be considered a tentative estimate. Finally, we note that all the studies conducted so far on the excitation level of radio sources have been applied only to RL AGNs samples (e.g., Baldi & Capetti, 2008; Hardcastle et al., 2007b; Janssen et al., 2012; Gürkan et al., 2013). For a radio selected sample of RQ AGNs the distinction between low and high excitation sources would be difficult even having good quality optical spectra since the host galaxy can strongly contaminate the optical emission. Also the method based on the MIR luminosity can not be applied as it assumes no contribution from young stars at 22 μm that is usually not true for the hosts of RQ AGNs. Even if RQ AGNs host galaxies are more similar to the one of high excitation sources (e.g., blue colours, small masses), direct measurements of their excitation state have not yet been conducted.

4.6.3 Radio emission in RQ AGN

The origin of the radio emission in RQ AGNs has been debated for a long time. It has been suggested that RQ AGN are a scaled version of RL AGN at lower radio power (e.g., Miller et al., 1993a) or that the major contribution to the radio emission in these systems is due to the star formation in the host galaxy (e.g., Sopp & Alexander, 1991). In particular, in Padovani et al. (2011b) the latter hypothesis was supported by the study of the cosmological evolution and luminosity function. They found that both are significantly different for the two types of AGNs, while they are indistinguishable for SFGs and RQ AGNs.

In this paper, we have characterized the host galaxy properties for the three types of sources. We find that the host galaxy of RQ AGNs and our radio selected SFGs have many similarities. Both RQ AGNs and SFGs have luminosity profiles preferentially with low Sérsic indexes ($n < 2$) suggesting that, on average, both have disk-like morphology. The rest frame optical U-B colours reveal that they are dusty, but intrinsically blue as seen from the comparison of the right and left panels of Fig. 4.10. These results support the hypothesis that the origin of the radio emission is related to star formation processes in both SFGs and RQ AGNs, as proposed in Padovani et al. (2011b) and Kimball et al. (2011). This will be further discussed in coming papers, where we will investigate the star formation activity in the host galaxies of our radio selected RQ AGNs using Herschel data (Bonzini et al., 2014). We will also study the luminosity function and evolution for the

different population of the larger sample considered in this work (P. Padovani et al., in preparation) to be compared with the results of Padovani et al. (2011b).

4.7 Summary and conclusions

The sub-mJy radio population turns out to be a mixture of different kinds of sources due to the synchrotron emission from the relativistic particles accelerated either by the black hole, or associated with star formation processes.

In this work we present a simple scheme, which expands upon that of Padovani et al. (2011b), to disentangle the different populations of the sub-mJy radio sky: RL AGNs, RQ AGNs, and SFGs. We have shown that the ratio between the IR and radio emission, parametrized by the q_{24obs} value, is the key parameter needed to identify RL AGNs. To differentiate between SFGs and RQ AGNs it is instead necessary to consider other AGN activity indicators, namely the X-ray luminosity and the MID-IR observed colours. Classification methods based only on optical properties are inefficient in finding RQ AGNs since their emission can be dominated by the host galaxy or be heavily absorbed at these wavelengths. The simplicity of our scheme makes it suitable to be applied to large radio samples with ancillary X-ray and IR data, without the need of spectroscopic follow-up.

We confirm the increasing predominance at lower flux densities of SFGs, which make up $\sim 60\%$ of our sample down to $\sim 32 \mu\text{Jy}$ and become the dominant radio population below $\approx 0.1 \text{ mJy}$. RQ AGNs are also confirmed to be an important class of sub-millijansky sources, accounting for 26% of the sample and $\sim 60\%$ of all AGNs, and outnumbering RL AGNs at $< 0.1 \text{ mJy}$.

We study the host galaxy properties of the three types of sources. Stellar masses and rest-frame optical colours of the galaxy are obtained using a two component SED fitting technique (galaxy+AGN) that allows us to subtract the AGN contribution. Morphological properties are based on ACS/HST images. We observe differences in the host galaxy properties of RL and RQ AGNs both in the rest frame optical colours and in the morphology. RL AGNs are preferentially hosted in more massive, red, elliptical galaxies, while RQ AGNs have typically stellar masses of $10^{10.5} M_\odot$, bluer colours and late type morphology. This result is in agreement with what is found in previous works and support our classification method. It also suggests that the radio activity associated with the black hole is linked to the properties of the host galaxy. One possible scenario is that they represent two different evolutionary stages of the BH-galaxy evolution. In the RQ phase the radio emission from the AGN is low or even absent and the galaxy is young and still forming stars. In a later stage, the radio activity of the AGN becomes more important as the galaxy gets older and stops forming stars.

Comparing our radio selected SFGs and the host galaxies of RQ AGNs we find many similarities. This result further supports the hypothesis that the radio emission in RQ AGNs predominately comes from the star formation processes in the host galaxy rather than from the BH activity, in agreement with Padovani et al. (2011b), Kimball et al. (2011). In an upcoming paper we will discuss further this topic (Bonzini et al., 2014).

Based on this conclusion, we developed a powerful tool to disentangle the two radio emission mechanisms. Indeed, using the q_{24obs} only, we can separate AGN powered radio emitters from systems where radio emission comes mostly from star formation. This result can be applied to large radio samples such as the ones that existing and planned radio facilities will provide (e.g., Norris et al., 2013).

Chapter 5

Star formation and black hole activity in the faint radio sky

*Submitted as **Bonzini, M.**; Mainieri, V.; Padovani, P.; Andreani, P.; Miller, N.; Berta, S.; Bethermin, M.; Lutz, D.; Roldighiero, G.; Rosario, D., Tozzi, P., 2014, to Monthly Notices of the Royal Astronomical Society.*

Abstract

Using a radio selected sample of radio quiet active galactic nuclei in the redshift range $z = [\sim 1 - 3]$, we address the long standing question about the origin of the radio emission in these sources. We compare the star formation rate (SFR) derived from the far infrared luminosity, as traced by *Herschel*, with the SFR computed from their radio emission. The good agreement between these two independent estimates reveals that the main contribution to the radio emission in RQ AGN comes from the star formation in the host galaxy rather than from the accretion onto the black hole.

5.1 Introduction

The faint radio sky is a complex mixture of star forming galaxies (SFG) and active galactic nuclei (AGN) (e.g., Mauch & Sadler, 2007; Smolčić et al., 2008; Padovani et al., 2009). Indeed, the radio emission can either be due to the relativistic jets powered by the AGN or to the synchrotron emission from electrons accelerated by supernova explosions. In the latter case, the radio emission can then be used as star formation rate (SFR) tracer (e.g., Yun et al., 2001; Pannella et al., 2009) which opens the possibility of using radio survey to study the cosmic star formation history (CSFH). The radio band has also the advantage compared to UV or optical frequencies to be almost unaffected by dust extinction. However, up to now the majority of radio surveys available were only sensitive to the radio loud (RL) AGNs, whose radio emission is mainly due to the relativistic jets. Indeed, it is only below 0.1 mJy (e.g., Bonzini et al., 2013) that the SFGs become the dominant radio population.

Moreover, at the mJy level, only the most extreme starburst galaxies, with SFRs of thousands of solar masses per year, can be detected. It is only going deeper, that we can start to detect the bulk of the SFGs population. Such a sensitivity has been reached so far only for small patches of the sky like with the VLA survey of the Extended Chandra Deep Field South (E-CDFS) considered in this work.

A further problem that has limited so far the use of radio surveys to study the CSFH is the possible AGN contamination, in particular from radio-quiet (RQ) AGNs. Indeed, while RL AGNs can be relatively easily distinguished from SFGs (see Bonzini et al., 2013, for details), RQ AGNs can have host galaxy properties very similar to SFGs, especially in type II objects where the AGN emission is obscured by dust (Bonzini et al., 2013). The origin of radio emission in RQ AGNs has been matter of debate for a long time. It has been proposed that these sources are a scaled down version of RL objects (e.g., Miller et al., 1993b; Giroletti & Panessa, 2009) or that the radio emission is mostly due to the star formation in the host galaxy (e.g., Sopp & Alexander, 1991). In the former case, the SFR derived from the radio power would be overestimated compared to the one obtained by other SFR tracers like for example the far-infrared (FIR) luminosity.

If instead the radio emission in RQ AGNs is due to SF, the radio power could be used as SFR tracer even when the RQ AGNs emission strongly contaminates the optical-to-MIR host galaxy light. These bright AGNs are usually excluded a priori from SFR studies leading to a biased view of the actively star-forming population. Moreover, estimating the SF activity in AGNs host galaxies is particularly important to investigate the possible impact of the AGN in shaping its host galaxy properties. Indeed, both from the theoretical and observational side, there has been a lot of debate on the role the AGN can have in regulating the SF activity, either triggering or suppressing it (e.g., Mullaney et al., 2012; Rosario et al., 2012; Page et al., 2012; Harrison et al., 2012; Zubovas et al., 2013).

In this work we exploit the star-formation properties of a large sample of radio sources selected in a deep VLA survey of the E-CDFS down to a 5σ flux density limit of about 32 μ Jy. The paper is organized as follows. In section 5.2 we described our radio sample, how it splits in the different source populations and the ancillary data used for the analysis. After describing the method adopted to estimate the FIR luminosity of the radio sources (Sec.5.3), we present the radio-FIR correlation for radio selected SFGs. In section 5.5 we compute the SFR from the radio and FIR luminosity and we compare them in Sec.5.6. The position of our radio selected sources in the SFR-stellar mass plane is described in Sec.5.7 and Sec.5.8 their SF activity is investigated. In Sec. 5.9 and 5.10, we discuss and summarize our results, respectively. Finally, Appendix 5.A is dedicated to the description of an empirical model to which we compare our observation and in Appendix 5.B we publish the catalog with the physical properties of the radio sources used in this work.

In this paper we assume a cosmology with $H_0 = 70 \text{ km s}^{-1} \text{ Mpc}^{-1}$, $\Omega_M = 0.27$, and $\Omega_\Lambda = 0.73$ and a Chabrier initial mass function (IMF; Chabrier, 2003).

5.2 Sample description

5.2.1 Radio data

The Extended Chandra Deep Field South (E-CDFS) has been observed with the Very Large Array (VLA) at 1.4 GHz between June and September 2007 (Miller et al., 2008). The survey reaches a best rms sensitivity of $6\mu\text{Jy}$ and the average 5σ flux density limit is $37\mu\text{Jy}$ with near-uniform sensitivity. A catalog including sources down to peak flux density of five times the local rms noise has been extracted. A description of the survey strategy and the data reduction details are given in Miller et al. (2013). The radio catalog includes 883 sources. Using a likelihood ratio technique, the optical/infrared counterparts of the radio sources have been identified (Bonzini et al., 2012). Excluding the outermost region as defined in Bonzini et al. (2012), the wealth of multi-wavelength data available for the E-CDFS allows robust estimates of photometric redshifts (Santini et al., 2009; Taylor et al., 2009; Cardamone et al., 2010; Rafferty et al., 2011). The area with photometric redshifts coverage includes 779 radio sources that will constitute our main sample for the analysis presented in this paper. Combining the photometric redshifts with the output of several spectroscopic campaign in the E-CDFS, we were able to assign a redshift to a total of 675 radio sources, 37% of which are spectroscopic (see Bonzini et al., 2012, for details). The average redshift is $\langle z \rangle \sim 1.1$.

5.2.2 Radio source populations

As mentioned in Section 5.1, the sub-mJy radio population is a mixture of SFG and AGN. The latter further divides in RQ and RL AGN. To separate these different populations we use a multi-wavelength approach combining radio, mid-infrared, and X-ray data. A detailed description of our classification scheme is given in Bonzini et al. (2013), here we briefly summarize the main characteristics. We select RL AGN using the $q_{24\text{obs}}$ parameter, which is the logarithm of the ratio between the observed $24\mu\text{m}$ flux density and the observed 1.4 GHz flux density. Indeed we can define a “SFGs locus” based on the radio–FIR correlation for SFG (see Bonzini et al., 2013, for details). Sources below this locus display a radio excess that is the signature of an AGN contribution to the radio luminosity and are therefore classified as RL AGNs.

Within and above this locus, a source is classified as RQ AGN if there is evidence of AGN activity in the other bands considered: it has a hard band [2–10 keV] X-ray luminosity greater than $10^{42}\text{ erg s}^{-1}$ or it lies in the “AGN wedge” of the IRAC color-color diagram, as defined by Donley et al. (2012). Otherwise, the object is classified as a SFG. According to this scheme, our sample of 779 radio sources includes 167 RL AGNs, 188 RQ AGNs, and 424 SFGs.

5.2.3 *Herschel* data

The E-CDFS has been observed by *Herschel* as part of the PEP (PACS Evolutionary Probe) program (Lutz et al., 2011). The *Herschel* observations are deeper in the central part of the field, the GOODS field, and shallower in the outskirts. The whole field has been observed at 100 and 160 μm and for the central part 70 μm data are also available. For GOODS proper we use the combined reduction of PEP and GOODS-*Herschel* (Elbaz et al., 2011) PACS data as described in Magnelli et al. (2013). The 5σ flux level of the 100 (160) μm maps are 0.85 (2.1) mJy and 6.25 (13.05) mJy in the GOODS and E-CDFS, respectively. The 70 μm 5σ flux density limit is 1.35 mJy. *Herschel* photometry was performed through point spread function (PSF) fitting, adopting Spitzer MIPS 24 μm detected sources as positional priors (Berta et al., 2013). Blind catalogs are also extracted by means of PSF-fitting using the StarFinder IDL code (Diolaiti et al., 2000a,b) and include all sources with $S/N > 3\sigma$. We cross-correlate this *Herschel*/PACS catalogs with our radio sample using a $1.5''$ searching radius. We find a total of 490 matches, 33% in the GOODS field and 67% in the outer region of the E-CDFS.

In particular, in the PACS-radio sub-sample we have 42 RL AGN, 130 RQ AGN, and 311 SFG. We note that in the PACS sample we recover 69% of the RQ AGN, 78% of the SFG but only 25% of the RL AGN from the original radio selected sample considered in this paper. The small fraction of RL AGN is not surprising since they are preferentially hosted in passive, dust poor, galaxies. We therefore expect only a small little fraction of them to be detected in the FIR.

For the radio sources without a PACS counterpart we compute 5σ upper limits from the local rms noise, therefore taking into account the non uniform coverage of the *Herschel* observations in this field.

5.3 FIR luminosity of radio sources

The *Herschel* photometry is crucial to have a good estimate of the FIR emission since it allows to trace the cold dust emission. At a typical redshift of ~ 1 , the PACS measurements probe the rising part and/or the peak of the rest-frame FIR dust emission bump. We apply a fitting technique to the full UV-to-FIR spectral energy distribution (SED) to better constrain the FIR luminosity of our radio sample, taking advantage from the exquisite multi-wavelength coverage available in the E-CDFS.

The UV-NIR photometry is obtained combining the BVR selected Cardamone et al. (2010) catalogue, the K selected Taylor et al. (2009) catalogue, and the Damen et al. (2011) IRAC selected SIMPLE catalogue (see Bonzini et al., 2013, for details). In the MIR, we used the MIPS 24 and 70 μm observations from the Far-Infrared Deep Extragalactic Legacy Survey (FIDEL) (Dickinson & FIDEL Team, 2007). Longer wavelengths are covered by the *Herschel* photometry described in the previous section. In the GOODS field, the PACS 70 μm detection rather than the MIPS one is adopted when available. In summary, for each radio source we have on average 16 photometric points.

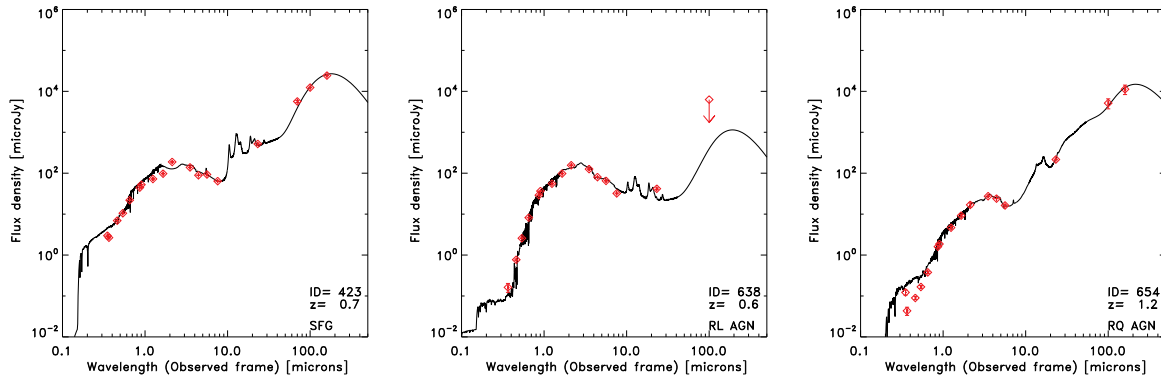


Figure 5.1: Examples of the optical-to-FIR SED fitting for the three class of sources. The combined photometry is plotted as red symbols and the solid line show the best fit template. Source ID, class, and redshift are given in the bottom left corner.

To fit the UV-to-FIR photometry we use the Berta et al. (2013) template library that is based on the observed SED of PACS detected sources. It is a collection of 32 templates, mostly SFGs, of which twelve also include an AGN component. We chose this library mostly for its wide range of SED shapes. This is important if we want to fit the photometry of our radio selected sample since, as already mentioned, it is highly non-homogeneous: it includes both normal star forming and starburst galaxies, objects with the clear presence of a powerful AGN and sources whose SED is dominated at all wavelengths by the emission from stars. However, as the Berta et al. (2013) library is based on PACS detected sources, it lacks galaxies with very old stellar population and consequently very low emission in the FIR. Therefore, we decided to add three templates of elliptical galaxies from the SWIRE template library (Polletta et al., 2007).

We use a standard χ^2 minimization technique to find the best fit template. For sources without *Spitzer* and/or *Herschel* detections we imposed the best fit template to not exceed the 5σ upper limits in these bands. We finally compute the total FIR luminosity (L_{FIR}) integrating the best fit template between 8 and $1000\mu\text{m}$. Errors are computed repeating the fitting procedure 100 times for each source, randomly modifying the photometry within the uncertainties and then taking the standard deviation of the L_{FIR} distribution obtained.

We note that for sources without PACS detection the FIR luminosity is derived from the best fit based only on the optical-MIR photometry, taking into account the upper limits in the FIR. These luminosity estimates are therefore less robust than the one constrained by the PACS measurements.

5.4 Radio-FIR correlation

The radio and FIR luminosity in SFGs follow a tight empirical relation, the so-called ”radio-FIR correlation” (RFC) (e.g., Dickey & Salpeter, 1984; de Jong et al., 1985; Bell, 2003).

The physical reason for its tightness and linearity over several decades in luminosity has been investigated by several theoretical models (e.g., Lacki et al., 2010; Lacki & Thompson, 2010; Schleicher & Beck, 2013), but remains still unclear. These works also predict that the RFC should break at high z where inverse Compton losses start to dominate over the non-thermal synchrotron emission.

From the observational point of view, there are some hints of possible deviations at high z or in extreme objects like sub-millimetre galaxies, nevertheless these observations are still consistent with no significant evolution (e.g., Ivison et al., 2010b; Mori c et al., 2010; Sargent et al., 2010; Magnelli et al., 2012; Lutz, 2014, and reference therein).

Deep radio surveys would be needed to investigate the behaviour of the RFC at high redshift for normal SFGs. Indeed, even to detect star forming galaxies with SFR of hundreds of solar masses per year at $z > 2$, a μJy radio sensitivity is required. Such a sensitivity has been reached so far only for small patches of the sky like in the VLA survey of the E-CDFS considered in this work.

In this section we therefore investigate the radio-FIR correlation for our radio selected SFGs up to $z \sim 3$. In Figure 5.2 we show the radio power versus the FIR luminosity for SFGs with a clear detection in at least one PACS filter since their FIR luminosity estimate are more robust. With the exception of two clear outliers¹, the two luminosities are tightly correlated and lie along the empirical RFC (e.g., Kennicutt, 1998a) plotted as dot-dashed line and parametrized by:

$$\log(Pr_{1.4\text{GHz}}) = \log(L_{\text{FIR}}) + 11.47 \quad (5.1)$$

where $Pr_{1.4\text{GHz}}$ is the radio power in W Hz^{-1} at 1.4 GHz and L_{FIR} is the FIR luminosity in unit of solar luminosity expressed in erg s^{-1} . The average dispersion is 0.2 dex. The color scale in Fig. 5.2 represents the redshift of the sources. Thanks to the μJy sensitivity of the VLA observation, we can detect SFG in a wide redshift range, from $z \sim 0.1$ to $z \sim 3$ and we find that the RFC holds over the whole redshift range with almost constant dispersion. Moreover, our data probe four orders of magnitudes in luminosity and therefore include both normal SFG as the most active systems with SFR of a thousand of solar masses per year. The SF in these latter systems is thought to be triggered by episodic violent events such as major mergers rather than by secular processes as in normal SFGs (e.g., Daddi et al., 2010b). Our study suggests that the correlation between radio and FIR emission is the same in both kinds of systems, at least down to the luminosities probed by our observations. However, we still cannot exclude a breakdown at lower star formation surface densities as predicted by e.g. Schleicher & Beck (2013) for which even deeper radio data would be needed.

This results justify the use of both the FIR and radio luminosity as independent but equivalent SFR tracers for our radio selected SFGs. It will be a useful element in our investigation on the origin of the radio emission in RQ AGN (see Sec. 5.6).

¹RID 521 (dark point) is a resolved edge-on spiral whose $24\mu\text{m}$ emission has been probably underestimated due to aperture photometry. As a consequence the fit is poor and the FIR luminosity is underestimated. RID 577 (light point): there is a small offset between the radio and optical-MIR emission hence it is possible that the radio emission is associated with a background object.

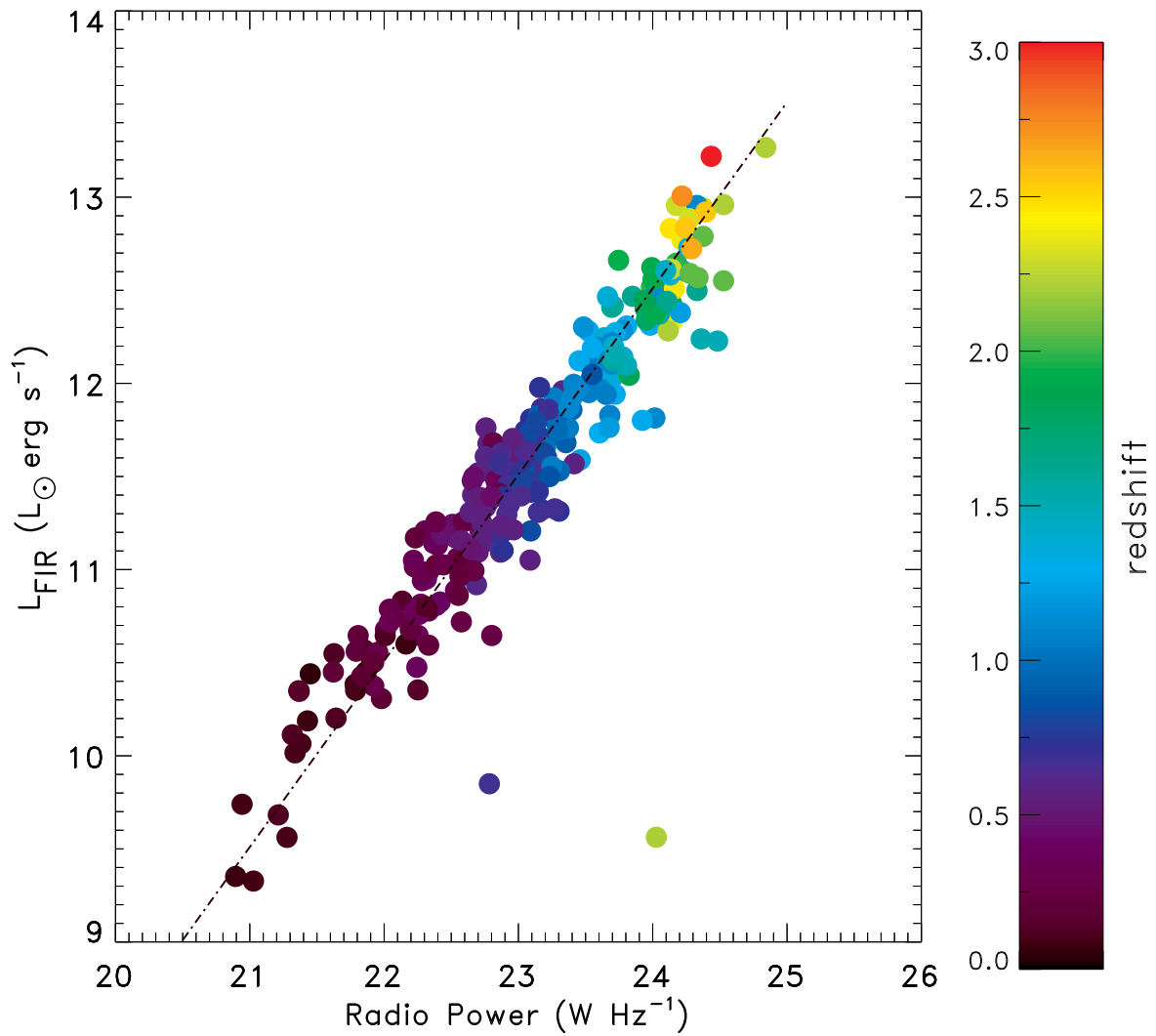


Figure 5.2: Radio power at 1.4 GHz versus FIR luminosity for SFGs detected by *Herschel*. The color scale represent the redshift of the sources and the dashed line shows the relation given in Eq. 5.3.

5.5 Star formation rate estimate

The FIR luminosity is a tracer of recent SF activity as the UV radiation from young stars is absorbed by the dust and re-emitted at longer wavelengths, in the FIR. The L_{FIR} provide a better estimate of the SFR compared to the one derived from the UV or line emission since these measurements are highly affected by dust extinction. Moreover, computing the SFR from the FIR is particularly useful for bright AGN hosts. Indeed, the AGN emission can overshadow the emission of the whole galaxy at optical wavelength, while it represents a tiny fraction ($<10\%$) of the total luminosity in the FIR in most of the cases (e.g., Hatziminaoglou et al., 2010; Rosario et al., 2012; Berta et al., 2013). We adopt the Kennicutt (1998a) relation to compute the SFR from the FIR luminosity:

$$SFR_{\text{FIR}}[M. yr^{-1}] = 4.5 \times 10^{-44} L_{\text{FIR}}[ergs^{-1}]. \quad (5.2)$$

As this equation assume a Salpeter IMF, we rescaled it for a Chabrier IMF multiplying by a factor of 0.6.

Also the radio continuum emission can be used as a tracer of recent star formation in SFGs since it is nearly all due to synchrotron emission from relativistic electrons associated to SN remnants (Condon, 1992). The empirical conversion between the radio power at 1.4 GHz and the SFR of the galaxy according to Yun et al. (2001) is:

$$SFR_r[M. yr^{-1}] = 5.9 \pm 1.8 \times 10^{-22} Pr_{1.4GHz}[WHz^{-1}]. \quad (5.3)$$

We multiply the derived SFR by a factor of 0.6 to convert from a Salpeter to a Chabrier IMF.

5.6 Radio emission in RQ AGN

In Figure 5.3 we compare the SFR computed from the FIR luminosity with the SFR derived from the radio luminosity for all the 675 radio sources with redshift. Different colors represent different classes of objects. Sources detected in at least one *Herschel* band are plotted with full symbols. We first concentrate on these sources since their SFR_{FIR} is more reliable.

As described in Section 5.4, we find that the SFGs follow the RFC in the whole range of luminosities accessible to our survey. Therefore, the two SFR estimates are in agreement over four decades in SFR with a typical dispersion of 0.2 dex. More interestingly, we find good agreement between the SFRs derived from the two different tracers also for RQ AGN. The results of a linear regression fit (least square bisector) are:

$$\log(SFR_{\text{FIR}}) = 0.97 \pm 0.02 \times \log(SFR_r) + 0.02 \pm 0.04 \quad (5.4)$$

and

$$\log(SFR_{\text{FIR}}) = 0.96 \pm 0.05 \times \log(SFR_r) - 0.09 \pm 0.10 \quad (5.5)$$

for SFGs and RQ AGNs with PACS detections, respectively. The two relations are fully consistent within the uncertainties. This implies that the radio power is a good tracer for the SFR also in RQ AGNs. Therefore, this strongly suggests that the main contribution to the radio emission in this type of AGN is due to the SF in the host galaxy rather than being powered by black hole activity. The behaviour of the RL AGNs further supports this hypothesis: they scatter out from the one-to-one relation in Fig.5.3 since the SFR computed from the radio luminosity is overestimated due to the jet contribution to the radio emission. Note that this is true not only for very powerful RL objects but also for low-power radio AGN. The comparison of the two SFR tracers allows us also to isolate sources that have been misclassified; indeed there are some RQ AGNs ($\sim 5\%$) with PACS detections that are below the relation, especially at high redshift. In Bonzini et al. (2013), we estimated a contamination to the RQ AGNs population from RL AGNs with a strong contribution from the AGN to the $24\ \mu\text{m}$ flux density that boosted their $q_{24\text{obs}}$ value into the SFGs locus of about 5%, in agreement with our findings. Therefore, we believe that most of the outliers are indeed RL AGNs². These outliers are also the main responsible for the slightly larger scatter (0.23 dex) of RQ AGNs as compared to the SFGs population (0.2 dex).

5.6.1 AGN contribution in the FIR

As already mentioned in Sec. 5.3, twelve of the SED templates in the library used to fit the photometry of our radio sample include an AGN component. The AGN contribution to the FIR luminosity in these templates has been estimated in Berta et al. (2013). We have therefore the opportunity to subtract the AGN contribution to the SFR_{FIR} and analyse its impact on our conclusions. About 50% of the RQ AGNs and 35% of the SFGs are best fitted by a template that has an AGN component. However, it is important to note that the fit solutions are highly degenerate; in particular, templates with small AGN contribution and pure SFGs ones might provide equivalent good fits to the source photometry. Hence, the analysis results reported in the following are valid only in a statistical sense. Nevertheless, the fact that only half of our RQ AGNs are best fitted by an AGN template shows that a classification based only on the optical-to-FIR properties can miss a significant fraction of AGNs. For these latter sources, the AGN contribution to the optical-to-FIR SED is typically minor and, in most of the cases (80%), they are identified as AGNs due to their high X-ray luminosity. On the other hand, the fact that we find some SFGs that are best fitted by an AGN template does not mean that they are all real AGNs. As already highlighted, the SED fitting technique often yields degenerate solutions, especially in the case of discrete libraries. However, it is possible that some of these SFGs are indeed AGNs since our classification scheme was aimed to select a clean sample of RQ AGNs and a contamination from low-luminosity AGNs in SFG population is expected (see Bonzini et al., 2013, for details).

²We will keep the original classification in the rest of the paper. Nevertheless, we checked if our conclusions change reclassifying these sources, finding no significant differences.

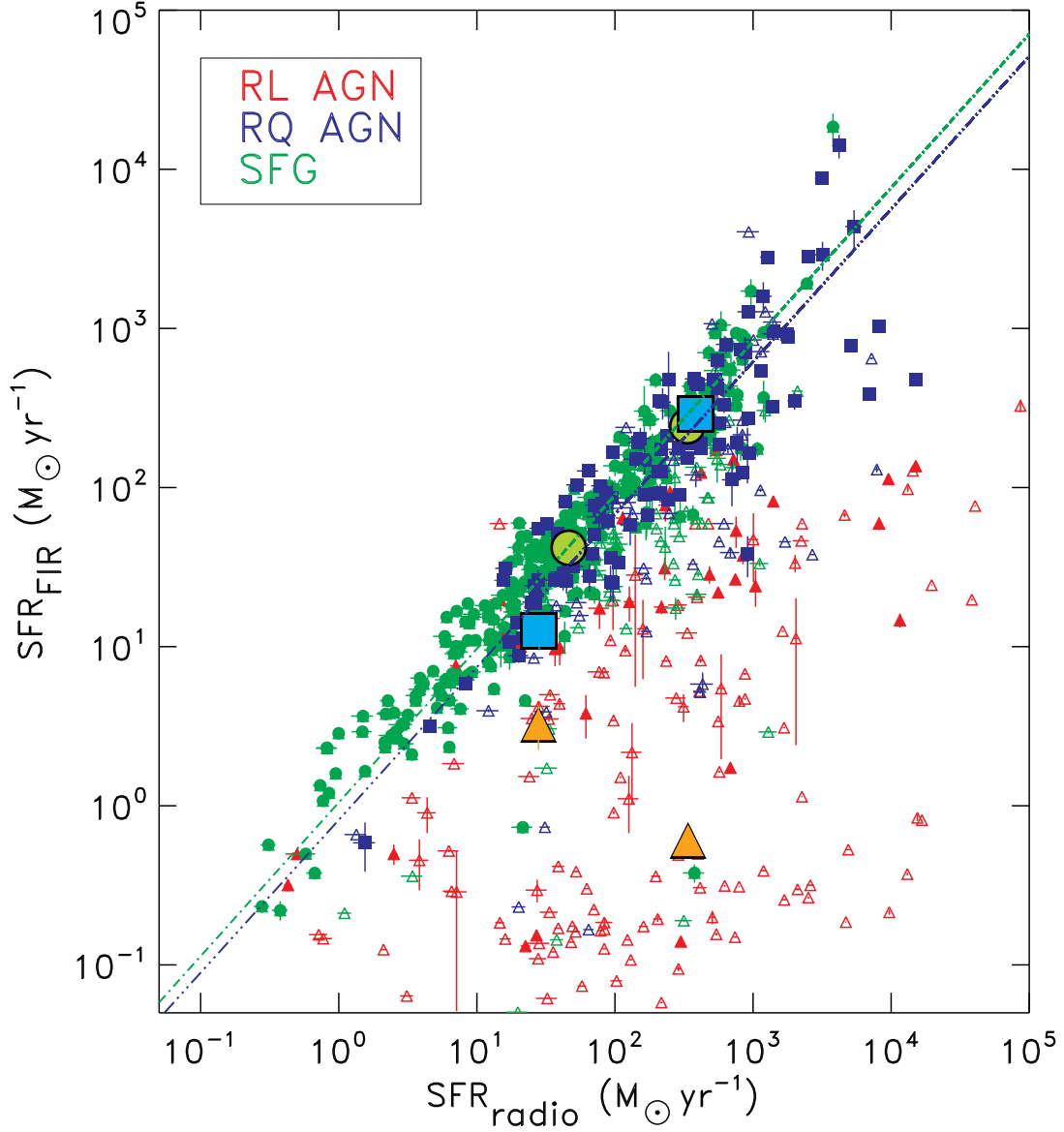


Figure 5.3: SFR derived from the FIR luminosity versus the SFR from the radio power at 1.4 GHz. SFGs are plotted as green circles, RQ AGNs as blue squares and RL AGNs as red triangles. Full symbols represent sources detected in at least one PACS filter, while sources shown as empty symbols are *Herschel* non-detections. Large symbols with lighter colors are the results of the stacking analysis (see Section 5.6.2 for details).

For all these sources we subtracted the AGN contribution to the FIR luminosity and re-computed the corresponding SFR. The new best linear regressions have a slope of 0.95 for both SFGs (± 0.02) and RQ AGNs (± 0.05) and the offset from the 1:1 correlation are 0.04 ± 0.05 and -0.10 ± 0.11 , respectively. They are therefore consistent with the previous estimates within the uncertainties. The only difference is a slightly larger scatter around the best fit relation of 0.21 dex and 0.25 dex for SFGs and RQ AGNs, respectively.

We conclude that the AGN contribution to the FIR emission as computed from the best fit template has negligible impact on our results. We will therefore consider the SFR_{FIR} non-corrected for AGN contribution in the rest of this paper.

5.6.2 Stacking of *Herschel* undetected sources

As already discussed above, for sources without a PACS detection the estimate of the FIR luminosity is less robust. Indeed, the best fit template has been obtained considering the photometry only up to $24\mu\text{m}$, with upper limits at longer wavelengths. To estimate how this can impact the SFR estimate, we have re-computed, with the same method, the SFR for sources *with* PACS detection but considering only their photometry up to $24\mu\text{m}$. In Fig.5.4 we plot the ratio of the two SFR measurements, considering or not the PACS data, as a function of redshift. Large symbols represent the median and the standard deviation in different redshift bins. We note the large number of outliers ($\sim 25\%$) and a slight tendency to underestimate the FIR emission especially above $z \sim 1$ (~ 0.16 dex) when the *Herschel* data are not included in the fitting procedure.

This test explains the larger scatter of the empty symbols in Fig.5.3 and justifies their exclusion from the linear regression analysis. However, it could be that the good agreement we find between the two SFR tracers holds only for the FIR-brightest objects while it breaks for the *Herschel* undetected sources.

Therefore, we performed a mean stacking analysis (Béthermin et al., 2010) of the PACS-undetected sources to estimate their average SFR_{FIR} . We divide the undetected sources in classes and for each class we split the sample in two bins of radio power ($21.5 < Pr < 23.5$ and $23.5 < Pr < 24.5$). We then stacked both the 100 and $160\mu\text{m}$ *Herschel* maps at the position of the PACS-undetected radio sources using the error maps (Lutz et al., 2011) as weights. Flux densities are extracted from the stacked images through PSF-fitting; aperture corrections and correlated noise corrections are applied (Berta et al., 2013). Uncertainties are estimated using a bootstrap approach (Béthermin et al., 2010) and corrected also for high-pass filtering effects. Table 5.1 summarize the stacking analysis results. We obtain $> 2\sigma$ detections for SFG and RQ AGN in both bands in each bin, with the only exception of the $100\mu\text{m}$ stacked image for RQ AGN in the lower radio power bin. We note that this bin has also the smallest number of sources (12) and therefore the S/N ratio is lower. RL AGN are detected with a similar S/N in the low radio power bin while they are only marginally detected at higher radio power.

To compute the average FIR luminosity for each sub-sample of sources, we build their average optical-to-FIR SED and then we proceed as described in Sec. 5.3. Stacked flux densities below the 2σ threshold are treated as upper limits in the fitting procedure.

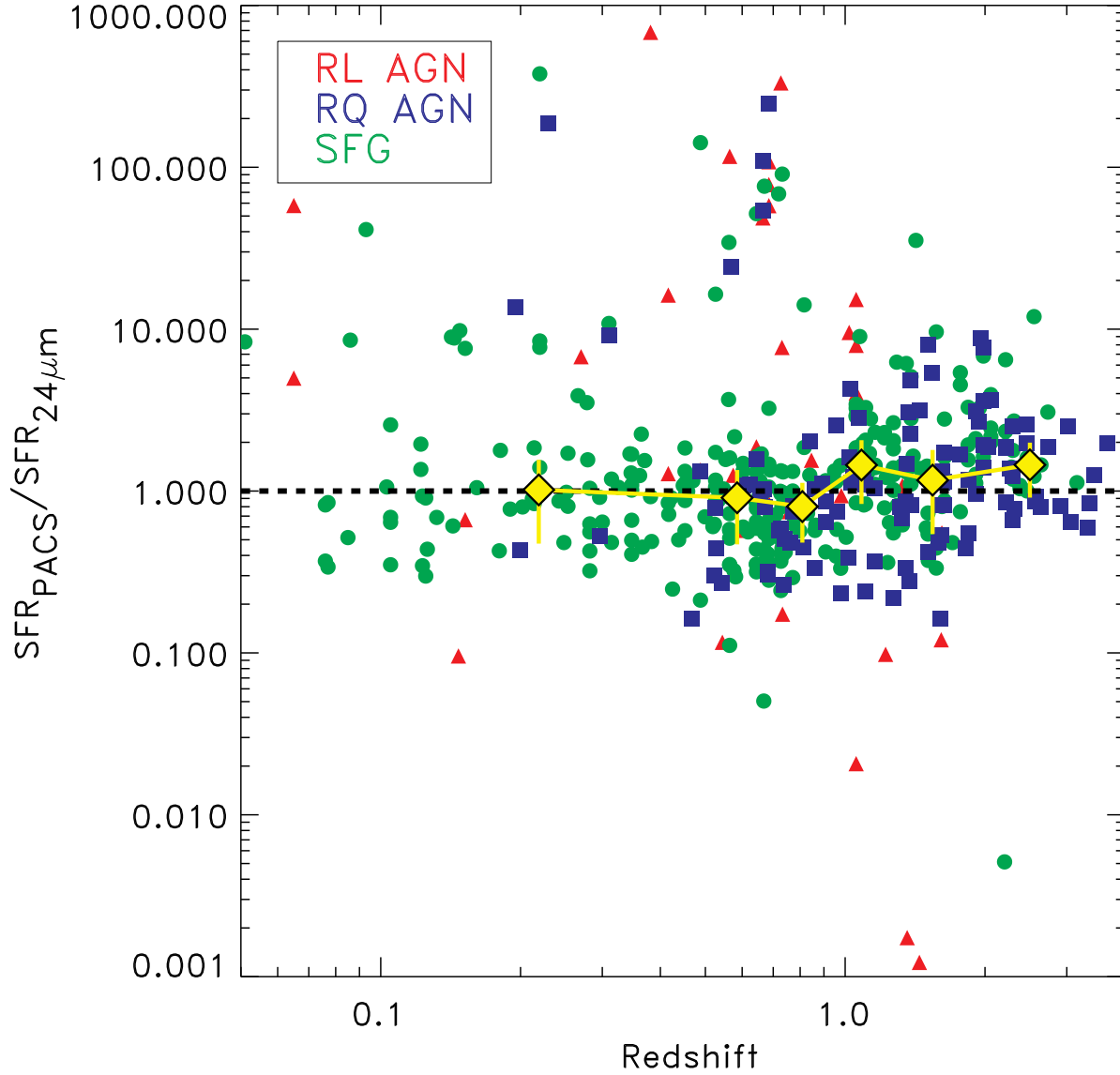


Figure 5.4: Ratio of the SFR computed from the fit to the whole photometry and the one obtained using only the UV-to-24 μm data as a function of redshift. Different colors correspond to different classes of sources as in Fig. 5.3. Large diamonds represent the median and the standard deviation in different redshift bins.

Table 5.1: Results of the stacking analysis.

(1)	(2)	(3)	(4)	(5)	(6)	(7)	(8)
Class	# sources	mean z	mean $\text{Pr}_{1.4\text{GHz}}$ [log (W Hz $^{-1}$)]	$f_{100\mu\text{m}}$ mJy	$f_{160\mu\text{m}}$ mJy	$S/N_{100\mu\text{m}}$	$S/N_{160\mu\text{m}}$
SFG	21	0.86	23.12	7.78	12.90	2.9	2.7
SFG	41	1.88	23.98	2.39	8.08	3.6	2.9
RQ AGN	12	0.68	22.90	1.49	6.48	1.7	4.2
RQ AGN	24	2.03	24.04	4.88	11.10	2.9	2.4
RL AGN	49	0.57	22.90	1.66	3.04	2.6	1.9
RL AGN	37	1.25	23.98	1.09	2.85	1.3	1.4

The corresponding average SFR_{FIR} are plotted in Fig.5.3 as large full symbols, with colors slightly lighter than the ones of the their corresponding source class. The average SFR_{FIR} of PACS-undetected SFGs and RQ AGNs lie within the scatter of the corresponding linear relations. We can therefore conclude that the two SFR tracers are equivalent for our populations of RQ AGNs and SFGs regardless of their IR brightness.

The average SFR_{FIR} of the RL AGNs not detected by *Herschel* (the majority of the population) is in both radio power bins lower than in the other two classes and does not agree with the corresponding SFR_{r} . This confirms that their radio luminosity has a significant contribution from the jets and therefore cannot be used to estimate their star-formation rate.

5.7 SFR versus stellar mass

The SF activity of a galaxy can occur in two different modes (e.g., Daddi et al., 2010a; Genzel et al., 2010): a starburst one, probably triggered by major mergers or in dense SF regions; and a quiescent one, associated with secular process, which is observed in the majority of the SFGs. In this second mode, the SFR is correlated with the stellar mass of the galaxy, forming the so called “main sequence” (MS) of SFGs. The MS has nearly the same slope both at low and high redshift but the normalization increases of about a factor of 20 from the local Universe to $z \approx 2$ (e.g., Noeske et al., 2007; Daddi et al., 2007a; Elbaz et al., 2007; Pannella et al., 2009; Peng et al., 2010; Rodighiero et al., 2011; Wuyts et al., 2011a).

In this framework, it is then interesting to locate our sources on the SFR-stellar mass plane. In Figure 5.5, we plot the SFR_{FIR} as a function of the galaxy stellar mass for our objects divided in four redshift bins. Since we have already verified that radio and the FIR are equivalently good tracers of the SFR for our SFGs and RQ AGNs, we decided to use in the following the SFR derived from the FIR luminosity because it allows us to carry on the analysis also for RL AGNs for which the SFR_{r} would instead be meaningless. Moreover, since the SFR_{FIR} is most widely used in the literature, it makes easier the comparisons with previous studies. Stellar masses are computed using a two component

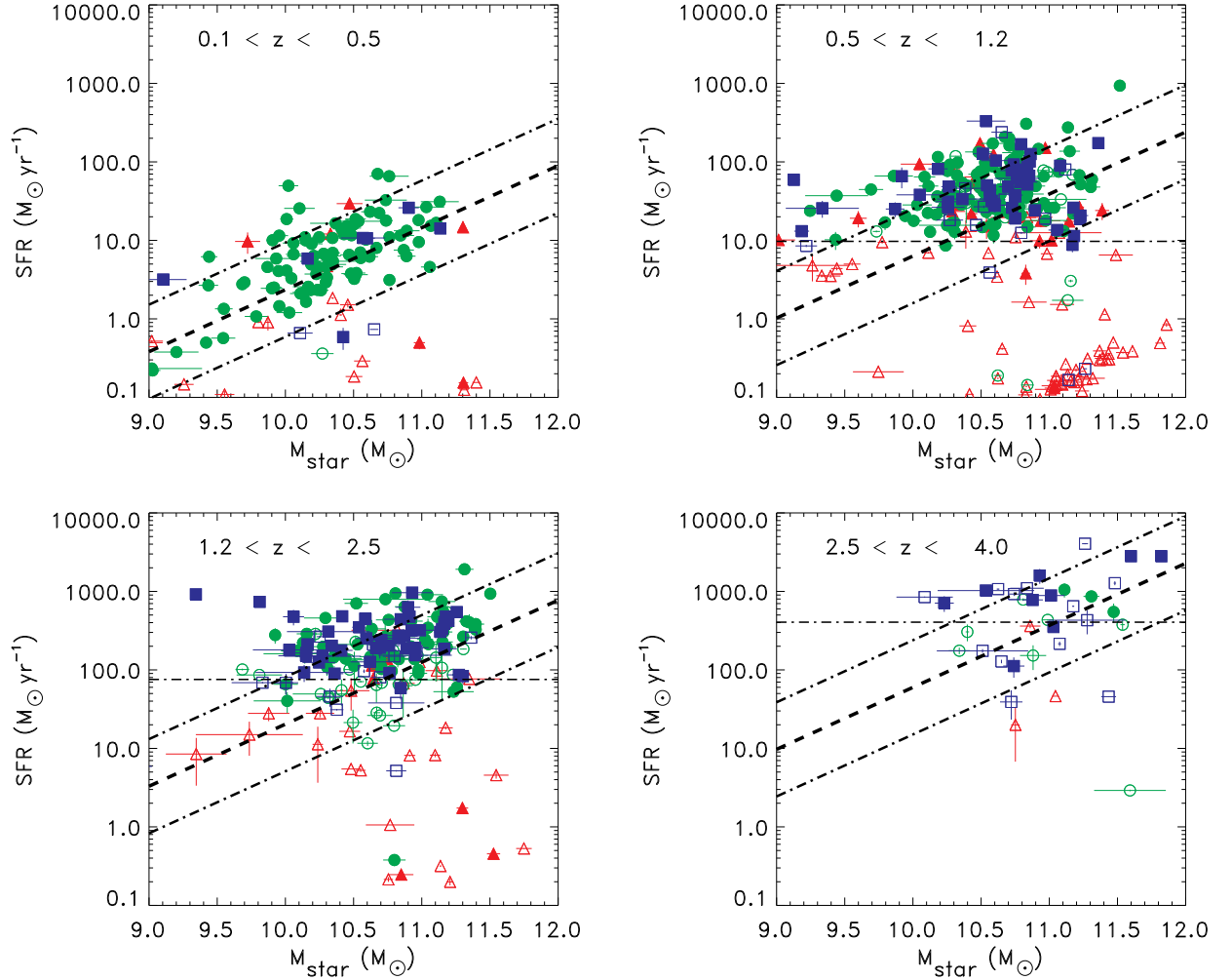


Figure 5.5: SFR versus stellar mass for different redshift bins. The symbols are the same as in Figure 5.3. The horizontal lines marks the minimum SFR accessible to our survey in each redshift bin (see Text for details). The dashed lines indicates the position of the MS at the average redshift of the sources in each panel. The loci of starburst and passive galaxies are delimited by the dot-dashed lines (± 0.6 dex) above and below the MS respectively.

(AGN+galaxy) optical-to-MIR SED fitting technique as described in Bonzini et al. (2013), assuming a Chabrier IMF.

The horizontal line in each panel³ of Fig. 5.5 marks the minimum SFR (SFR_{min}) accessible to our survey, i.e. the SFR that correspond to the flux density limit of the VLA observations at the minimum redshift in the specified bin based on equation 5.3 and corrected for a Chabrier IMF. Note that SFGs and RQ AGNs mostly lie above these lines, being the radio emission in both classes associated to star formation related process. RL AGN instead are detected even when they have SFR well below the SFR_{min} since their radio emission is boosted by the presence of the jets.

The dashed lines indicates the position of the MS at the average redshift of the sources in each bin. We adopt the following law for the redshift evolution of the MS:

$$\log(SFR(M, z)) = -7.77 + 0.79 * \log(M) + 2.8 * \log(1 + z) \quad (5.6)$$

where M is the stellar mass expressed in unit of solar masses. The slope and the redshift evolution are based on the results of Rodighiero et al. (2011) and the normalization provides the best agreement with our data (see Appendix 5.A for details) and it is consistent with the normalizations adopted in the literature. The dot-dashed lines above and below the MS correspond to ± 0.6 dex.

Due to our radio flux density limit, we are able to detect MS galaxies with low stellar mass ($M < 10^{10.5} M_\odot$) only in the first redshift bin while at higher redshift we probe the bulk of the main sequence only at the high mass end.

We note that RQ AGNs occupy the same locus in the $M_{star} - SFR$ plane as SFGs suggesting that the majority of the host galaxies of radio selected RQ AGNs are not significantly different from the inactive galaxies population (see Sec. 5.8.3 for a more detailed discussion).

5.8 Specific Star Formation Rate

Since the SFR is correlated with the stellar mass, a useful quantity to describe the SF regime of a galaxy is its specific SFR (sSFR), i.e. the SFR divided by the stellar mass. Sources with sSFR particularly higher with respect to the MS are undergoing extremely intense star formation activity, possibly triggered by major mergers, while passive galaxies are characterized by very low sSFRs. In this work, we will define as "starburst" those sources whose distances with respect to the MS ($\Delta \log(sSFR)_{MS} = \log[sSFR(galaxy)/sSFR_{MS}(M_{star}, z)]$) is larger than 0.6 dex, and we will call "passive galaxies" those with $\Delta \log(sSFR)_{MS} < 0.6$ dex (similarly to (Rodighiero et al., 2011)).

In the following, we will discuss the star-formation properties of the three classes of sources introduced in Sec. 5.2.2. We will treat RL AGN separately as their properties are significantly different from the other two classes and the flux density limit of the VLA survey has a less direct impact on the minimum star-formation rate detectable in these objects (see Sec. 5.7).

³In the first redshift bin the minimum SFR is $0.07 M_\odot \text{ yr}^{-1}$

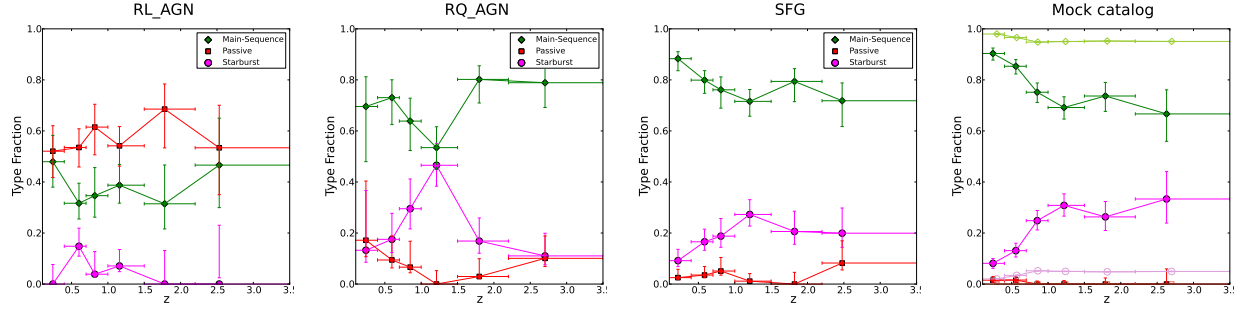


Figure 5.6: Fraction of starburst (magenta), MS galaxies (green), and passive galaxies (red) versus redshift. The panels refer from left to right to RL AGNs, RQ AGNs, SFGs and mock catalog sources. In this latter panel empty (light colors) symbols refer to the mass selected sample, while full (dark colors) symbols to the mock sample "observed" with the same radio flux density limit of our VLA survey.

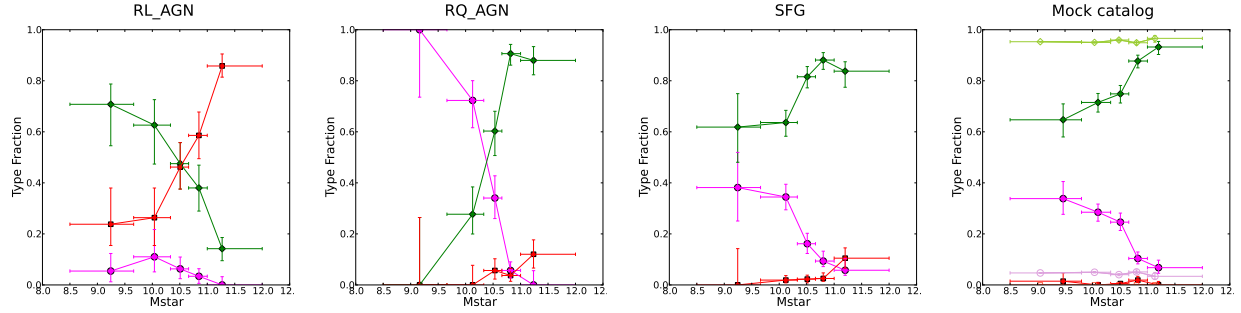


Figure 5.7: Fraction of starburst (magenta), MS galaxies (green), and passive galaxies (red) versus stellar mass. The panels refer from left to right to RL AGNs, RQ AGNs, SFGs and mock catalog sources. In this latter panel empty (light colors) symbols refer to the mass selected sample, while full (dark colors) symbols to the mock sample "observed" with the same radio flux density limit of our VLA survey.

5.8.1 SF in RL AGNs

RL AGN are generally thought to be hosted in massive red and dead galaxies. Indeed, the majority (56%) of our RL AGN are hosted in passive galaxies but a significant fraction of them are in MS star-forming galaxies and a small fraction (5%) is even hosted in starburst systems. Examples of powerful radio loud AGNs hosted in starburst galaxies has been found at high redshift ($z > 3$) (e.g., Ivison et al., 2012). We have investigated whether the fraction of actively star forming host galaxies increases with redshift. As it is shown in the left panel of Fig. 5.6, we find no significant trend up to $z \sim 3$. On the contrary, we see a strong trend with the stellar mass of the host (see left panel of Fig 5.7). Passive galaxies are the vast majority of RL AGN hosts at masses $> 10^{10.5} M_{\odot}$ while at lower masses they

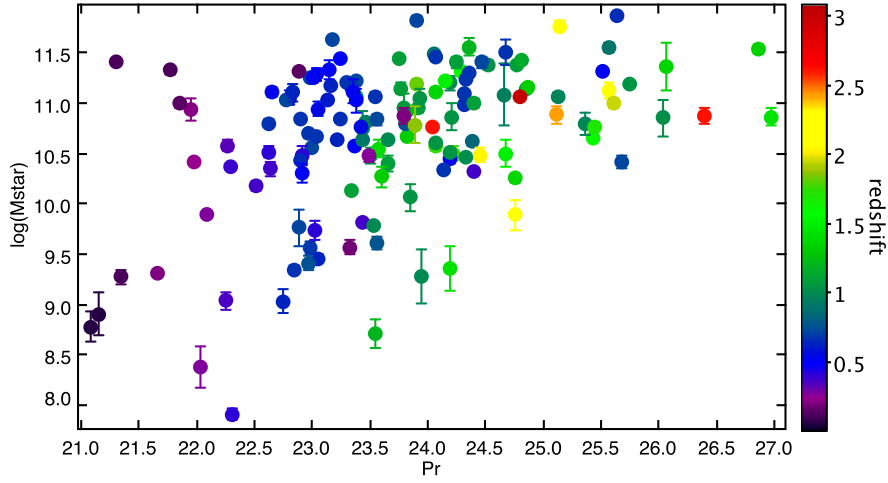


Figure 5.8: Stellar mass versus radio power for RL AGN. The colors correspond to the redshift.

are mostly MS galaxies. This trend is similar to what is observed in the overall galaxy population; the fraction of active galaxies increases as the stellar mass decreases (e.g., Peng et al., 2010; Ilbert et al., 2010, 2013). Therefore it seems that there is no strong connection between the presence of radio jets and the SF activity of the host. On the other hand, we observe a large spread in stellar masses at low radio power, while the most powerful RL AGNs are only found in the most massive objects (see Fig. 5.8) suggesting a link between the maximal energy that could be released by the jet and the mass of the black hole, assuming the $M_{BH} - M_{bulge}$ relation. That could also explain why in shallower radio surveys the fraction of RL AGN hosted in actively star forming systems is generally lower than what we observe.

Finally, it is unlikely that we are simply misclassifying SFGs as RL AGN since these objects are clear outliers from the radio-fir correlation, suggesting that there is indeed a significant radio emission associated with jets from the central black hole.

5.8.2 SF in RQ AGNs and SFGs

Once removed the contribution from RL AGN, a deep radio survey, as the one presented in this work, can be used to study the SFG population, its distribution in sSFR and its evolution with redshift. Moreover, we have shown that we can use the radio as SFR tracer also for the hosts of RQ AGNs, giving to radio surveys the advantage, with respect to i.e. UV, optical or X-ray surveys, not to exclude from the analysis sources where the AGN emission dominates over the stellar emission. This allows for a more complete census of SFGs and permits to study the AGN contribution in the SFGs population.

Our VLA survey is one of the deepest radio surveys available but still it is strongly affected by our flux density limit that, as described in Sec.5.7, allows us to detect the

bulk of the SFGs population only in the local Universe. Therefore, it is important to carefully take into account selection effects when drawing any conclusion. In this context, a comparison with a mass selected catalog can be useful. We used a mass selected mock catalog (Bernhard et al., in preparation) of SFGs based on the empirical model for the SFG population described in Sargent et al. (2012) and Béthermin et al. (2012). We will now briefly describe the model and the mock catalog before continuing with the analysis of the SF properties of our radio selected SFGs and RQ AGNs.

Mock catalog description

The two basic ingredients to build the mock catalog are: (i) a description of the observed SFG mass function (MF) and its redshift evolution; (ii) a prescription to associate to each source a SFR. For the MF we adopt a parametrization similar to the one used in Sargent et al. (2012), based on the results of Peng et al. (2010) and Ilbert et al. (2010) (see Appendix 5.A for more details). This allows us to build a mass selected SFG catalog down to a stellar mass of $10^7 M_\odot$ (which is smaller than the minimum mass measured in our sample) for a mock observation on an area equal to the size of our field (0.285 deg^2).

A SFR is then assigned to each source in order to reproduce the observed MS of SFGs with its redshift evolution (e.g. Daddi et al., 2007a; Elbaz et al., 2007; Rodighiero et al., 2011; Peng et al., 2010), and the distribution of sSFR at a fixed stellar mass. The latter is modelled as the sum of two Gaussian components (Sargent et al., 2012) one associated to MS galaxies and the second to starbursts. The full width half maximum (FWHM) of the two Gaussian, the relative contribution of the two components and its evolution with redshift are free parameters. We refer to Sargent et al. (2012) and Béthermin et al. (2012) for a better description of this model and to appendix 5.A for an illustration of the model parameters adopted in this work.

In order to directly compare this mock catalog with our radio sample we need to "observe" it with the same flux density limit of our VLA survey. To do that, we converted the SFR of the sources in the mock catalog to the corresponding radio power according to equation 5.3, adding a 0.2 dex random scatter, in agreement with what we measure (see Sec. 5.4). We then computed the corresponding radio flux density given the source redshift and selected only objects with radio flux densities above $37 \mu\text{Jy}$, the average flux density limit of our VLA survey. Finally we added random uncertainties with 0.2 dex dispersion on the mass and SFR of the mock objects to take into account the uncertainties affecting real measurements.

Sources in the mock catalog are flagged as starburst or MS object according to which of the two Gaussian components they belong to. Recovering this information in real observations is not possible for individual sources, but only statistically. Therefore, to compare the starburst fraction and its dependence on physical parameters (e.g. stellar mass or radio power) in the mock catalog and in our sample, we will adopt the same definition of starburst, MS and passive based on the distance of the source from the MS as defined in section 5.8. Note that even if the mock catalog include in principle only active galaxies, due to the errors we added to the mock catalogs quantities and to the wings of the MS

gaussian distribution, some sources in the mock catalog are "passive" according to our definition.

Starburst contribution

In our observed VLA sample the large majority of SFGs and RQ AGNs are MS objects ($\sim 74\%$). The remaining sources are mainly starbursts ($\sim 22\%$) with a small contribution from passive galaxies ($\sim 4\%$) (see also Fig. 5.5). The total observed fraction of SB ($f_{\text{SB,obs}}$) is slightly larger in RQ AGNs compared to SFGs (25% vs. 20%). We emphasize that these fractions refer to our radio-flux limited sample, and should not be confused with fractions for a mass selected sample.

In more detail, we can follow the $f_{\text{SB,obs}}$ as a function of stellar mass for the two classes of sources (middle panels in Fig. 5.7). For both SFGs and RQ AGNs, the $f_{\text{SB,obs}}$ decrease quickly with increasing stellar mass as at low masses we are highly biased towards high sSFR due to our flux density limit. The behaviour in RQ AGNs is even more extreme and the SB galaxies become the majority at masses smaller than $\sim 10^{10.5} M_{\odot}$. This is mainly due to the fact that we are able to detect low mass objects only at low redshift (see first panel of Fig. 5.5), but, since the volume that we probe at $z < 0.5$ is small, the chance of detecting AGNs is very low. We are able to sample the MS at low masses only for more numerous objects as the SFGs. The effect of the flux density limit becomes clearer looking at the right panel of Fig. 5.7; we show the starburst and main sequence galaxies relative fraction for the mass selected mock catalog (light colors and empty symbols) and for the same sample after applying the flux density cut (dark colors and full symbols). In the mass selected case, the SB fraction is constant with stellar mass while the "observed" mock catalog shows the same trend as in the real VLA samples.

More interestingly, we can also follow the evolution of the $f_{\text{SB,obs}}$, that is equivalent to the relative SB contribution to the SFR density, as a function of redshift. Some hydrodynamic simulations suggest an increase of the SB fraction out to $z \sim 2$ due to the increase of the merger-induced star formation at high redshift (e.g., Hopkins et al., 2010). In our VLA sample, we observe a fast growth from the local Universe up to $z \sim 1$ followed by a flattening both for RQ AGNs and SFGs (see middle panels of Fig. 5.6). This is not only a consequence of our flux density limits but also reflects the intrinsic growth of the starburst contribution from the local Universe to the peak of the star formation activity.

Again, the comparison with the mock catalog allows us to better quantify our results. The evolution of the fraction of starburst in a mass selected sample ($f_{\text{SB,mass}}$), is one of the ingredients of the empirical model used to build the mock catalog (see Appendix 5.A) and we can therefore use our observation to constrain the model parameters. We fixed the local value of $f_{\text{SB,mass}}$ to 1.2% as computed by Sargent et al. (2012) as our small field does not allow us to have enough volume to properly constrain it, while varying the slope of the growth and the redshift above which the evolution stops. We find that a growth as $(1+z)^2$ up to $z=1$ of $f_{\text{SB,mass}}$ and constant thereafter is required to match the total $f_{\text{SB,obs}}$ in our combined sample of SFGs and RQ AGNs and to reproduce its behaviour as a function of redshift (see Fig. 5.6). A steeper growth of the $f_{\text{SB,mass}}$ compared to the one assumed in

B  thermin et al. (2012) has been also confirmed by Gruppioni et al. (2013).

In summary, the "observed" mock sample well reproduces the behaviours of the relative fraction of SB, MS and passive galaxies in our SFGs, both as a function of redshift and stellar mass (see the last two panels of Fig. 5.6 and Fig. 5.7, respectively). We note that also when combining SFGs and RQ AGNs, that are the minority in number, the fraction of SB as a function of stellar mass and redshift is consistent with the model within the uncertainties. Also the total $f_{\text{SB,obs}}$ is the same in the VLA and mock flux limited samples ($\sim 20\%$). Therefore, we conclude that the empirical model of Sargent et al. (2012) is suitable to describe the star forming galaxy populations with only little tuning of the model parameters.

Therefore, we could use the model prediction to study the behaviour of a mass selected sample rather than a flux limited ones. In the last panels of both Fig. 5.6 and 5.7 we show we light colors and empty symbols the fraction of SB and MS galaxies for the mass selected catalog. As expected, the "real" $f_{\text{SB,mass}}$ is much lower compared to the one observed in a flux limited sample and SB sources contribute to less than 10% to the total SFR density. This result is also in agreement with the results of Rodighiero et al. (2011) and the models of Hopkins et al. (2010).

5.8.3 AGN content as a function of sSFR

In Fig. 5.9 we plot the relative fraction of the different classes of sources as a function of the distance with respect to the MS (i.e., $\Delta\log(s\text{SFR})_{\text{MS}} = \log[s\text{SFR}(\text{galaxy})/s\text{SFR}_{\text{MS}}(M_{\text{star}}, z)]$). Below the MS (left side of Fig.5.9) the population is dominated by RL AGN. This is due to two main reasons. The first is related to selection effects since we are sensitive to low sSFR only for sources whose radio emission is enhanced by AGN activity, i.e., RL AGN. On the other hand, the probability of hosting a RL AGN has been observed to be higher in massive passive galaxies (e.g., Best et al., 2005) even if its physical reason is still unclear.

On the right side of the plot, i.e. above the MS, we observe a rising of the RQ AGNs fraction from ~ 25 to 40%. To investigate if this rising can be due to some AGN selection effects we considered two SFG sub-samples matched in redshift and mass with the RQ AGN distributions. The trend remains in both cases. We also checked if it can be explained by some AGN contribution to the FIR luminosity in two ways: (i) using the SFR derived from the radio power rather than SFR_{FIR} and (ii) using the SFR_{FIR} corrected for the AGN contribution (as describe in Sec.5.6.1) to compute the $\Delta\log(s\text{SFR})_{\text{MS}}$. Again the fraction of RQ AGNs increases as the $\Delta\log(s\text{SFR})_{\text{MS}}$ increases. The most extreme SF activity seems therefore often associated with an active phase of the black hole. Such scenario has been predicted by simulation of merging systems (e.g., Di Matteo et al., 2005; Hopkins et al., 2008); the instabilities generated by such a violent event trigger both a burst in the SF and feed efficiently the central BH.

As discussed in the previous section, sources with SB activity represent a small fraction of the SFGs population. Similarly, the large majority of our RQ AGNs (75%) are hosted in MS or passive galaxies. This fraction only represents a lower limit since our observation do not fully sample the MS especially at high redshift. Hence, the most common triggering

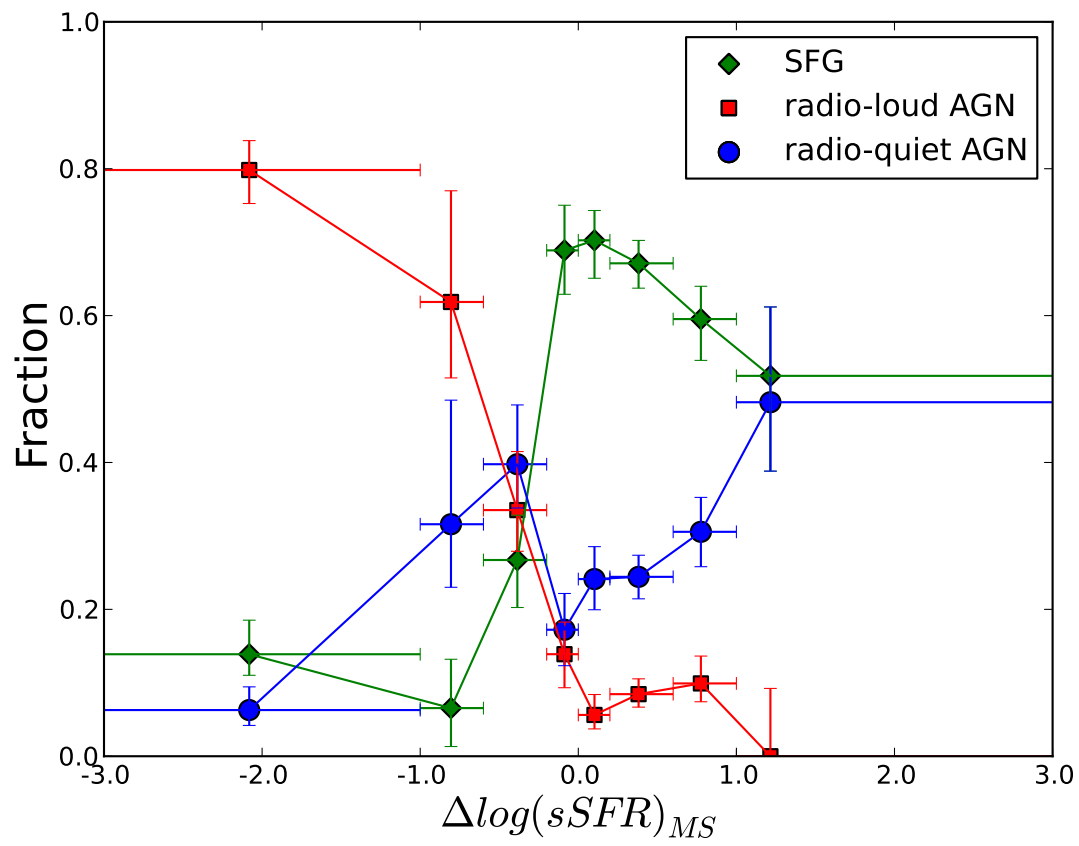


Figure 5.9: Relative fraction of sources classes as a function of $\Delta \log(sSFR)_{MS}$.

mechanisms of the black hole activity is probably related to steady process like gas inflows from the inter galactic medium rather than extreme events like major mergers (e.g., Mainieri et al., 2011; Rosario et al., 2012).

5.9 Discussion

Since the separation between RQ and RL AGNs is based on their q_{24obs} value (see sec.5.2.2), our finding that the radio emission in RQ AGNs is mainly due to SF is probably not surprising but it is important. Indeed we have shown that using only two bands, the radio (1.4 GHz) and the MIR band (24 μ m), we can efficiently and with few outliers separate sources powered by the two different radio emission mechanisms, namely jets or SF. We have shown that the radio power is a tracer for the SFR as good as the FIR luminosity for both SFGs and RQ AGNs. Since the UV-optical and also the MIR emission can be heavily contaminated by the AGN emission in powerful AGN, like most of our RQ objects, the radio power could provide a better estimate of the SF in their host galaxy compared to i.e., UV-based tracers. In addition, being radio frequencies almost unaffected by dust extinction, it is suitable for both type I and type II AGNs.

Hypothetically, the good agreement between SFR_r and SFR_{fir} for RQ AGNs could be the result of a conspiracy where the contribution to the radio luminosity from tiny jets is exactly compensated by an extra contribution in the FIR. This will boost both the SFR estimates by the same amounts. With the current resolution of the VLA data we cannot exclude the presence of jets in the center of these AGNs (e.g., Giroletti & Panessa, 2009) and higher resolution radio observations with the VLBI would be needed to spatially resolve them.

5.9.1 Comparison with a FIR selected sample

We want to investigate the possibility to use deep radio surveys as a useful tool to study the cosmic SF history, alternative or complementary to FIR surveys. We have therefore compared our sample with the *Herschel*/PACS detected sample.

As described in section 5.2.3 only $\sim 60\%$ of our VLA sample has a counterpart in the *Herschel* catalogue of the E-CDFS. Excluding the RL AGNs, for which we expected a low detection rate since most of them are hosted in passive galaxies (but see Sec. 5.8.1), the fraction increases to $\sim 70\%$. As for the 30% of unmatched radio sources, this at least partly is due to the dispersion of the RFC: a radio and a FIR flux density limited sample would tend to be biased towards sources on opposite sides of the relation. To test this hypothesis, we made use of the mass selected mock catalog described in Sec. 5.8.2. We "observed" it with a FIR-luminosity limit equivalent to our 37 μ Jy flux density limit computing the minimum SFR corresponding to the radio flux density limit at each source redshift and selecting only the objects with SFR above this threshold. The resulting FIR-selected catalog contains ~ 780 sources, roughly the same number of objects as in the radio selected mock catalog described in Section 5.8.2. In Fig. 5.10 we show the RFC for the

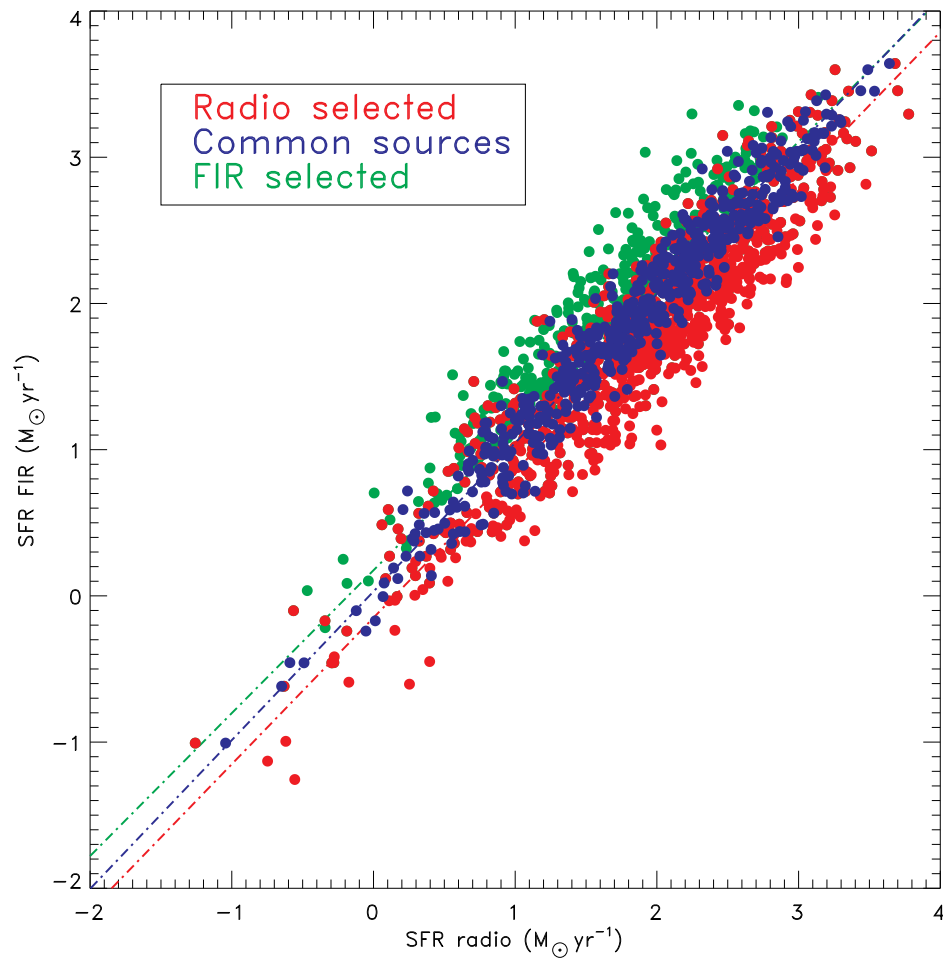


Figure 5.10: SFR derived from the FIR luminosity versus the SFR from the radio luminosity for the sources in the FIR selected mock catalog (green), the radio selected mock catalog (red) and the matched sample (blue). The dashed lines are the linear fit to the data.

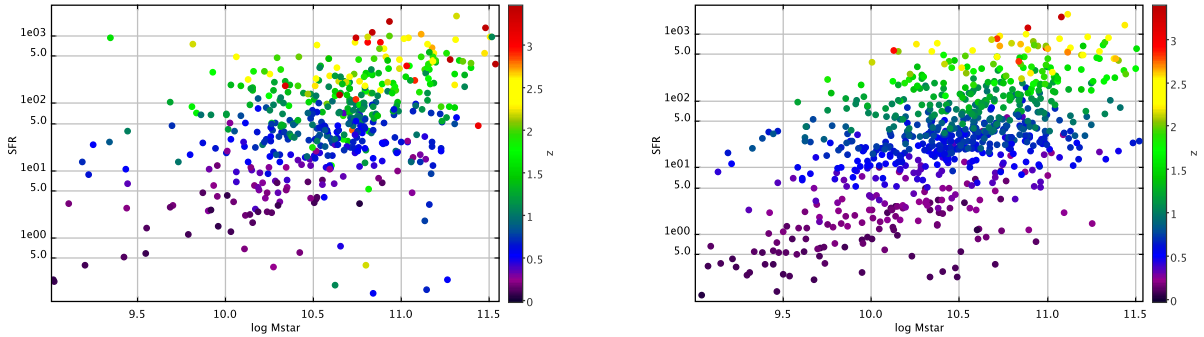


Figure 5.11: .

SFR versus stellar mass for the VLA sample (left) and for the PACS sample (right).

FIR selected mock catalog in green, the radio selected in red, and for the matched sources, in blue. The latter are only 60% of the total number of objects in each catalog, a fraction similar to the one obtained matching the real VLA and *Herschel* samples. The offset from the 1:1 correlation is ~ 0.15 dex above and below for the FIR and radio selected samples, respectively. This plot explains also why most of the VLA sources without PACS detection are just below the correlation found for the VLA sources with *Herschel* counterpart in Fig. 5.3; being radio-detected only they have a slight radio excess.

On the other hand, about 40% of the PACS detected sources have a counterpart in the VLA image. This means that the FIR observations reach a lower flux density limit, also thanks to the much deeper maps in the central GOODS field compared to the outskirts (see Sec. 5.2.3). We have compared the SFR_{FIR} computed in Gruppioni et al. (2013) for the sources in common and we find very good agreement with our estimates. Also the stellar masses are consistent; we find a larger scatter but no systematic shifts. This reflects the fact that the SFR is well constrained when FIR photometry is available, while on the stellar masses there are larger uncertainties, especially in AGN host galaxies, depending on the fitting technique and especially on the model library adopted (e.g. Ilbert et al., 2010).

In Fig. 5.11, we show the VLA (RQ AGNs and SFGs only) and the *Herschel* sample on the SFR–stellar mass plane with the sources coloured according to their redshift. The two sets of data show the same trends and the same evolution with redshift. We also find a similar fraction of SB (20%) in the PACS sample compared to the radio one. Being a bit deeper, especially in the GOODS field, the PACS observations probe better the local population and the small stellar mass end. Already ongoing deeper radio surveys, as well as those planned with future facilities, will allow to probe these small masses also in the radio (Norris et al., 2013). Indeed, going down to the nanoJy sensitivity level, they will be able to probe the bulk of the SFGs population. An illustration of that is given in Fig. 5.12 where we plot the fractions of MS and SB galaxies as a function of the radio flux density in μJy for the mass selected mock catalog. Below about $10 \mu\text{Jy}$ the number density of SB remains nearly constant around 8%, while at the flux density limit of our survey (vertical

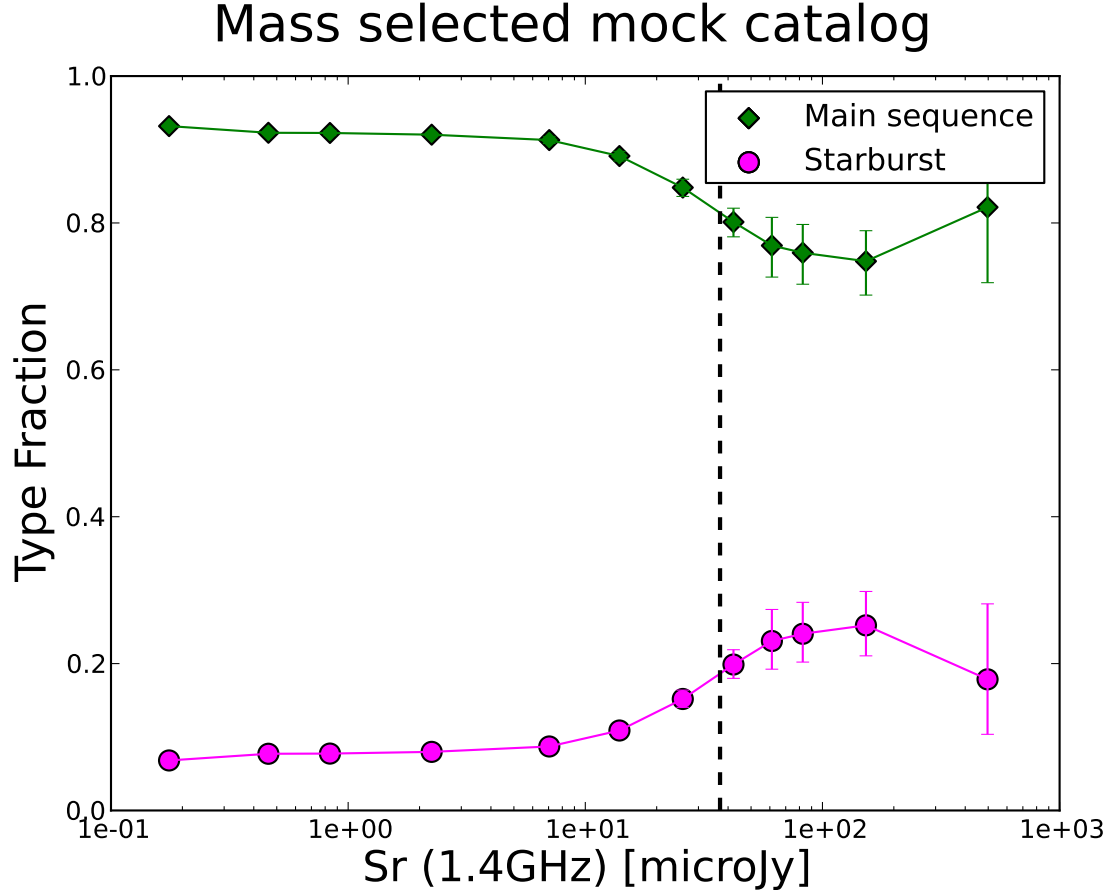


Figure 5.12: Fraction of MS and starburst sources in the mass selected mock catalog as a function of the radio flux density.

line) we are biased towards higher sSFRs.

5.9.2 What changes using a different SFR tracer?

As discussed in the previous section, due to the RFC dispersion, a sample selected with a radio flux density limit would be slightly biased towards those object on the right side of the relation, i.e. with a radio power larger than the one given by the relation for a given FIR luminosity.

That means that, especially for the sources without *Herschel* counterpart, the SFR derived from the two different tracers can be slightly different. As quantities like the fraction of SB are extremely sensitive to these changes due to small number statistics, we investigated how the choice of a different SFR tracer, namely the radio power, can affect our conclusions. Of course that cannot be done for RL AGN as in these objects the radio power is not tracing the SF activity in the host galaxy but it is highly contaminated by the jets emission. For RQ AGNs and SFGs instead we repeated the same analysis as in

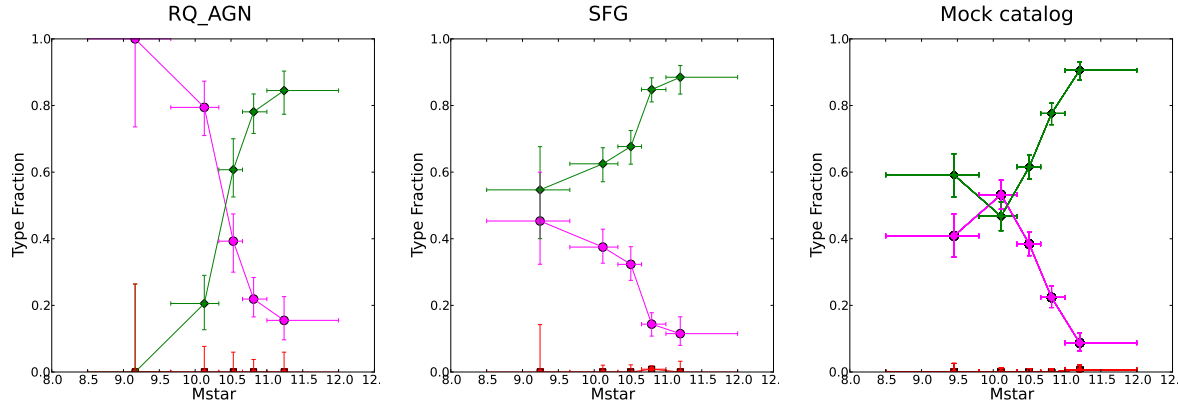


Figure 5.13: Fraction of starburst (magenta), MS galaxies (green), and passive galaxies (red) derived using the SFR_r , versus stellar mass. The panels refer from left to right to RQ AGNs, SFGs and mock catalog sources.

Sec. 5.8 using the SFR_r to compute the $\Delta \log(sSFR)_{MS}$ and therefore to determine the level of their SF activity.

The total fraction of SB in this radio flux-limited sample increases to $\sim 30\%^4$ but the trends as a function for example of stellar masses remain the same (see Fig.5.13). Also in the radio flux density limited mock catalog, if we compute the $\Delta \log(sSFR)_{MS}$ from their radio power we obtain a $f_{SB,obs}$ of 30%, in agreement with our data.

The larger differences appear at $z > 1$, where the fraction of starbursts is up to a factor of two larger using the SFR_r , but this effect is mainly due to the sources without PACS detection. Indeed, as shown in Fig. 5.4, the SFR extrapolated from the optical-to-MIR photometry tends to be underestimated at high redshift. Hence, the differences between the two SFR tracers appear larger. As a further consequence, the $f_{SB,obs}$ at high redshift shown in the central panels of Fig. 5.6 are slightly underestimated as also suggested by the predictions of the empirical model.

5.9.3 $L_X - L_{FIR}$ relation

The hard band X-ray luminosity (L_X) is another SFR tracer; the 2–10 keV rest-frame emission in SFG is dominated by high-mass X-ray binaries (HMXB). Being the companion of the accreting object a sort-lived high mass star, the L_X is linked to the recent star formation activity. The conversion factor between L_X and the SFR has been calibrated for local sample (e.g., Ranalli et al., 2003; Lehmer et al., 2012) At higher redshift this correlation has been less studied as very long exposure times are necessary to detect MS objects. In the central part of the E-CDFS, one of the deepest *Chandra* observation has been taken with a total integration time of 4 Ms (Lehmer et al., 2005) allowing us to detect a sample of 44 SFGs up to $z \sim 1$ (see also Vattakunnel et al. (2012)). For this sub-sample of X-ray detected SFGs, we can therefore study the relation between L_X and L_{FIR} and

⁴Note that, on the contrary, the fraction of passive goes almost to zero.

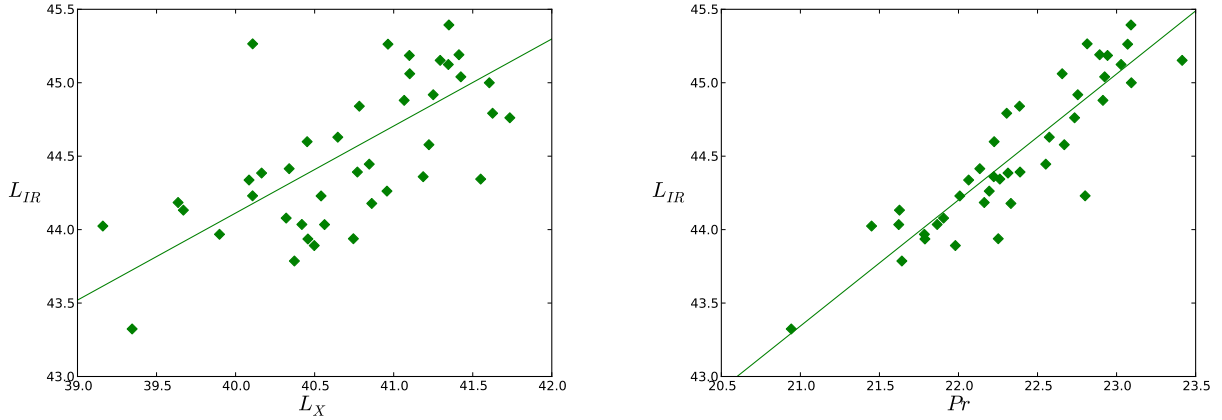


Figure 5.14: Infrared luminosity versus radio power at 1.4 GHz (*left panel*) and hard X-ray luminosity (*right panel*) for the sub-sample of SFGs with X-ray counterpart.

compare it with the RFC. In particular, we are interested in the relation scatter in order to estimate the accuracy of the L_X as SFR tracer. We find that the dispersion is ~ 0.33 dex, about two times larger than the one between L_{FIR} and radio power (0.17 dex) for the same sources (see Fig. 5.14).

A possible explanation is that, as the redshift increases, the observed 2–10 keV band corresponds to a softer rest-frame emission where the contribution from low mass X-ray binaries (LMXB) becomes more important. The emission from LMXB depends on the past star formation history on longer times-scales compared to HMXB and is proportional to the stellar mass of the galaxy. Hence, the L_X at high redshift is contaminated by emission that is not related to the recent SF activity and the radio power remains a more robust SFR indicator.

5.10 Summary

In this work, we investigated the star formation properties of the faint radio population as detected by one of the deepest 1.4 GHz survey up-to-date conducted with the VLA in the Extended Chandra Deep Field South. This study builds upon the results presented in Bonzini et al. (2012) and Bonzini et al. (2013) where we have exploited the wealth of multi-wavelength data available in this field to identify the AGNs, further divide them in radio-loud and radio-quiet, and to characterize the properties of the radio selected galaxies (e.g. redshift, stellar mass). The main results of this paper are the following:

- We have derived the FIR luminosity, fitting the UV-to-FIR SED of our VLA sources; radio selected SFGs follow the RFC up to $z \sim 3$ with a nearly constant dispersion of 0.2 dex (Sec. 5.4)
- Comparing the SFR derived from the FIR luminosity and the radio power (Table 5.2),

we show that the two SFR tracers are equivalently good not only in non-active SFGs but also for the host galaxies of RQ AGNs. This implies that the main contribution to the radio emission in RQ AGN is associated with SF activity in the host rather than to radio jets (if present) powered by the black hole (Sec. 5.6)

- As the SFR in SFG correlates with their stellar mass, we made use of the sSFR to determine the SF activity level in our sample (Sec. 5.8). The data are consistent with models that predict that the SB galaxies represent a small fraction ($\sim 8\%$) of a mass selected SFGs population (e.g., Sargent et al., 2012; Béthermin et al., 2012). We have also discussed the impact of our flux density limit on a mass selected mock catalog (Sec. 5.8.2).
- The majority of our RL AGNs are hosted in passive galaxy, but we detect significant SF activity in $\sim 40\%$ of the RL AGNs hosts. This suggests that, at least for low radio power, the presence of radio jets does not always prevent active star-formation (Sec. 5.8.1).
- We find hints of a higher fraction of AGNs in the most extreme SB galaxies (Sec. 5.8.3). This is in agreement with scenarios where both the intense SF activity and the efficient accretion on the black hole are triggered by gas rich major mergers (e.g., Chen et al., 2013; Symeonidis et al., 2013).
- The vast majority ($\sim 75\%$) of our RQ AGNs lie along the main sequence suggesting that the bulk of the black hole activity is associated with secular processes.

Finally, we have shown that deep radio continuum surveys are a powerful tool to investigate the star formation history up to high redshift. The current and coming radio facilities like the JVLA and the Square Kilometre Array (SKA) pathfinders will be able to observe with nanoJy sensitivity large areas of the sky (Norris et al., 2013) hence detecting the bulk of the SF population. We have shown how to efficiently discriminate RQ and RL AGNs using the $24\ \mu\text{m}$ emission ⁵. Therefore, our finding that the main contribution of radio emission in RQ AGNs is due to star formation in their host galaxy, opens the possibility to use the radio emission to estimate the SFR even in the host galaxy of bright quasars.

⁵Deep $24\ \mu\text{m}$ observations are already available on most of the usual deep fields

5.A Choice of the model parameter

In this appendix we describe in more details the empirical model used to build the mock catalog (Bernhard et al., in preparation) and discuss the set of model parameters adopted. The physical motivation for the model and the underlying equations are described in Sargent et al. (2012) and Béthermin et al. (2012).

The motivation for this Appendix is that the original set of parameters adopted in Béthermin et al. (2012) needed to be modified in order to reproduce our observations. Indeed, the corresponding mock catalog, "observed" with the same flux density limit of our survey (see Sec. 5.8.2), while reproducing approximatively the radio counts, does not well reproduce some host galaxy properties of the sample; the mock catalog has a mass distribution that peaks at higher masses compared to the distribution for our VLA sources. As a consequence, also the SFR properties are not well reproduced in the mock catalog having on average lower SFR and therefore a significantly lower fraction of starburst galaxies compared to the data.

Therefore, we investigated the possible reasons for this discrepancy and looked for a set of parameters that is able to reproduce our observations in terms of mass and sSFR distribution together with the radio counts.

5.A.1 SFGs mass function

The mass distribution of the mock catalog objects is set by the SFG mass function (MF). The MF adopted in the model is based on the fits by Peng et al. (2010) of the SFGs MF presented in (Ilbert et al., 2010). It is described as a single Schechter function with characteristic mass (M_b) and faint-end slope that are redshift invariant and by a constant characteristic density up to $z \sim 1$ followed by a decline as $(1 - z)^{0.46}$ (see Béthermin et al. (2012) for details). Our radio observations are relatively shallow compared to the K-band data used to compute the MF in Ilbert et al. (2010), consequently we are more sensitive to the high mass end of the distribution. Therefore, we are particularly sensitive to the value of M_b , that set the position of the MF break followed by the exponential cut off. Since our sample is small and highly incomplete at low masses, we cannot perform a real fit of the MF. We chose to keep all the other parameter describing the MF fixed. As already mentioned our observations have a mass distribution that peaks at lower masses compared to the corresponding mock catalog. To reconcile the model with our observations we assume a M_b of $10^{11} M_\odot$ rather than $10^{11.2} M_\odot$ as in Béthermin et al. (2012). Adopting this value the mass distributions of the mock catalog and of our data are consistent as confirmed by a Kolmogorov-Smirnov (KS)-test (Prob > 0.99). The possible reasons for this shift are twofold: on one hand, stellar mass measurements have large uncertainties and can be up to 0.3 dex systematically different depending on the stellar population synthesis model adopted (see e.g. Ilbert et al., 2010). To check this hypothesis we computed the stellar mass using the same method adopted for the VLA sources (Bonzini et al., 2013) for

a sub-sample of the Ilbert et al. (2010) sources⁶ and compared the mass measurements. We indeed noted that the Ilbert et al. (2010) stellar masses are on average larger than the one obtained with our method. On the other hand, there is no one-to-one correspondence between the color-color based method used to identify the SFG population in Ilbert et al. (2010) and our scheme causing. Finally, we note that the simple prescription adopted in the empirical model and the set of parameters chosen is only an approximation for the SFGs MF while a more complex description as e.g. in Ilbert et al. (2013) would be needed.

5.A.2 Main sequence and its redshift evolution

The two modes of SF are described by two Gaussian. We assume a FWHM of 0.2 dex for the MS galaxies as measured in Rodighiero et al. (2011). For the second Gaussian we use the same parameter adopted in (Béthermin et al., 2012), i.e. a FWHM of 0.2 dex, a displacement from the MS peak of 0.6 dex. The relative fraction of SB evolves with redshift as:

$$f_{SB} = 0.012 * (1 + z)^2 \text{ for } z < 1 \quad (5.7)$$

The local fraction is taken from Béthermin et al. (2012) but we set a steeper growth of the starburst fraction up to redshift 1 as suggested by our observations (see Sec. 5.8.2).

The normalization of the MS is another critical parameter in determining both the number counts and the observed SB fraction. Keeping fixed the slope of the MS to the value measured in Rodighiero et al. (2011) and its evolution with redshift to $(1 + z)^{2.8}$ (Sargent et al., 2012), we looked for the best value for the MS normalization. We adopt a normalization of the MS ($\log SFR(z = 0, M = 10^{11} M_{\odot}) = 10.08$) that is lower than in Béthermin et al. (2010) but it is in better agreement with what was found in Rodighiero et al. (2011) and our own measurement.

5.A.3 Comparison with VLA observations

With the few changes in the model parameters described above, we are able to reproduce both the radio counts and the physical properties of our radio sources with the mock catalog. Indeed the mass selected mock catalog, "observed" with the same flux density limit of our VLA survey (see Sec. 5.8.2), on a mock field with the same area of our observation, contains about 790 sources. The exact number of sources varies of some units for different runs of the model since we add random uncertainties on the mock galaxies properties and a random dispersion for the RFC. The VLA sample considered in this work contains 779 sources. Considering only the RQ AGNs and the SFGs, where the main contribution to the radio flux is due to SF, but correcting for the not perfect uniformity of the sky coverage (Padovani et al., in prep.), the number of RQ AGNs and SFGs detectable at $37 \mu\text{Jy}$ flux density limit in our field is 784. Considering that some of the RL AGNs, according to our analysis, contribute to the SFG population, we conclude that the number counts predicted by the empirical model are in good agreement with the observed one. A complete analysis

⁶A sample of X-ray selected AGNs for which we have optical-to- $24 \mu\text{m}$ photometry and redshift.

of the impact of the various model parameters on the mock catalog physical characteristics is beyond the scope of this paper.

The goal of this investigation was to check the consistency between our observation and the model for the SF population proposed in Sargent et al. (2012) and to better control the effects of the flux density limit on our results.

5.B Stellar masses and SFRs catalog of VLA sources

We make publicly available the physical properties derived for our radio sample and used in this work. They are summarized in table 5.2. The catalog columns are organized as follows:

- (1) Identification number of the radio source (RID).
- (2) Source classification.
- (3) Source activity: "SB" for starburst galaxies, "MS" for main sequence galaxies, and "P" for passive galaxies according to the definition given in section 5.8.
- (4) Source redshift.
- (5) Stellar mass.
- (6) SFR derived from the radio power.
- (7) SFR derived from the FIR luminosity.
- (8) distance with respect to the main sequence in the $SFR - M_{star}$ plane (Sec. 5.8.3)

Table 5.2: Star formation properties of the VLA sources.

(1)	(2)	(3)	(4)	(5)	(6)	(7)	(8)
id	class	type	z	M_{star} [$\log(M.)$]	SFR_r [$\log(M.yr^{-1})$]	SFR_{FIR} [$\log(M.yr^{-1})$]	$\Delta\log(sSFR)_{MS}$
712	SFG	MS	0.56	10.79 \pm 0.05	15.4 \pm 4.7	21 \pm 1.1	0.07
713	RQ AGN	MS	0.49	10.60 \pm 0.06	17.2 \pm 3.3	10 \pm 0.8	-0.01
714	SFG	MS	0.77	10.30 \pm 0.02	41.0 \pm 9.3	30 \pm 4.0	0.47
715	SFG	SB	0.18	9.95 \pm 0.07	13.3 \pm 0.8	11 \pm 0.2	0.81
716	RQ AGN	MS	1.16	10.78 \pm 0.10	80.2 \pm 25.1	79 \pm 20.9	0.27
717	SFG	MS	0.52	10.13 \pm 0.02	17.7 \pm 3.8	12 \pm 0.9	0.41
718	SFG	SB	2.46	10.52 \pm 0.09	478.7 \pm 141.2	703 \pm 86.2	0.84
719	RL AGN	MS	1.03	10.84 \pm 0.19	38394.1 \pm 20.2	19 \pm 0.2	-0.31
720	SFG	MS	0.25	10.59 \pm 0.02	16.5 \pm 2.4	10 \pm 0.5	0.19
721	RQ AGN	MS	1.27	10.84 \pm 0.05	129.0 \pm 35.5	58 \pm 15.5	0.02
722	RQ AGN	MS	0.96	10.76 \pm 0.16	89.4 \pm 16.2	61 \pm 7.5	0.29

Chapter 6

Conclusions

In this Chapter I summarize the main results of my Thesis and outline some possible further development of this research.

In my Thesis, I exploited the multi-wavelength properties of one of the deepest radio surveys available up to date (Kellermann et al., 2008; Miller et al., 2013). This work is particularly useful for paving the way to upcoming radio surveys that current and future radio facilities will provide. Indeed, we are at the dawn of a bright era for radio astronomy as many radio facilities have been recently upgraded or are in construction phase (e.g., APERTIF, ASKAP, JVLA, e-MERLIN, LOFAR, MeerKAT). Radio continuum surveys with these new facilities have been planned with the goal of studying the formation and evolution of galaxies and AGNs over cosmic time. It is therefore extremely important to be able to predict which kind of sources these facilities will be able to observe and what are the key data in other spectral windows necessary to complement the radio information to maximize the scientific output.

My work is based on radio observations performed with the VLA at 1.4 GHz on the E-CDFS. The average 5σ flux density limit is $37\mu\text{Jy}$ but reaches $32.5\mu\text{Jy}$ in the deepest part of the field. The spatial resolution (beam size) is $2''.8$ by $1''.6$. I contributed to the compilation of the source catalog that includes 883 radio objects, the large majority of which ($\sim 90\%$) below the mJy limit (see Chapter 2). Using a likelihood ratio technique, I identified the optical/IR counterparts of the radio sources with a completeness of 94%. For about 80% of the sources I was able to associate a redshift, 40% of which are spectroscopic (see Chapter 3). The counterparts and redshift catalog have been made publicly available (Bonzini et al., 2012) and represents one of the highest identification rate radio sample. This first part of my Thesis was crucial for the subsequent analysis and also demonstrated the key role played by MIR bands in the identification of radio sources. Indeed, a significant fraction of them (25%) are not detected even in deep HST optical surveys, probably due either to obscuration or to their high redshift. This is an important point when planning future radio surveys. In my work I used *Spitzer* data but this space telescope has now reduced capabilities after the exhaustion of the helium supply for the cryogenic system. The WISE satellite has similar spectral coverage to *Spitzer*, has observed the whole sky, but

the sensitivity is much lower and therefore would not be able to detect the counterparts of the majority of the sub-mJy radio sources. Some new deep radio surveys have been therefore planned on sky fields with deep *Spitzer* observation already available, like the JVLA COSMOS survey (PI: V. Smolcic). Future IR space telescopes like JWST and SPICA have been proposed and will have enough sensitivity to provide follow up for the faint radio sources detect by the SKA and its pathfinders (Padovani et al., 2011a) but, in case their construction will be approved, they will not be launched before ~ 2020 .

The second step of the project was aimed at disentangling the different radio populations that contribute to the faint radio sky (see Chapter 4). I developed a simple method that combines radio, MIR, and X-ray data, to efficiently separate the radio sources in three classes: SFGs, RQ AGNs and RL AGNs. I have shown that selection methods commonly used in the literature based on the optical properties of the radio sources (e.g., optical colors, optical to radio ratios) may miss a significant fraction (up to $\sim 70\%$) of AGNs, especially in the RQ population. I determined the relative contribution of the different classes of sources as a function of radio flux density confirming the overcoming of SFGs over AGNs below 0.1 mJy. Additionally, my work demonstrated that RQ AGNs become increasingly important for decreasing flux density and represent the dominant AGN population below 0.1 mJy as well. That means that in the upcoming radio surveys, that will be deeper than the observation considered in this work reaching the nanoJy sensitivity, the classical RL AGNs will be a minority of the sources and the population will be dominated by normal star forming galaxies and the bulk of the AGN class, i.e. the RQ ones.

I have shown that a crucial parameter to identify RL AGNs is the ratio between the $24\ \mu\text{m}$ and 1.4 GHz flux densities, while to separate RQ AGNs and SFGs other AGN activity indicators, like the X-ray luminosity or the MIR spectral shape, are necessary (Bonzini et al., 2013). The reason is that the origin of the radio emission in RQ AGNs and SFGs is the same, namely star-formation. This is one of the main results of my Thesis. The evidences in support of this conclusion are twofold; one is indirect, through the study of the host galaxy properties of the different classes of sources, further complemented by the estimation of their evolution and luminosity function (P. Padovani, M. Bonzini et al, in preparation). The second is more direct and based on the comparison of the SFR as traced by the FIR and radio luminosity (see Chapter 5). In more detail, I have characterized the host galaxies properties of my radio sources in terms of stellar masses, morphology and optical colors. Both RQ AGNs and SFGs are preferentially hosted in dusty late type (disks) objects, with smaller stellar masses and younger stellar populations compared to RL AGNs (Bonzini et al., 2013). This suggests that the RQ and RL AGN activity may represent two different evolutionary stages of the galaxy-BH co-evolution. It is plausible that the RQ phase occurs at earlier stages when the galaxy is still gas rich and actively forming stars. The radio activity of the black hole instead appears later when the galaxy has already formed the bulk of its stellar population, the gas supply is lower and the SF is considerably reduced. In such scenario it is also possible that the radio jets play a role in suppressing the SF and contribute to the quenching of the overall activity in the galaxy.

To directly prove that the main contribution to the radio emission in RQ AGNs is

due to the SF in their hosts, I computed the SFR from the FIR and radio luminosity and compared the results (see Chapter 5). The FIR luminosity has been estimated using *Herschel*/PACS data to better constrain the emission due to the dust heated by young stars and fitting the whole UV-to-FIR SED. I found good agreement between the two SFR tracers for both SFGs and RQ AGNs over about four orders of magnitude in SFR and in the redshift range $z = [0.1 - 3]$. For RL AGNs instead the agreement is poor as their radio power is enhanced by the presence of the jets. A very important implication of this result is that it is therefore possible to use the radio band to estimate the SFR even in the hosts of bright quasars, like many of the RQ AGNs in my sample. The AGN emission in these sources can over shine the stellar luminosity at optical and MIR wavelength, making the SFR estimate largely uncertain when derived from these bands. Moreover, as future surveys will go even deeper than the one presented in this Thesis, detecting many more RQ AGNs, they will represent powerful tools to study the SF properties of quasars hosts. Future samples of radio selected AGNs will be sufficiently numerous to allow detailed studies of their SF activity as a function, for example, of AGN luminosity or BH accretion rate.

The last part of the Thesis was dedicated to the comparison of my observations with an empirical model for the SF cosmic evolution. This model is based on few observational evidences like the existence of a main sequence (MS) of SFGs and the decrease from $z \sim 2$ of its average sSFR. According to the model, there are two main regimes of SF; one regular mode, triggered by secular processes, that is responsible for the bulk of the SFG population and a starburst regime possibly triggered by extreme events like major mergers. This model has been successfully applied to reproduce the observed FIR LF (e.g., Sargent et al., 2012).

I checked the consistency of my data with the model predictions building a mass selected mock catalog based on the model assumptions and "observing" it with the same flux density limit of the VLA observation. I was able to reproduce in the mock catalog both the radio number counts and the SF properties of the VLA sources. The comparison with the model had two main goals: to better control the impact of selection effects on the results, and to extrapolate from the flux density limit selected sample the properties of the underlying mass selected population. Indeed, the flux density limit of the VLA survey considered in this work ($\sim 37 \mu\text{Jy}$) allows me to probe the MS only at the high mass end while at low stellar masses and high redshift the radio observations detect only the most active systems. Hence, the observed fraction of starburst is about 20-25% but I estimated a contribution to the total SFR density of only $\sim 8\%$ when correcting for the selection effects. This is in agreement with what inferred from surveys at other wavelengths (especially FIR; e.g., Rodighiero et al., 2011; Gruppioni et al., 2013), and with the predictions of cosmological simulations (Hopkins et al., 2010). I also investigated the evolution of the starburst fraction as a function of cosmic time. My data suggest a steep rising of the starburst contribution as $(1+z)^2$ up to redshift $z \approx 1$ followed by a flattening. However, larger samples are necessary to better characterize the starburst fraction evolution, also in the local Universe.

I believe that my study of the SF properties of the VLA sources have demonstrated the possibility of using radio selected samples as powerful tools to investigate the cosmic SF history, alternative or complementary to FIR surveys. This is important as in the near

future there will be no other deep FIR surveys after the end of the *Herschel* mission, while deep radio observations on large areas are already on-going or have been proposed.

Finally, I have investigated the AGN content as a function of the distance from the main sequence. I found that the majority of RQ AGNs ($\sim 75\%$) are hosted in normal MS galaxies suggesting that the bulk of the AGN activity is triggered by secular processes. However, I also found that the relative fraction of RQ AGNs increases in the starburst regime indicating that the mechanisms responsible for the onset of the intense SF is also triggering efficient accretion onto the BH. Moreover, I found tentative evidence for an increase in the RQ AGN fraction just below the MS. These AGNs represent the perfect target for follow-up investigations aimed at detecting signatures of AGN feedback caught in the act. Indeed, if AGN activity is playing a role in shutting off SF, one might expect that its effect is stronger in sources that are going to leave the main sequence. In particular, IFU spectroscopic observations could be used to measure the outflow rate and outflow morphology using the [OIII] and $H\alpha$ maps, and to assess the impact that such feedback may have on the host galaxy SF, traced by the narrow component of $H\alpha$, as a function of the distance from the MS.

Concerning the RL AGNs population, an interesting output of my Thesis is that, while the majority of them are hosted in quenched galaxies, about a third of the RL AGN hosts have significant SF. It will be therefore intriguing to characterize the accretion properties of these BHs and their excitation state. Studies on low and high-excitation RL AGNs have been so far limited to the local Universe or to higher radio powers than those probed by my sample.

Bibliography

Aird J. et al., 2012, ApJ, 746, 90

Alexander D. M., Bauer F. E., Chapman S. C., Smail I., Blain A. W., Brandt W. N., Ivison R. J., 2005, ApJ, 632, 736

Alexander D. M., Swinbank A. M., Smail I., McDermid R., Nesvadba N. P. H., 2010, MNRAS, 402, 2211

Antonucci R., 1993, ARA&A, 31, 473

Baade W., Minkowski R., 1954, ApJ, 119, 206

Baldi R. D., Capetti A., 2008, A&A, 489, 989

Baldry I. K., Glazebrook K., Brinkmann J., Ivezić Ž., Lupton R. H., Nichol R. C., Szalay A. S., 2004, ApJ, 600, 681

Baldwin J. A., Phillips M. M., Terlevich R., 1981, PASP, 93, 5

Balestra I. et al., 2010, A&A, 512, A12

Barger A. J., Cowie L. L., Mushotzky R. F., Yang Y., Wang W. H., Steffen A. T., Capak P., 2005, AJ, 129, 578

Beckwith S. V. W. et al., 2006, AJ, 132, 1729

Begelman M. C., 1994, in G. V. Bicknell, M. A. Dopita, & P. J. Quinn, ed., The Physics of Active Galaxies. Astronomical Society of the Pacific Conference Series, Vol. 54, p. 51

Bell E. F., 2003, ApJ, 586, 794

Bell E. F. et al., 2004, ApJ, 608, 752

Berta S. et al., 2013, A&A, 551, A100

Bertin E., Arnouts S., 1996, A&AS, 117, 393

Best P. N., Heckman T. M., 2012, MNRAS, 421, 1569

- Best P. N., Kauffmann G., Heckman T. M., Brinchmann J., Charlot S., Ivezić Ž., White S. D. M., 2005, MNRAS, 362, 25
- Béthermin M., Dole H., Beelen A., Aussel H., 2010, A&A, 512, A78
- Béthermin M. et al., 2012, ApJ, 757, L23
- Biggs A. D. et al., 2011, MNRAS, 413, 2314
- Bolton J. G., Stanley G. J., Slee O. B., 1949, Nature, 164, 101
- Bongiorno A. et al., 2012, MNRAS, 427, 3103
- Bonzini M. et al., 2012, ApJS, 203, 15
- Bonzini M., Padovani P., Mainieri V., Kellermann K. I., Miller N., Rosati P., Tozzi P., Vattakunnel S., 2013, MNRAS, 436, 3759
- Bottini D. et al., 2005, PASP, 117, 996
- Bouché N. et al., 2010, ApJ, 718, 1001
- Bourne N., Dunne L., Ivison R. J., Maddox S. J., Dickinson M., Frayer D. T., 2011, MNRAS, 410, 1155
- Brammer G. B., van Dokkum P. G., Coppi P., 2008, ApJ, 686, 1503
- Brandt W. N., Hasinger G., 2005, ARA&A, 43, 827
- Bridle A. H., Hough D. H., Lonsdale C. J., Burns J. O., Laing R. A., 1994, AJ, 108, 766
- Brightman M., Nandra K., 2011, MNRAS, 413, 1206
- Broos P. S., Getman K. V., Povich M. S., Townsley L. K., Feigelson E. D., Garmire G. P., 2011, ApJS, 194, 4
- Bross S., Lapidoth A., Tinguely S., 2007, ArXiv e-prints
- Bruzual G., Charlot S., 2003, MNRAS, 344, 1000
- Buat V., Boselli A., Gavazzi G., Bonfanti C., 2002, A&A, 383, 801
- Buat V. et al., 2010, MNRAS, 409, L1
- Caldwell J. A. R. et al., 2008, ApJS, 174, 136
- Calzetti D., 2001, New A Rev., 45, 601

- Calzetti D., 2008, in J.H. Knapen, T.J. Mahoney, A. Vazdekis, eds, Pathways Through an Eclectic Universe. Astronomical Society of the Pacific Conference Series, Vol. 390, p. 121
- Calzetti D., Armus L., Bohlin R. C., Kinney A. L., Koornneef J., Storchi-Bergmann T., 2000, *ApJ*, 533, 682
- Calzetti D. et al., 2007, *ApJ*, 666, 870
- Cano-Díaz M., Maiolino R., Marconi A., Netzer H., Shemmer O., Cresci G., 2012, *A&A*, 537, L8
- Cardamone C. N. et al., 2010, *ApJS*, 189, 270
- Chabrier G., 2003, *PASP*, 115, 763
- Chartas G., Brandt W. N., Gallagher S. C., Garmire G. P., 2002, *ApJ*, 579, 169
- Chen C. T. J. et al., 2013, *ApJ*, 773, 3
- Cicone C. et al., 2014, *A&A*, 562, A21
- Ciliegi P., Zamorani G., Hasinger G., Lehmann I., Szokoly G., Wilson G., 2003, *A&A*, 398, 901
- Comastri A., Fiore F., 2004, *Ap&SS*, 294, 63
- Comastri A. et al., 2011, *A&A*, 526, L9
- Condon J. J., 1984, *ApJ*, 284, 44
- Condon J. J., 1992, *ARA&A*, 30, 575
- Condon J. J., 1997, *PASP*, 109, 166
- Condon J. J. et al., 2012, *ApJ*, 758, 23
- Conselice C. J. et al., 2011, *MNRAS*, 413, 80
- Cooper M. C. et al., 2012, *MNRAS*, 425, 2116
- Coppin K. E. K. et al., 2009, *MNRAS*, 395, 1905
- Crenshaw D. M., Kraemer S. B., Boggess A., Maran S. P., Mushotzky R. F., Wu C. C., 1999, *ApJ*, 516, 750
- Daddi E. et al., 2007a, *ApJ*, 670, 156
- Daddi E. et al., 2007b, *ApJ*, 670, 173

- Daddi E. et al., 2010a, *ApJ*, 714, L118
- Daddi E. et al., 2010b, *ApJ*, 713, 686
- Damen M. et al., 2011, *ApJ*, 727, 1
- Danielson A. L. R., Lehmer B. D., Alexander D. M., Brandt W. N., Luo B., Miller N., Xue Y. Q., Stott J. P., 2012, *MNRAS*, 422, 494
- De Breuck C., van Breugel W., Stanford S. A., Röttgering H., Miley G., Stern D., 2002, *AJ*, 123, 637
- de Jong T., Klein U., Wielebinski R., Wunderlich E., 1985, *A&A*, 147, L6
- de Zotti G., Massardi M., Negrello M., Wall J., 2010, *A&A Rev.*, 18, 1
- Del Moro A. et al., 2013, *A&A*, 549, A59
- Di Matteo T., Springel V., Hernquist L., 2005, *Nature*, 433, 604
- Dickey J. M., Salpeter E. E., 1984, *ApJ*, 284, 461
- Dickinson M., FIDEL Team, 2007, in American Astronomical Society Meeting Abstracts. Bulletin of the American Astronomical Society, Vol. 39, p. 822
- Dickinson M., Giavalisco M., The Goods Team, 2003, in R. Bender, A. Renzini, eds, *The Mass of Galaxies at Low and High Redshift*. p. 324
- Diolaiti E., Bendinelli O., Bonaccini D., Close L., Currie D., Parmeggiani G., 2000a, *A&AS*, 147, 335
- Diolaiti E., Bendinelli O., Bonaccini D., Close L. M., Currie D. G., Parmeggiani G., 2000b, in P.L. Wizinowich, ed., *Adaptive Optical Systems Technology*. Society of Photo-Optical Instrumentation Engineers (SPIE) Conference Series, Vol. 4007, pp. 879–888
- Domínguez Sánchez H. et al., 2012, *MNRAS*, 426, 330
- Donley J. L., Rieke G. H., Pérez-González P. G., Barro G., 2008, *ApJ*, 687, 111
- Donley J. L. et al., 2012, *ApJ*, 748, 142
- Dunlop J. S., McLure R. J., Kukula M. J., Baum S. A., O’Dea C. P., Hughes D. H., 2003, *MNRAS*, 340, 1095
- Dye S. et al., 2009, *ApJ*, 703, 285
- Elbaz D. et al., 2007, *A&A*, 468, 33
- Elbaz D. et al., 2011, *A&A*, 533, A119

- Elvis M. et al., 1994, *ApJS*, 95, 1
- Engel H. et al., 2010, *ArXiv e-prints*
- Evans D. A., Worrall D. M., Hardcastle M. J., Kraft R. P., Birkinshaw M., 2006, *ApJ*, 642, 96
- Fabbiano G., 1989, *ARA&A*, 27, 87
- Fabbiano G., 2006, *ARA&A*, 44, 323
- Fabian A. C., 2012, *ARA&A*, 50, 455
- Fan X., 1999, *AJ*, 117, 2528
- Fanaroff B. L., Riley J. M., 1974, *MNRAS*, 167, 31P
- Fardal M. A., Katz N., Weinberg D. H., Davé R., 2007, *MNRAS*, 379, 985
- Fazio G. G. et al., 2004, *ApJS*, 154, 10
- Feldmann R. et al., 2006, *MNRAS*, 372, 565
- Feruglio C., Maiolino R., Piconcelli E., Menci N., Aussel H., Lamastra A., Fiore F., 2010, *A&A*, 518, L155
- Fiore F. et al., 2008, *ApJ*, 672, 94
- Fiore F. et al., 2009, *ApJ*, 693, 447
- Fiore F. et al., 2012, *A&A*, 537, A16
- Fomalont E. B., Kellermann K. I., Wall J. V., Weistrop D., 1984, *Science*, 225, 23
- Fontana A. et al., 2004, *A&A*, 424, 23
- Förster Schreiber N. M. et al., 2014, *ApJ*, 787, 38
- Gabor J. M. et al., 2009, *ApJ*, 691, 705
- Gandhi P., Horst H., Smette A., Hönig S., Comastri A., Gilli R., Vignali C., Duschl W., 2009, *A&A*, 502, 457
- Gawiser E. et al., 2006, *ApJ*, 642, L13
- Gehrels N., 1986, *ApJ*, 303, 336
- Genzel R. et al., 2010, *MNRAS*, 407, 2091
- Genzel R. et al., 2011, *ApJ*, 733, 101

- Giacconi R. et al., 2002, *ApJS*, 139, 369
- Giavalisco M. et al., 2004, *ApJ*, 600, L93
- Giroletti M., Panessa F., 2009, *ApJ*, 706, L260
- Grazian A. et al., 2006, *A&A*, 449, 951
- Griffith R. L. et al., 2012, *ApJS*, 200, 9
- Grimm H. J., Gilfanov M., Sunyaev R., 2003, *MNRAS*, 339, 793
- Grogin N. A. et al., 2011, *ApJS*, 197, 35
- Gruppioni C. et al., 2013, *MNRAS*, 432, 23
- Gürkan G., Hardcastle M. J., Jarvis M. J., 2013, *ArXiv e-prints*
- Hardcastle M. J., Evans D. A., Croston J. H., 2007a, *MNRAS*, 376, 1849
- Hardcastle M. J., Evans D. A., Croston J. H., 2007b, *MNRAS*, 376, 1849
- Harrison C. M., Alexander D. M., Mullaney J. R., Swinbank A. M., 2014, *ArXiv e-prints*
- Harrison C. M. et al., 2012, *ApJ*, 760, L15
- Hasinger G., Miyaji T., Schmidt M., 2005, *A&A*, 441, 417
- Hatziminaoglou E. et al., 2005, *AJ*, 129, 1198
- Hatziminaoglou E. et al., 2010, *A&A*, 518, L33
- Häußler B., Barden M., Bamford S. P., Rojas A., 2011, in I.N. Evans, A. Accomazzi, D.J. Mink, A.H. Rots, eds, *Astronomical Data Analysis Software and Systems XX*. Astronomical Society of the Pacific Conference Series, Vol. 442, p. 155
- Häussler B. et al., 2007, *ApJS*, 172, 615
- Hazard C., Mackey M. B., Shimmins A. J., 1963, *Nature*, 197, 1037
- Heckman T., Best P., 2014, *ArXiv e-prints*
- Heckman T. M., Robert C., Leitherer C., Garnett D. R., van der Rydt F., 1998, *ApJ*, 503, 646
- Helou G., Soifer B. T., Rowan-Robinson M., 1985, *ApJ*, 298, L7
- Hey J. S., 1946, *Nature*, 157, 47
- Hildebrandt H. et al., 2006, *A&A*, 452, 1121

- Ho L. C., 2008, *ARA&A*, 46, 475
- Hogg D. W. et al., 2002, *AJ*, 124, 646
- Hopkins A. M., Beacom J. F., 2006, *ApJ*, 651, 142
- Hopkins A. M., Connolly A. J., Haarsma D. B., Cram L. E., 2001, *AJ*, 122, 288
- Hopkins P. F., Hernquist L., Cox T. J., Kereš D., 2008, *ApJS*, 175, 356
- Hopkins P. F., Younger J. D., Hayward C. C., Narayanan D., Hernquist L., 2010, *MNRAS*, 402, 1693
- Hoyle F., Fowler W. A., 1963, *MNRAS*, 125, 169
- Huynh M. T., Jackson C. A., Norris R. P., Prandoni I., 2005, *AJ*, 130, 1373
- Huynh M. T., Hopkins A. M., Lenc E., Mao M. Y., Middelberg E., Norris R. P., Randall K. E., 2012, *MNRAS*, 426, 2342
- Ibar E., Ivison R. J., Best P. N., Coppin K., Pope A., Smail I., Dunlop J. S., 2010, *MNRAS*, 401, L53
- Ilbert O. et al., 2010, *ApJ*, 709, 644
- Ilbert O. et al., 2013, *A&A*, 556, A55
- Ivison R. J. et al., 2010a, *MNRAS*, 402, 245
- Ivison R. J. et al., 2010b, *A&A*, 518, L31
- Ivison R. J. et al., 2012, *MNRAS*, 425, 1320
- Janssen R. M. J., Röttgering H. J. A., Best P. N., Brinchmann J., 2012, *A&A*, 541, A62
- Kartaltepe J. S. et al., 2010, *ApJ*, 721, 98
- Kauffmann G. et al., 2003, *MNRAS*, 346, 1055
- Kellermann K. I., Pauliny-Toth I. I. K., 1969, *ApJ*, 155, L71
- Kellermann K. I., Sramek R., Schmidt M., Shaffer D. B., Green R., 1989, *AJ*, 98, 1195
- Kellermann K. I., Fomalont E. B., Mainieri V., Padovani P., Rosati P., Shaver P., Tozzi P., Miller N., 2008, *ApJS*, 179, 71
- Kennicutt R. C., Evans N. J., 2012, *ARA&A*, 50, 531
- Kennicutt Jr. R. C., 1983, *ApJ*, 272, 54

- Kennicutt Jr. R. C., 1998a, ARA&A, 36, 189
- Kennicutt Jr. R. C., 1998b, ApJ, 498, 541
- Kimball A. E., Kellermann K. I., Condon J. J., Ivezić Ž., Perley R. A., 2011, ApJ, 739, L29
- King A., 2003, ApJ, 596, L27
- Koekemoer A. M. et al., 2011, ApJS, 197, 36
- Kormendy J., Ho L. C., 2013, ARA&A, 51, 511
- Lacki B. C., Thompson T. A., 2010, ApJ, 717, 196
- Lacki B. C., Thompson T. A., Quataert E., 2010, ApJ, 717, 1
- Lacy M. et al., 2004, ApJS, 154, 166
- Laing R. A., Jenkins C. R., Wall J. V., Unger S. W., 1994, in G.V. Bicknell, M.A. Dopita, P.J. Quinn, eds, The Physics of Active Galaxies. Astronomical Society of the Pacific Conference Series, Vol. 54, p. 201
- Le Fèvre O. et al., 2004, A&A, 428, 1043
- Le Floch E. et al., 2005, ApJ, 632, 169
- Lehmer B. D. et al., 2005, ApJS, 161, 21
- Lehmer B. D. et al., 2012, ApJ, 752, 46
- Lilly S. J., Longair M. S., 1984, MNRAS, 211, 833
- Lilly S. J., Le Fevre O., Hammer F., Crampton D., 1996, ApJ, 460, L1
- Lilly S. J., Carollo C. M., Pipino A., Renzini A., Peng Y., 2013, ApJ, 772, 119
- Luo B. et al., 2008, ApJS, 179, 19
- Luo B. et al., 2010, ApJS, 187, 560
- Luo B. et al., 2011, ApJ, 740, 37
- Lutz D., 2014, ArXiv e-prints
- Lutz D. et al., 2011, A&A, 532, A90
- Lynden-Bell D., 1969, Nature, 223, 690
- Lynden-Bell D., Pringle J. E., 1974, MNRAS, 168, 603

- Madau P., Pozzetti L., Dickinson M., 1998, *ApJ*, 498, 106
- Magnelli B., Elbaz D., Chary R. R., Dickinson M., Le Borgne D., Frayer D. T., Willmer C. N. A., 2009, *A&A*, 496, 57
- Magnelli B., Elbaz D., Chary R. R., Dickinson M., Le Borgne D., Frayer D. T., Willmer C. N. A., 2011, *A&A*, 528, A35
- Magnelli B. et al., 2012, *A&A*, 539, A155
- Magnelli B. et al., 2013, *A&A*, 553, A132
- Mainieri V. et al., 2008, *ApJS*, 179, 95
- Mainieri V. et al., 2011, *A&A*, 535, A80
- Mao M. Y., Huynh M. T., Norris R. P., Dickinson M., Frayer D., Helou G., Monkiewicz J. A., 2011, *ApJ*, 731, 79
- Mao M. Y. et al., 2012, *MNRAS*, 426, 3334
- Maraschi L., Chiappetti L., Falomo R., Garilli B., Malkan M., Tagliaferri G., Tanzi E. G., Treves A., 1991, *ApJ*, 368, 138
- Martínez-Sansigre A., Rawlings S., Lacy M., Fadda D., Marleau F. R., Simpson C., Willott C. J., Jarvis M. J., 2005, *Nature*, 436, 666
- Mauch T., Sadler E. M., 2007, *MNRAS*, 375, 931
- Mauduit J. C. et al., 2012, *PASP*, 124, 714
- Menci N., Fiore F., Puccetti S., Cavaliere A., 2008, *ApJ*, 686, 219
- Middelberg E. et al., 2011, *A&A*, 526, A74
- Miller N. A., Fomalont E. B., Kellermann K. I., Mainieri V., Norman C., Padovani P., Rosati P., Tozzi P., 2008, *ApJS*, 179, 114
- Miller N. A. et al., 2013, *ApJS*, 205, 13
- Miller P., Rawlings S., Saunders R., 1993a, *MNRAS*, 263, 425
- Miller P., Rawlings S., Saunders R., 1993b, *MNRAS*, 263, 425
- Minkowski R., 1960, *PASP*, 72, 354
- Moncelsi L. et al., 2011, *ApJ*, 727, 83
- Mor R., Netzer H., 2012, *MNRAS*, 420, 526

- Morić I., Smolčić V., Kimball A., Riechers D. A., Ivezić Ž., Scoville N., 2010, *ApJ*, 724, 779
- Moustakas J., Kennicutt Jr. R. C., Tremonti C. A., 2006, *ApJ*, 642, 775
- Mullaney J. R. et al., 2012, *MNRAS*, 419, 95
- Muxlow T. W. B. et al., 2005, *MNRAS*, 358, 1159
- Nandra K., Pounds K. A., 1994, *MNRAS*, 268, 405
- Nandra K. et al., 2007, *ApJ*, 660, L11
- Narayan R., Quataert E., 2005, *Science*, 307, 77
- Narayan R., Yi I., 1994, *ApJ*, 428, L13
- Narayan R., Yi I., 1995, *ApJ*, 444, 231
- Nesvadba N. P. H., Lehnert M. D., Eisenhauer F., Gilbert A., Tecza M., Abuter R., 2006, *ApJ*, 650, 693
- Nesvadba N. P. H., Lehnert M. D., De Breuck C., Gilbert A., van Breugel W., 2007, *A&A*, 475, 145
- Nesvadba N. P. H., Lehnert M. D., De Breuck C., Gilbert A. M., van Breugel W., 2008, *A&A*, 491, 407
- Nesvadba N. P. H. et al., 2010, *ArXiv e-prints*
- Netzer H. et al., 2007, *ApJ*, 666, 806
- Neugebauer G., Green R. F., Matthews K., Schmidt M., Soifer B. T., Bennett J., 1987, *ApJS*, 63, 615
- Noeske K. G. et al., 2007, *ApJ*, 660, L43
- Nonino M. et al., 2009, *ApJS*, 183, 244
- Nordon R. et al., 2013, *ApJ*, 762, 125
- Norman C. et al., 2004, *ApJ*, 607, 721
- Norris R. P. et al., 2006, *AJ*, 132, 2409
- Norris R. P. et al., 2013, *PASA*, 30, e020
- Oliver S. J. et al., 2012, *MNRAS*, 424, 1614
- Olsen L. F. et al., 2006, *A&A*, 456, 881

- Owen F. N., Morrison G. E., 2008, *AJ*, 136, 1889
- Padovani P., 2011, *MNRAS*, 411, 1547
- Padovani P., Miller N., Kellermann K. I., Mainieri V., Rosati P., Tozzi P., 2011a, *ApJ*, 740, 20
- Padovani P., Miller N., Kellermann K. I., Mainieri V., Rosati P., Tozzi P., 2011b, *ApJ*, 740, 20
- Padovani P., Mainieri V., Tozzi P., Kellermann K. I., Fomalont E. B., Miller N., Rosati P., Shaver P., 2009, *ApJ*, 694, 235
- Page M. J. et al., 2012, *Nature*, 485, 213
- Pannella M. et al., 2009, *ApJ*, 698, L116
- Paolillo M., Schreier E. J., Giacconi R., Koekemoer A. M., Grogin N. A., 2004, *ApJ*, 611, 93
- Peng Y. j. et al., 2010, *ApJ*, 721, 193
- Perley R. A., Chandler C. J., Butler B. J., Wrobel J. M., 2011, *ApJ*, 739, L1
- Perola G. C., Matt G., Cappi M., Fiore F., Guainazzi M., Maraschi L., Petrucci P. O., Piro L., 2002, *A&A*, 389, 802
- Polletta M., Weedman D., Hönig S., Lonsdale C. J., Smith H. E., Houck J., 2008, *ApJ*, 675, 960
- Polletta M. et al., 2007, *ApJ*, 663, 81
- Pope A. et al., 2008, *ApJ*, 675, 1171
- Pozzetti L. et al., 2007, *A&A*, 474, 443
- Prandoni I., Gregorini L., Parma P., de Ruiter H. R., Vettolani G., Zanichelli A., Wieringa M. H., Ekers R. D., 2001, *A&A*, 369, 787
- Prevot M. L., Lequeux J., Prevot L., Maurice E., Rocca-Volmerange B., 1984, *A&A*, 132, 389
- Rafferty D. A., Brandt W. N., Alexander D. M., Xue Y. Q., Bauer F. E., Lehmer B. D., Luo B., Papovich C., 2011, *ApJ*, 742, 3
- Ranalli P., Comastri A., Setti G., 2003, *A&A*, 399, 39
- Ravikumar C. D. et al., 2007, *A&A*, 465, 1099

- Retzlaff J., Rosati P., Dickinson M., Vandame B., Rit   C., Nonino M., Cesarsky C., GOODS Team, 2010, *A&A*, 511, A50
- Richards G. T. et al., 2001, *AJ*, 121, 2308
- Richards G. T. et al., 2006, *ApJS*, 166, 470
- Rieke G. H. et al., 2004, *ApJS*, 154, 25
- Rix H. W. et al., 2004, *ApJS*, 152, 163
- Rodighiero G. et al., 2011, *ApJ*, 739, L40
- Rosa-Gonz  lez D., Terlevich E., Terlevich R., 2002, *MNRAS*, 332, 283
- Rosario D. J. et al., 2012, *A&A*, 545, A45
- Roseboom I. G., Lawrence A., Elvis M., Petty S., Shen Y., Hao H., 2013, *MNRAS*, 429, 1494
- Roseboom I. G. et al., 2012, *MNRAS*, 426, 1782
- Rupke D. S. N., Veilleux S., 2011, *ApJ*, 729, L27
- Ryle M., Scheuer P. A. G., 1955, *Royal Society of London Proceedings Series A*, 230, 448
- Salim S. et al., 2007, *ApJS*, 173, 267
- Sandage A., Luyten W. J., 1969, *ApJ*, 155, 913
- Sandage A., V  ron P., Wyndham J. D., 1965, *ApJ*, 142, 1307
- Sanders D. B., Mirabel I. F., 1996, *ARA&A*, 34, 749
- Sanders D. B., Soifer B. T., Elias J. H., Neugebauer G., Matthews K., 1988, *ApJ*, 328, L35
- Santini P. et al., 2009, *A&A*, 504, 751
- Sargent M. T., B  thermin M., Daddi E., Elbaz D., 2012, *ApJ*, 747, L31
- Sargent M. T. et al., 2010, *ApJS*, 186, 341
- Schawinski K., Thomas D., Sarzi M., Maraston C., Kaviraj S., Joo S. J., Yi S. K., Silk J., 2007, *MNRAS*, 382, 1415
- Schawinski K. et al., 2014, *MNRAS*, 440, 889
- Schinnerer E. et al., 2010, *ApJS*, 188, 384
- Schleicher D. R. G., Beck R., 2013, *ArXiv e-prints*

- Schmidt M., 1963, *Nature*, 197, 1040
- Scodeggio M. et al., 2005, *PASP*, 117, 1284
- Scott K. S. et al., 2010, *MNRAS*, 405, 2260
- Sérsic J. L., 1963, *Boletín de la Asociación Argentina de Astronomía La Plata Argentina*, 6, 41
- Seymour N. et al., 2008, *MNRAS*, 386, 1695
- Shakeshaft J. R., Ryle M., Baldwin J. E., Elsmore B., Thomson J. H., 1955, *MmRAS*, 67, 106
- Shakura N. I., Sunyaev R. A., 1973, *A&A*, 24, 337
- Shankar F., Weinberg D. H., Miralda-Escudé J., 2009, *ApJ*, 690, 20
- Shu F. H., 1991, *Physics of Astrophysics, Vol. I. University Science Books*
- Silk J., Rees M. J., 1998, *A&A*, 331, L1
- Silverman J. D. et al., 2010, *ApJS*, 191, 124
- Smolčić V. et al., 2006, *MNRAS*, 371, 121
- Smolčić V. et al., 2008, *ApJS*, 177, 14
- Sopp H. M., Alexander P., 1991, *MNRAS*, 251, 14P
- Springel V., Di Matteo T., Hernquist L., 2005, *MNRAS*, 361, 776
- Stern D., 2000, *PASP*, 112, 1411
- Stern D. et al., 2005, *ApJ*, 631, 163
- Strateva I. et al., 2001, *AJ*, 122, 1861
- Sturm E. et al., 2011, *ApJ*, 733, L16
- Sullivan M., Mobasher B., Chan B., Cram L., Ellis R., Treyer M., Hopkins A., 2001, *ApJ*, 558, 72
- Sutherland W., Saunders W., 1992, *MNRAS*, 259, 413
- Symeonidis M. et al., 2013, *MNRAS*, 433, 1015
- Szokoly G. P. et al., 2004, *ApJS*, 155, 271
- Tacconi L. J. et al., 2008, *ApJ*, 680, 246

- Taylor E. N. et al., 2009, *ApJS*, 183, 295
- Tombesi F., Cappi M., Reeves J. N., Palumbo G. G. C., Yaqoob T., Braito V., Dadina M., 2010, *A&A*, 521, A57
- Tozzi P. et al., 2009, *ApJ*, 698, 740
- Treister E. et al., 2009, *ApJ*, 693, 1713
- Truch M. D. P. et al., 2009, *ApJ*, 707, 1723
- Turner T. J., 1988, Ph.D. thesis, Leicester Univ. (England).
- Ueda Y., Akiyama M., Ohta K., Miyaji T., 2003, *ApJ*, 598, 886
- Ueda Y., Akiyama M., Hasinger G., Miyaji T., Watson M. G., 2014, *ApJ*, 786, 104
- Urry C. M., Padovani P., 1995, *PASP*, 107, 803
- Vanzella E. et al., 2008, *A&A*, 478, 83
- Vattakunnel S. et al., 2012, *MNRAS*, 420, 2190
- Wagner A. Y., Bicknell G. V., 2011, *ApJ*, 728, 29
- Wall J. V., 1994, *Australian Journal of Physics*, 47, 625
- Wang B., Heckman T. M., 1996, *ApJ*, 457, 645
- Wei A. et al., 2009, *ApJ*, 707, 1201
- White R. L., Becker R. H., Helfand D. J., Gregg M. D., 1997, *ApJ*, 475, 479
- Windhorst R. A., van Heerde G. M., Katgert P., 1984, *A&AS*, 58, 1
- Wolf C., Hildebrandt H., Taylor E. N., Meisenheimer K., 2008, *A&A*, 492, 933
- Wolf C. et al., 2004, *A&A*, 421, 913
- Wuyts S. et al., 2011a, *ApJ*, 742, 96
- Wuyts S. et al., 2011b, *ApJ*, 738, 106
- Xue Y. Q. et al., 2011, *ApJS*, 195, 10
- Yan L. et al., 2007, *ApJ*, 658, 778
- Yun M. S., Reddy N. A., Condon J. J., 2001, *ApJ*, 554, 803
- Yun M. S. et al., 2012, *MNRAS*, 420, 957
- Zubovas K., King A., 2012, *ApJ*, 745, L34
- Zubovas K., Nayakshin S., King A., Wilkinson M., 2013, *MNRAS*, 433, 3079

Acknowledgments

First of all, I would like to thank my ESO supervisors, Vincenzo Mainieri and Paolo Padovani, for all the time and effort they have put into guiding me through my entire Ph.D.. Thanks for always being there, ready for answering my questions and teaching me. Then, a special thanks goes to all my collaborators, in particular Piero Rosati, Neal Miller, Ken Kellermann, Paolo Tozzi and Shaji Vattakunnel, for the useful discussions and the careful revisions of my papers. I acknowledge my LMU supervisor, Prof. Joe Mohr, for his help, and Eric Emsellem for his continuous support especially during my maternity and after the birth of my baby.

Thanks to Luca, Carlo, Dominika, Anja, Anna, Oscar, Guillaume, Pierr-Yves, Iva, just to mention some of all the great friends I meet between the ESO students and fellows during these years. A special thanks to all my numerous office mates, in particular Ulf, Lu, Nora, Alvaro, Nikolay for making me always feel home. Thanks to Lucia e Giovanni for being such a friendly and welcoming presence for me in Garching from the very beginning. Finally, my greatest thanks goes to Giovanni and my little Teresa.

Margherita BONZINI

Curriculum Vitae

Personal Data

Date of birth: 26th December 1985
Nationality: Italian
Family status: Married, one child
Home institution: European Southern Observatory (ESO)
Address: Karl-Schwarzschild-Strasse, 2
85748 Garching bei München, Germany
E-mail: mbonzini@eso.org
Current position: PhD student

Research Interests

Active Galactic Nuclei (AGN), evolution of galaxies, observational cosmology, feedback mechanisms between AGN and their surrounding environments, multi-wavelength observations.

Education

July 2014	PhD in Astronomy Thesis: “ <i>The sub-mJy population in the Extended Chandra Deep Field South</i> ”; advisors: Dr. Mainieri V., Prof. Mohr J.; International Max Planck Research School; ESO/Ludwig-Maximilians-Universität Munich, Germany
Apr. 2010	Master Degree in Astrophysics Thesis: “ <i>Lifting the veil of the host galaxy to reveal the dust in obscured quasars at high redshift</i> ”; advisors: Prof. Lodato G., Dr. Polletta M.; Universit degli Studi, Milan, Italy; Grade: 110/110 <i>cum laude</i>
Feb. 2008	Bachelor Degree in Physics Thesis: <i>Simulated performances of lens horns to study the polarization of the Cosmic Microwave Background</i> ; advisors: Dr. Mennella A., Dr. Villa F.; Universit degli Studi, Milan, Italy; Grade: 110/110 <i>cum laude</i>
Jul. 2004	Scientific High School Diploma Liceo Scientifico “G.B. Grassi”, Saronno , Italy; Grade: 100/100

Publications

First author:

- “*Star formation rate of sub-mJy radio sources*” **Bonzini, M.**; Mainieri, V.; Padovani, P.; Anderani, P.; Miller, N.; Berta, S.; Bethérmin, M.; Lutz, D.; Righiero, G.; Rosario, D.; Tozzi, P.; Submitted to MNRAS.
- “*The sub-mJy radio sky in the Extended Chandra Deep Field South: source population*” **Bonzini, M.**; Padovani, P.; Mainieri, V.; Kellermann, K. I.; Miller, N.; Rosati, P.; Tozzi, P.; Vattakunnel, S., 2013, Monthly Notices of the Royal Astronomical Society, 436, 2342
- “*The Sub-mJy Radio Population of the E-CDFS: Optical and Infrared Counterpart Identification*” **Bonzini, M.**; Mainieri, V.; Padovani, P.; Kellermann, K. I.; Miller, N.; Rosati, P.; Tozzi, P.; Vattakunnel, S.; Balestra, I.; Brandt, W. N.; Luo, B.; Xue, Y. Q., 2012, Astrophysical Journal Supplement Series, 203, 15

Co-author:

- “*Linking the X-ray and infrared properties of star-forming galaxies at $z < 1.5$* ”, Symeonidis, M.; Georgakakis, A.; Page, M. J.; Bock, J.; **Bonzini, M.**; Buat, V.; Farrah, D.; Franceschini, A.; Lutz, D.; Magnelli, B.; Magdis, G.; Oliver, S.J.; Pannella, M.; Paolillo, M.; Rosario, D.; Roseboom, I.G.; Vaccari, M.; Villforth, C.; Submitted to MNRAS
- “*The AGN content of deep radio surveys and radio emission in radio-quiet AGN. Why every astronomer should care about deep radio fields*”, Padovani, P.; **Bonzini, M.**; Miller, N.; Kellermann, K. I.; Mainieri, V.; Rosati, P.; Tozzi, P.; Vattakunnel, S., 2014, to appear in IAU S304 conference proceedings, arXiv:1401.1342
- “*The Very Large Array 1.4 GHz Survey of the Extended Chandra Deep Field South: Second Data Release*”, Miller, N. A.; **Bonzini, M.**; Fomalont, E. B.; Kellermann, K. I.; Mainieri, V.; Padovani, P.; Rosati, P.; Tozzi, P.; Vattakunnel, S., 2013, Astrophysical Journal Supplement Series, 205, 13
- “*The radio-X-ray relation as a star formation indicator: results from the Very Large Array-Extended Chandra Deep Field-South*”. Vattakunnel, S.; Tozzi, P.; Matteucci, F.; Padovani, P.; Miller, N.; **Bonzini, M.**; Mainieri, V.; Paolillo, M.; Vincoletto, L.; Brandt, W. N.; Luo, B.; Kellermann, K.I.; Xue, Y.Q., 2012, Monthly Notices of the Royal Astronomical Society, 420, 2190

Workshops & Conferences

- May. 2014 *Multiwavelength-surveys: Galaxy formation and evolution from the early universe to today*, Dubrovnik, Croatia, (Contributed Talk)
- Feb. 2014 *Transformational Science with the SKA: Synergies with ALMA and other contemporary instruments*, Stellenbosch, South Africa, (Contributed Talk)
- Oct. 2013 *Multi-wavelength AGN Surveys and Studies – IAU Symposium*, Byurakan, Armenia (Poster)
- Aug. 2013 *The Co-evolution of Black Holes and Galaxies – EWASS Symposium*, Turku, Finland (Poster)
- Sep. 2012 *Active Galactic Nuclei X*, Universit La Sapienza, Rome, Italy (Contributed Talk)
- Aug. 2012 *Galactic Scale Star Formation*, Heidelberg, Germany (Poster)
- Dec. 2011 *Star Formation Across The Universe*, ESO workshop , Garching, Germany (Contributed Talk)
- Sep. 2011 *Starburst-AGN Connection Under the Multi-wavelength Limelight*, ESA, Madrid, Spain (Contributed Talk)
- Jul. 2011 *Galaxy Formation*, Durham University, United Kingdom (Poster)
- Jul. 2011 *Combined Radio/X-rays Approaches to Relativistic Astrophysics – JENAM 2011*, St. Petersburg, Russia (Contributed Talk)
- May 2010 *Active Galactic Nuclei IX: Black Holes and Revelations*, Ferrara, Italy (Contributed Talk)

Seminars

- Mar. 2014 *Star formation and Black hole activity in the faint radio sky*, University of Zagreb, Croatia
- Oct. 2013 *Star formation rate in AGN host galaxies*, INAF-IASF Milan, Italy
- Oct. 2012 *The sub-mJy Radio Sky: Star Formation and Black Hole Activity – USM Colloquium*, Universitäts-Sternwarte München, Germany
- Sep. 2012 *Star formation and BH activity in the sub-mJy radio population.*, CEA Saclay, Paris, France
- Jul. 2012 *Host galaxy properties of radio selected AGN – IMPRS Evaluation Workshop*, Max Planck Institute für Extraterrestrische Physik, Garching, Germany (Invited Talk)
- Nov. 2011 *The sub-mJy radio population in the Extended Chandra Deep Field Sky – IMPRS Seminar*, Max Planck Institute für Extraterrestrische Physik, Garching, Germany
- Since 2011 Numerous small talks at ESO (Journal Club, Student Session, Science Day), Garching, Germany

Proposals and Schools

- ALMA Cycle 2, Co-I, *Cold gas in AGNs hosts: walking along the 'main-sequence' of star-forming galaxies.*, (PI: V. Mainieri), Accepted
- KMOS/VLT, P94, Co-I *Linking inflow and outflow mass rates in supermassive black holes: towards a physical understanding of AGN feedback.*, (PI:v. Mainieri), Submitted
- ALMA Community Days: tutorials for the ALMA Observing Tool and the Simulators, November 2013, ESO Garching.
- Data Analysis School: VIPERS redshift measurements, November 2009, IASF-INAF Milan.

Organization activities

Nov. 2012	Cooperated in the organization of the ESO workshop: <i>Island in the Cosmos: multi-wavelength view of galaxy formation and evolution</i> , (SOC and LOC), ESO, Garching, Germany.
2011 - 2012	ESO student representative.
Nov. 2011	ESO Observing Programmes Committee (OPC) assistant for Period 87.

Professional Experiences

Since 2014	referee for Monthly Notices of the Royal Astronomical Society
------------	---

Teaching:

2011	Tutor for Maths and Physics at the Scientific High School " <i>C.Gnocchi</i> ", Carate, Italy
Since 2007	Taught lessons on astrophysical topics in schools, from High School to Primary

Educational Outreach:

Autumn 2009	Operated telescope for students and general public, International Year of Astronomy 2009, Triuggio, Italy
2006 - 2009	Euresis: Association for the Promotion of Scientific Endeavour, Milan

Cooperated in creation and presented scientific exhibitions: *Things never seen before. Galileo: The fascinating and laborious birth of a new gaze on the world, Light, eyes, meaning: the human experience of seeing, Why so many lights? The Milky Way amid science, history and art* .

2007 - 2008 Organized and acted theatrical performance for children about matter properties and light: *Shed Light on Matter*, in cooperation with Prof M. Carpineti, Prof. M. Giliberti and Prof N. Ludwig of the Physics Department, University of Milan

Computer Skills

Virtual Observatory tools:	Aladin, TOPCAT (Tool for operations on catalogues and tables)
Astronomical Packages:	DS9, EZ (Tool for Automatic Spectral Parameters Measurement), VIPGI (VIMOS interactive pipeline graphical interface), GRASP9 (General Reflector Antenna Software Package), SRSR (Simulation software for axisymmetrical radiating structures)
Programming Languages:	IDL, Fortran, C++
Computer Platforms:	Mac, Linux, Unix, Windows

Languages

ITALIAN:	Native
ENGLISH:	Fluent
GERMAN:	Conversational